A Quantitative Analysis of Finite-Rate Surface Ablation Models for Hypersonic Flight

By

ERIN ELIZABETH MUSSONI

DISSERTATION

Submitted in partial satisfaction of the requirements for the degree of

DOCTOR OF PHILOSOPHY

in

Mechanical and Aerospace Engineering

in the

OFFICE OF GRADUATE STUDIES

of the

UNIVERSITY OF CALIFORNIA

DAVIS

Approved:

Jean-Pierre Delplanque, Chair

Stephen Robinson

Benjamin Shaw

Ross Wagnild

Committee in Charge

2024

Sandia National Laboratories is a multimission laboratory managed and operated by National Technology & Engineering Solutions of Sandia, LLC, a wholly owned subsidiary of Honeywell International Inc., for the U.S. Department of Energy's National Nuclear Security Administration under contract DE-NA0003525.

To Esther, David, Jason, and Charlie (the cat)

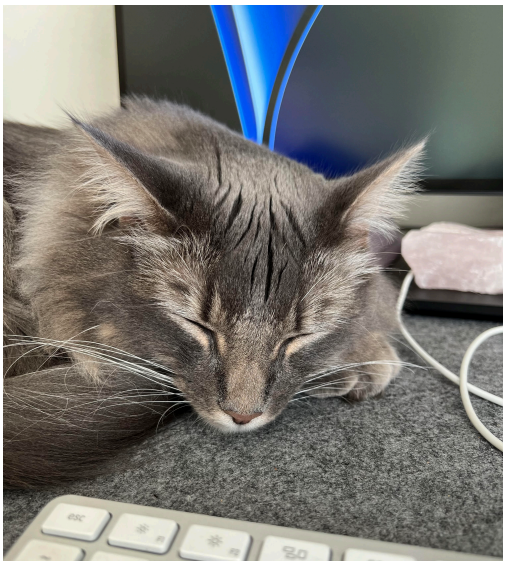

Contents

List of Figures

List of Tables

A Quantitative Analysis of Finite-Rate Surface Ablation Models for Hypersonic Flight

Abstract

During hypersonic flight, a vehicle heat shield encounters harsh aerothermal environments and undergoes complex surface chemical and physical processes that impact its mass loss, shape change, and surface heating responses. Thermal protection system design requires credible ablation models that describe the gas-surface interactions under these extreme conditions. An uncertainty quantification methodology was implemented to characterize legacy and recently developed air/carbon surface ablation models for nonequilibrium high-enthalpy flow conditions.

Validation assessments compared model predictions of carbon monoxide, a primary ablation product, quantities in the boundary layer with measured laser absorption spectrometry data. Experiments were conducted at the hypersonic reflected shock tunnel at Sandia National Laboratories. Simulations were performed to model the graphite cylindrical test articles that were preheated to surface temperatures ranging from 1250-2150 K for 4 km/s freestream conditions. Sensitivity analyses assessed the influence of epistemic reaction rate uncertainties on predicted gas species quantities at the surface and in the boundary layer. Dominant rate uncertainties were propagated through the model to quantify the comparison error between predicted and measured carbon monoxide quantities. Results show near agreement between finite-rate and equilibrium model predictions, which overpredict carbon monoxide number density for analyzed experimental conditions.

An approach to identify reaction- and diffusion-limited ablation regimes through a Damköhler analysis is employed to compare ablation model predictions between 3 and 4 km/s freestream shock tunnel test conditions. The predicted surface ablation regimes for each test condition agree with observed ablation rate trends between finite-rate and equilibrium models. Companion sensitivity analyses further characterized model behavior differences by identifying dominant reaction rate and chemical pathways in predicting gas species quantities

for each test case. The demonstrated analysis framework enables researchers to interrogate complex models to understand potential chemical pathways as part of the ablation process. It also provides a flexible validation methodology as more experimental data becomes available and models continue to be developed and matured.

Acknowledgments

I am grateful to my research advisor, Jean-Pierre Delplanque, for his guidance and support during my time at UC Davis. Thank you for your wisdom and encouragement throughout this research effort. I also want to thank my Sandia collaborators and friends who played a really important role in this work as well. Ross Wagnild, thank you for your technical mentorship throughout this project and for introducing me to US3D. It has been so much fun taking on this learning curve, and I have learned a lot from you. Justin Winokur, thank you for lending your expertise about sensitivity analysis and useful ways to communicate data. Also, thank you for letting me know that Sobol' does in fact have an apostrophe. Bryan Morreale, thank you for sharing your grid generation expertise and US3D tricks. Also, this work could not have been completed without Josh Hargis, Justin Wagner, and Kyle Lynch. It has been so helpful working with you throughout these Sandia HST campaigns. I have really enjoyed our discussions and experiencing the roller coaster that is part of the experimental process. Thank you for including me as a modeling and simulation teammate as part of this work. I also want to thank Amanda Dodd, Justin Smith, Cheryl Lam, and Camron Proctor. Thank you for all of your support and investment throughout this process. Sarah Kieweg, I am really thankful for your mentorship and support as well. Ellen Wagman, thank you for your guidance and introducing me to the category of research productivity literature out there. It has meant a ton, even if I only successfully adopted one or two positive habits. Jason Trask, thank you for all of the chemistry discussions and for your support as someone who went through this process before. I am lucky to have you as my partner. Mom and Dad, thank you for your consistent guidance and support over the years and getting me hooked on coffee at a young age.

Davis, California, May 2024

Nomenclature

ACA Air-carbon ablation

ACE Aerothermal Chemical Equilibrium code

CMA Charring Material Ablation code

C/C Carbon-carbon

CFD Computational fluid dynamics

C/P Carbon-phenolic

DFT Density-functional theory

DSMC Direct simulation Monte Carlo

ER Eley-Rideal

GSI Gas-surface interactions

HEEET Heatshield for Extreme Entry Environment Technology

HST Hypersonic shock tunnel

LH Langmuir-Hinshelwood

LHS Latin hypercube sampling

MURI Multidisciplinary University Research Initiatives

QoI Quantity of interest

RANS Reynolds-averaged Navier-Stokes

SPARC Sandia Parallel Aerodynamics and Reentry Code

TPS Thermal protection system

TWCP Tape-wrapped carbon-phenolic

US3D UnStructured 3-Dimensional code

UQ Uncertainty quantification

ZA Zhluktov and Abe

Chapter 1

Introduction

1.1 The Need for Credible Finite-Rate Surface Ablation Models in the Design of Hypersonic Vehicles

1.1.1 Gas-Surface Interactions

Accurate predictions of thermal performance and ablation of heat shield materials are critical to the design of thermal protection systems for hypersonic vehicles. These designs require a reliable barrier against harsh aerothermal loading that involves complex thermochemical and thermophysical processes interacting at the surface. Credible models enable engineers to better understand their design space, where gas-surface chemistry predictions impact a vehicle's aerodynamic performance, boundary layer transition, wakes, signatures, and internal heat transfer.

A flow is generally considered hypersonic when its Mach number is greater than five. For an atmospheric reentry body, a bow shock forms near the surface where the kinetic energy of the flow is converted to internal energy as it passes through the shock [7, 8]. The rise in gas temperature across the shock layer, defined as the flowfield between the shock wave and body, causes the vibrational energy to increase, which results in the dissociation of molecular oxygen and nitrogen into atoms. At higher temperatures, the flow becomes increasingly dissociated and eventually begins to ionize [6]. Consequently, a heat shield (or ablator) material may undergo a series of surface altering and catalytic gas-surface reactions of varying complexity. For a carbon-based ablator, these include processes such as adsorption, desorp-

tion, oxidation, nitridation, recombination, and sublimation [3]. As ablation products are injected into the boundary layer, they are entrained in the flow and react in the gas phase.

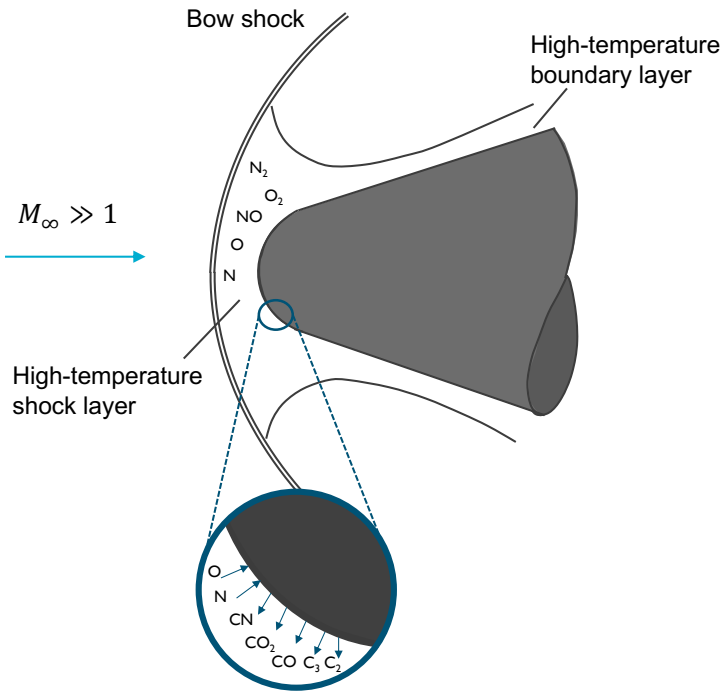

Figure 1.1: High-temperature effects on gas-surface interactions for a reentry body.

If the timescales at which a flow experiences vibrational excitation and chemical reactions are small compared to that at which the fluid element travels through the flowfield, the flow is in a state of thermochemical equilibrium. If the chemical timescales are large compared to the flow time scales, the flow is in a state of thermochemical nonequilibrium, which requires a finite-rate gas-phase reaction modeling approach to solve [8].

Ablation regimes at the surface may also be in a state of thermochemical equilibrium or nonequilibrium, also known as diffusion- or reaction-limited regimes. These states depend on the ratio of timescales between the flux of gas species diffusing through the boundary layer to the surface and chemical reactions between the impinging gas species and heat shield material. The surface is in a diffusion-limited regime if the boundary layer diffusion rate is much smaller than the rate of gas-surface chemical kinetics. If the boundary layer diffusion rate is much larger than the rate of gas-surface chemical kinetics, ablation is limited by the

kinetic barrier and the surface is in a reaction-limited regime [4, 9].

1.1.2 Historical Application Space

Common carbon-based composite ablators can be categorized into two classes: non-decomposing and decomposing, where non-decomposing ablators include materials such as pyrolytic and polycrystalline graphite and woven 2D and 3D carbon-carbon materials. These carbon-carbon (C/C) composite materials have been used in NASA's Genesis probe design and were part of the nose and leading edges of the Space Shuttle, where they were coated in a nonablative barrier ceramic. Carbon-carbon composites can also be found in ablative nozzles and on various experimental and other reentry vehicles due to their strong mechanical and thermal properties [10, 11].

Decomposing ablators may be composed of a carbon fiber network with phenolic or polymer resin, which also undergoes pyrolysis at high temperatures [10, 12]. Examples include NASA's low-density Phenolic Impregnated Carbon Ablator (PICA) and SpaceX's PICA-X materials. PICA is a primary workhorse for a range of NASA's planetary missions that include Stardust, Mars Science Laboratory, Mars 2020, and the upcoming Dragonfly and Mars Sample Return missions. PICA-X is a variant of PICA developed by SpaceX for its Dragon spacecraft heat shield. It is composed of a carbon fiber preform, FiberForm, and impregnated with a phenolic resin [13]. Tape wrapped carbon-phenolic (TWCP) is a common mid- to high-density woven structure that is made from strips of carbon-resin fabric cut at a bias and sewn together. It has been used as a heat shield material in previous NASA missions that include Pioneer Venus and Galileo probes and in solid rocket booster nozzle designs [10, 14, 15]. In order to meet future mission needs with very high heating entry environments, NASA has developed Heatshield for Extreme Entry Environment Technology (HEEET), which is a mid-density 3D woven dual layer carbon-phenolic [16]. Woven TPS materials enable designers to easily tailor the design to reduce entry loads and heat shield mass for future outer planet and sample return missions, where vehicles will encounter high

heat loads [17].

Carbon-based ceramic matrix composites (CMCs) are another class of materials that have favorable high temperature properties. CMCs include ultra-high temperature ceramic (UHTC) constituents, such as borides, carbides, and nitrides of transition elements like zirconium. They have very high melting points along with favorable thermal shock resistance, mechanical strength, and high thermal conductivity. These materials conduct energy and reradiate it through cooler surfaces on the vehicle [18, 19]. C/SiC is a widely studied heat shield material where carbon fiber is reinforced with silicon carbide. Examples of where C/SiC has been demonstrated on a large scale include the aeroshell design in the UK Ministry of Defense's Sustained Hypersonic Flight Experiment (SHyFE) vehicle, the German Aerospace Center's Sharp Edge Flight Experiment (SEFEX) aeroshell design, and in the body flap design for NASA's X-38 crew return vehicle prototype [11, 20].

Modern-day approaches of modeling ablation for carbon-based materials use thermochemical equilibrium assumptions at the surface to describe gas-surface interactions. Historical mission spaces (e.g., ballistic planetary entry) have enabled equilibrium assumptions to be simple, acceptable, and conservative. Widely used ablation models for non-decomposing and decomposing ablators are heavily based off the 1-D Charring Materials Ablation (CMA) code formulation, which assumes thermochemical equilibrium at the surface, where reactions occur so rapidly that the limiting factor in the ablation rate is the rate of oxygen diffusion through the boundary layer to the surface [21]. Namely, any species that diffuses through the boundary layer to the surface immediately reacts to full completion. The CMA code relies on surface thermochemistry tables generated by an equilibrium chemistry code (e.g., ACE) where a nondimensional mass flux of material from the surface, $B^{'}$, is computed for an input temperature and pressure [22]. For high heating environments, this approximation has resulted in accurate predictions of ablation and thermal performance.

There is evidence that a thermochemical equilibrium assumption may overestimate surface recession over a flight trajectory, indicating the need for a finite-rate approach. Large

differences in model predictions and flight data reveal challenges with an equilibrium assumption. While developing the Mars Science Laboratory PICA heat shield, inadequate ablation model validation resulted in poor confidence of model predictions in flight. Substantial margins and conservatism increased the designed heat shield thickness by approximately 40% over the nominal model predictions. At low heat fluxes (<100 W/cm^2), flight data showed that equilibrium ablation models overpredicted surface recession by up to 160% at selected sensor locations [23]. Equilibrium and nonequilibrium ablation models were also leveraged to predict recession at the surface for the Stardust return capsule PICA heat shield. While the equilibrium model overpredicted recession by 50% at some probed locations, a nonequilibrium (finite-rate) ablation model was found to overpredict recession by a smaller margin at 11% [17, 24]. Additionally, Kuntz [25] compared equilibrium and early rate-limited approaches for various generic reentry vehicle trajectories and found model choice strongly influenced computed surface recession and surface temperature for flights with a sustained cruise phase. As missions move beyond legacy applications and become more demanding, there is a need for higher performance TPS materials and credible ablation models.

1.1.3 Current and Future Application Spaces

Emerging vehicle designs include reusable access-to-space systems, cruisers, airplanes, and reentry systems. With new mission spaces, advanced hypersonic flight trajectories may include sustained flight under thermochemical nonequilibrium conditions, where modeling gas-surface interactions requires a finite-rate approach. Early studies identified approximate surface ablation regimes for graphites as a function of edge pressure and wall temperature [26–28], which relied heavily on theory and experiment. These analyses laid the groundwork in defining reaction-limited, transition, and diffusion-limited regimes. Recent investigations have proposed analytical frameworks that can be tailored to leading edge geometries and freestream environments for air/carbon systems [4, 9]. These frameworks are powerful tools to map surface ablation regimes and corresponding surface assumptions and

required models. However, more validation of these frameworks is needed to build confidence in each method.

Recent advances in finite-rate surface ablation model development show promise in capturing gas-surface interactions. New experiment-driven models leverage surface chemistry data via molecular beam-surface scattering experiments. This method enables the measurement of individual reactions and rate parameters by using a continuous or pulsed beam of gas species to impinge a heated material surface and measure reaction products [29, 30]. New models have leveraged these experiments for atomic and molecular oxygen and atomic nitrogen for vitreous carbon and carbon-fiber, where surface temperature is assumed to drive reactions [12, 31, 32]. These models notably include the air-carbon ablation (ACA) model by Prata et al. [31] and MURI oxidation model by Poovathingal et al. [12]. Direct Simulation Monte Carlo (DSMC) techniques have simulated molecular beam experiments of atomic and molecular oxygen with vitreous carbon to validate experiments and develop models for carbon fiber materials [33–35]. While newer model development techniques isolate fundamental processes, legacy finite-rate models were developed by fitting reaction rate parameters to empirical data from arc-jet, plasmatron, and gas-phase laboratory experiments [5, 36]. Commonly used models include Chen and Milos's Park [37] and Zhluktov and Abe's ZA [36] models. However, new and legacy finite-rate models use a consistent surface chemistry formulation described by Marschall and MacLean [3]. These surface chemistry reactions are coupled to a CFD flow solver through a mass and/or energy balance at the surface [38, 39].

While there have been ongoing efforts to model the surface chemical kinetics of air/carbon, conclusions on the main chemical processes occurring at a carbon surface differ. Consequently, there has been no universally supported air/carbon finite-rate surface ablation model. Active development is ongoing in the community to create finite-rate models for heat shield materials, including carbon-carbon, carbon-phenolic, and carbon-ceramic matrix composites. As new models are deployed, it will be critical to build model credibility evidence

in current and emerging mission spaces.

1.1.4 Ablation Model Credibility

Accurate predictions of gas-surface interactions are critical to assess the thermal and ablative performance of heat shield materials. In order to determine the credibility of a physics model for an application, we may apply a verification, validation, and uncertainty quantification framework [2]. This process provides a series of quantitative metrics to establish the confidence of a model, where a key metric is determined from model validation with experimental data. Within the past ten years, there has been a growing effort to validate air/carbon finite-rate models.

Given the complexities of simulating high-enthalpy flow conditions, experimental facilities are geared toward different forms of environmental conditions and data acquisition. Additionally, experimental uncertainties in the flowfield and measurement uncertainties that are present across facilities are not well characterized [40–47]. High-enthalpy shock and expansion tunnels produce realistic flight environments to test subscale models on the order of milliseconds [48]. These facilities provide a validation tool for gas-phase kinetics models using various measurement diagnostics techniques for planetary entry flow environments [45, 49, 50]. New capabilities in resistive heating have enabled realistic test sample surface temperatures and validation opportunities for gas-surface chemistry models [40, 51]. Alba and Lewis [6, 41] compared Park and ZA model predictions using CN spectral data in the shock layer around a heated graphite cylindrical strip at the X-2 facility at the University of Queensland. CN is a strong emitter and radiates in the UV spectrum, which makes it an ideal quantity of interest for UV spectrometry. While the Park model over-predicted CN near the surface, the ZA model significantly under-predicted CN. It should be noted that the original ZA model does not include a nitridation reaction mechanism, which Alba [52] later included in a modified version of the ZA model to fit to experimental data. Benerji [53] also compared Park and ZA model predictions for spectral radiance with a carbon-phenolic

blunt sphere-cone geometry in the X-2 facility using experimental spectra in the UV, visible, and IR wavelength ranges.

Plasma torch and arc-jet facilities run at subsonic to low supersonic Mach numbers and capture realistic heating environments for long time durations [54]. Test articles are typically outfitted with pyrometers and thermocouples to acquire surface and in-depth temperature measurements. Recession rates, surface topology, and mass loss are usually measured as well. Prata compared the ZA and MURI finite-rate models to measured surface recession data for seven air/graphite experiments at VKI's Plasmatron facility. Recession rate predictions were within 50% to experimental values but disagreed with each other depending on test pressure and enthalpy conditions [4]. Zibitsker recently compared the ACA model to high-enthalpy arc-jet data for a graphite sphere-cone and found good temperature and recession agreement with measurements at and near the stagnation point [55].

Characterization and validation assessments of coupled CFD and gas-surface chemistry ablation models are needed to understand how nonequilibrium gas-surface and gas-phase chemistry models interact in realistic environments and impact final quantities of interest (QoIs) like surface recession rate, species concentrations, and heat loads. Development and application of uncertainty quantification (UQ) approaches are needed to understand how model uncertainties impact final predictions, which includes development of quantitative metrics that incorporate parametric, structural, and experimental uncertainties. Combining sensitivity analyses with validation cases would provide valuable data in understanding dominant reaction parameters and mechanisms, which would supplement further UQ or calibration efforts. The purpose of this dissertation is to demonstrate the importance of uncertainty quantification as a tool to understand and accurately evaluate complex gas-surface chemistry models for hypersonic flight environments.

1.2 Research Goals

The goal of this research is to quantitatively assess the predictive behavior of finite-rate carbon ablation models in describing the surface state within a chemically ablating boundary layer for nonequilibrium high-enthalpy flow. This work leverages recent advances in finite-rate model development to characterize selected surface ablation models and develops and demonstrates a rigorous validation and uncertainty quantification framework. The following aims are identified to achieve this goal.

Aim 1 – Evaluate current state-of-the-art air/carbon finite-rate gas-surface interaction modeling approaches through in-depth computational comparison.

Aim 2 – Determine the influence of reaction parameters and mechanisms on surface state quantities.

Aim 3 – Quantify the uncertainty of surface state predictions between finite-rate and equilibrium modeling approaches.

1.3 Scope and Dissertation Structure

Quantitative assessments in this work target air/graphite gas-surface interactions for hypersonic shock tunnel experiments. Finite-rate and equilibrium surface ablation modeling approaches are compared in predicting carbonaceous products near the surface. The presented cases are only a small subset of relevant environments; however, this work provides a comprehensive analysis that may be leveraged for other experimental facilities and conditions.

Chapter 2 presents the theory and methodology of the gas-surface interaction models and credibility framework. This includes discussion of ablation model definitions, surface

chemistry coupling to a computational fluid dynamics code, and selected methods in verification, validation, and uncertainty quantification.

Chapter 3 provides a sensitivity analysis framework to characterize prediction differences and identify appropriate finite-rate models of interest for validation. Simulations are performed on a sphere-cone geometry for selected freestream conditions. Differences in predicted surface species mass fluxes are evaluated.

Chapter 4 presents a validation framework to assess equilibrium and finite-rate models for a series of hypersonic shock tunnel experiments. Simulations are performed on a half-cylinder graphite test sample for a high-enthalpy flow condition for a series of surface temperatures. Model predictions of carbon monoxide number density are compared to measurements taken with laser absorption spectrometry (LAS).

Chapter 5 applies the proposed sensitivity analysis framework to finite-rate models for a second high-enthalpy condition in the hypersonic shock tunnel to characterize kinetic behavior of the models and identify dominant input parameters. An approach to identify reaction- and diffusion-limited ablation regimes (Damköhler analysis) is introduced and demonstrated for each shock tunnel condition. Differences in predicted mass fractions at and near the surface are evaluated.

Chapter 6 discusses conclusions and proposes future research to supplement our understanding of gas-surface interaction models through applied sensitivity and validation studies.

Chapter 2

Theory and Methodology

The following chapter highlights the governing equations, gas transport and chemistry models, and numerical methods used to model the chemically reacting high-enthalpy flows and gas-surface interactions in this study. A 3D unstructured flow solver, US3D, is used to simulate the nonequilibrium flowfield where the surface chemistry is implemented as a boundary condition at the wall [56–59]. The Predictive Capability Maturity Model (PCMM) model credibility framework is then presented with an overview of selected sensitivity and uncertainty quantification methods used to assess the credibility and characterize finite-rate surface ablation models.

2.1 Nonequilibrium Flow Modeling

2.1.1 Mathematical Models

Governing Equations

The compressible Navier-Stokes equations for flows in thermochemical nonequilibrium are presented. Mass, momentum, and energy equations are described for individual gas species, s, for a chemically reacting flow. The following expressions are based on the mass density of each species and presented in Cartesian coordinates, x_i, where the mass conservation for each species is

$$\frac{\partial \rho_s}{\partial t} + \frac{\partial}{\partial x_i}(\rho_s u_i) = -\frac{\partial}{\partial x_i}(\rho_s v_{si}) + w_s, \tag{2.1}$$

where ρ_s are the species densities, u_i is the fluid velocity in the x_i direction, v_{si} is the species diffusion velocity in the x_i direction, and w_s is a chemical source term that represents the species mass production rates from chemical reactions. Einstein summation notation is used to simplify the equation set.

Conservation of momentum is defined as

$$\frac{\partial}{\partial t}(\rho u_i) + \frac{\partial}{\partial x_j}(\rho_s u_i u_j) = \frac{\partial P}{\partial x_i} + \frac{\partial \tau_{ij}}{\partial x_j}, \tag{2.2}$$

where ρ is the total mixture density, P is the fluid pressure, and τ_{ij} is the viscous shear stress tensor.

Park's [60] two-temperature thermochemical model characterizes the thermal state of the flow, which is assumed to be in nonequilibrium. Translational and rotational energy modes are represented by a common temperature, T. This is due to the assumption that the rotational state of the gas quickly equilibrates with the translational state. Additionally, vibrational, electronic excitation, and electron translational energy modes are represented by a single temperature, T_v. The coupling among the latter three energy modes are considered to occur quickly as well. The energy conversation formulation for total energy is described as

$$\frac{\partial E}{\partial t} + \frac{\partial}{\partial x_j}[u_j(E+P)] = \frac{\partial}{\partial x_j}(u_i \tau_{ij}) - \frac{\partial q_i}{\partial x_i} - \frac{\partial q_{v,i}}{\partial x_i} - \frac{\partial}{\partial x_i}\left(\sum_s \rho_s h_s v_{si}\right), \tag{2.3}$$

where E is the total energy, q_i is the heat flux of translational and rotational energy in the i direction, $q_{v,i}$ is the heat flux of vibrational energy in the i direction, and h_s is the enthalpy contained in each species. In order to model molecular vibration, energy exchanges between vibrational modes are assumed to occur fast enough that vibrational modes are in equilibrium. Therefore, only one equation for total vibrational energy is needed. It is given by

$$\frac{\partial E_v}{\partial t} + \frac{\partial}{\partial x_j}(E_v u_j) = -\frac{\partial q_{v,i}}{\partial x_i} - \frac{\partial}{\partial x_i}\left(\sum_s \rho_s e_{vs} v_{si}\right) + Q_{t-v} + \left(\sum_s e_{vs} w_s\right), \tag{2.4}$$

where E_v is the vibrational energy, e_{vs} is the vibrational energy per unit mass of a species, and Q_{t-v} represents the translational-vibrational energy exchange.

Vibrational Energy Source Terms

The Landau-Teller model [61] provides the translational-rotational energy exchange rate for vibrational mode, m, by

$$Q_{T-v,m} = \rho_m \frac{e^*_{vm}(T) - e_{vm}(T_v)}{\langle \tau_m \rangle}, \tag{2.5}$$

where $e^*_{vm}(T)$ is the local equilibrium vibrational energy and $e_{vm}(T_v)$ is the current vibrational energy. The molar averaged Landau-Teller relaxation time, $\langle \tau_m \rangle$, is

$$\langle \tau_m \rangle = \frac{\sum_s [S]}{\sum_s [S]/\tau_{ms}} = \frac{1}{\sum_s [X_s]/\tau_{ms}}, \tag{2.6}$$

where $[S]$ is the molar concentration of each species and τ_{ms} is the Landau-Teller inter-species relaxation time. The species mole fraction, X_s, is defined by

$$X_s = \frac{y_s M}{M_s}, \tag{2.7}$$

where y_s is the species mass fraction, M is the total molecular weight of the mixture, and M_s is the species molecular weight. These quantities are related by

$$y_s = \frac{\rho_s}{\rho}, \tag{2.8}$$

and

$$M = \left(\sum_s \frac{y_s}{M_s} \right)^{-1}. \tag{2.9}$$

The Millikan and White curve fit [62] provides an approximation for τ_{ms} as

$$\tau_{ms} = \frac{1}{P} \exp\left[A_{ms} \left(T^{-1/3} - B_{ms} \right) - 18.42 \right], \tag{2.10}$$

where P is the total gas pressure in units of atmospheres. The Millikan-White Coefficients, A_{ms} and B_{ms}, are

$$A_{ms} = 1.16 \times 10^{-3} \mu_{ms}^{1/2} \theta_{vm}^{4/3}, \tag{2.11}$$

and

$$B_{ms} = 0.015 \mu_{ms}^{1/4}, \tag{2.12}$$

where $\theta_{v,m}$ is the characteristic vibrational temperature of each mode and μ_{ms} is the reduced mass of collision partner species and defined by

$$\mu_{ms} = \frac{M_m M_s}{M_m + M_s}. \tag{2.13}$$

Thermodynamic State Equations

The total energy per unit volume, E, is defined by

$$E = \frac{1}{2} \rho u_i u_i + \sum_s \rho_s c_{vs} T + \sum_s \rho_s h_s^\circ + \sum_s \rho_s e_{vs}, \tag{2.14}$$

where T is the translational-rotational temperature and specific heat of each species at constant volume, c_{vs}, is the summation of translational and rotational components for a polyatomic species

$$c_{vs} = c_{vs}^{tr} + c_{vs}^{rot} = \frac{3}{2} R_s + R_s, \tag{2.15}$$

where R_s is the species gas constant

$$R_s = \frac{R}{M_s}. \tag{2.16}$$

Species enthalpy, h_s, is defined as

$$h_s = c_{v,s} T + R_s T + e_{v,s} + h_s^\circ, \tag{2.17}$$

where $e_{v,s}$ is the species vibrational energy per unit mass and h_s° is the heat of formation. The species vibrational energy per unit mass is

$$e_{v,s} = R_s \sum_{m=1}^{nms} \frac{\theta_{v,m}}{\exp(\frac{\theta_{v,m}}{T_v}) - 1}, \tag{2.18}$$

where $\theta_{v,m}$ is the vibrational temperature of each mode, m, and nms is the number of modes for each species. The total pressure of the fluid is defined as

$$P = \rho R_s T = \sum_s \frac{\rho_s}{M_s} RT. \tag{2.19}$$

Phenomenological Laws and Transport Properties

The fluid is assumed to be Newtonian, so the viscous shear stress tensor of the fluid is expressed as

$$\tau_{ij} = \mu \left(\frac{\partial u_i}{\partial x_j} + \frac{\partial u_j}{\partial x_i} \right) + \lambda \frac{\partial u_k}{\partial x_k} \delta_{ij}, \tag{2.20}$$

where μ is the dynamic viscosity of the mixture, δ_{ij} is the Kronecker delta. The Stokes' hypothesis is used to relate the second coefficient of viscosity, λ, to μ such that

$$\lambda = -\frac{2}{3}\mu. \tag{2.21}$$

The mixture viscosity, μ, of a gas in thermal equilibrium is defined using the Wilke mixing rule [63]

$$\mu = \sum_s \left(\frac{\mu_s X_s}{\phi_{w,s}} \right), \tag{2.22}$$

where $\phi_{w,s}$ is a dimensionless constant that is defined by

$$\phi_{w,s} = \sum_r X_r \left[1 + \sqrt{\frac{\mu_s}{\mu_r}} \left(\frac{M_r}{M_s} \right)^{1/4} \right]^2 \left[8 \left(1 + \frac{M_s}{M_r} \right) \right]^{-1/2}. \tag{2.23}$$

Blottner's formula is used to compute the viscosity of each species, μ_s, with a three parameter curve fit

$$\mu_s = 0.1 \exp[(A_s \ln T + B_s) \ln T + C_s]. \tag{2.24}$$

Fourier's Law provides the translational-rotational heat flux vector, q_i, and vibrational heat flux vector, $q_{v,i}$, as

$$q_i = -k\frac{\partial T}{\partial x_i} = (k_{tr} + k_{rot})\frac{\partial T}{\partial x_i}, \tag{2.25}$$

and

$$q_{v,i} = -k_v\frac{\partial T_v}{\partial x_i}, \tag{2.26}$$

where k is the translational-rotational thermal conductivity and k_v is the vibrational thermal conductivity of the gas mixture.

Translational, rotational, and vibrational species thermal conductivity relations for are defined using the Eucken formula [64] as a function of species viscosity, μ_s, and specific heat at constant volume, c_{vs},

$$k_{tr,s} = \frac{5}{2}\mu_s c_{vs}, \tag{2.27}$$

$$k_{rot,s} = \mu_s c_{vs}, \tag{2.28}$$

and

$$k_{v,s} = \mu_s c_{vvs} = \mu_s\frac{\partial e_{vs}}{\partial T_v}. \tag{2.29}$$

Fick's law is used to quantify the species mass diffusion fluxes

$$\rho_s v_{si} = -\rho D_s\frac{\partial y_s}{\partial x_i} = -\rho D_s\frac{\partial}{\partial x_i}\left(\frac{\rho_s}{\rho}\right), \tag{2.30}$$

where v_{si} is the species diffusion velocity and D_s is the species binary diffusion coefficient. Assuming that the diffusion coefficients for each species are equal for a gas mixture and a constant Lewis number, a single Diffusion coefficient, D, is found by

$$D = \frac{k}{\rho c_p Le}, \tag{2.31}$$

where k is the thermal conductivity and c_p is the specific heat at constant pressure of the

gas mixture. Mass-weighted properties such as c_p, c_v, e_v, and h° are computed by

$$\phi = \sum_{n}^{ns} \phi_s y_s. \tag{2.32}$$

Chemical Reaction Source Terms

In Park's 11-species, finite-rate gas-phase chemistry model for air, exchange and dissociation reactions are considered. They have the general form

$$AB + CD \rightleftharpoons AD + BC \tag{2.33}$$

and

$$AB + M \rightleftharpoons A + B + M. \tag{2.34}$$

The total mass production rate of each species, w_s, is found by summing the reaction rates for species, s, over each reaction, r, and multiplying the summed quantity by its molecular weight

$$w_s = M_s \sum_{r} (\beta_{s,r} - \alpha_{s,r})(R_{f,r} - R_{b,r}), \tag{2.35}$$

where $\alpha_{s,r}$ and $\beta_{s,r}$ are stoichiometric coefficients for the reactants and products [8, 65] and the forward and backward reaction rates, $R_{f,r}$ and $R_{b,r}$, are defined as

$$R_{f,r} = k_{f,r} \prod_{s} \left(\frac{\rho_s}{M_s} \right)^{\alpha_{s,r}} \tag{2.36}$$

and

$$R_{b,r} = k_{b,r} \prod_{s} \left(\frac{\rho_s}{M_s} \right)^{\beta_{s,r}}. \tag{2.37}$$

The forward reaction rate coefficients are determined from Park's model [65]

$$k_{f,r} = C_{f,r} T_{x_{f,r}}^{\eta_{f,r}} \exp\left(-\frac{T_{d_{f,r}}}{T_{x_{f,r}}} \right), \tag{2.38}$$

where $C_{f,r}$ is the collision coefficient, $\eta_{f,r}$ is a pre-exponential empirical coefficient, $T_{d_{f,r}}$ is the activation temperature of reaction, and $T_{x_{f,r}}$ the controlling temperature that is dependent on reaction type. For an exchange reaction, the translational-rotational temperature, T, is the controlling temperature that the rates are dependent on. Whereas, for a dissociation reaction, the rates are dependent on an effective temperature, T_{eff}, which is the geometric mean of translational-rotational temperature, T, and vibrational temperature, T_v, where

$$T_{eff} = \sqrt{TT_v}. \tag{2.39}$$

Backwards reaction rates, $k_{b,r}$ are computed using an equilibrium constant, $K_{eq,r}$, and forward reaction rate, $k_{f,r}$, for each reaction

$$K_{eq,r} = \frac{k_{f,r}}{k_{b,r}}. \tag{2.40}$$

The equilibrium constant for each reaction is computed using Park's empirical fit equation [66]

$$K_{eq,r} = C \exp\left[A_1(\frac{10000}{T})^{-1} + A_2 + A_3 \ln(\frac{10000}{T}) + A_4(\frac{10000}{T}) + A_5(\frac{10000}{T})^2\right], \tag{2.41}$$

where C is a unit conversion pre-exponential factor and A_i are empirical fit coefficients. The Park gas-phase chemistry mechanism is shown in Table 2.1 [65]. It contains three additional reactions to include direct oxidation, nitridation, and dissociation of C_3 that extends the basic mechanism [67]. These reactions become important under sublimation conditions.

2.1.2 Numerical Methods

The CFD solver used in this work is US3D, which is a three-dimensional unstructured code that solves the compressible reacting Navier-Stokes equations using a finite-volume approach [56–58]. It uses many of the same numerical methods as NASA's DPLR (data-parallel line

Table 2.1: Park 11-species gas-phase chemistry reaction set.

Number	Reaction	Number	Reaction
1	$CO_2 + M \leftrightarrow CO + O + M$	11	$CO + O \leftrightarrow O_2 + C$
2	$CO + M \leftrightarrow C + O + M$	12	$CO + C \leftrightarrow C_2 + O$
3	$N_2 + M \leftrightarrow N + N + M$	13	$CO + N \leftrightarrow CN + O$
4	$O_2 + M \leftrightarrow O + O + M$	14	$N_2 + C \leftrightarrow CN + N$
5	$NO + M \leftrightarrow N + O + M$	15	$CN + O \leftrightarrow NO + C$
6	$C_2 + M \leftrightarrow C + C + M$	16	$CN + C \leftrightarrow C_2 + N$
7	$CN + M \leftrightarrow C + N + M$	17	$CO_2 + O \leftrightarrow O_2 + CO$
8	$C_3 + M \leftrightarrow C_2 + C + M$	18	$C_2 + C_2 \leftrightarrow C_3 + C$
9	$NO + O \leftrightarrow O_2 + N$	19	$O + C_3 \leftrightarrow CO + C_2$
10	$N_2 + O \leftrightarrow NO + N$	20	$N + C_3 \leftrightarrow C_2 + CN$

relaxation) code [68] including forms of upwind numerical flux functions and the implicit data-parallel line relaxation method. It also includes numerical flux functions with different levels of accuracy and dissipation levels.

For steady-state laminar simulations in this work, the code uses a modified Steger-Warming flux-vector splitting method to compute the convective flux terms. A Monotonic Upstream-centered Scheme for Conservation Laws (MUSCL) scheme is applied to prevent numerically inaccurate values due to large gradients, shocks, or other discontinuities (e.g., unrealistic pressure variations). The code also uses a kinetic energy consistent (KEC) flux to produce a numerical flux consistent with the compressible energy transport equation, where a discontinuity sensor is used to add dissipation and a scaled dissipative flux is then added from the Steger-Warming flux. US3D includes a weighted least squares method for the viscous flux calculation to compute the flow variable gradients.

A modification of the data-parallel line relaxation method for unstructured grids is used as the time integration method and solves the implicit linearized system of equations along lines of cells normal to the wall. Users specify how lines are grown (e.g., from the wall boundary) and a point implicit method is used in regions that are excluded from the line-solve. Higher order implicit and explicit methods are available for unsteady problems to enable RANS and high fidelity turbulence modeling approaches but are outside the scope of this study.

2.2 Air/Carbon Surface Ablation Modeling

2.2.1 Finite-Rate Models

Surface Chemistry Formulation

The surface chemistry formulation presented here was developed by Marschall and MacLean [3, 38] and presented in 2011. This framework covers the theory and implementation of general surface chemistry reaction sets and coupling to a CFD solver in the gas-phase. The surface chemistry model framework accommodates a finite number of active surface sites that compete with each other for reactants. Forward reaction rate coefficients include kinetics-based mechanisms like adsorption, recombination, and sublimation reactions, and a general Arrhenius mechanism. Backwards reaction rate coefficients are computed using an equilibrium constant. Descriptions of suggested transition-state theory rate coefficient formulations are defined for desorption reactions. A general outline of the surface chemistry formulation is discussed here for an ablating carbon surface. For additional detail, the reader is advised to consult the cited references.

Figure 2.1 depicts three domains considered in the model that consist of gas, surface, and a bulk material environments. For this work, the bulk environment is carbon. The gas environment contains a set number of air species considered in the flowfield including carbon ablation products. Reactions take place at active sites on the surface and each species occupies only a single site at a time.

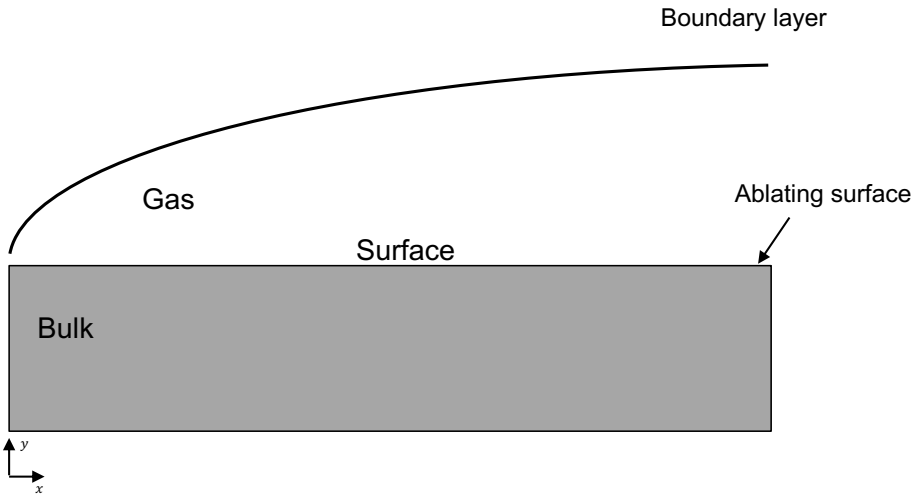

Figure 2.1: Gas, surface, and bulk model environments.

A description of generalized gas-surface reactions between gas species, A and B, active available site, (s), adsorbed species onto the surface, $A(s)$ and $B(s)$, and bulk species, $A(b)$ and $B(b)$, are shown in Table 2.2. Examples of selected reactions are shown in Figure 2.2.

Table 2.2: Examples of commonly used gas-surface reactions.

Reaction Type	Form
Adsorption/desorption	A + (s) $\leftrightarrow$ A(s)
Eley-Rideal recombination	A + B(s) $\leftrightarrow$ AB + (s)
Langmuir-Hinshelwood recombination	A(s) + B(s) $\leftrightarrow$ AB + 2(s)
Oxidation/reduction	A + (s) + B(b) $\leftrightarrow$ AB + (s)
Sublimation/condensation	(s) + A(b) $\leftrightarrow$ A + (s)

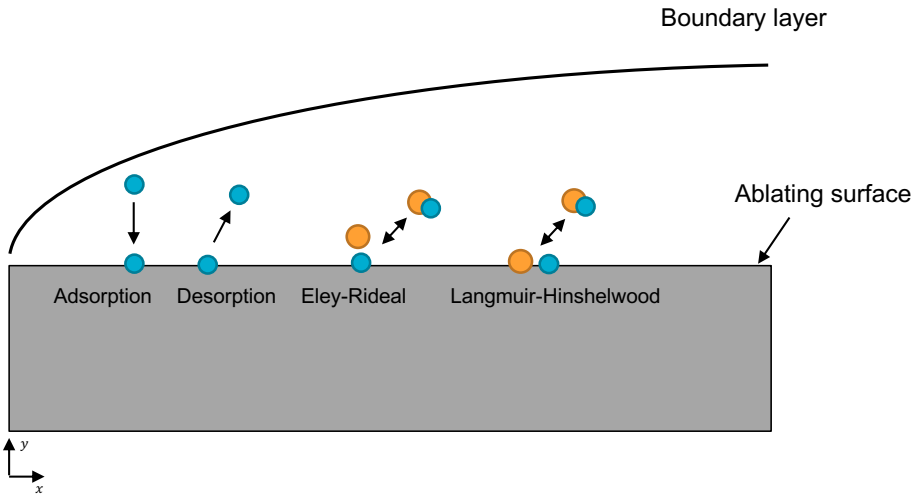

Figure 2.2: Example surface chemistry reactions from Table 2.2.

Forward rate coefficients for the analyzed models are defined in Table 2.3. Reaction probability values are specified by γ and sticking coefficients are defined by S, which are dimensionless and range from zero to unity. Other specified dimensionless quantities include β and T' ($T' = T/1K$). Activation energy, E, is in units of J mole^{-1}. The Arrhenius pre-exponential factor, A, is in units of s^{-1} for reactions involving one surface and bulk reactant. Total active site density, B, is a surface quantity and is in units of moles m^{-2}, T_s is the

Table 2.3: Forward reaction rate coefficients [3, 4].

Reaction Type	Rate Coefficient
Adsorption	$k_f = \left[\frac{\overline{v}_s}{4B}\right] S \exp\left(-\frac{E_{ad}}{RT_s}\right)$
Eley-Rideal	$k_f = \left[\frac{\overline{v}_s}{4B}\right] \gamma_{er} \exp\left(-\frac{E_{er}}{RT_s}\right)$
Langmuir-Hinshelwood	$k_f = \sqrt{\frac{A_v}{B}} \overline{v}_{s,2D} \gamma_{lh} \exp\left(-\frac{E_{lh}}{RT_s}\right)$
Sublimation	$k_f = \left[\frac{\overline{v}_s}{4BRT_s}\right] \gamma_{sub} \exp\left(-\frac{E_{sub}}{RT_s}\right)$
Arrhenius	$k_f = AT_s'^{\beta} \exp\left(-\frac{E_{Arr}}{RT_s}\right)$

surface temperature, and A_v is Avogadro's number. The mean thermal velocity of impinging gas species, $\overline{v}_s$, is defined by

$$\overline{v}_s = \sqrt{\frac{8k_BT}{\pi m_s}}, \tag{2.42}$$

where T is the gas temperature and m_s is the mass of the impinging species. The mean thermal speed of the mobile adsorbed surface species for the Langmuir-Hinshelwood reaction, $\overline{v}_{s,2D}$, is

$$\overline{v}_{s,2D} = \sqrt{\frac{\pi k_B T}{2m_s}}. \tag{2.43}$$

The backward rate coefficient for the recombination, sublimation, and Arrhenius reactions is computed by

$$k_{b,i} = \frac{k_{f,i}}{K_{eq,i}}, \tag{2.44}$$

where k_{fi} is the forward rate coefficient for surface reaction, i, and $K_{eq,i}$ is the equilibrium constant for the surface composition. The equilibrium constant is computed using thermodynamic data from NASA's Chemical Equilibrium with Applications (CEA) database and Park's empirical fit equation [66]

$$K_{eq,i} = C \exp\left[A_1(\frac{10000}{T_s})^{-1} + A_2 + A_3 \ln(\frac{10000}{T_s}) + A_4(\frac{10000}{T_s}) + A_5(\frac{10000}{T_s})^2\right], \tag{2.45}$$

where C is a unit conversion pre-exponential factor, T_s is surface temperature, and A_i are empirical fit coefficients. Rate coefficients for thermal desorption may be defined using transition state theory (TST) to approximate the pre-exponential factor. The general form of the desorption rate coefficient is

$$k_{des} = A_{des} T_s'^{\beta} \nu \exp\left(-\frac{E_{des}}{RT_s}\right), \tag{2.46}$$

where A_{des} is the pre-exponential factor in units of $\mathrm{m}^2\ \mathrm{kmol}^{-1}$ and ν is an attempt frequency in units of s^{-1}. A constant value for ν is used by the ZA air/carbon finite-rate model for atomic oxygen and nitrogen desorption reactions [1, 36]. Recent MURI and ACA models have leveraged the work of Pitt et al. [12, 31, 69] to define an analytical form of the desorption rate coefficient

$$k_{des} = \frac{2\pi m_s k_B^2 T_s^2}{h^3} \exp\left(-\frac{E_{des}}{RT_s}\right), \tag{2.47}$$

where m_s is the mass of the desorbing species, k_B is Boltzmann's constant, and h is Planck's constant. The species molar production rate, w_s, per unit surface area per unit time is defined as

$$\dot{w}_s = \sum_{i=1}^{NR} (\nu_{si}^{''} - \nu_{si}^{'}) r_i, \tag{2.48}$$

where $\nu_{si}^{'}$ and $\nu_{si}^{''}$ are the stoichiometric coefficients for forward and backward reactions for each surface reaction, i, respectively. The total number of reactions is denoted by NR. For each reaction, the net reaction flux, r_i, is computed by

$$r_i = k_{f,i} \prod_s X_s^{\nu_{si}^{'}} - k_{b,i} \prod_s X_s^{\nu_{si}^{''}}, \tag{2.49}$$

where X_s is the species concentration. The rate of bulk species loss from the surface is solved to calculate an effective blowing rate of bulk carbon material from the surface by

$$\dot{m}_b = -\sum_{n=1}^{Nb} M_b \dot{w}_b. \tag{2.50}$$

Coupling to Flow Solver

To integrate the surface chemistry model with a CFD solver, a mass balance is set as the boundary condition for each species in the gas-phase model. This relationship is shown in Figure 2.3, which depicts fluxes of mass entering and leaving an infinitely thin control volume that is shown in blue and represents a mass flux of each gas-phase species at the surface in units of kg m^{-2} s^{-1}. It expresses the balance between the mass flux entering the surface due to diffusion, species production from surface reactions, and the rate at which the mixture is convected away from the surface (Equation 2.51).

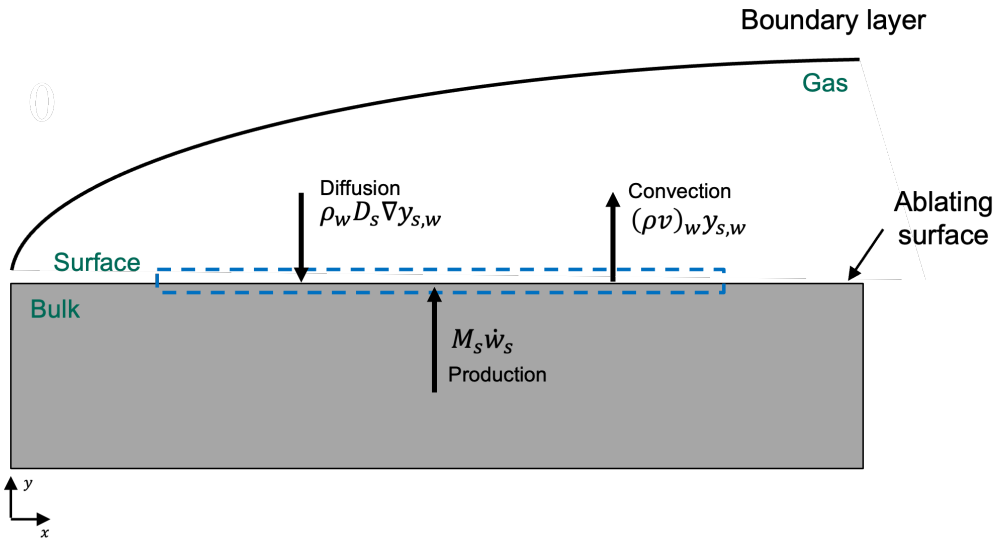

Figure 2.3: Mass balance at the surface.

$$-(\rho D_s)_w \nabla y_s \Big|_w + (\rho v)_w y_{s,w} = M_s \dot{w}_s \tag{2.51}$$

Fickian diffusion is assumed where ρ_w is the total mixture density at the wall and y_s is the species mass fraction. The convection term is the mass flux at the surface for each gas-phase species, $(\rho v)_w$, multiplied by the species mass fraction. The surface chemistry source term from Equation 2.48, $\dot{w}_s$, is multiplied by its corresponding species molecular weight, M_s to obtain the surface mass production term.

Although not included in the presented analysis, an energy balance may be included that solves for wall temperature and heat transfer at the surface. Figure 2.4 depicts relevant heating sources with an infinitely thin control volume at the surface.

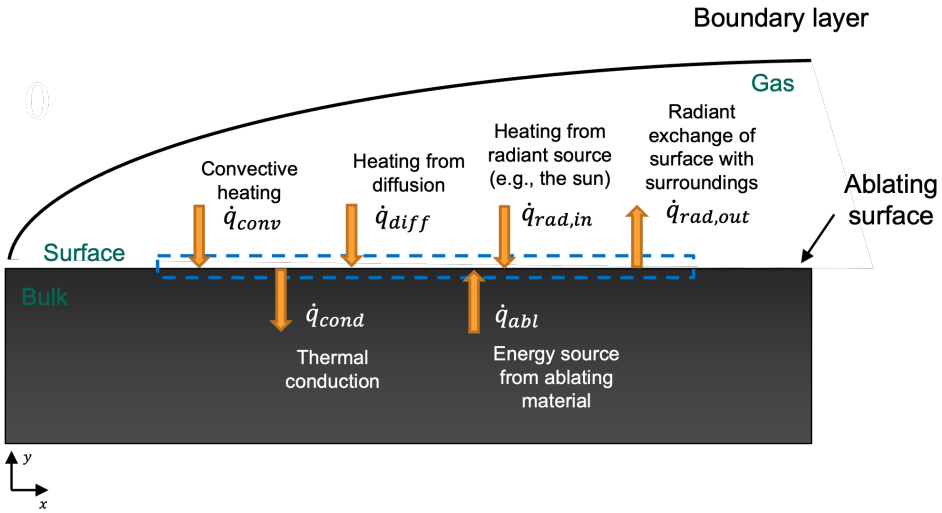

Figure 2.4: Energy balance at the surface.

We can describe the energy balance using a radiative equilibrium boundary condition with an added enthalpy term from the bulk material. This approach assumes that the conduction term into the material is negligible and the gas temperature is equal to the temperature of material produced from the bulk. The steady-state energy balance equation is then defined by

$$\sum_m k_m \nabla T_m - k_b \nabla T_b + \sum_s h_s \rho D_s \nabla y_s \Big|_w + \alpha_w \dot{q}_{rad} = (\rho v)_w (h_w - h_b) + \sigma \epsilon T_w^4, \tag{2.52}$$

where k_m and T_m are thermal conductivities and temperatures of thermal modes of the gas, which is described in Section 2.1.1. Thermal conductivity and temperature of the bulk solid material are k_b and T_b respectively. Enthalpy of each gas species, s, is designated by h_s, h_w is the enthalpy of the gas mixture at the wall, h_b is the enthalpy of the bulk material, α_w is the absorption coefficient of the surface, σ is the Stefan-Boltzmann constant, and ϵ is the emissivity of the surface. Additional implementation details are found in MacLean and Marschall [38] and Candler et al. [56].

Air/Carbon Finite-Rate Ablation Models

Current finite-rate ablation models leverage the existing surface chemistry formulation and coupling to CFD described above. These models rely on competing finite-rate kinetic processes operating at active sites on a carbon surface, where resulting gas-surface reactions are coupled to CFD. Four common air-carbon gas-surface chemistry models are:

- Park [37]
- Zhluktov and Abe (ZA) [36]
- MURI [12]
- Air-Carbon Ablation (ACA) [31]

Chen and Milos [37] developed the five reaction Park model by leveraging previous work of Park [5, 66, 70, 71]. The gas-surface reaction set is shown in Table 2.4 and uses the rate coefficients documented by MacLean et al. [38] and Alba [1]. It contains reactions for irreversible oxidation with both atomic and molecular oxygen, irreversible nitridation with atomic nitrogen, and C_3 sublimation and consensation. The reaction rates are based on kinetic theory, and reaction efficiencies are assigned for each surface reaction and based on experimental data in the literature. A modification of the nitridation reaction efficiency is made from the original formulation that leverages work from Driver and MacLean [72].

Table 2.4: Park air-carbon surface chemistry reaction set.

Number	Reaction	γ	E	Type
P1	$O + (s) + C(b) \rightarrow CO + (s)$	0.63	9.644	Oxidation
P2	$O_2 + 2(s) + 2C(b) \rightarrow 2CO + 2(s)$	0.50	0	Oxidation
P3	$N + (s) + C(b) \rightarrow CN + (s)$	0.003	0	Nitridation
P4	$3(s) + 3C(b) \rightarrow C_3 + 3(s)$	1.0	775.81	Sublimation
P5	$C_3 + 3(s) \rightarrow 3(s) + 3C(b)$	0.10	0	Condensation

The Zhluktov and Abe (ZA) model includes 12 reversible surface reactions that describe adsorption/desorption, recombination of adsorbed atoms and gas-phase species with adsorbed atoms, oxidation of bulk carbon, and sublimation to produce atomic and molecular

carbon gas [36]. Table 2.5 shows the gas-surface reaction set and rate coefficient parameters from MacLean et al. [38]. Both Park and ZA models are dependent on input parameters empirically obtained through curve fits from conventional experiments like arc-jet, plasmatron, and gas-phase laboratory test campaigns [3].

Table 2.5: ZA gas-surface chemistry model reaction set.

Number	Reaction	S_0,γ,or A	β	E	Type
Z1	O + (s) $\rightarrow$ O(s)	1.0	-	0	Adsorption
Z2	N + (s) $\rightarrow$ N(s)	1.0	-	0	Adsorption
Z3	2O(s) $\leftrightarrow$ O_2 + 2(s)	3.58×10^{10}	1.0	256.07	Arrhenius
Z4	O_2 + (s) $\leftrightarrow$ O + O(s)	1.0	-	118.06	Eley-Rideal
Z5	CO_2 + (s) $\leftrightarrow$ CO + O(s)	0.9	-	0	Eley-Rideal
Z6	O(s) + C(b) $\leftrightarrow$ CO + (s)	2.08×10^{9}	1.0	332.56	Arrhenius
Z7	O + O(s) + C(b) $\leftrightarrow$ CO_2 + (s)	0.8	-	16.63	Eley-Rideal
Z8	2O(s) + C(b) $\leftrightarrow$ CO_2 + (s)	3.58×10^{14}	1.0	332.56	Arrhenius
Z9	C + (s) $\leftrightarrow$ (s) + C(b)	0.24	-	0	Sublimation
Z10	C_2 + 2(s) $\leftrightarrow$ 2(s) + 2C(b)	0.5	-	0	Sublimation
Z11	C_3 + 3(s) $\leftrightarrow$ 3(s) + 3C(b)	0.023	-	0	Sublimation
Z12	N_2 + (s) $\leftrightarrow$ N + N(s)	1.0	-	636.85	Eley-Rideal
Z1b	O + (s) $\rightarrow$ O(s)	1.72×10^{4}	-	374.13	Desorption
Z2b	N + (s) $\rightarrow$ N(s)	1.72×10^{4}	-	304.29	Desorption

New techniques in molecular beam-surface scattering techniques with TPS material constituents [29, 30, 32, 73, 74] have recently been used to isolate fundamental processes to inform surface ablation models. Two recent models include the MURI oxidation model and air-carbon ablation (ACA) model developed by Poovathingal et al. [12] and Prata et al. [31] respectively. For both MURI and ACA models, a combination of theory and molecular beam data is used to inform reaction mechanisms and rate coefficients. Corresponding experiments were performed by Murray et al. [29, 30] for O/O_2 and N/N_2 beams interacting with vitreous carbon. Observed thermal scattering dynamics showed that surface reactions are driven by surface coverage and temperature, which may be applicable to boundary layer conditions for partially dissociated gas. Therefore, the formulation for each model is surface pressure and temperature dependent.

The MURI model includes low temperature (800-1100 K) and high temperature (1200-

2100 K) regimes that correlate to high and low surface coverage of adsorbed atomic oxygen. Desorption of O atoms from the carbon surface is a rate activated process with a corresponding energy barrier [29]. The gas-surface chemistry reaction set in Table 2.6 contains irreversible oxidation, adsorption, and desorption of atomic oxygen. It is meant to model the adsorption and desorption of O atoms on the carbon surface, formation of CO and CO_2 molecules through coverage dependent mechanisms, and the formation of CO through a coverage-indepdendent mechanism between incident O-atoms and the carbon surface. The final reaction is meant to maintain CO production at high temperatures and low surface coverage of adsorbed atomic oxygen, although it was documented as a non-physical reaction mechanism [75].

Table 2.6: MURI gas-surface chemistry model reaction set.

Number	Reaction	S_0 or γ	E	Type
M1	$O + (s) \rightarrow O(s)$	1.0	0	Adsorption
M2	$O(s) \rightarrow O + (s)$	1.0	368.12	Desorption
M3	$O + O(s) + C(b) \rightarrow CO + O(s)$	57.37	38.80	Eley-Rideal
M4	$O + O(s) + C(b) \rightarrow CO_2 + (s)$	8.529×10^{-6}	57.85	Eley-Rideal
M5	$O + C(b) + (s) \rightarrow CO + (s)$	0.1203	19.01	Oxidation

The ACA model incorporates additional data from Murray et al. [30] that includes incident O and N species on a carbon surface. Prata et al. [31] also leveraged recent molecular beam and historical chemistry data for incident O_2 with a carbon surface [28, 76, 77]. The 20-reaction model shown in Table 2.7 describes oxidation by atomic and molecular oxygen, nitridation by atomic nitrogen, adsorption and desorption of atomic oxygen, adsorption and desorption of atomic nitrogen, and catalyzed recombination of oxygen and nitrogen. Incident O and O_2 reaction classes defined in reactions 1-9 and 16-20 includes weakly and strongly (single and double) bonded adsorbed atomic oxygen that is represented by O(s) and O^*(s) that aims to capture high-temperature CO formation trends seen in molecular beam experiments [29–31]. Neither MURI nor ACA models include sublimation reaction mechanisms due to the scope of experimental data collected to inform the models. Future extensions of these models may need to include them for extreme temperature and pressure environments.

Table 2.7: ACA gas-surface chemistry model reaction set.

Number	Reaction	S_0 or γ	E	Type
A1	$O + (s) \rightarrow O(s)$	0.3	0	Adsorption
A2	$O(s) \rightarrow O + (s)$	1.0	368.12	Desorption
A3	$O + O(s) + C(b) \rightarrow CO + O + (s)$	100.0	33.26	Eley-Rideal
A4	$O + O(s) + C(b) \rightarrow CO_2 + (s)$	1.0	4.16	Eley-Rideal
A5	$O + (s) \rightarrow O^*(s)$	0.7	0	Adsorption
A6	$O^*(s) \rightarrow O + (s)$	1.0	802.30	Desorption
A7	$O + O^*(s) + C(b) \rightarrow CO + O + (s)$	1000	33.26	Eley-Rideal
A8	$O^*(s) + O^*(s) \rightarrow O_2 + 2(s)$	10^{-3}	124.71	Langmuir-Hinshelwood
A9	$O(s) + O(s) \rightarrow O_2 + 2(s)$	5.0×10^{-5}	124.71	Langmuir-Hinshelwood
A10	$N + (s) \rightarrow N(s)$	1.0	20.79	Adsorption
A11	$N(s) \rightarrow N + (s)$	1.0	614.99	Desorption
A12	$N + N(s) + C(b) \rightarrow CN + N + (s)$	1.5	58.20	Eley-Rideal
A13	$N + N(s) \rightarrow N_2 + (s)$	0.5	16.63	Eley-Rideal
A14	$N(s) + N(s) \rightarrow N_2 + 2(s)$	0.1	174.59	Langmuir-Hinshelwood
A15	$N(s) + C(b) \rightarrow CN + (s)$	10^8	171.90	Eley-Rideal
A16	$O_2 + 2(s) \rightarrow 2O(s)$	1.0	66.51	Adsorption
A17	$O_2 + O(s) + C(b) \rightarrow CO + O_2 + (s)$	100.0	33.26	Eley-Rideal
A18	$O_2 + O(s) + C(b) \rightarrow CO_2 + O + (s)$	1.0	4.16	Eley-Rideal
A19	$O_2 + 2(s) \rightarrow 2O^*(s)$	1.0	66.51	Adsorption
A20	$O_2 + O^*(s) + C(b) \rightarrow CO + O_2 + (s)$	1000.0	33.26	Eley-Rideal

2.2.2 Equilibrium Model

Air/Carbon B' Curve

A common equlibrium ablation modeling approach uses a nondimensional mass blowing rate, B', to define a gas-surface boundary condition. It assumes that the gas mixture is in a saturated thermodynamic equilibrium state with the surface, where bulk carbon is added to the air mixture until the carbon begins to condense into a solid. This condensation point provides the quantity, B', which is prescribed for a specified surface pressure and temperature or two other thermodynamic variables [67]. Figure 2.5 depicts several B' curves for an air-carbon mixture [1] for relevant surface pressure and temperature conditions. The primary ablation product transitions from CO_2 to CO as temperature increases and more atomic oxygen reacts with bulk carbon until all oxygen is consumed. Once the tempera-

ture approaches the equilibrium vapor pressure of the carbon gas mixture, the solid carbon sublimes into carbon gas.

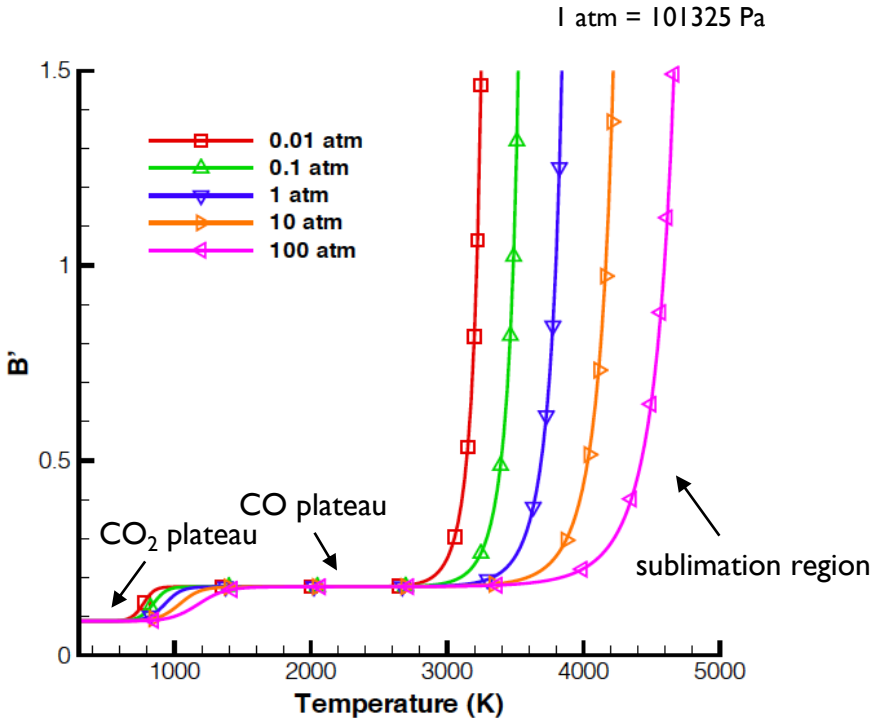

Figure 2.5: $B^{'}$ curve for given pressure and temperature conditions. Adapted from Alba [1].

Surface Chemistry Formulation

For a mixture of air and carbon gas interacting with a bulk carbon surface, the mass flux of carbon gas, $\dot{m}_c$, from the surface can be computed using a mass balance at the wall for carbon (Equation 2.51)

$$-\rho D_c \nabla y_c \Big|_w + \dot{m}_c y_{c,w} = \dot{m}_c, \tag{2.53}$$

where y_c is the mass fraction of carbon gas. Solving for $\dot{m}_c$,

$$\dot{m}_c = \dot{m} = -\frac{1}{1 - y_{c,w}} (\rho D_c)_w \nabla y_c \Big|_w . \tag{2.54}$$

To derive an expression for $B^{'}$, we can define the Stanton numbers for mass blowing and heat transfer using boundary layer transfer coefficient methodology [59, 78] as

$$C_M = \frac{\dot{m}}{\rho_e u_e B'} \quad \text{and} \quad C_H = \frac{q_w}{\rho_e u_e (h_{o,e} - h_w)}, \tag{2.55}$$

where ρ_e, u_e, and $h_{o,e}$ are the boundary layer edge density, velocity, and total enthalpy quantities respectively. The mass transfer coefficient, C_M, and heat transfer coefficient, C_H, may be related by the Lewis number, Le, which is the ratio of thermal to mass diffusivity. This appoximation assumes that the boundary layer is thin and its properties remain constant. Spalding [79] defines the semi-empirical relationship

$$C_M = C_H Le^{2/3}, \tag{2.56}$$

where the Lewis number is commonly approximated as unity and $C_M \approx C_H$ [59, 80]. Diffusion to the surface is approximated by

$$(\rho D_c)_w \nabla y_c \Big|_w \approx \rho D \frac{y_{c,e} - y_{c,w}}{\delta} \approx -\rho D \frac{y_{c,w}}{\delta}, \tag{2.57}$$

where $y_{c,e}$ is the mass fraction of carbon at the boundary layer edge and δ is the boundary layer thickness. Heat flux to the surface may also be approximated by

$$q_w \approx \frac{k}{c_p} \frac{h_{oe} - h_w}{\delta}, \tag{2.58}$$

where k and c_p is the thermal conductivity and specific heat of the gas. Plugging Equation 2.57 and 2.58 into Equation 2.55, the nondimensional mass blowing rate, $B^{'}$, is

$$B^{'} = \frac{\dot{m}}{\rho_e u_e C_M} \approx \frac{\rho D c_p}{k} \frac{y_{c,w}}{1 - y_{c,w}} = \frac{1}{Le} \frac{y_{c,w}}{1 - y_{c,w}} \approx \frac{y_{c,w}}{y_{a,w}}, \tag{2.59}$$

where $y_{a,w}$ is the mass fraction of air species at the wall [59]. Energy and mass balance relations using the legacy film coefficient approach are defined by Moyer and Rindal [81] and are outside of the scope of this study.

2.3 Verification, Validation, and Uncertainty Quantification Approach

2.3.1 Model Credibility Background

In order to provide a common tool to assess credibility of a computational model, Oberkampf et al. [82] developed the Predictive Capability Maturity Model (PCMM) framework in collaboration with experts at NASA and Johns Hopkins Applied Physics Laboratory. The key elements of the model are shown in Figure 2.6. These verification, validation, and uncertainty quantification (V&V/UQ) activities produce evidence that informs the credibility of a model.

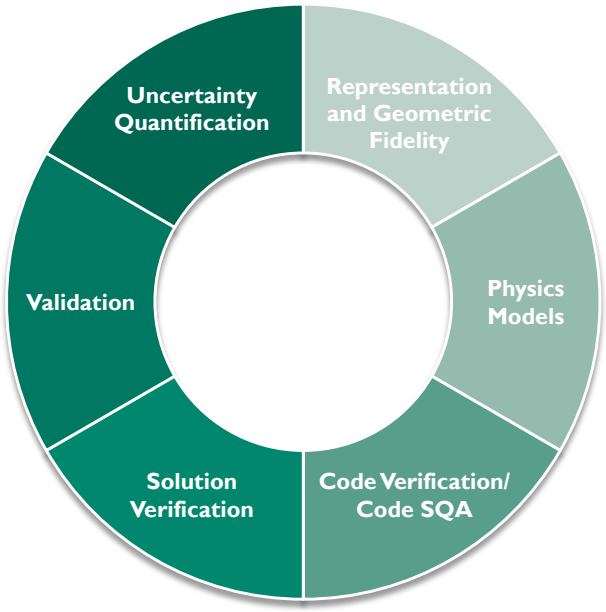

Figure 2.6: Predictive Capability Maturity Model (PCMM) credibility framework. Adapted from Mullins [2].

In application, the assessment is performed early in an analysis and revisited throughout the life of the model. Results are shared with stakeholders as a communication tool to identify gaps and monitor progress in the model development and analysis. Key outputs from this process include [2, 82]:

- Delivering evidence to assess readiness of a model capability for use in a selected application
- Identifying gaps in the current evidence for an application and prioritize needed V&V/UQ activities
- Measuring the maturity of a model over the lifetime of an analysis

A comprehensive description of the current-day PCMM framework is described by Mullins et al. [2]. Each element contains analysis themes to be addressed by experts associated with the model capability and analysis. The following studies in this work will target elements of solution verification, validation, and uncertainty quantification. For the completeness of this overview, a high-level summary of all PCMM elements are provided.

Representation and Geometric Fidelity

The goal of the representation and geometric fidelity element is to understand the impact to final model predictions due to defeatured model geometries. Output from this element informs how simplifications are being made and how geometric features are important to the analysis.

Physics and Material Model Fidelity

Key physics and material models are analyzed for their readiness in computational simulations. Math models, code implementation, validation data availability, and parameters are assessed for their adequacy given a specified application and related phenomena. Determi-

nation of how close the application and validation domains intersect for physics and material models may also be analyzed and documented.

Code Verification

The code verification element determines the code pedigree and readiness for use in a model. Software development processes, maintenance, and relevant verification activities are documented.

Solution Verification

Solution verification considers temporal, spatial, and/or stochastic resolution limitations of a model for an application. Evidence in model convergence due to model approximations or simplifications is gathered. Peer review in data analysis scripts and model input files may also included in this assessment.

Validation

Validation of a model for an application focuses on quantifying its physical accuracy and analyzing the degree of extrapolation from the validation conditions to its application. A validation hierarchy with a series of experimental datasets may be constructed to analyze pieces of a model from simple phenomena to complex combined environments.

Uncertainty Quantification (UQ)

The uncertainty quantification element addresses the characterization and identification of uncertainty sources (e.g., aleatoric, epistemic) and their impact on predicted quantities of interest (QoIs). Sensitivity analysis may be performed to identify the most influential uncertain model inputs for relevant QoIs to down-select sources parameters for uncertainty propagation and/or identify properties that need better characterization. An example may include a thermal conductivity material property that is highly influential on a predicted

temperature in a heat transfer model that needs additional experimental analysis to build more accurate uncertainty bounds.

2.3.2 V&V/UQ Tools for Present Analysis

Sensitivity Analysis and UQ Sampling

To perform a global sensitivity analysis for complex physics models, a statistical approach is needed to answer how QoIs respond when input parameters are varied according to some selected probability distribution and eventually answer targeted questions related to quantifying the uncertainty of these selected model outputs. While a conventional approach like Monte Carlo (MC) sampling generates a random sample of points for each input parameter of a model, an alternative approach is Latin Hypercube Sampling (LHS), which was developed by McKay, Conover, and Beckman [83]. LHS is considered a constrained Monte Carlo sampling scheme and statistical method that creates near-random samples of input parameters and takes into account previously generated samples. It avoids inefficiencies of MC methods due to uneven distributions of sample points, requires less samples, and converges faster than MC random sampling methods. An additional advantage of LHS is that it may be used for forward uncertainty propagation assessments. Simulations are performed using the Dakota software package, which includes methods in sensitivity analysis, optimization, UQ, and parameter estimation [84]. An incremental LHS method within Dakota can generate batches of increasing sample points to provide control in the creation of newly generated model runs and allows monitoring of sensitivity study convergence as samples are generated.

Variance-Based Decomposition

Sobol' sensitivity analysis [85] is a powerful, variance-based approach to identify the most sensitive parameters of a model. It relies on the so-called Sobol'-Decomposition of a function $f(\boldsymbol{x}), \boldsymbol{x} \in \mathbb{R}^n$ into 2^n orthogonal components. The Sobol' decomposition is a unique

decomposition of an arbitrary function in $\mathcal{L}^2$ with n *independent variables* of the form

$$f(\boldsymbol{x}) = f_{\emptyset} + \sum_{1\leq i\leq n} f_i(x_i) + \sum_{1\leq i<j\leq n} f_{ij}(\boldsymbol{x}_{ij}) + \cdots = \sum_{\boldsymbol{d}\in\mathcal{P}(\mathcal{D})} f_{\boldsymbol{d}}(\boldsymbol{x}_{\boldsymbol{d}}), \tag{2.60}$$

where $\mathcal{P}(\mathcal{D})$ is the power-set of $\mathcal{D} = \{x_1, ..., x_n\}$ and $\text{Card}(\mathcal{D}) = 2^n$. Simplifying notation by dropping the functional dependence, the components, $f_{\boldsymbol{d}}$ are orthogonal with respect to the covariance such that

$$\text{Cov}[f_i, f_j] = \delta_{ij}\mathbb{V}[f_i].$$

where δ_{ij} is the Kronecker delta function. The operator $\mathbb{E}[\cdot]$ (and therefore $\mathbb{V}[\cdot]$, $\text{Cov}[\cdot]$, and conditional versions thereof) include the relevant probability distributions. The orthogonal components are defined in a Gram–Schmidt-like process based the *conditional expectation* to find [86]

$$\begin{aligned} f_{\emptyset} &= \mathbb{E}[f] \\ f_i &= \mathbb{E}\left[f\middle|x_i\right] - f_{\emptyset} \\ f_{ij} &= \mathbb{E}\left[f\middle|x_i, x_j\right] - f_i - f_j - f_{\emptyset} \\ &\cdots \\ f_{\boldsymbol{d}} &= \mathbb{E}\left[f\middle|\boldsymbol{x}_{\boldsymbol{d}}\right] - \sum_{\boldsymbol{k}\in\mathcal{P}(\boldsymbol{d})\setminus\boldsymbol{d}} f_{\boldsymbol{k}}. \end{aligned} \tag{2.61}$$

Due to the orthogonality condition, Eq. (2.61), the variance of Eq. (2.60) can move into the summation:

$$\begin{aligned} \mathbb{V}[f] &= \mathbb{V}\left[f_{\emptyset} + \sum_{1\leq i\leq n} f_i + \sum_{1\leq i<j\leq n} f_{ij} + \cdots\right] \\ &= \sum_{\boldsymbol{d}\in\mathcal{P}(\mathcal{D})} \mathbb{V}[f_{\boldsymbol{d}}]. \end{aligned}$$

Noting that $\mathbb{V}[f_{\emptyset}] = \mathbb{V}[\text{constant}] = 0$, we find $\mathbb{V}[f]$ is therefore decomposed into $2^n - 1$

contributions. For models with even a modest number of dimensions, computing $2^n - 1$ variables is intractable. We therefore define the "main effect index" as

$$S_i = \frac{\text{variance due } \textbf{only} \text{ to } x_i}{\text{total variance}} = \frac{\mathbb{V}[f_i]}{\mathbb{V}[f]} = \frac{\mathbb{V}\left[\mathbb{E}\left[f\middle|x_i\right]\right]}{\mathbb{V}[f]}. \tag{2.62}$$

We note that we remove the subtraction of $f_\emptyset$ inside the variance operator of Eq. (2.62) because it is a constant and $\mathbb{V}[f + c] = \mathbb{V}[f]$. We further note that Eq. (2.62) is *not* restricted to just single dimensions and may instead represent a *vector* of dimensions. We also define a "total effect index" as

$$T_i = \frac{\text{variance due to } \textbf{any} \text{ component of } x_i \text{ with interactions}}{\text{total variance}} = 1 - \frac{\mathbb{V}[f_{\sim i}]}{\mathbb{V}[f]} = \frac{\mathbb{V}\left[\mathbb{E}\left[f\middle|x_{\sim i}\right]\right]}{\mathbb{V}[f]}, \tag{2.63}$$

where $\sim i = \mathcal{D} \setminus i$ in Eq. (2.63) is the compliment of i [86]. It follows that, for any $\text{Card}(i)$

$$0 \leq S_i \leq T_i \leq 1, \tag{2.64}$$

and that for *single dimension*, (i.e. $\text{Card}(i) = 1$)

$$0 \leq \sum_{i \in \mathcal{D}} S_i \leq 1 \leq \sum_{i \in \mathcal{D}} T_i. \tag{2.65}$$

For the purpose of this research, we compute main effect indices to estimate the sensitivity of individual rate parameters on predicted gas species quantities at and near the surface. Interaction effects between input parameters are not discussed in the current work.

Chapter 3

Model Characterization for a Flight Application

3.1 Introduction

To characterize the chemical kinetic behavior of air/carbon finite-rate ablation models for sample flight conditions, simulations are performed on a blunt sphere-cone geometry for selected freestream conditions where oxidation, nitridation, and sublimation of the carbon surface may occur. Differences in predicted surface state quantities of gas species are evaluated, and sensitivity analysis is performed to determine the influence of reaction parameters and mechanisms.

3.2 Vehicle Modeling Approach

3.2.1 Model Description

Simulations are run to analyze Park, MURI, and ACA finite-rate surface ablation models for freestream conditions corresponding to altitudes of 20 and 40 km and a velocity of 7 km/s for a 10 cm radius spherical nosetip – 8° cone half-angle geometry. The grid of the flowfield used for these cases is shown in Figure 3.1 and contains 37,050 hexahedral elements. This test case was previously designed by Candler [67] as a model comparison tool across relevant altitude

freestream conditions. Specified inflow conditions are shown in Table 3.1. The reacting flowfield in the post-shock region is assumed to be in thermochemical nonequilibrium, and Park's 11-species mechanism shown in Table 2.1 is used to simulate the gas-phase kinetics. All cases are run with a laminar boundary layer and at zero degree angle of attack.

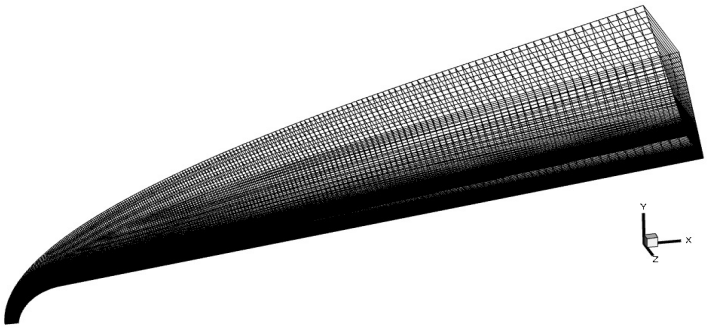

Figure 3.1: Flowfield grid for axisymmetric 10 cm radius spherical nosetip – 8° cone half-angle geometry.

Table 3.1: Freestream conditions for 20 and 40 km altitude cases.

Inflow Parameter	Quantity (20 km)	Quantity (40 km)
U_∞	7000 m/s	7000 m/s
T	217 K	250 K
T_v	217 K	250 K
ρ_∞	8.891×10^{-2} kg/m^3	3.996×10^{-3} kg/m^3
y_{N_2}	0.767	0.767
y_{O_2}	0.233	0.233

To obtain relevant surface temperatures for the study, simulations are initially run with a non-ablating non-catalytic radiative equilibrium boundary condition at the wall. Computed temperature contours of the resulting flowfields are shown in Figure 3.2. Surface temperatures in Figure 3.3 are extracted and reduced by 1000 K to provide profiles along the surface for each flight condition and are used as boundary conditions for the finite-rate models. The shift in temperature is to obtain more realistic wall conditions for an ablating surface [67].

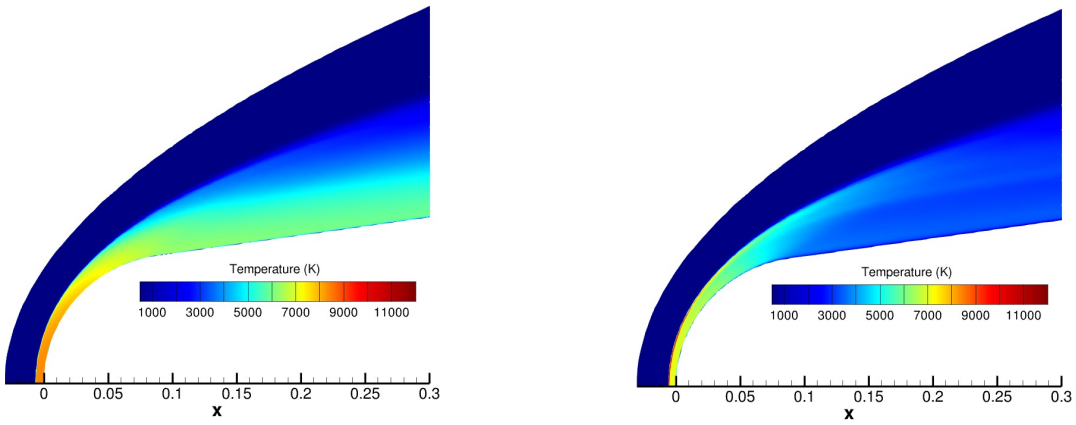

(a) 20 km (b) 40 km

Figure 3.2: Temperature contours of flowfield for freestream velocity of 7 km/s at altitude conditions. Streamwise distance, x, is in meters.

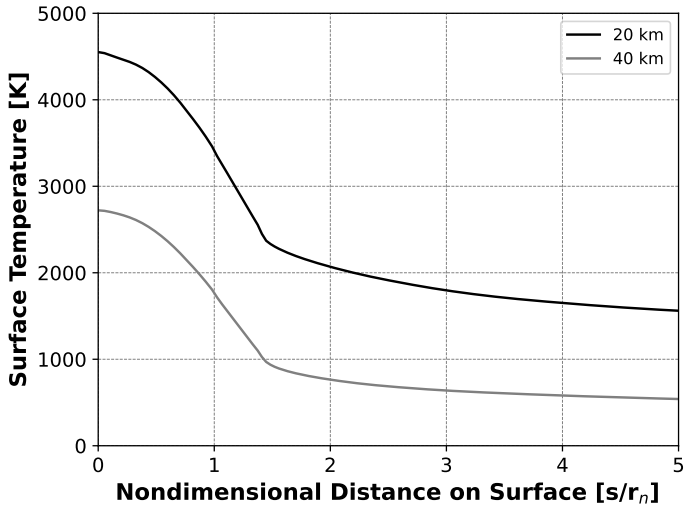

Figure 3.3: Extracted surface temperature boundary conditions from Figure 3.2 for finite-rate surface ablation simulations.

3.2.2 Parametric Uncertainty

Input parameters and corresponding reactions for the Park, ZA, MURI, and ACA models are shown in Tables 2.4-2.7. Only the forward rates and two backwards rates (Z1b, Z2b) are varied in the ZA model since all other backwards rates are separately determined using equilibrium constants. Active site density, B, used in the ZA, MURI, and ACA models are

in units of moles m^{-2} and is set to a nominal value of 1×10^{-5} [12, 31]. This parameter corresponds to the number of carbon atoms per surface area on a sheet of graphene, which are approximated as the locations where atomic oxygen may adsorb [1, 87].

Sensitivity bounds are computed by scaling input parameters (e.g., reaction efficiency and sticking coefficients) by ±50% unless constrained by physical bounds such as the sticking coefficient limit. The ranges remain within an order of magnitude, so a uniform distribution is chosen to compute the samples. Scatter data are monitored to avoid over-constraining the uncertainty bounds. In order to perform an uncertainty assessment on predicted quantities, input uncertainties and distribution types would need to be more rigorously defined. For this study, predicted quantities of interest are surface mass flux of gas species at four locations along the surface. Flux terms for carbonaceous species are correlated to an estimated removal of carbon from the surface known as a recession rate.

3.3 Global Sensitivity Analysis Results and Discussion

Sensitivity analysis is performed for Park, ZA, and MURI finite-rate surface ablation models. Ensembles of simulations are performed for each flight condition and finite-rate model. Main effect Sobol' indices are presented in Figures 3.4-3.5 and 3.8-3.13, and model quantities of interests are surface mass flux quantities for N_2, O_2, NO, CO_2, CO, C_2, C_3, CN, C, N, and O. Sobol' indices close to unity indicate that the quantity of interest is highly sensitive to the input parameter, which is shown by a dark contour color. For each condition, Sobol' indices are computed at four locations along the surface, which corresponds to locations in Fig. 3.2 for reference. At the 40 km altitude condition, the locations from the stagnation point (0.0 m) to 0.25 m correspond to surface temperatures of 2722, 2481, 893, and 631 K. For the higher heating condition at 20 km, these locations correspond to temperatures of 4552, 4264, 2277, and 1777 K respectively.

Sobol' indices for the Park model at the 40 km altitude case is shown in Figure 3.4. The

nitridation reaction (P3) efficiency, γ_3, has a moderate to high influence on CO, C_3, CN, O, O_2, and N species flux at the surface. Moving away from the stagnation point at lower surface temperatures, γ_1 becomes more correlated to CO, CN, O, O_2, and N fluxes at the surface, which corresponds to O-atom oxidation reaction (P1) to produce CO and an open active surface site. Figure 3.5 provides Sobol' data for the 20 km case, where sublimation and condensation reactions (P4 and P5) appear to dominate CO, C_3, CN, O, O_2, and N surface fluxes at and near the stagnation point. As surface temperature decreases moving further away from the stagnation point, γ_3, becomes correlated to C_3, CN, and N species fluxes. We can get more information on model behavior by enlisting scatter data to confirm the correlations and to quantitatively assess the predictions.

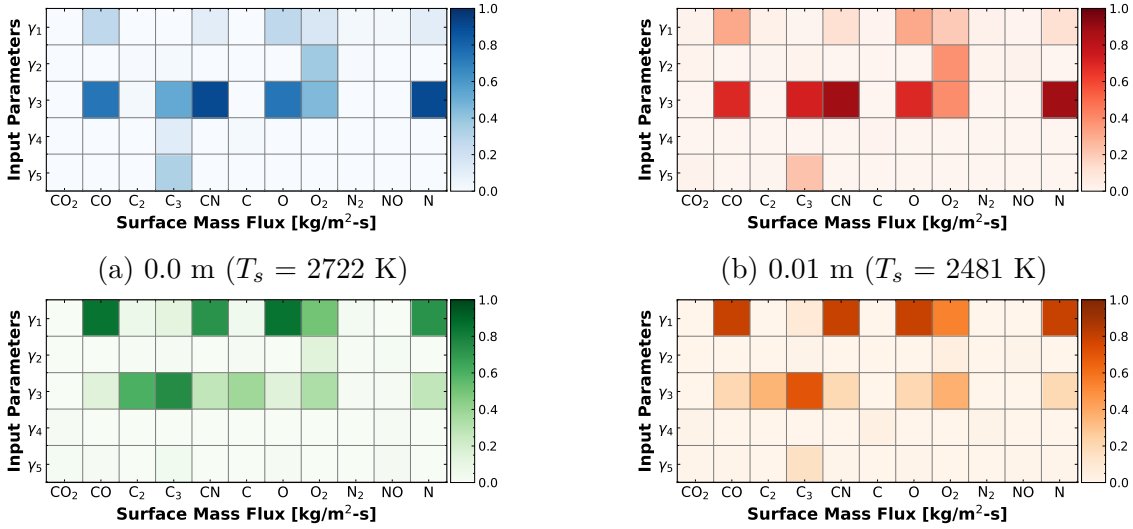

(a) 0.0 m (T_s = 2722 K)

(b) 0.01 m (T_s = 2481 K)

(c) 0.10 m (T_s = 893 K)

(d) 0.25 m (T_s = 631 K)

Figure 3.4: Sobol' indices for the Park model at 40 km and 7 km/s freestream conditions for gas species surface mass flux quantities computed at x-axis locations.

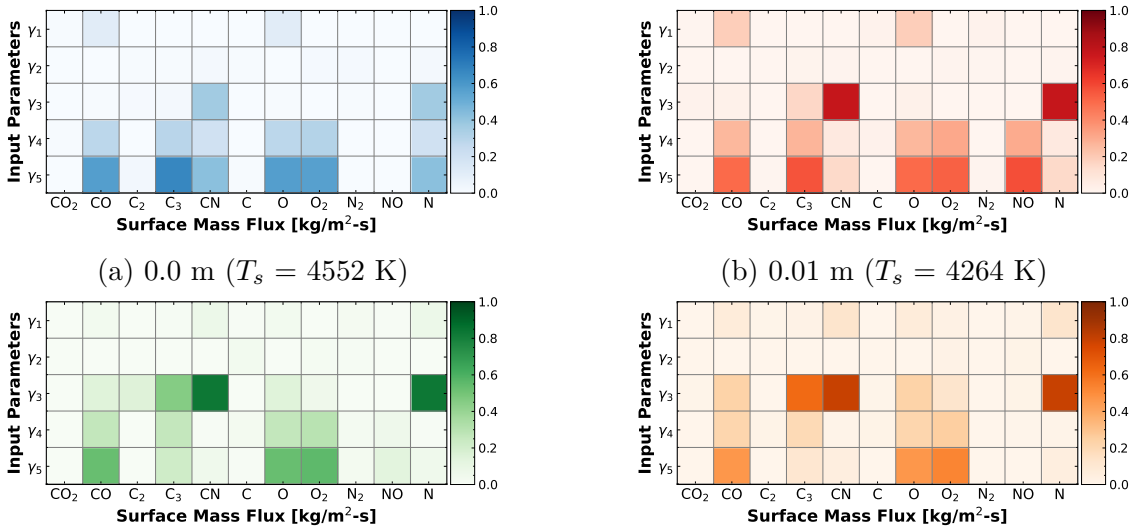

(a) 0.0 m (T_s = 4552 K)

(b) 0.01 m (T_s = 4264 K)

(c) 0.10 m (T_s = 2277 K)

(d) 0.25 m (T_s = 1777 K)

Figure 3.5: Sobol' indices for the Park model at 20 km and 7 km/s freestream conditions for gas species surface mass flux quantities computed at x-axis locations.

Figures 3.6-3.7 show the individual surface mass flux quantities as a function of input parameter value at the stagnation point for both 40 and 20 km altitude conditions. Sensitivity coloring is mapped over from Figures 3.4a and 3.5a. A positive mass flux indicates that the species is diffusing to the surface where it reacts with the bulk carbon surface or other species or adsorbs. A negative mass flux shows that the species is produced at the surface and diffuses from the body. Using a combination of sensitivity and scatter data, we can make some detailed judgments on behavior of the models in these environments. At 20 km, lower C_3 sublimation reaction (P4) efficiency in γ_4 correlates to less C_3 at the surface. Additionally, lower C_3 condensation reaction (P5) efficiency in γ_5 is correlated to more C_3 mass flux at the surface, as less C_3 is condensing into bulk carbon. As expected, a much higher magnitude of C_3 is produced at 20 km compared to 40 km where surface temperatures are 4552 and 2722 K respectively. More CO is produced at the surface at the 40 km condition than at 20 km, where increased O-atom oxidation reaction (P1) efficiency, γ_1, is correlated to increased production.

These conclusions require understanding the reaction rates in Park's 11-species gas-phase

kinetics model shown in Table 2.1, as concentrations of species in the flowfield that serve as reactants in the ablation models are important to consider. For example, the high sensitivity of species flux to the nitridation reaction efficiency, γ_3, at the 40 km altitude case provides reason to explore the concentration of N in the boundary layer. Lower efficiency in γ_3 is also strongly correlated to higher CO production, lower CN production, and more O reacting with the surface. This correlation may be due to CO production in the flowfield, which may tie to reaction 13 and possibly reactions 6, 15, 16, and 20 in the gas-phase model.

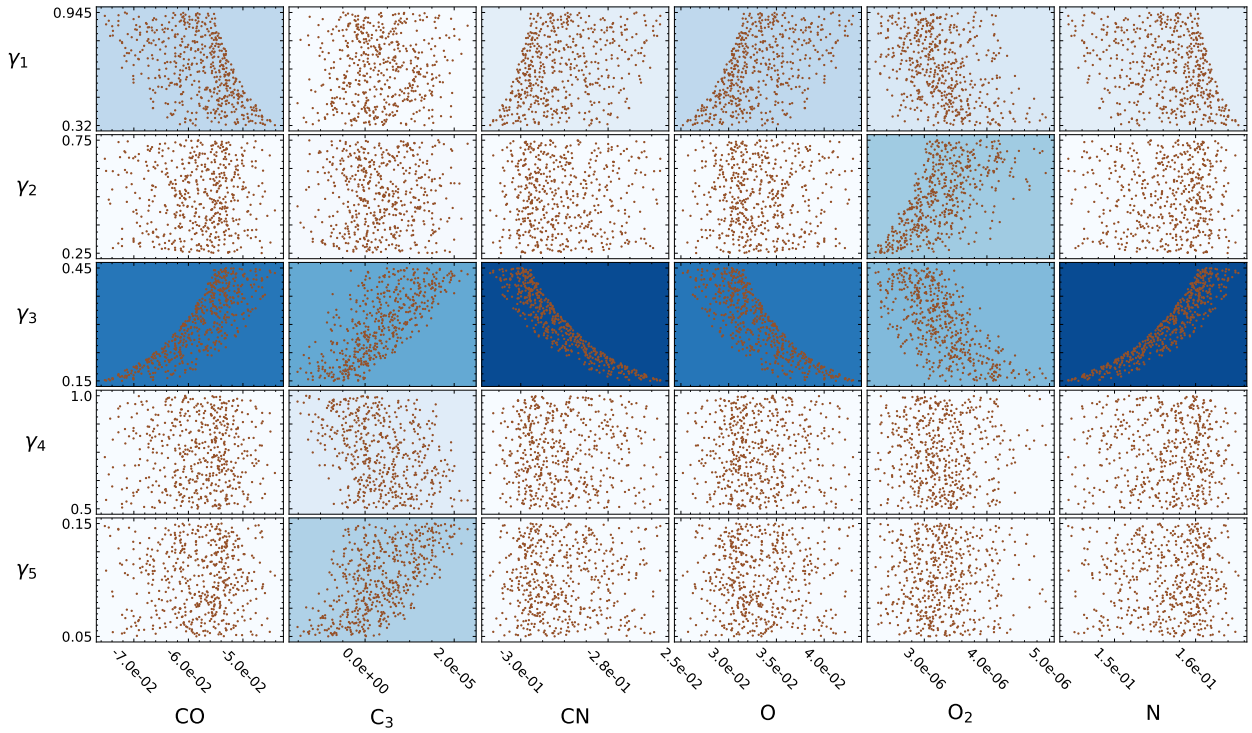

Figure 3.6: Scatter data for the Park model at 40 km and 7 km/s freestream conditions. Sensitivity input parameters are defined along the y-axis with corresponding lower and upper bounds used for sampling. Surface mass flux predictions are shown along the x-axis in units of kg/m^2-s. Sobol' index contours are mapped onto plots from Fig. 3.4a.

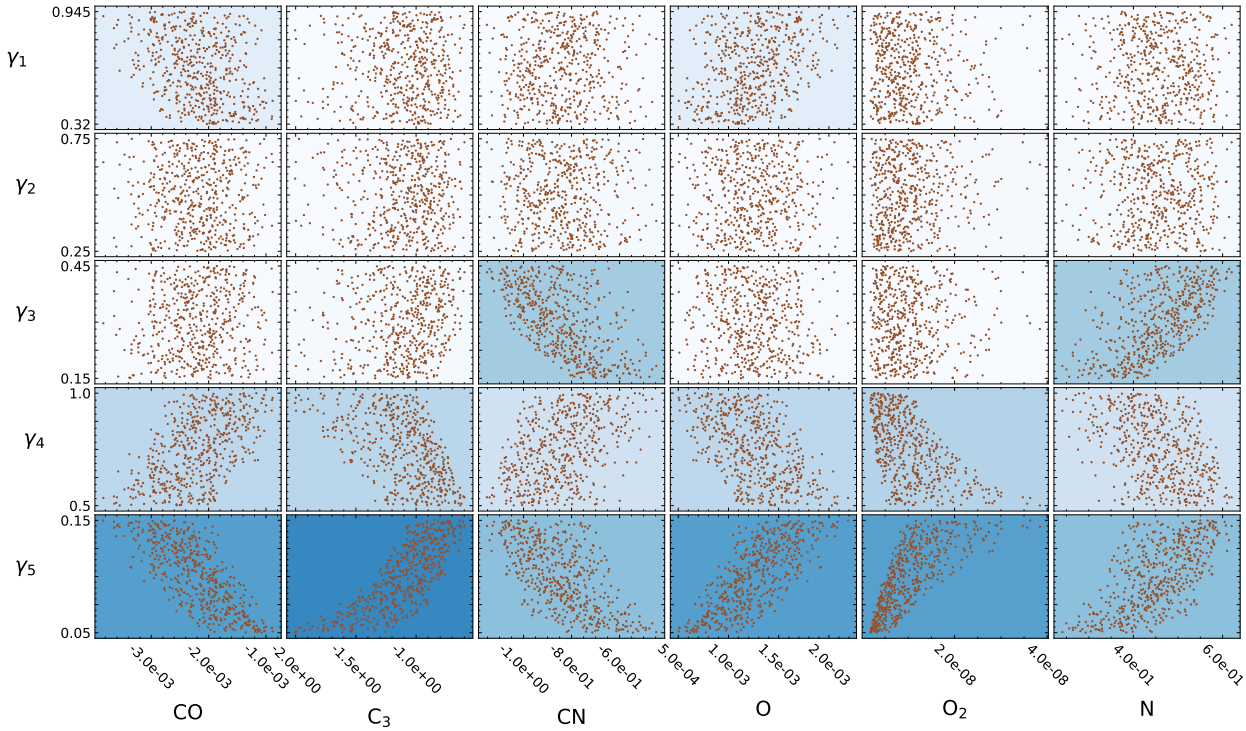

Figure 3.7: Scatter data for the Park model at 20 km and 7 km/s freestream conditions. Sensitivity input parameters are defined along the y-axis with corresponding lower and upper bounds used for sampling. Surface mass flux predictions are shown along the x-axis in units of kg/m^2-s. Sobol' index contours are mapped onto plots from Fig. 3.5a.

Figures 3.8-3.9 provide Sobol' indices for the ZA model at both 40 km and 20 km cases and show a similar relationship between the sublimation/condensation and oxidation/nitridation reactions at each altitude condition. At the stagnation point at 20 km, the C_3 sublimation and condensation reaction (Z11) efficiency, γ_{11}, is strongly correlated to CO_2, CO, C_2, C_3, and C species flux at the surface. At 40 km, there is a low to moderate correlation between B, A_1, A_2, and γ_7 with ablation product fluxes, which show that total active site density, O and N desorption (Z1b and Z2b), and Eley-Rideal CO_2 production (Z7) are influential reactions at these conditions. The influence of reaction Z7 may drive the dominant surface flux of CO_2 as an ablation product seen by Candler [67] at 40 km altitude conditions. It should be noted that there are no reactions that produce CN in the ZA model.

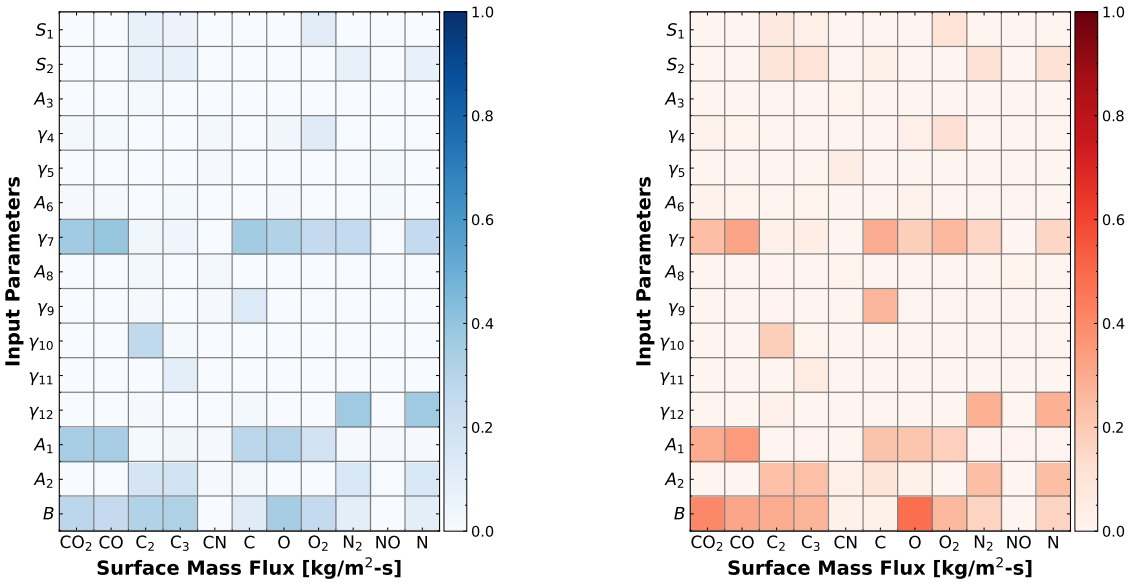

(a) 0.0 m ($T_s = 2722$ K)

(b) 0.01 m ($T_s = 2481$ K)

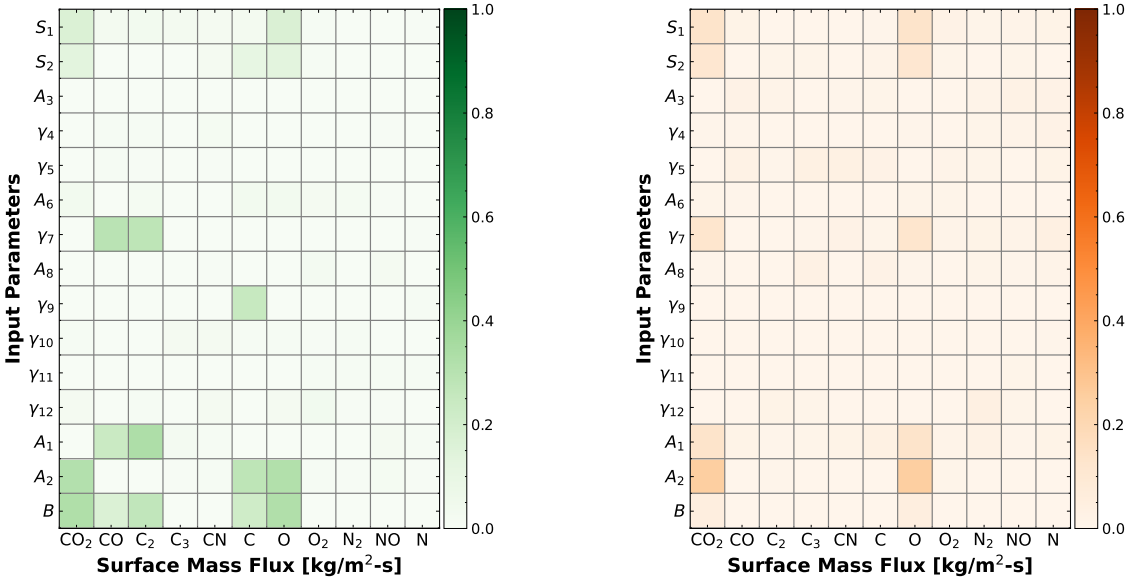

(c) 0.10 m ($T_s = 893$ K)

(d) 0.25 m ($T_s = 631$ K)

Figure 3.8: Sobol' indices for the ZA model at 40 km and 7 km/s freestream conditions for gas species surface mass flux quantities computed at x-axis locations.

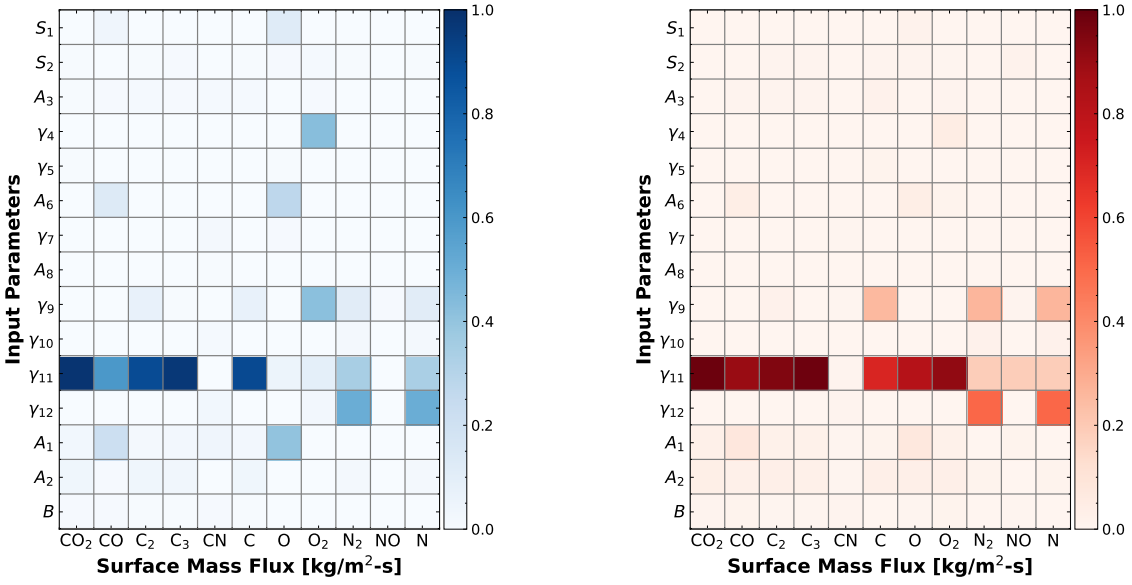

(a) 0.0 m (T_s = 4552 K)

(b) 0.01 m (T_s = 4264 K)

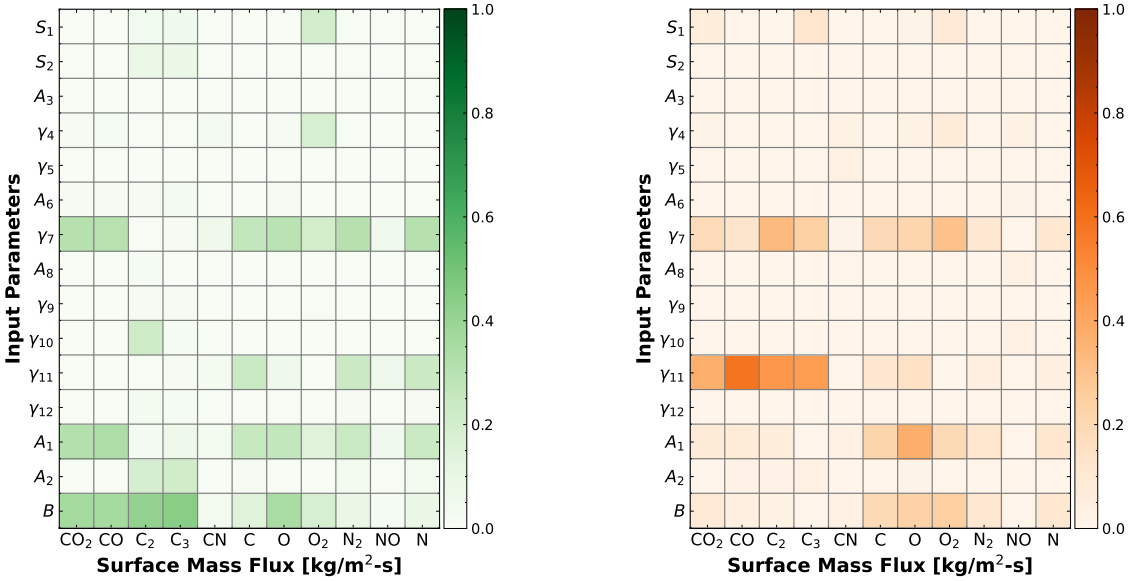

(c) 0.10 m (T_s = 2277 K)

(d) 0.25 m (T_s = 1777 K)

Figure 3.9: Sobol' indices for the ZA model at 20 km and 7 km/s freestream conditions for gas species surface mass flux quantities computed at x-axis locations.

Sobol' sensitivity results for the MURI and ACA models are shown in Figures 3.10-3.13. Neither published model includes mechanisms for sublimation, which is expected to occur at surface temperatures greater than approximately 2100 K. Additionally, while the ACA model includes a more thorough set of nitridation and oxidation mechanisms, the MURI model is a simplified atomic oxygen oxidation model.

At 40 km in Figure 3.10, strong sensitivity of oxidation reaction (M5) efficiency, γ_5, with CO_2, CO, and O species fluxes near the stagnation point show the influence of O-atom oxidation at high temperature. The corresponding reaction was defined by Poovathingal et al. [75] as a theoretical mechanism to maintain CO production at high temperatures and low surface coverage of adsorbed atomic oxygen. This influence of γ_5 on CO_2, CO, and O fluxes is also seen at probed locations for the 20 km case in Figure 3.11, which is expected due to high surface temperatures.

The MURI model is designed such that oxygen is adsorbed onto the surface until a high-temperature transition threshold is met when surface coverage is lost, which is seen in the sensitivity data. In Figure 3.10a, the surface temperature is 2722 K, which explains why species fluxes are not sensitive to reactions M1, M3, and M4. However, in Figure 3.10c, the surface temperature is 893 K and is fully saturated with adsorbed oxygen, which is seen in the sensitivity to reactions M3 and M4 due to their dependence on adsorbed oxygen. In Figure 3.10d, the surface temperature is 631 K and is partially saturated, which helps to explain the difference in active reactions in these locations. It should also be noted that the raw values of C_2 and C surface mass fluxes shown in Figure 3.10c are on the order of 10^{-28} and 10^{-19} respectively. The strong sensitivity of these quantities to reaction M3 may be due to interactions between the gas-phase model and higher CO production in the flowfield with increased γ_3.

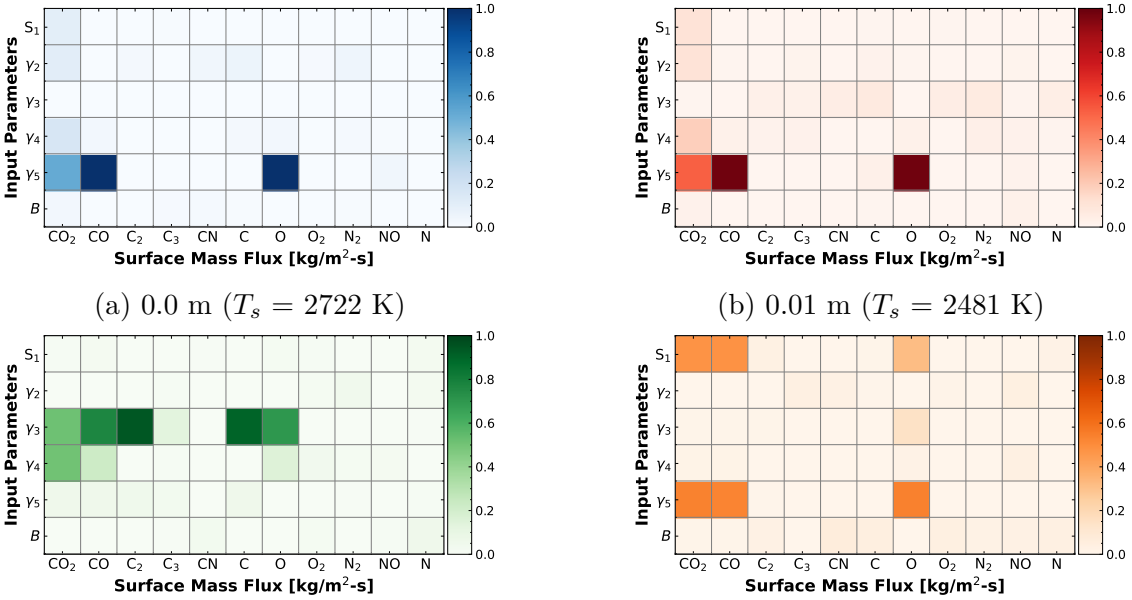

(a) 0.0 m (T_s = 2722 K)

(b) 0.01 m (T_s = 2481 K)

(c) 0.10 m (T_s = 893 K)

(d) 0.25 m (T_s = 631 K)

Figure 3.10: Sobol' indices for the MURI model at 40 km and 7 km/s freestream conditions for gas species surface mass flux quantities computed at x-axis locations.

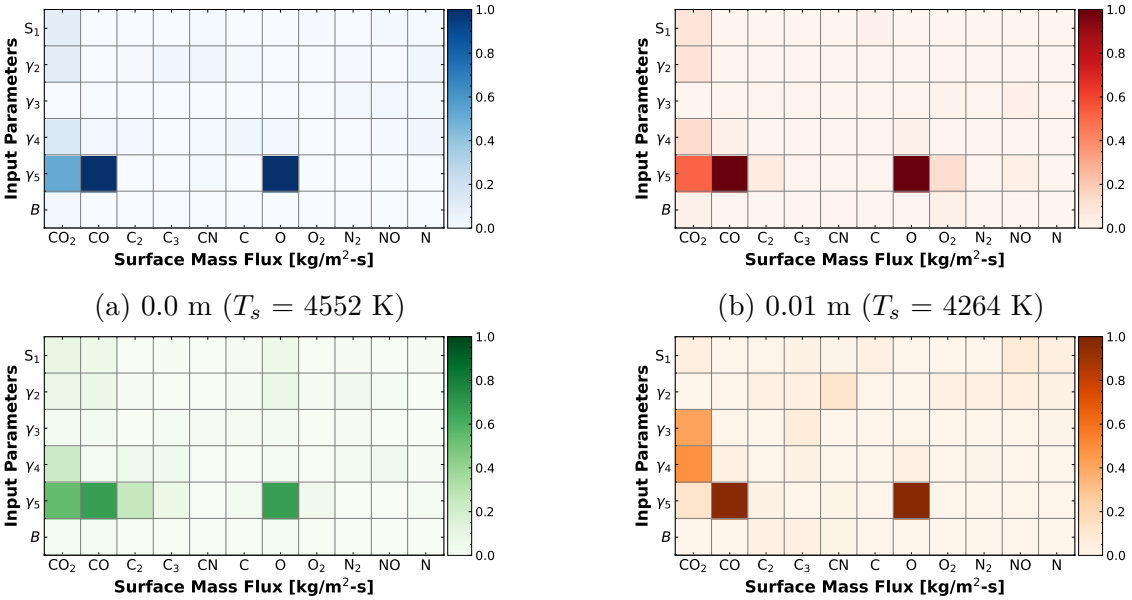

(a) 0.0 m (T_s = 4552 K)

(b) 0.01 m (T_s = 4264 K)

(c) 0.10 m (T_s = 2277 K)

(d) 0.25 m (T_s = 1777 K)

Figure 3.11: Sobol' indices for the MURI model at 20 km and 7 km/s freestream conditions for gas species surface mass flux quantities computed at x-axis locations.

ACA model weakly (single) and strongly (double) bonded adsorption reaction (A1 and A5) sticking coefficients, S_1 and S_5, have a moderate to strong influence on CO_2 and CO

fluxes, which are shown in Figures 3.12 and 3.13. Prata et al. [4] built upon the MURI model to create a more complete set of reaction mechanisms, where they defined single and double bonded adsorbed oxygen, O(s) and O*, to capture high-temperature CO formation trends seen in molecular beam experiments.

Raw scatter data for Figures 3.12a and 3.12c are shown in Figures 3.14 and 3.15, where Sobol' sensitivity coloring is mapped over. Raw gas species data with surface flux quantities less than 1×10^{-12} kg/m^2-s are not shown. At a surface temperature of 2722 K in Figure 3.14, there is a strong influence of S_5 on decreasing CO_2 and increasing CO formation as the sticking coefficient increases. It should be noted that CO_2 and CO mass flux quantities are on the order of 10^{-4} and 10^{-1} kg/m^2-s respectively. At a surface temperature of 893 K in Figure 3.15, the same relationship exists and there is more CO_2 (on the order of 10^{-2}-10^{-3} kg/m^2-s) and smaller quantities of CO (10^{-2} kg/m^2-s) than at the stagnation point condition. A low to moderate influence of both sticking coefficients on O and O_2 fluxes are shown, which provide further insight into the chemical behavior of the model (e.g., an increase in S_5 correlates to an increase in O-atoms diffusing to the surface and reacting and an increase in CO production).

Additionally, the sticking coefficient for atomic nitrogen to adsorb in reaction A10, S_{10}, has a relationship with CN, N_2, and N fluxes. In Figures 3.14 and 3.15, an increase in S_{10} is correlated to an increase in N consumption and N_2 production. CN production is moderately influenced by a range of nitridation reactions. At the stagnation point at 2722 K, an increase in S_{10} is correlated to a decrease in CN formation. However, at 893 K in Figure 3.15, it is moderately to strongly influenced by reaction (A12 and A13) efficiencies γ_{12} and γ_{13}, which tie to CN production from N, N(s), and C(b) as well as N_2 formation from N(s). An increase in γ_{12} ties to an increase in CN production while an increase in γ_{13} ties to a decrease in CN production as well as an increase in N_2 production.The active site density parameter has a low to nonexistent direct sensitivity to the mass flux quantities across MURI and ACA models.

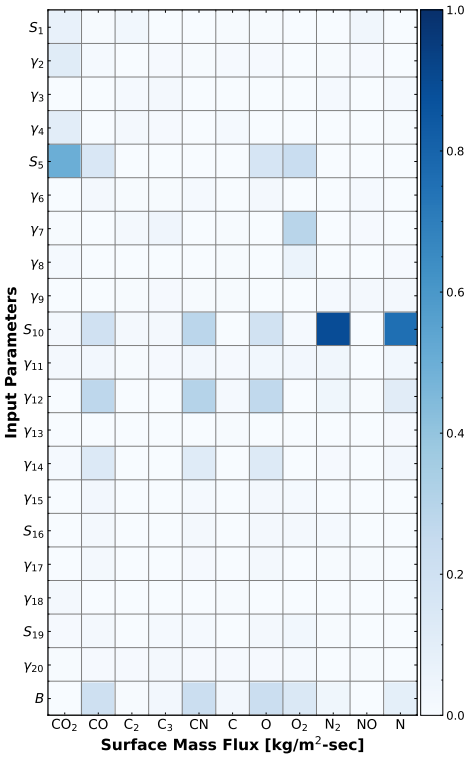

(a) 0.0 m ($T_s = 2722$ K)

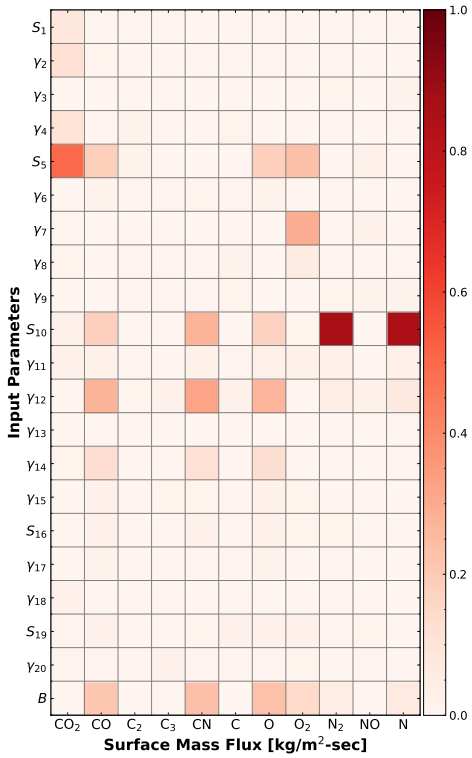

(b) 0.01 m ($T_s = 2481$ K)

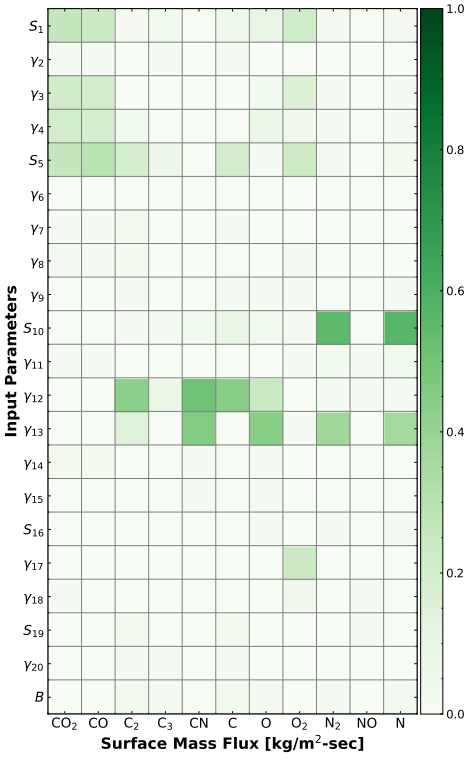

(c) 0.10 m ($T_s = 893$ K)

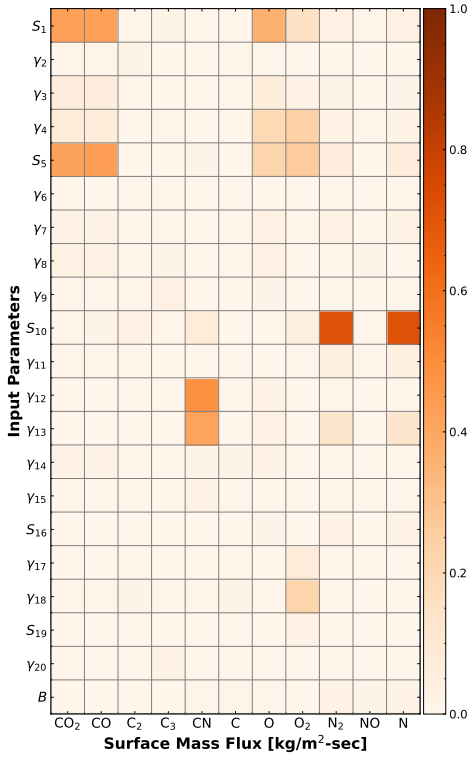

(d) 0.25 m ($T_s = 631$ K)

Figure 3.12: Sobol' indices for the ACA model at 40 km and 7 km/s freestream conditions for gas species surface mass flux quantities computed at x-axis locations.

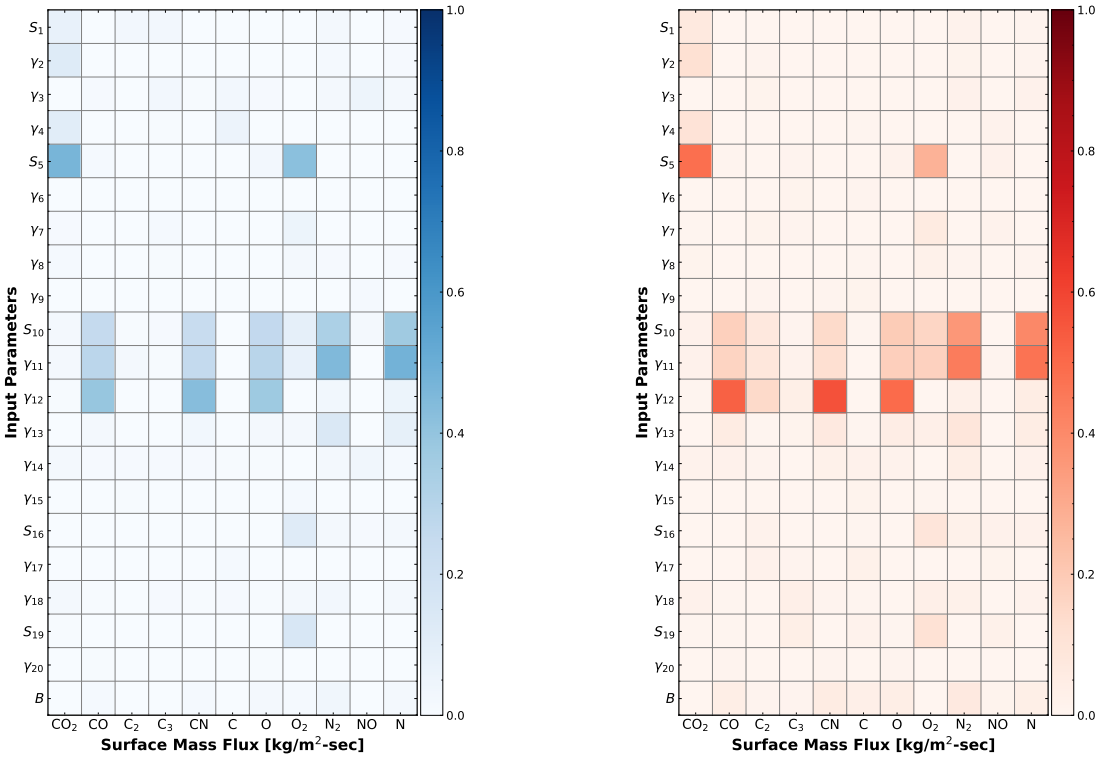

(a) 0.0 m ($T_s = 4552$ K)

(b) 0.01 m ($T_s = 4264$ K)

(c) 0.10 m ($T_s = 2277$ K)

(d) 0.25 m ($T_s = 1777$ K)

Figure 3.13: Sobol' indices for the ACA model at 20 km and 7 km/s freestream conditions for gas species surface mass flux quantities computed at x-axis locations.

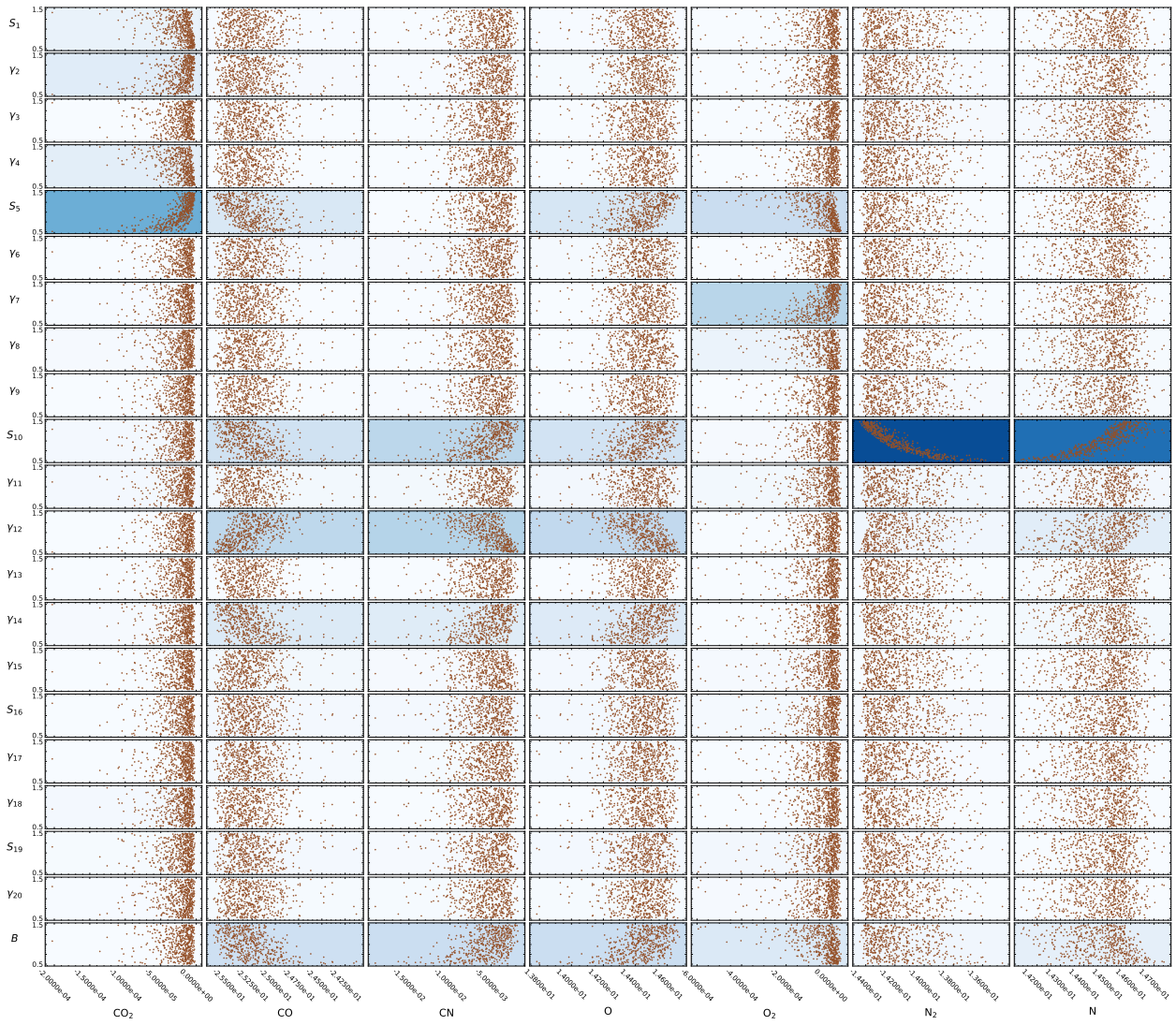

Figure 3.14: Scatter data for the ACA model at 40 km and 7 km/s freestream conditions at the stagnation point (x=0.0 m) with a surface temperature of 2722 K. Sensitivity input parameters are defined along the y-axis with corresponding lower and upper bounds used for sampling. Surface mass flux predictions are shown along the x-axis in units of kg/m^2-s. Sobol' index contours are mapped onto plots from Fig. 3.12a.

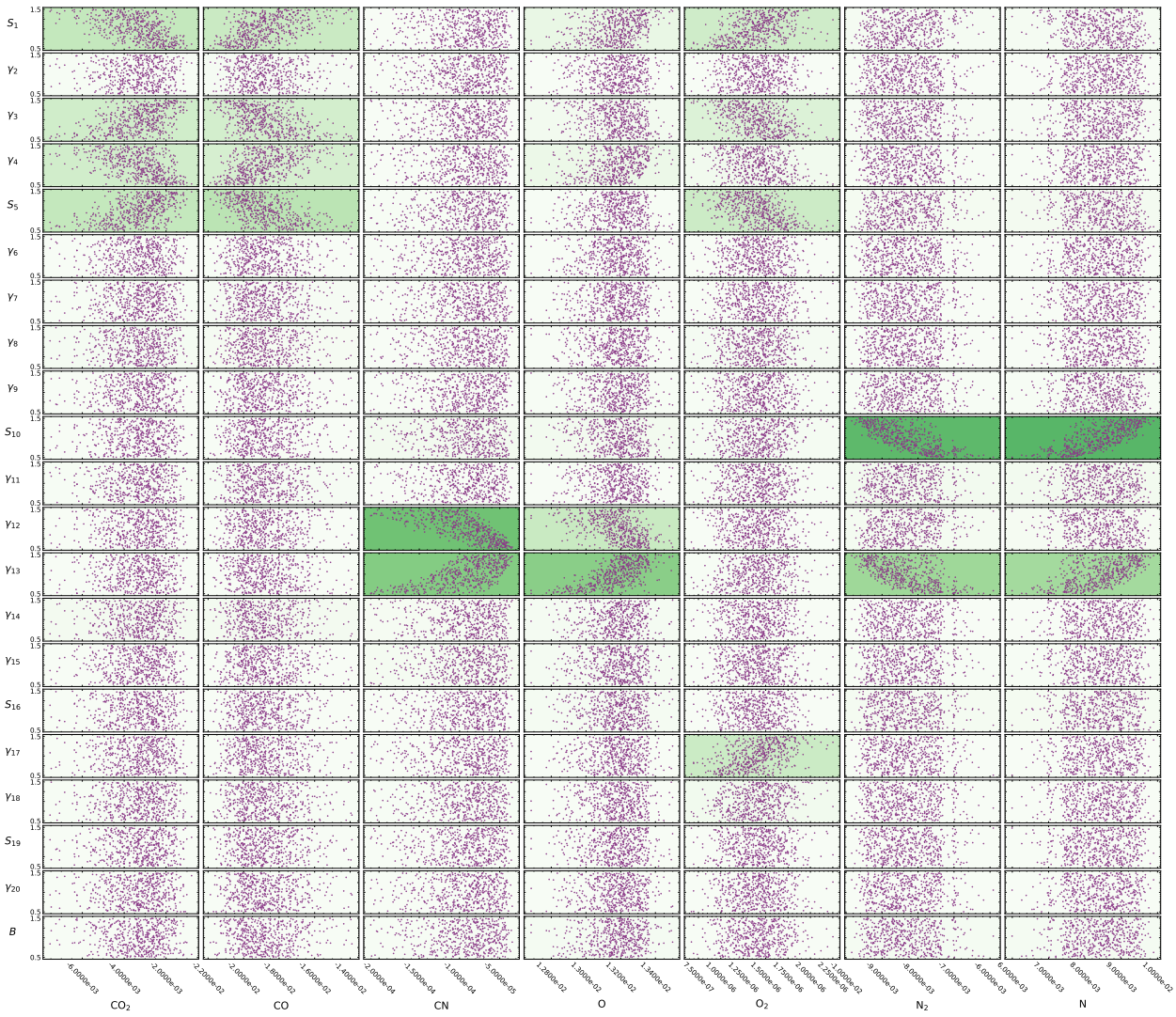

Figure 3.15: Scatter data for the ACA model at 40 km and 7 km/s freestream conditions at x=0.10 m with a surface temperature of 893 K. Sensitivity input parameters are defined along the y-axis with corresponding lower and upper bounds used for sampling. Surface mass flux predictions are shown along the x-axis in units of kg/m^2-s. Sobol' index contours are mapped onto plots from Fig. 3.12c.

3.4 Conclusions

A sensitivity analysis was performed to survey existing state-of-the-art finite-rate surface ablation models for a set of freestream conditions and a sphere-cone geometry. Park and ZA models successfully demonstrate the transition from oxidation to sublimation conditions

for the 40 and 20 km altitude cases considered. While the ACA model presently analyzed does not include needed gas-surface chemistry mechanisms for sublimation conditions, it may include the needed complexity to assess ablation regimes where a finite-rate approach is required and oxidation conditions dominate. Further studies will target Park and ACA models for additional characterization and validation to assess model credibility.

Chapter 4

Model Validation for a Shock Tunnel Environment

4.1 Introduction

New laser absorption spectroscopy (LAS) and sample heating techniques have been recently demonstrated at Sandia's hypersonic shock tunnel (HST) to measure carbon monoxide (CO) concentrations in a hypersonic boundary layer [88]. In this chapter, a validation framework is demonstrated to compare model predictions to measurements. Park and ACA finite-rate models are chosen due to differences in model complexity and mechanism development. A sensitivity analysis is performed to characterize reaction parameter influence on predicted species mass fraction quantities and reaction rate uncertainties are propagated to quantify uncertainty in model predictions. Ensemble predictions of CO number density are compared with equilibrium model predictions and LAS measurements.

4.2 Modeling Approach

4.2.1 Experimental Test Conditions

Sandia's Hypersonic Shock Tunnel uses a free-piston driver to achieve stagnation enthalpies required for producing hypersonic reentry conditions in its test chamber for Mach numbers

ranging between 8-10 [89]. The nozzle exhausts into a test chamber that is outfitted with various UV fused silica window ports installed for optical diagnostics and is connected to a vertical dump tank. An assembly of the test sample and mounting hardware in the test chamber is shown in Figure 4.1. The test sample material is a grade 2340 binderless graphite manufactured by Mersen Graphite Company. The half-cylinder test sample has a 50 mm diameter, a length of 100 mm, and a wall thickness of 2 mm. It is preheated via electric current through copper clamp electrodes connected to the material. Surface temperatures are obtained from a 2D imaging pyrometer.

Carbon monoxide concentration measurements are performed at 50 kHz using a quantum cascade laser passed near the graphite surface within the boundary layer. The laser is absorbed by exciting atomic/molecular transitions in the gas mixture containing CO. Number density and temperature of CO are found through the change in signal strength of the laser light at the output of the probed gas volume by fitting of the Beer-Lambert law. An infrared (IR) beam profiler measures the beam spot size through the probe volume, which is approximately 1.0 mm in diameter. Measurements are performed at a 65-degree angle from the stagnation streamline and 1.0 mm normal to the surface. Additional details about the experiment and data analysis are found in Hargis et al. [88].

4.2.2 Model Description

Simulations are run with US3D and gas-surface reaction sets are implemented into a user-modified finite-rate surface chemistry subroutine that couples to the CFD solver at the surface [67]. The flowfield geometry is a quarter section around the carbon test sample and copper clamp due to symmetry of the half-cylinder and sting assembly. A two-dimensional grid of the flowfield is shown in Fig. 4.2 and contains 62,000 hexahedral elements, where edge effects are ignored for the grid geometry due to the LAS measurement configuration for the experimental campaign. The flow is assumed to be in thermochemical nonequilibrium and Park's two-temperature model [60] and 11-species gas-phase kinetics model [65] are selected

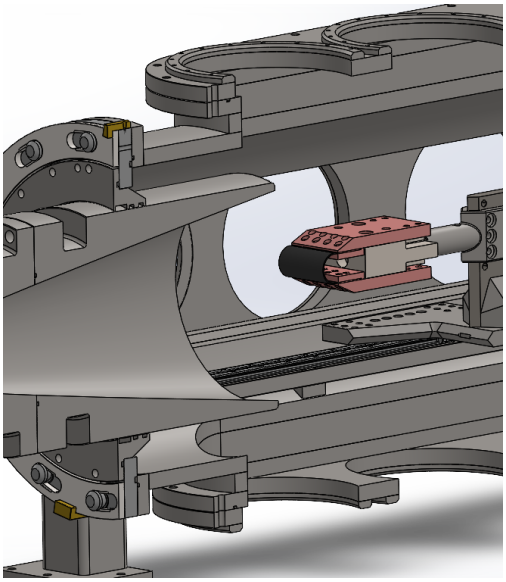

Figure 4.1: View of half-cylinder graphite strip clamped by copper electrodes in the HST test chamber.

to simulate the reacting flowfield. Table 2.1 describes the gas-phase kinetics model. The freestream flow is assumed to be laminar and inflow conditions are described in Table 4.1, which are extracted from a nonequilibrium flow simulation of the HST nozzle. A constant surface temperature, T_s, is prescribed along the strip to match the experiment, where sets of runs are performed for three temperature cases defined in Table 4.2. The boundary condition for the upper wedge surface that represents the clamp is set to an isothermal wall at 333 K.

Table 4.1: Computed 4 km/s freestream conditions for the HST test chamber.

Inflow Parameter	Quantity
U_∞	4070 m/s
T	614 K
T_v	1021 K
ρ_∞	2.24×10^{-3} kg/m^3
y_{N_2}	0.738
y_{O_2}	0.162
y_{NO}	0.059
y_O	0.041

Nominal definitions for Park and ACA models are described in Tables 2.4 and 2.7. Reaction rate coefficients are defined by Chen and Milos [37] and Prata [31]. O(s) and O*(s)

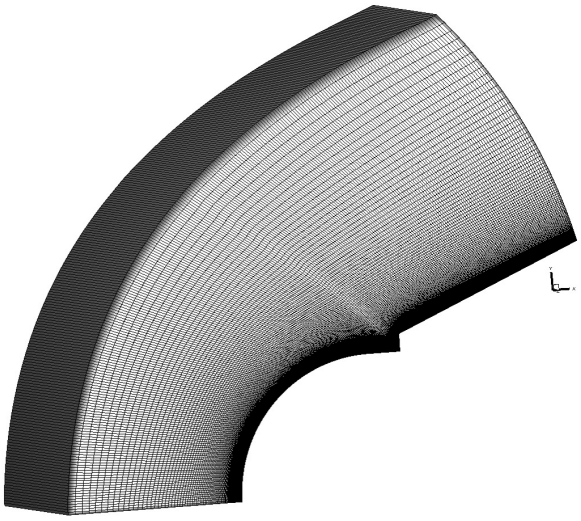

Figure 4.2: Flowfield grid for half-cylinder geometry.

Table 4.2: Prescribed HST graphite surface temperature cases.

	Case 1	Case 2	Case 3
T_s (K)	1246	1626	2146

describe atomic oxygen adsorbed onto the surface with a single and double bond respectively. N(s) represents atomic nitrogen adsorbed onto the surface and (s) describes an open surface site. C(b) is defined as bulk-phase carbon. Sticking coefficients, S_0, and reaction efficiency coefficients, γ, are found in the pre-exponential factors of the rate coefficients. The Park model shown in Table 2.4 is described by irreversible oxidation by atomic and molecular oxygen, nitridation by atomic nitrogen, and C_3 sublimation and condensation reactions. Surface coverage is assumed to be in steady state [37]. The ACA model is described in Table 2.7 and includes atomic oxygen, molecular oxygen, and atomic nitrogen as its primary reactants. It includes a series of adsorption, desorption, and recombination reactions to produce carbon ablation products and other species. Surface competition is modeled between single and double bonded atomic oxygen, atomic nitrogen, and open sites [31].

4.2.3 Solution Verification

A spatial resolution study is performed to assess error of flow quantities over a series of grids with increasing fidelity. The number of grid points are increased normal to the wall, where cell count at the wall and inflow boundary are increased approximately by a factor of 1.2 and are shown in Table 4.3 for three grids. For this convergence study, both cylindrical and clamp surfaces are set to an isothermal wall at 2146 K.

Table 4.3: Grid resolution characteristics.

	Coarse	Nominal	Fine
Boundary Cell Count	200 × 200	250 × 250	312 × 312
Total Cell Count	40,000	62,000	97,000

Surface pressure and heat flux comparisons are shown in Figure 4.3. While the nominal and fine grids show close agreement in heat flux, the coarse grid results show varying differences in heat flux predictions across the surface with maximum errors near the step interface between the half-cylinder and clamp at 0.03 m. Coarse grid surface pressure predictions also vary from the nominal and fine grid results downstream from and near the step interface. Comparisons of selected flow quantities in the boundary layer along the measurement plane and normal to the surface are shown in Figure 4.4. Predictions of gas temperatures, pressure, density, and mass fractions of oxidation species are in close agreement across mesh resolutions.

4.2.4 Parametric Uncertainty

Global Sensitivity Analysis

Variance-based sensitivity analysis is performed to rank reaction parameters and mechanisms with high influence on predicted gas species quantities in the boundary layer. This study leverages earlier methods to apply sensitivity analysis to gas-surface chemistry models, where Latin Hypercube Sampling is performed to sample selected reaction parameter inputs for

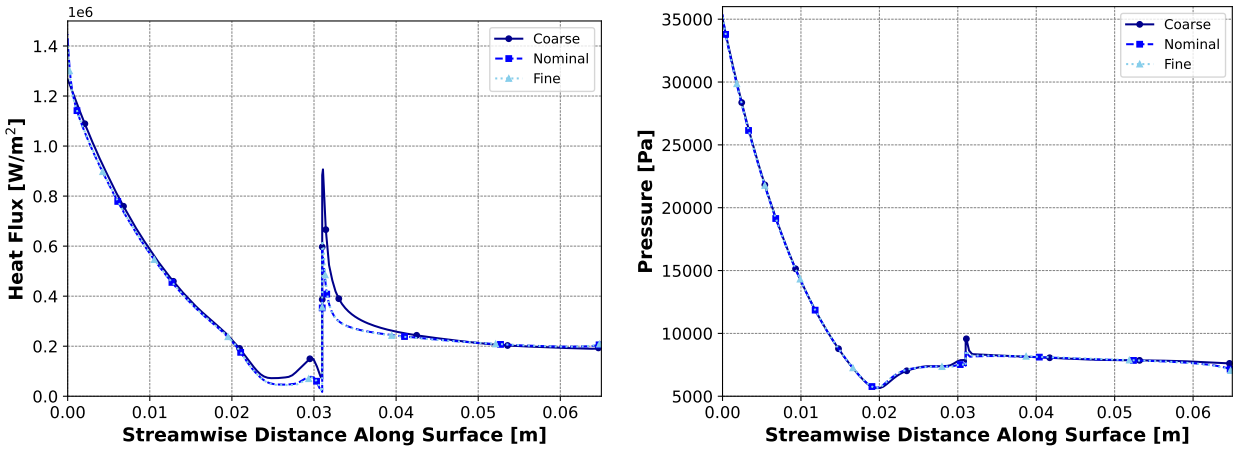

(a) Heat Flux.

(b) Pressure.

Figure 4.3: Grid convergence of boundary layer flow parameters with increasing mesh resolution. Profiles are shown along surface in the streamwise (x) direction. Surface is set to an isothermal wall at 2146 K.

each model [90]. We perform a Sobol' analysis to compute the variance for the final predicted quantities of interest across the input parameter space and apportioning the variance of each input parameter.

Sensitivity bounds are prescribed by applying a set scaling factor of $\pm 50\%$ to pre-exponential sticking coefficients and reaction efficiencies for each model's reaction rate coefficients. The scaling factor is also prescribed to the active site density term in the ACA model. Turchi et al. [91] suggested uniform distributions for coefficients with reaction efficiencies described with an exponential law, a log-uniform distribution for an input parameter whose uncertainty covers several orders of magnitude, and a uniform distribution for a parameter whose uncertainty covers a single order of magnitude. Using a log distribution for input parameters with high uncertainty ensures that model sampling is able to efficiently cover the uncertainty space. The prescribed sensitivity ranges for this study remain within an order of magnitude, so a uniform distribution is chosen to compute the samples. Quantities of interest are predicted mass fractions of gas species at 0.0 and 1.0 mm from the surface along a 65-degree measurement plane from the stagnation plane. Scatter data are monitored to avoid over-constraining the uncertainty bounds. Results enable a dimension reduction of

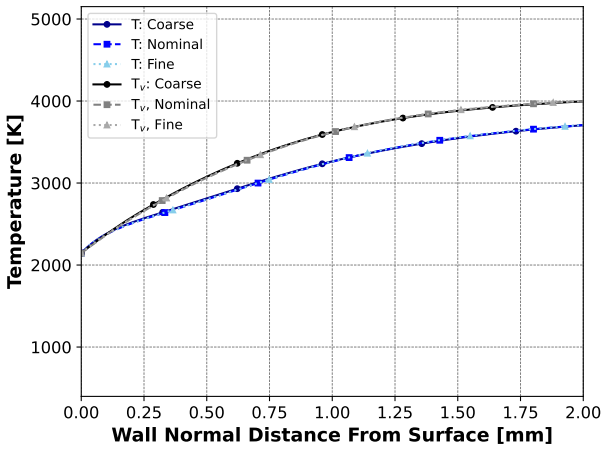

(a) Temperature.

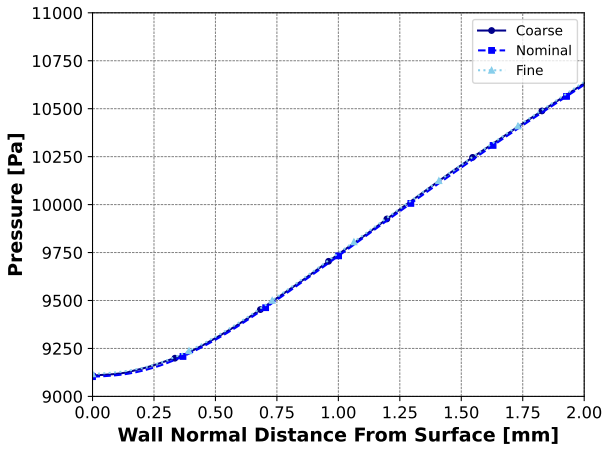

(b) Static pressure.

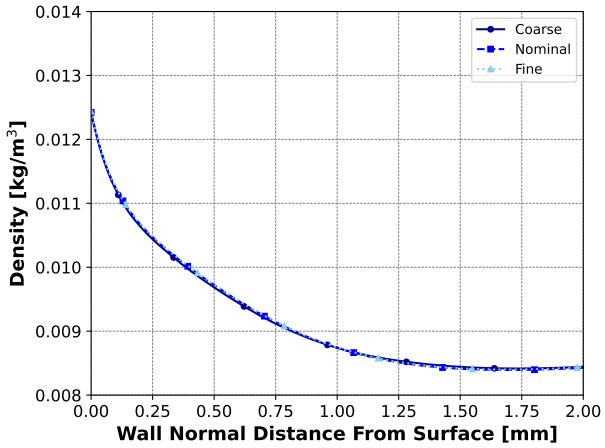

(c) Density.

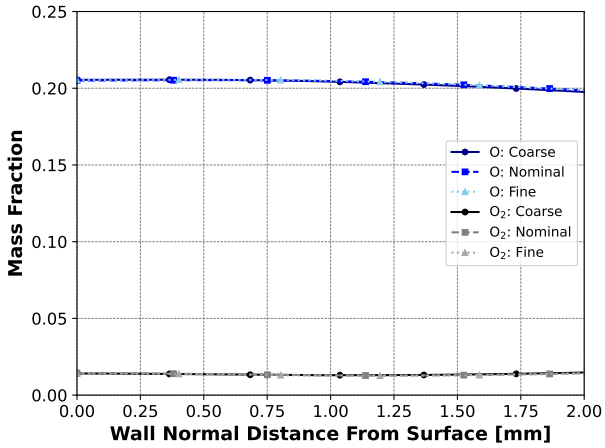

(d) Mass fraction of O and O_2.

Figure 4.4: Grid convergence of boundary layer flow parameters with increasing mesh resolution. Profiles are shown for 65-degree measurement plane. Surface is set to an isothermal wall at 2146 K.

model inputs for uncertainty propagation to support the following validation assessment.

Uncertainty Quantification

Uncertainty intervals for Park reaction efficiencies use existing data in the literature for each reaction [3, 91–93]. Uncertainties for sticking coefficients and reaction efficiencies for the ACA model are approximated using best judgment due to how the model was originally manually calibrated to experimental data in its development, which resulted in large values for reaction efficiencies. Estimated uncertainties are based on aligned research in gas-phase

kinetics and gas-surface interactions [94, 95]. Sticking coefficients were approximated by the model creators, so conservative uncertainty ranges are applied to these parameters and coupling for O adsorption to O(s) and O^*(s) reactions is maintained. To account for the largest uncertainty ranges and provide consistency over the remaining inputs, log-uniform distributions are used for each prescribed uncertainty range. Parameters with moderate to high influence on predicted CO are included in the uncertainty analysis, which are shown in Table 4.4.

4.3 Results and Discussion

4.3.1 Deterministic Model Comparisons

Simulations were performed for Park and ACA finite-rate surface ablation models at the prescribed freestream conditions for each surface temperature case. Carbon monoxide quantities predicted by the ACA model at the surface and in the boundary layer are shown in Figure 4.5 for Case 2. A positive mass flux indicates that CO is produced at the surface and diffuses from the body. Mass fraction predictions show the CO layer increase in thickness along the graphite in the streamwise direction.

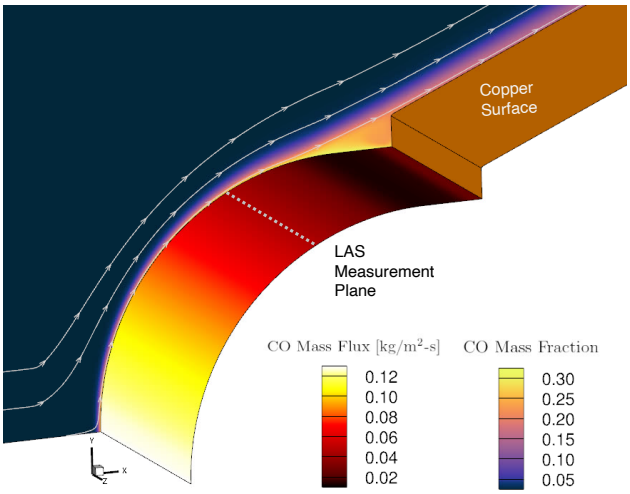

Figure 4.5: ACA carbon monoxide mass flux and mass fraction model predictions at the surface and in the flowfield respectively for 4 km/s freestream conditions. Surface temperature is set to 1626 K.

Nominal Park, ACA, and equilibrium model predictions are compared in Figure 4.6 for CO number density along the 65-degree LAS measurement plane from the stagnation streamline. Model predictions agree more closely with each other as surface temperature is increased. The simulation agreement between finite-rate and equilibrium approaches may be due to the surface existing in a diffusion-limited ablation regime, which is discussed and compared with reaction-limited regime predictions in Chapter 5. For all cases, the equilibrium model predicts the largest mass fraction of CO, which is followed by Park and ACA model predictions respectively. The experimental data (HST) includes a 95% confidence interval on the measured quantity and ±0.1 mm error on the measurement location. Gas temperature comparisons are shown in Figure 4.7 for each surface temperature case and converge at approximately 1.0 mm from the surface.

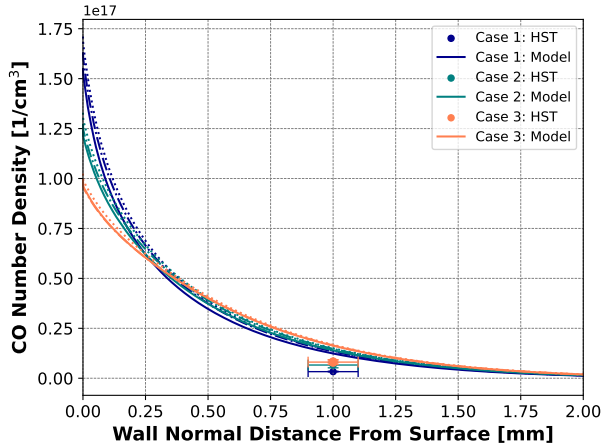

(a) Profile view across CO layer thickness.

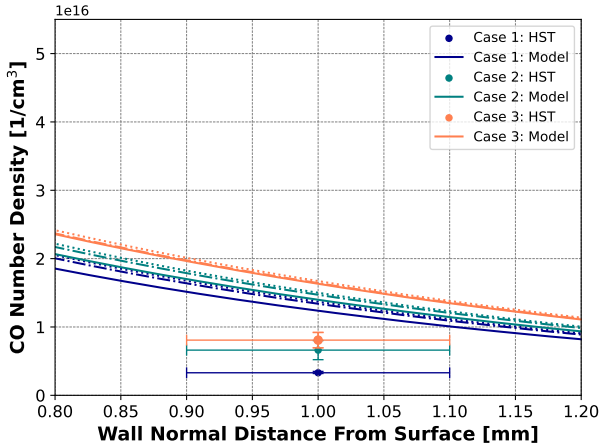

(b) Zoomed in view.

Figure 4.6: Carbon monoxide number density comparisons between Park (dash-dot), ACA (solid), and equilibrium (dotted) models and experiment (HST) along a 65-degree measurement plane for 4 km/s freestream conditions.

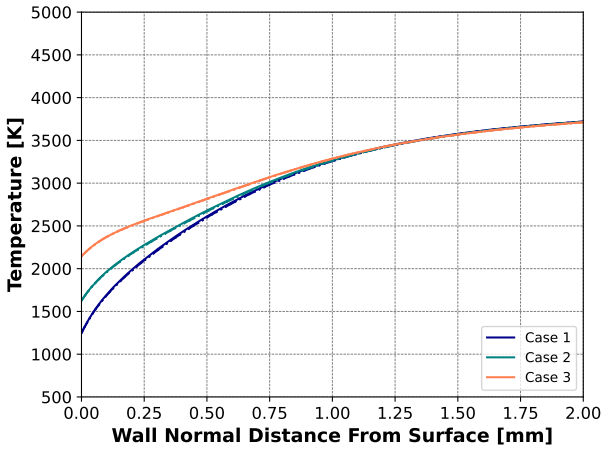

(a) Translational-rotational temperature.

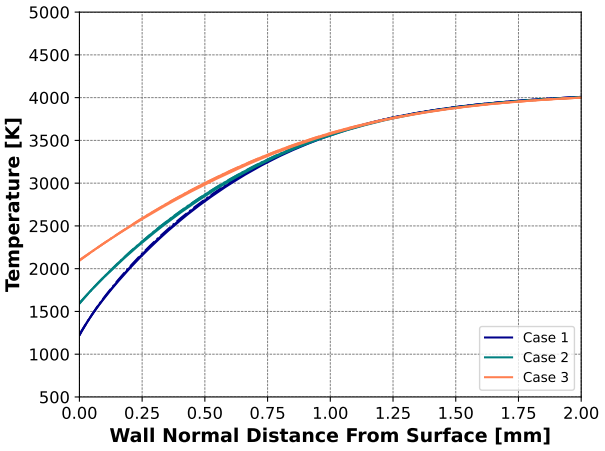

(b) Vibrational-electronic temperature.

Figure 4.7: Gas temperature comparisons between Park (dash-dot), ACA (solid), and equilibrium (dotted) models along a 65-degree measurement plane for 4 km/s freestream conditions.

Number density profiles for the full set of air and carbon ablation product species are plotted on a logarithmic scale in Figures 4.8 through 4.10. A large presence of atomic oxygen is observed due to dissociation in the shock layer. Partial dissociation of molecular nitrogen to form atomic nitrogen may be seen at much smaller concentrations, where an increase in N_2 may be due to recombination at the wall. Effects of consumption of O, N, and O_2

from gas-surface chemistry models may also be observed at the wall. Large differences in C_3 near-wall predictions may be due to differences in ablation models. While the Park model includes a C_3 sublimation mechanism, the ACA model does not. Model predictions of CO_2 also differ, where the Park model predicts less concentration than ACA and equilibrium models for Case 1 and 2. However, Park and ACA models agree more closely for Case 3. As stated previously, model predictions of CO concentration generally agree in the observed location.

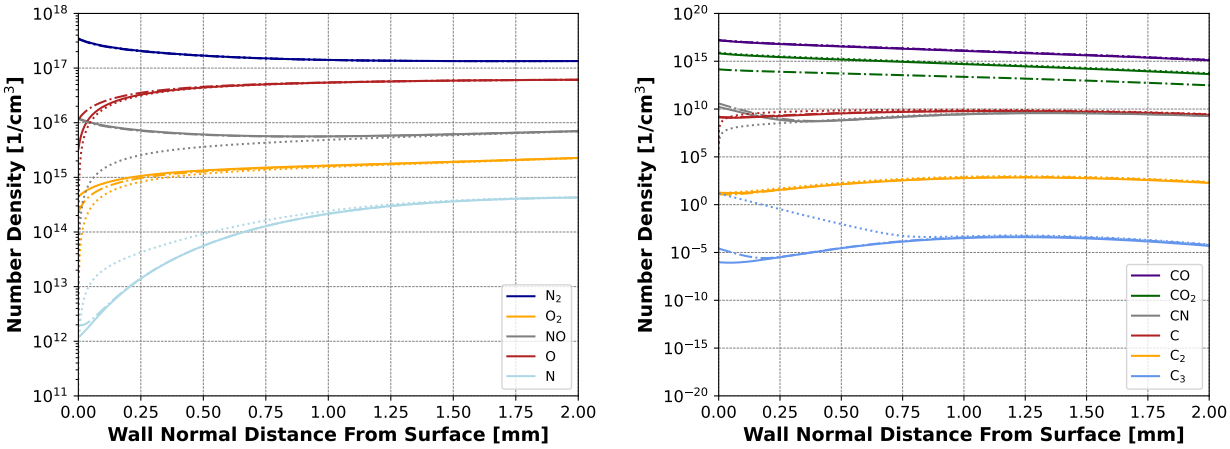

(a) Air species.

(b) Carbonaceous species.

Figure 4.8: Number density profile comparisons between Park (dash-dot), ACA (solid), and equilibrium (dotted) models along a 65-degree measurement plane for 4 km/s freestream conditions. Case 1 surface temperature is set to 1246 K.

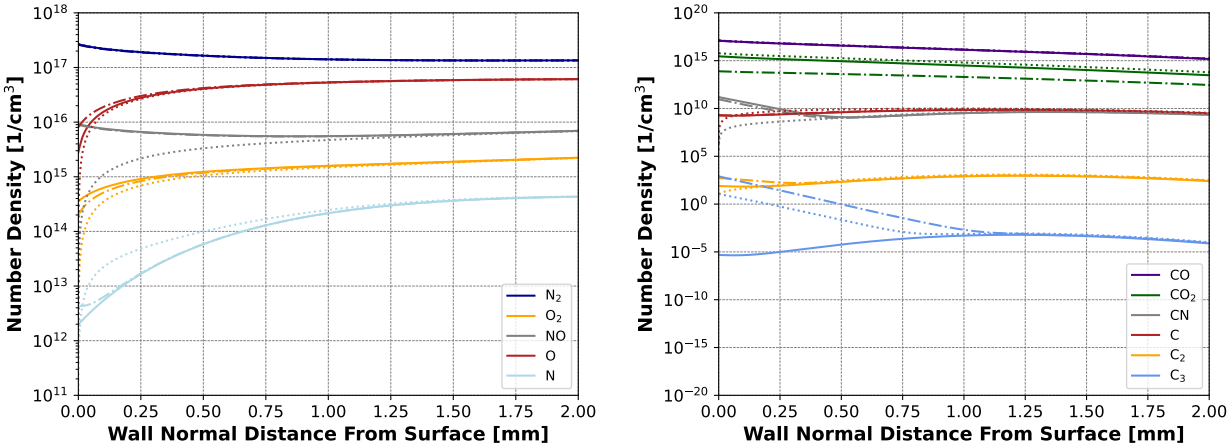

(a) Air species.

(b) Carbonaceous species.

Figure 4.9: Number density profile comparisons between Park (dash-dot), ACA (solid), and equilibrium (dotted) models along a 65-degree measurement plane for 4 km/s freestream conditions. Case 2 surface temperature is set to 1626 K.

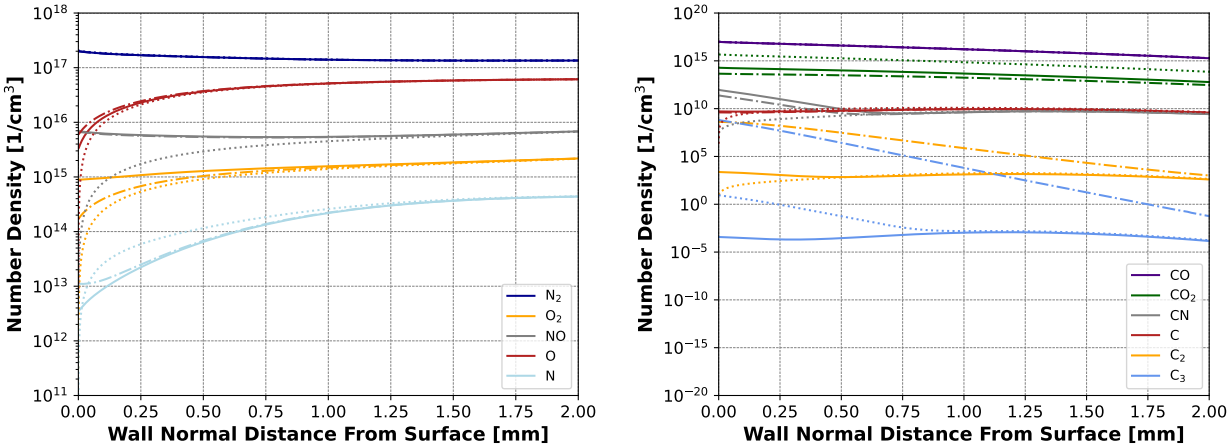

(a) Air species.

(b) Carbonaceous species.

Figure 4.10: Number density profile comparisons between Park (dash-dot), ACA (solid), and equilibrium (dotted) models along a 65-degree measurement plane for 4 km/s freestream conditions. Case 3 surface temperature is set to 2146 K.

4.3.2 Global Sensitivity Analysis

Sobol' indices for the Park and ACA models are shown in Figure 4.11 through Figure 4.28, and ensembles of 256 and 512 simulations were performed for each model respectively. Differences in sample size are due to the number of input parameters for Park and ACA models.

Incremental LHS simulation responses were monitored to ensure convergence of Sobol' indices. Index values close to unity indicate that the quantity of interest is highly sensitive to the input parameter and shown by a darker color.

In addition to the Sobol' quantities, companion scatter data of raw prediction models are plotted directly after the heat maps for each surface temperature case. Sensitivity coloring is mapped over and plotted over the scatter data. A limit was imposed in the scatter plots for mass fraction quantities below 10^{-12}, which results in C_2 and C_3 sometimes not included but captured in the Sobol' heat maps of the full gas species set. An example is shown for Case 1 in Figure 4.11, where C_3 is present. However, the raw predictions of C_3 mass fraction for the sampled data is near zero and therefore not shown in Figures 4.12 and 4.13. In this instance, the surface temperature is too low to sublimate and produce large enough quantities of gaseous C_3. The combination of Sobol' and raw scatter data is important to fully assess sensitivity and prediction behavior of analyzed models.

Over the three surface temperature cases considered, the rate coefficient for the O-atom oxidation reaction (P1) is strongly influential for the predicted mass fraction of CO at the surface and 1.0 mm from the surface. Specifically, an increase in the P1 reaction efficiency is correlated to an increase in CO mass fraction at each probed location seen in Figures 4.12 through 4.19. A reverse relationship is shown between the reaction efficiency of P1 and predicted CO_2. It should also be noted that the quantities of CO_2 are much less than that of CO by an approximate magnitude of 10^{-3}. This phenomena may be due to the fact there is no CO_2 production reaction in the Park gas-surface chemistry model itself; however, it is produced in the gas-phase kinetics model as a product of oxygen and CO reactants.

Additionally, the rate coefficient for the nitridation reaction (P3) strongly influences the predicted mass fraction of CN at the surface but is not influential on CN at the 1.0 mm location. Other notable trends include the predicted consumption of reactants such as O and O_2 with increased oxidation reaction efficiencies in reactions P1 and P2. At the highest surface temperature condition in Figure 4.18, an increase in the C_3 sublimation reaction

efficiency in reaction P4 is correlated to an increase in small quantities of C_2 and C_3 at the surface.

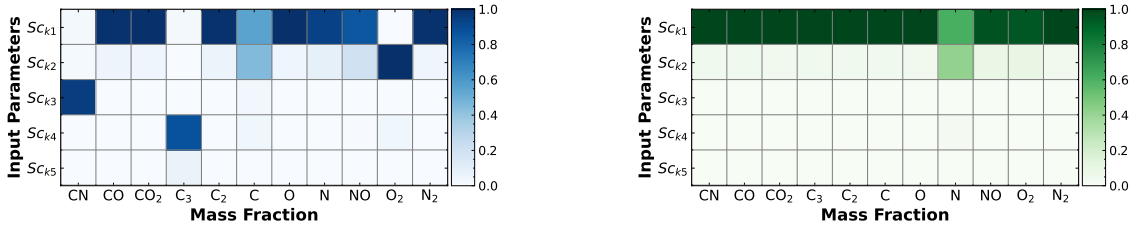

(a) 0.0 mm.

(b) 1.0 mm.

Figure 4.11: Case 1 Sobol' indices for the Park model that show influence of rate coefficient pre-exponential factors on predicted species mass fractions at locations normal to the surface along a 65-degree measurement plane for 4 km/s freestream conditions. Surface temperature is set to 1246 K.

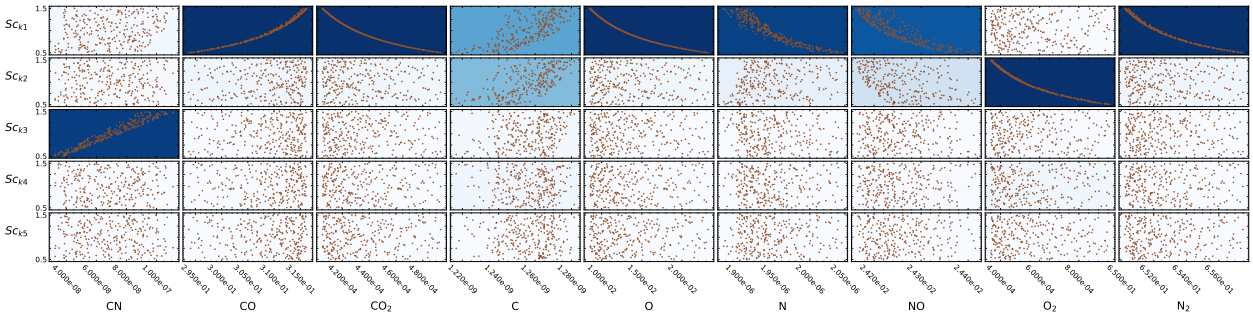

Figure 4.12: Case 1 scatter and Sobol' data for the Park model at surface on a 65-degree measurement plane for 4 km/s freestream conditions. Sensitivity scaling parameters are described along the y-axis with corresponding lower and upper bounds used for sampling. Predicted mass fractions are shown along the x-axis. Sobol' index contours are mapped onto plots from Fig. 4.11a.

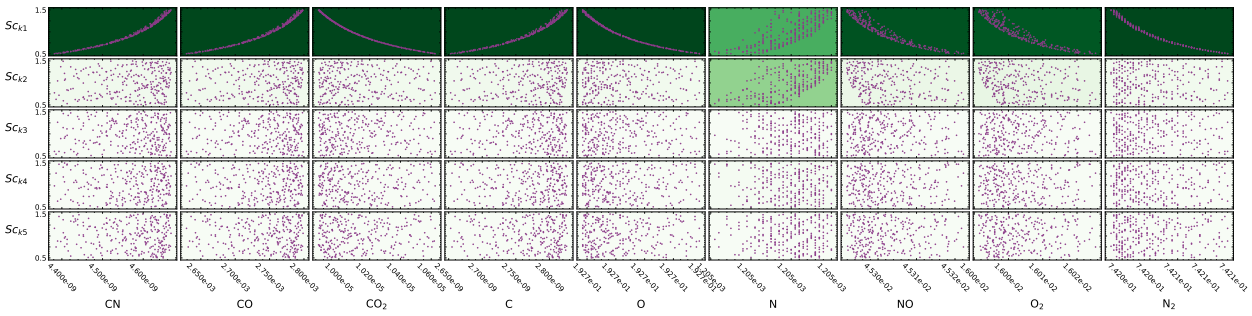

Figure 4.13: Case 1 scatter and Sobol' data for the Park model at surface on a 65-degree measurement plane for 4 km/s freestream conditions. Sensitivity scaling parameters are described along the y-axis with corresponding lower and upper bounds used for sampling. Predicted mass fractions are shown along the x-axis. Sobol' index contours are mapped onto plots from Fig. 4.11b.

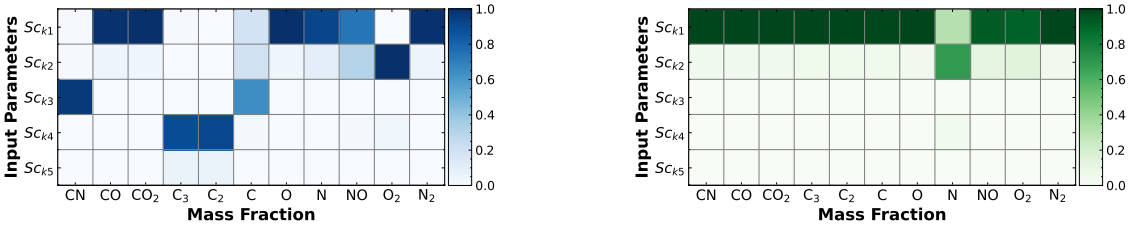

(a) 0.0 mm.

(b) 1.0 mm.

Figure 4.14: Case 2 Sobol' indices for the Park model that show influence of rate coefficient pre-exponential factors on predicted species mass fractions at locations normal to the surface along a 65-degree measurement plane for 4 km/s freestream conditions. Surface temperature is set to 1626 K.

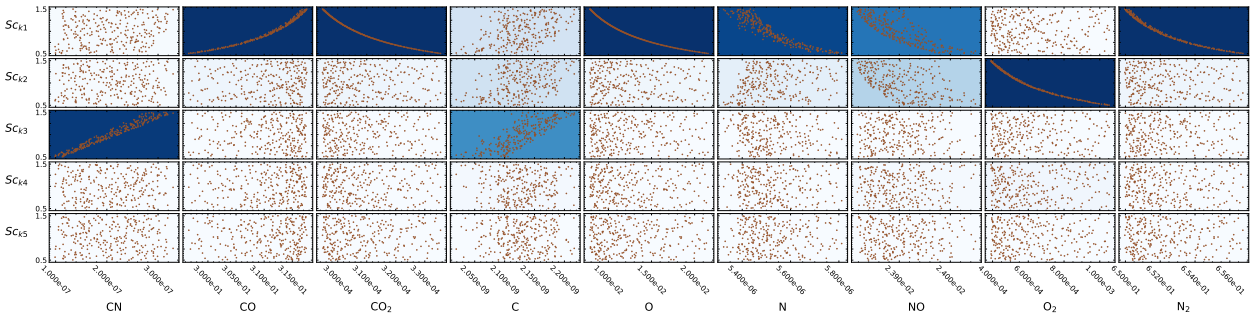

Figure 4.15: Case 2 scatter and Sobol' data for the Park model at surface on a 65-degree measurement plane for 4 km/s freestream conditions. Sensitivity scaling parameters are described along the y-axis with corresponding lower and upper bounds used for sampling. Predicted mass fractions are shown along the x-axis. Sobol' index contours are mapped onto plots from Fig. 4.14a.

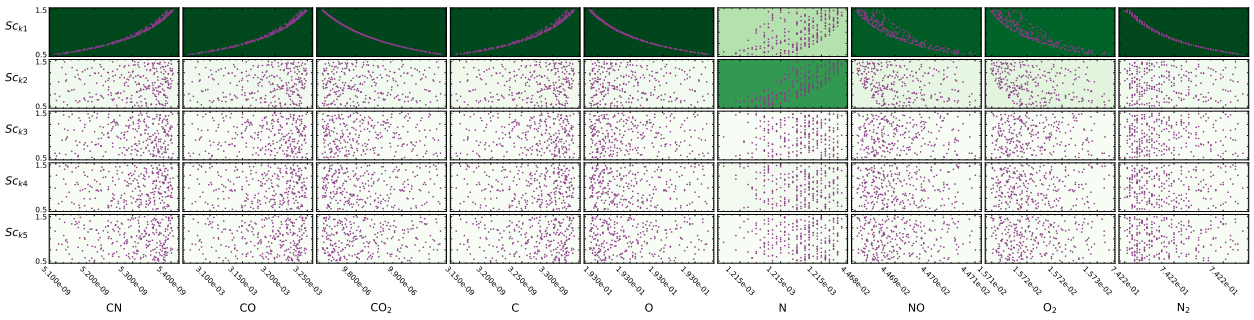

Figure 4.16: Case 2 scatter and Sobol' data for the Park model at surface on a 65-degree measurement plane for 4 km/s freestream conditions. Sensitivity scaling parameters are described along the y-axis with corresponding lower and upper bounds used for sampling. Predicted mass fractions are shown along the x-axis. Sobol' index contours are mapped onto plots from Fig. 4.14b.

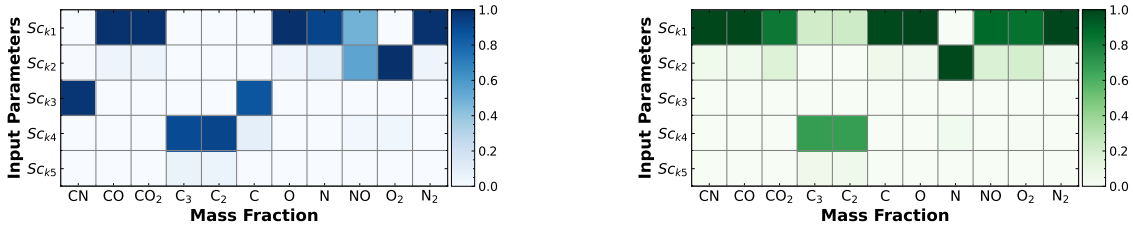

(a) 0.0 mm.

(b) 1.0 mm.

Figure 4.17: Case 3 Sobol' indices for the Park model that show influence of rate coefficient pre-exponential factors on predicted species mass fractions at locations normal to the surface along a 65-degree measurement plane for 4 km/s freestream conditions. Surface temperature is set to 2146 K.

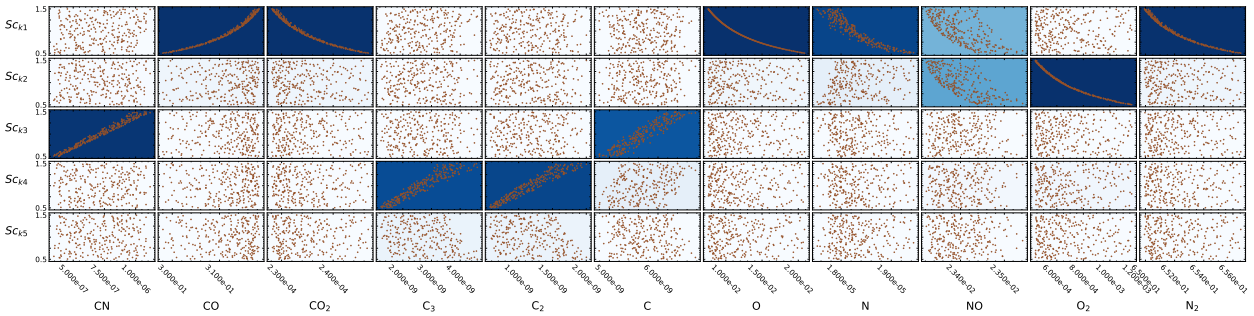

Figure 4.18: Case 3 scatter and Sobol' data for the Park model at surface on a 65-degree measurement plane for 4 km/s freestream conditions. Sensitivity scaling parameters are described along the y-axis with corresponding lower and upper bounds used for sampling. Predicted mass fractions are shown along the x-axis. Sobol' index contours are mapped onto plots from Fig. 4.17a.

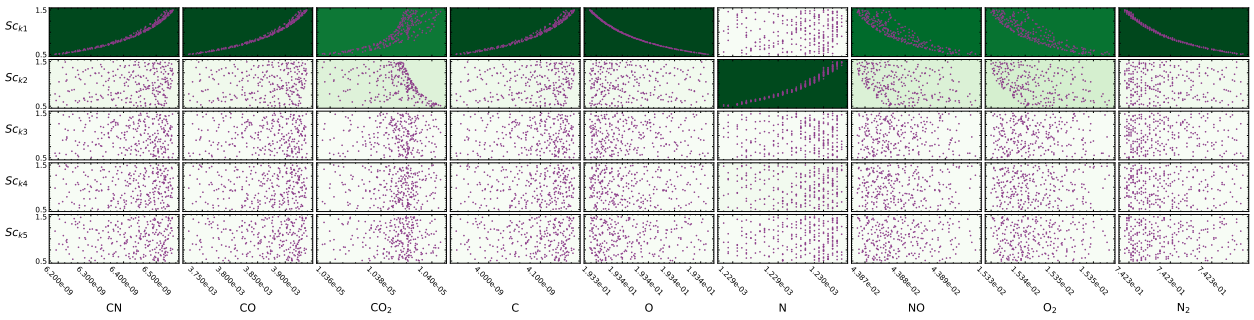

Figure 4.19: Case 3 scatter and Sobol' data for the Park model at surface on a 65-degree measurement plane for 4 km/s freestream conditions. Sensitivity scaling parameters are described along the y-axis with corresponding lower and upper bounds used for sampling. Predicted mass fractions are shown along the x-axis. Sobol' index contours are mapped onto plots from Fig. 4.17b.

The dominance of O-atom reactions is also present in ACA model CO sensitivity results for the analyzed experimental inflow conditions and surface temperature. For Case 1 and 2, Figures 4.20 through 4.25 show that reaction rate constant pre-exponential factors (e.g., sticking coefficients, reaction efficiency coefficients) for reactions A1, A3, A4, and A5 are slightly to moderately influential on the predicted CO at and near the surface. A reverse trend is shown in the adsorption of atomic oxygen to O(s). It should be noted that the model requires the sticking coefficients from A1 and A5 to sum to unity. The sensitivity study maintains this requirement by coupling the scaling of these two parameters.

As surface temperature increases, the adsorption reaction of atomic oxygen to strongly-bonded adsorbed oxygen, $O^*(s)$, is the most influential for both probed locations, where an increase in the sticking coefficient produces more O^* at the surface and may drive more CO production through reaction A7. For the highest surface temperature case (Case 3) sensitivity results shown in Figures 4.26 through 4.28, the sticking coefficient for this reaction (A5) is highly influential on CO production. Strongly-bonded oxygen was included in the model by Prata et al. to enable CO production at high temperatures above 1300 K, where one otherwise sees rapid desorption of oxygen from the surface [31]. This result is more pronounced at higher surface temperatures in Case 2 and 3.

A reverse trend in CO_2 is seen across surface temperature cases, where an increase in

the sticking coefficient for reaction A5 is increasingly influential on less predicted CO_2 at both probed locations as surface temperature increases. As more O^*(s) is formed in the sensitivity study, less O(s) is available. This results in less CO_2 formation through via O and O(s) interacting with bulk carbon in reaction A4. Quantities of CO_2 are smaller than CO by approximate magnitudes of 10^{-1} to 10^{-2} as surface temperature increases.

Reaction rate pre-exponential factors for N_2 formation through Langmuir-Hinshelwood recombination of N(s) (A14) and CN formation via Eley-Rideal recombination of N(s) and bulk carbon (A15) are moderately influential on predicted CN at the surface. As the reaction efficiency for A15 increases, the predicted CN also increases as this reaction is the dominant driver for CN formation given the low concentration of N near the surface. As the reaction efficiency of A14 increases, more N_2 is formed which reduces the pathway to CN formation at the surface. The ACA model published by Prata et al. [31] does not include a sublimation model in this study, so quantities of sublimation products (e.g. C_3) are not seen in the scatter data for the analyzed cases.

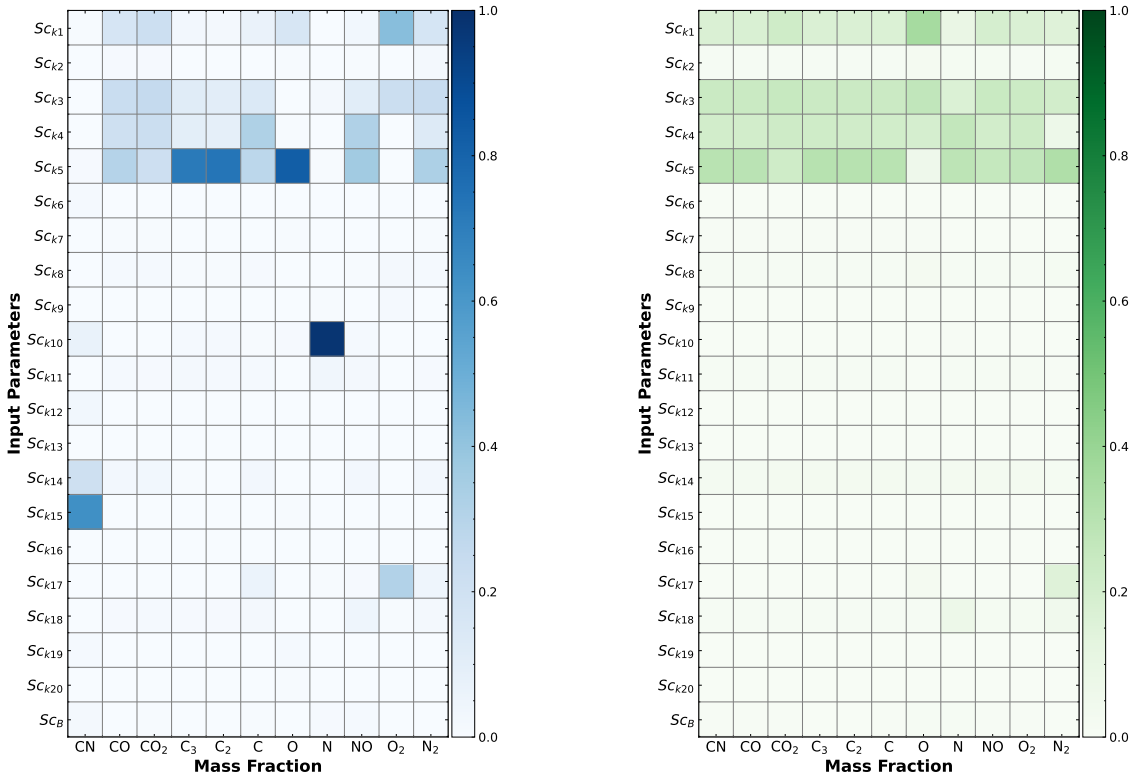

(a) 0.0 mm.

(b) 1.0 mm.

Figure 4.20: Case 1 Sobol' indices for the ACA model that show influence of rate coefficient pre-exponential factors on predicted species mass fractions at locations normal to the surface along a 65-degree measurement plane for 4 km/s freestream conditions. Surface temperature is set to 1246 K.

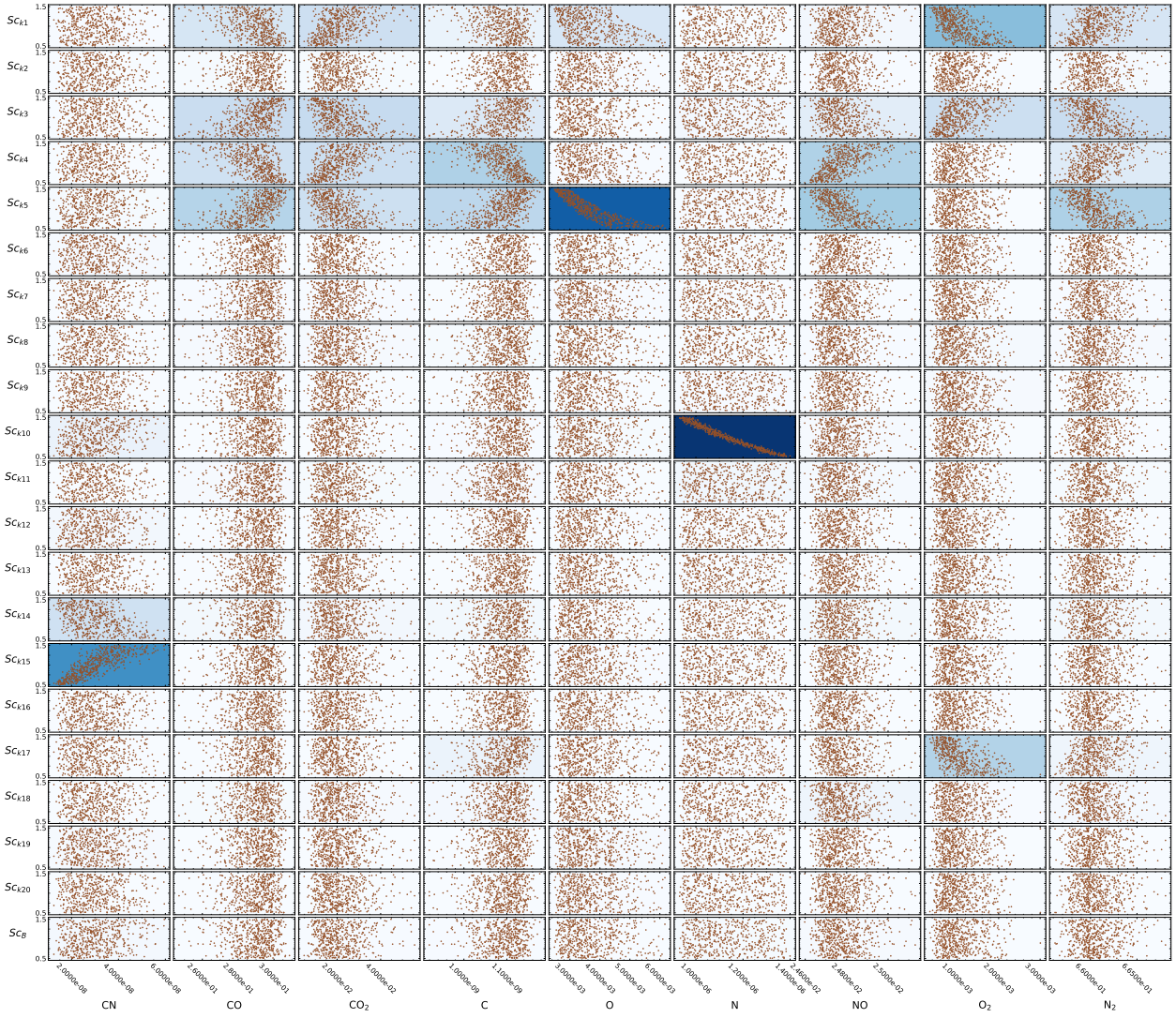

Figure 4.21: Case 1 scatter and Sobol' data for the ACA model at surface on a 65-degree measurement plane for 4 km/s freestream conditions. Sensitivity scaling parameters are described along the y-axis with corresponding lower and upper bounds used for sampling. Predicted mass fractions are shown along the x-axis. Sobol' index contours are mapped onto plots from Fig. 4.20a.

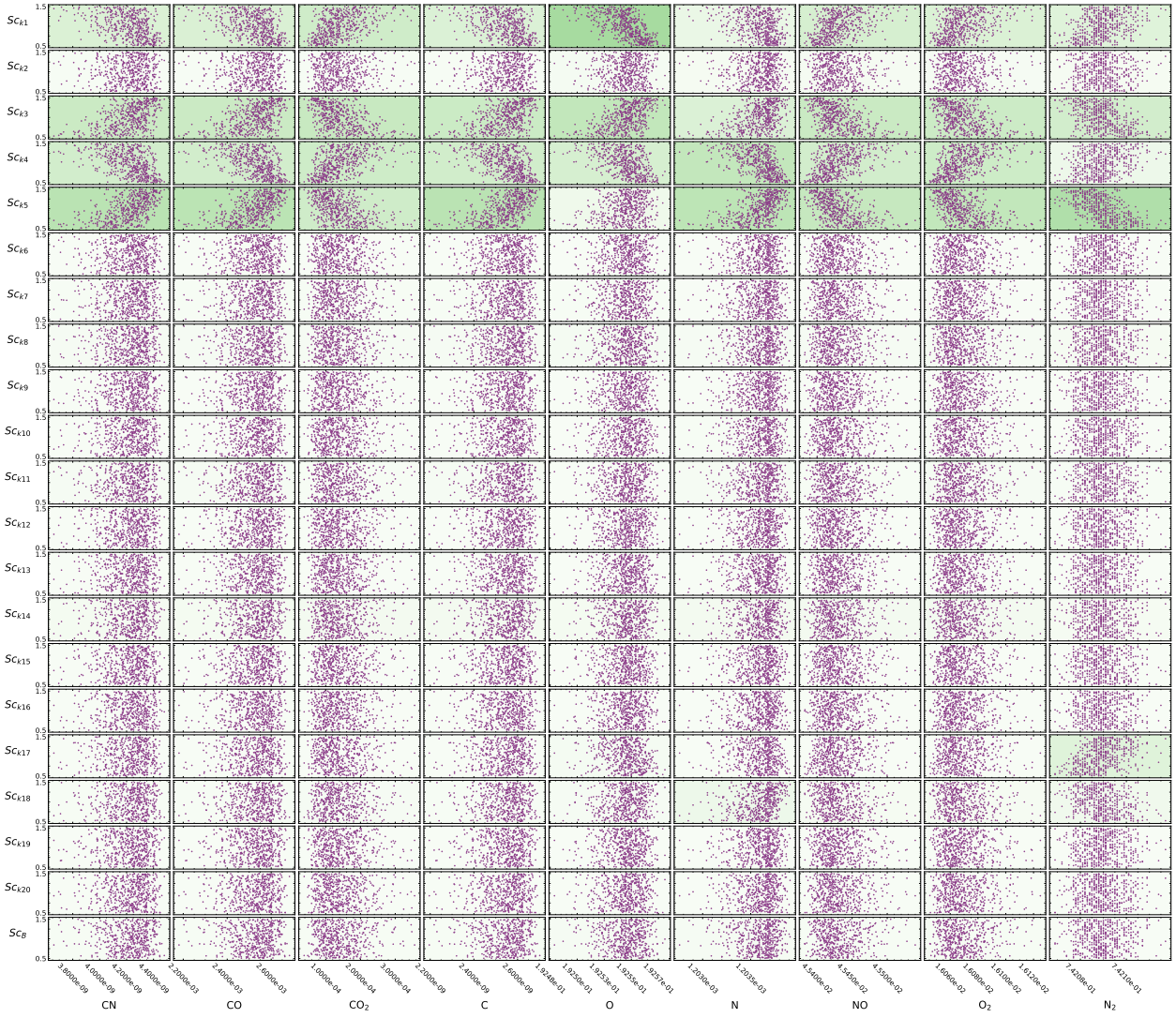

Figure 4.22: Case 1 scatter and Sobol' data for the ACA model at surface on a 65-degree measurement plane for 4 km/s freestream conditions. Sensitivity scaling parameters are described along the y-axis with corresponding lower and upper bounds used for sampling. Predicted mass fractions are shown along the x-axis. Sobol' index contours are mapped onto plots from Fig. 4.20b.

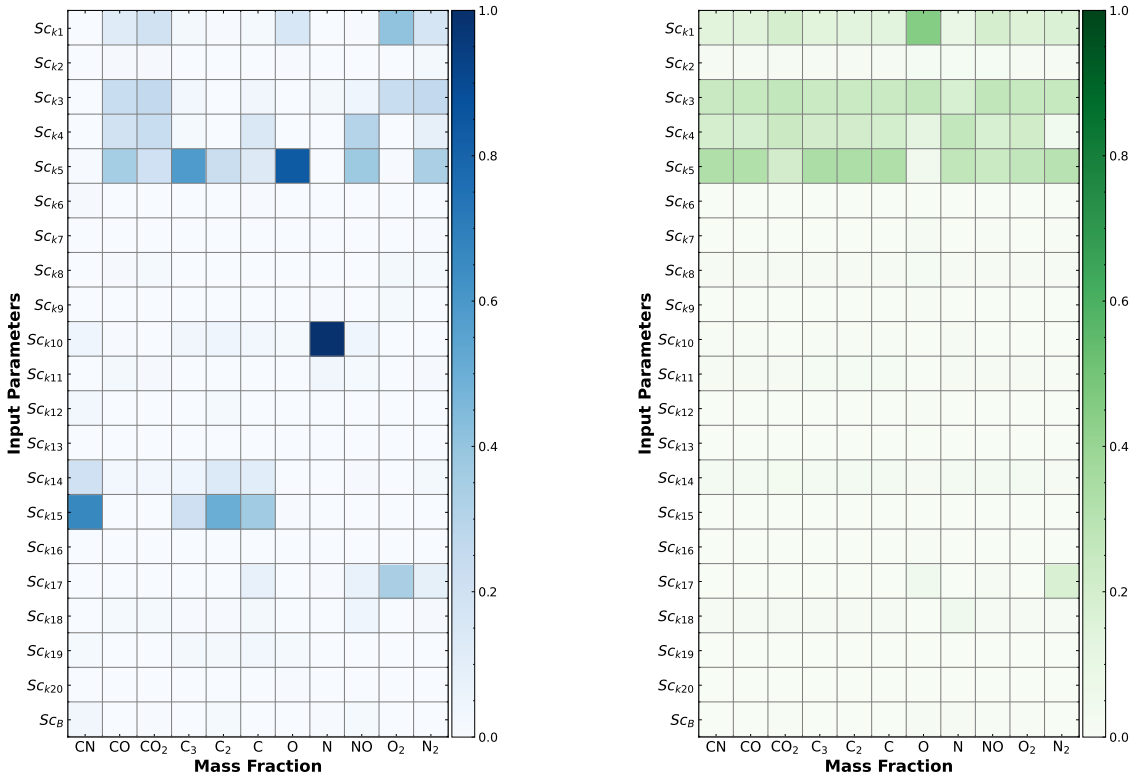

(a) 0.0 mm.

(b) 1.0 mm.

Figure 4.23: Case 2 Sobol' indices for the ACA model that show influence of rate coefficient pre-exponential factors on predicted species mass fractions at locations normal to the surface along a 65-degree measurement plane for 4 km/s freestream conditions. Surface temperature is set to 1626 K.

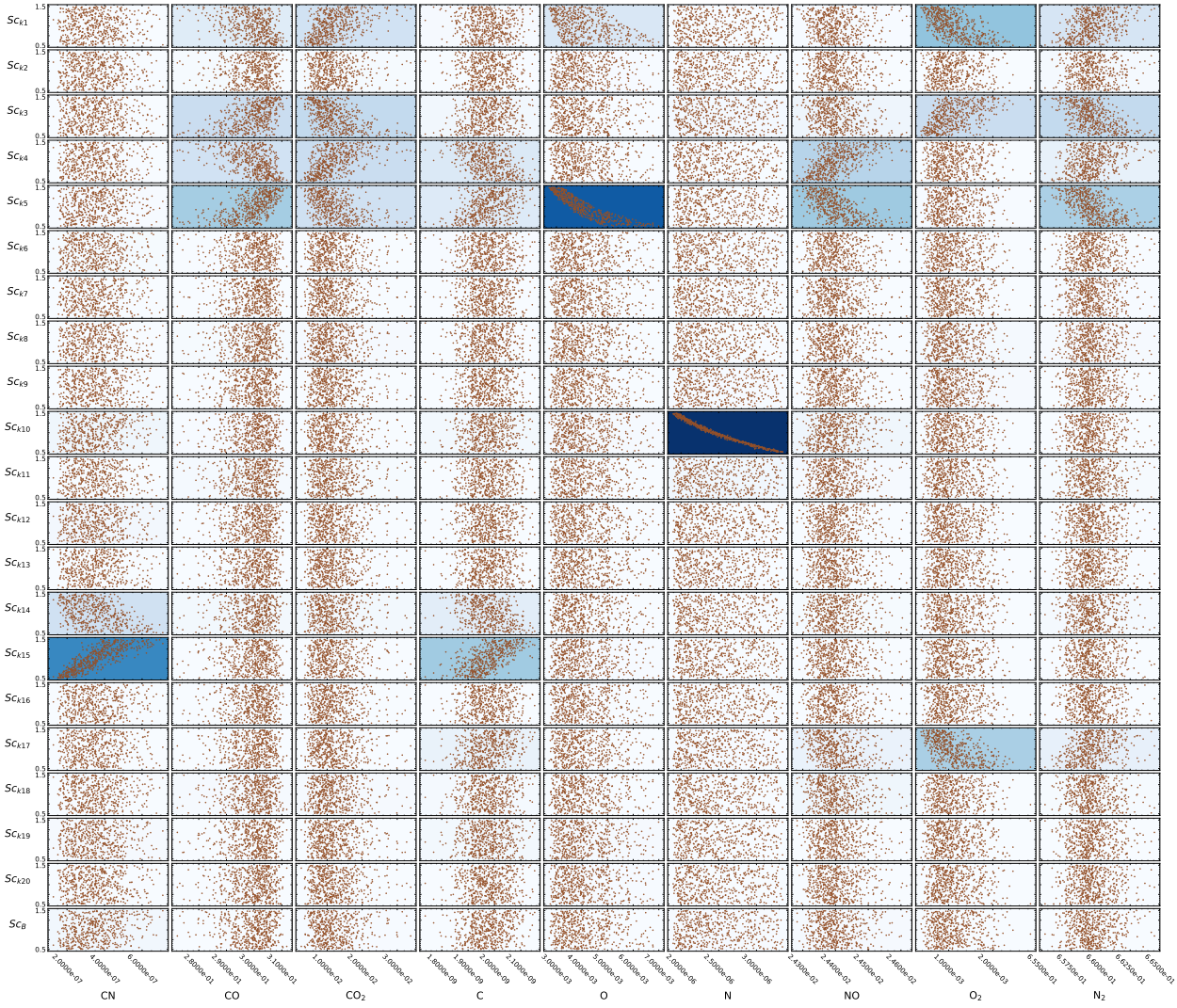

Figure 4.24: Case 2 scatter and Sobol' data for the ACA model at surface on a 65-degree measurement plane for 4 km/s freestream conditions. Sensitivity scaling parameters are described along the y-axis with corresponding lower and upper bounds used for sampling. Predicted mass fractions are shown along the x-axis. Sobol' index contours are mapped onto plots from Fig. 4.23a.

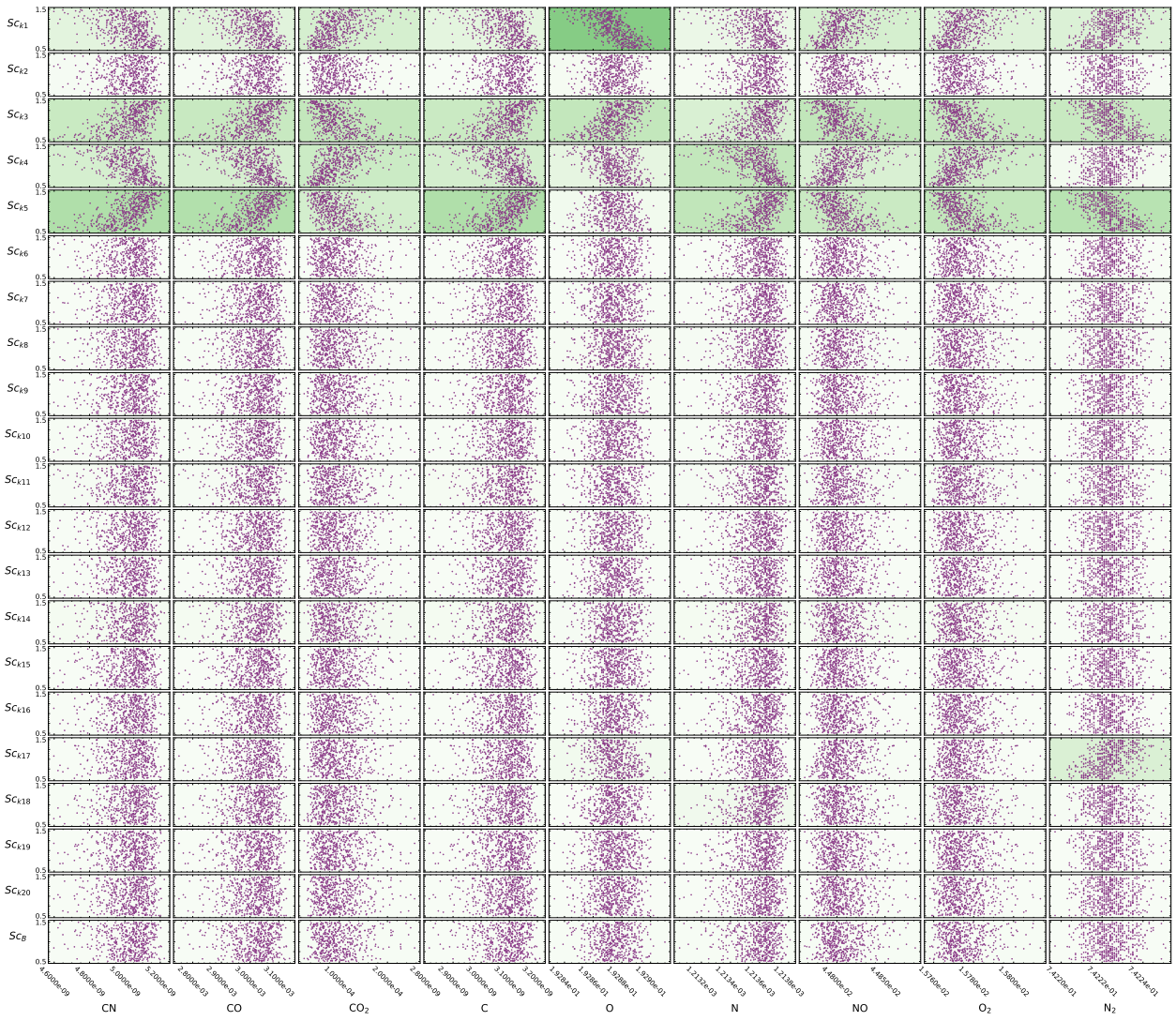

Figure 4.25: Case 2 scatter and Sobol' data for the ACA model at surface on a 65-degree measurement plane for 4 km/s freestream conditions. Sensitivity scaling parameters are described along the y-axis with corresponding lower and upper bounds used for sampling. Predicted mass fractions are shown along the x-axis. Sobol' index contours are mapped onto plots from Fig. 4.23b.

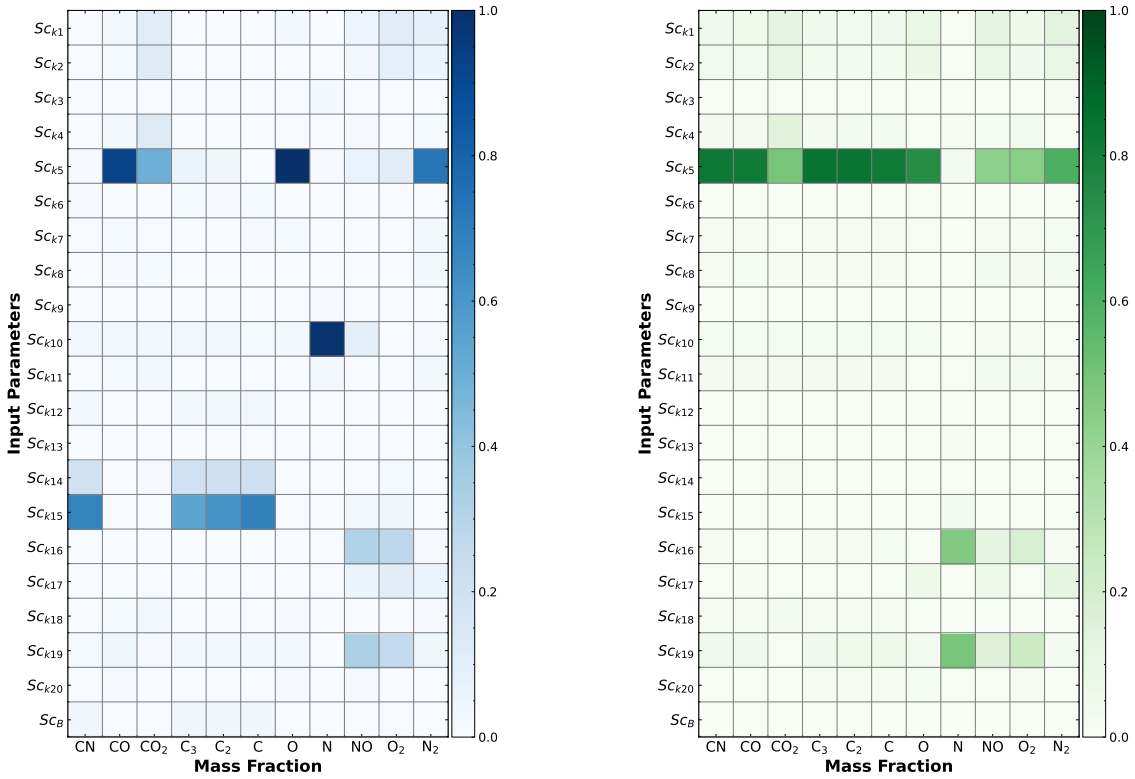

(a) 0.0 mm.

(b) 1.0 mm.

Figure 4.26: Case 3 Sobol' indices for the ACA model that show influence of rate coefficient pre-exponential factors on predicted species mass fractions at locations normal to the surface along a 65-degree measurement plane for 4 km/s freestream conditions. Surface temperature is set to 2146 K.

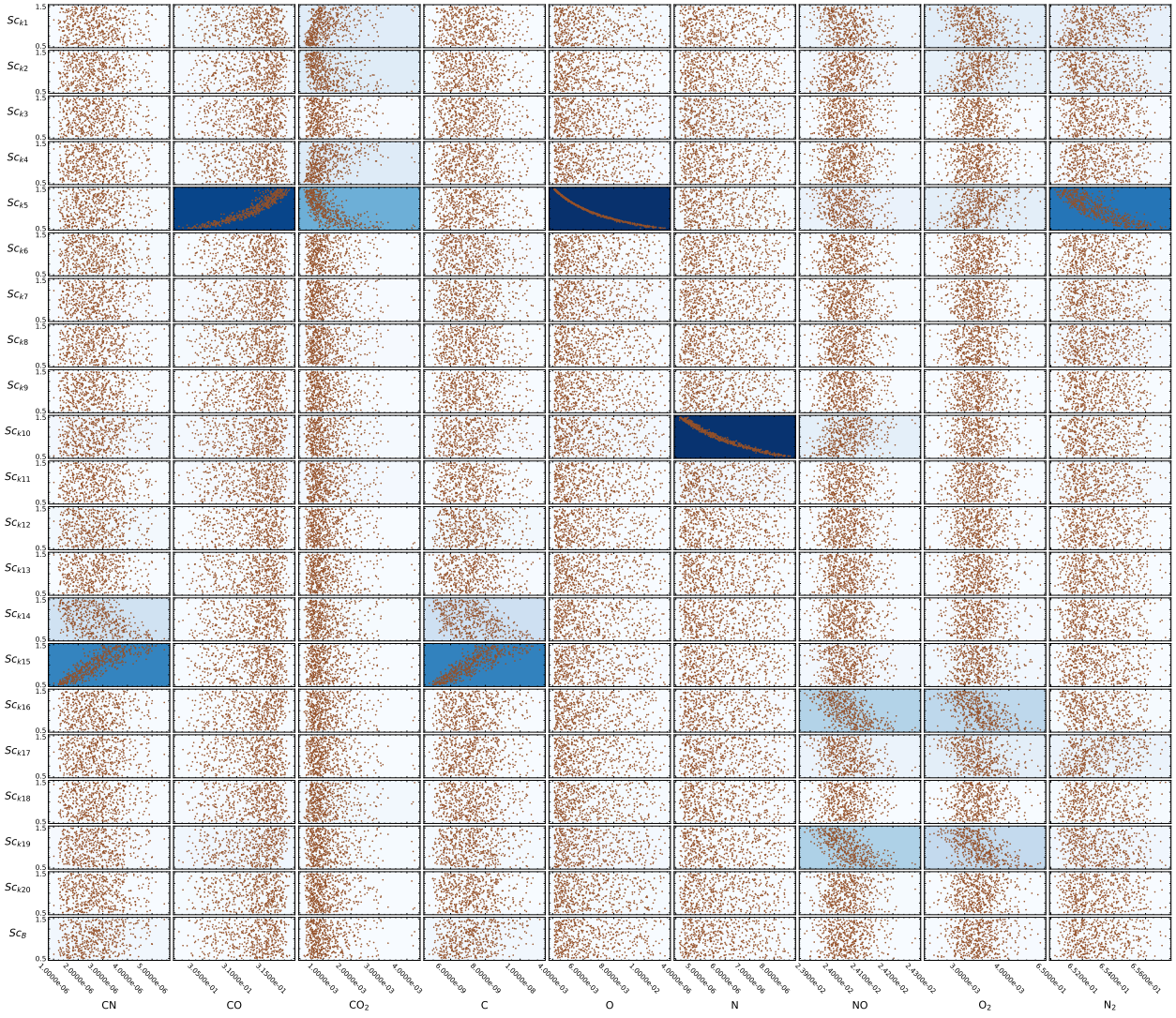

Figure 4.27: Case 3 scatter and Sobol' data for the ACA model at surface on a 65-degree measurement plane for 4 km/s freestream conditions. Sensitivity scaling parameters are described along the y-axis with corresponding lower and upper bounds used for sampling. Predicted mass fractions are shown along the x-axis. Sobol' index contours are mapped onto plots from Fig. 4.26a.

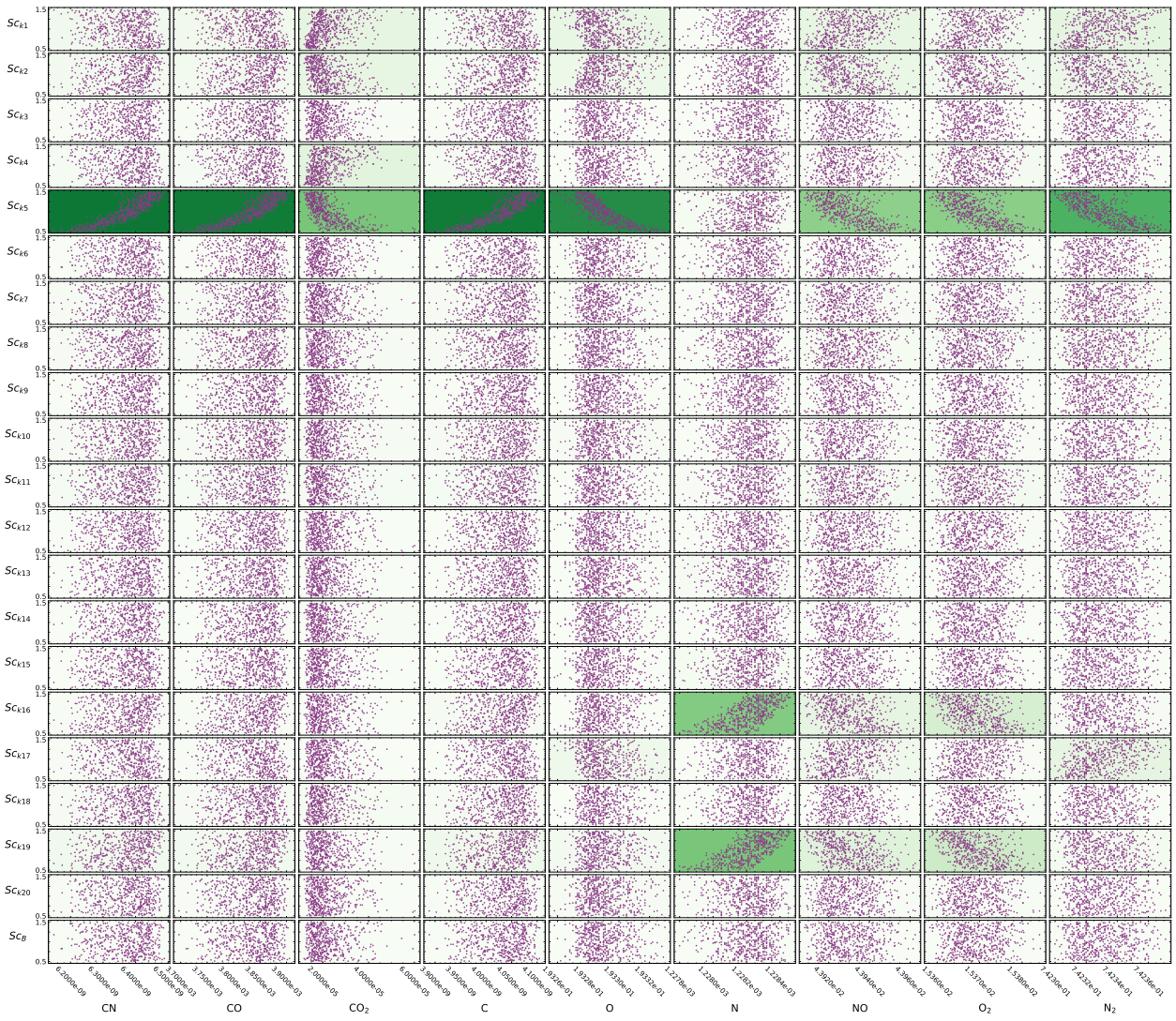

Figure 4.28: Case 3 scatter and Sobol' data for the ACA model at surface on a 65-degree measurement plane for 4 km/s freestream conditions. Sensitivity scaling parameters are described along the y-axis with corresponding lower and upper bounds used for sampling. Predicted mass fractions are shown along the x-axis. Sobol' index contours are mapped onto plots from Fig. 4.26b.

To assess predicted CO concentration with propagated model uncertainty, this study includes five pre-exponential factor coefficients from the sensitivity analysis. For the Park model validation assessment, the reaction efficiency coefficient for P1 is chosen, and the uncertainty range is defined from existing experimental data in the literature by Park [66]. The sticking and reaction efficiency coefficients for reactions A1, A3, A4, and A5 in the ACA model are also included as uncertainty inputs. Conservative uncertainty ranges are de-

rived from aligned gas-surface interaction studies in the literature [91, 95]; however, future work is needed to more precisely quantify the uncertainties of these reaction rate parameters. Coupling between sticking coefficients for A1 and A5 is maintained to agree with the model formulation. Uncertainty intervals are shown in Table 4.4 and log-uniform sampling distributions are chosen to accommodate the largest range.

Table 4.4: Prescribed uncertainties and ranges for Park and ACA models for HST cases.

Model	Parameter	Uncertainty Range
Park	γ_1	0.162 - 0.73
ACA	S_1	0 - 1.0
ACA	γ_3	$\pm$1 order magnitude
ACA	γ_4	$\pm$1 order magnitude
ACA	S_5	1.0 - S_1

4.3.3 Validation with Propagated Model Uncertainty

Park, ACA, and equilibrium (B') model predictions are compared in Figures 4.29 through 4.31 for CO number density along the 65-degree measurement plane and normal to the surface. Predicted profiles are plotted against LAS measurement data taken 1.0 $\pm$ 0.1 mm from the surface. The ACA model overpredicts the amount of CO the least, but the deterministic (nominal) results are 1.7-4.5 $\times$ greater than the mean measured value across the experimental measured domain for the suite of cases analyzed.

Reaction rate uncertainties are propagated and 5th, 25th, 50th (median), 75th, and 95th percentiles are computed for Park and ACA models and compared with the nominal equilibrium prediction and experimental data. Propagated model uncertainties provide an increase in spread of CO predictions near the wall with a decreased influence near the measurement location. Ensemble predictions are within an order of magnitude of the recorded measurement but are unable to capture the values in each case.

Ratios of model predictions to measured values are shown in Table 4.5 for the maximum upper and lower bounds along the measurement location span that correspond to compar-

isons seen in Figures 4.29d, 4.30d, and 4.31d. Overall, the model and measured quantities agree more at 1.0 and 1.1 mm than at 0.9 mm from the surface. Also, increasing surface temperature shows better general agreement between model comparisons and measured quantities.

To provide a more complete uncertainty assessment, activation energies should be included to fully characterize sources of model uncertainties. While this study leveraged conservative estimates of pre-exponential factor uncertainties for the ACA model, a better understanding of rate coefficient uncertainties is required for a better informed assessment.

Table 4.5: Prediction ratios between Park and ACA models and LAS measured CO number densities for surface temperature cases at 0.9 and 1.1 mm locations. Model and experiment upper and lower bounds are compared respectively.

		0.9 mm		1.1 mm	
Case Number	Model	Upper Bounds	Lower Bounds	Upper Bounds	Lower Bounds
Case 1	Park	4.6	4.5	3.1	3.0
	ACA	4.5	3.9	3.1	2.7
Case 2	Park	2.2	3.0	1.5	2.1
	ACA	2.2	2.9	1.5	2.0
Case 3	Park	2.1	2.5	1.5	1.7
	ACA	2.1	2.7	1.5	1.9

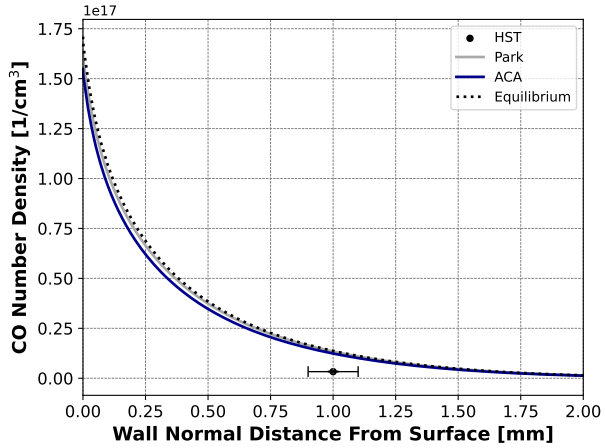

(a) Deterministic predictions.

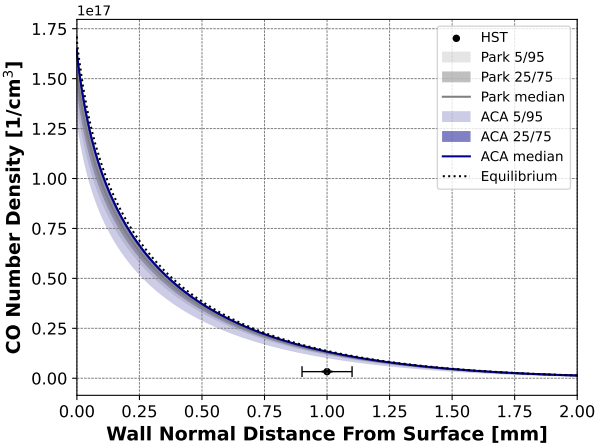

(b) Ensemble predictions.

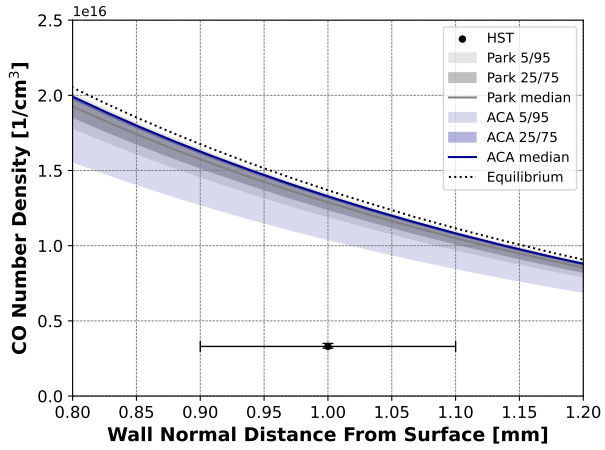

(c) Close up from Figure 4.29b.

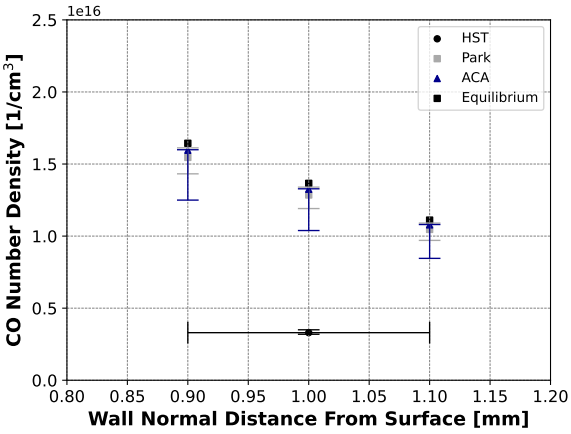

(d) Sampled comparisons.

Figure 4.29: Case 1 ensemble predictions of CO number density for Park and ACA models due to uncertainty in rate coefficient pre-exponential factors and compared to nominal equilibrium (B') solution. Data probed along profile normal to the surface along a 65-degree measurement plane for 4 km/s freestream conditions. Surface temperature is set to 1246 K. Experimental measurement from HST LAS system includes 95% confidence intervals and approximate $\pm$ 0.1 mm measurement location error.

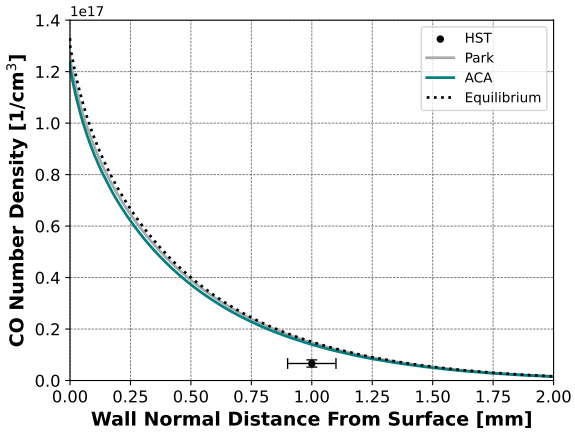

(a) Deterministic predictions.

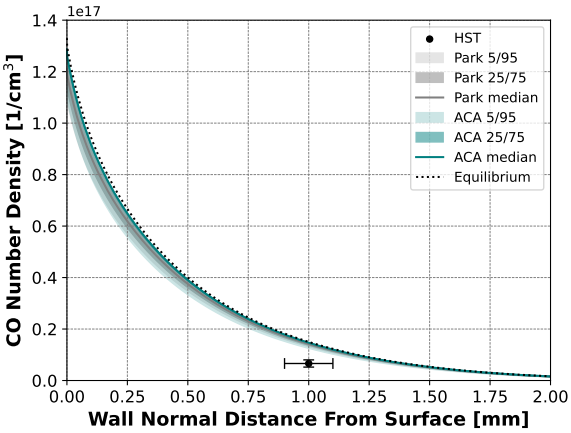

(b) Ensemble predictions.

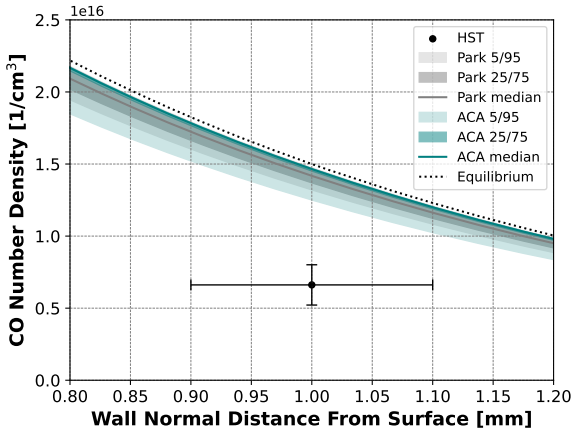

(c) Close up from Figure 4.30b.

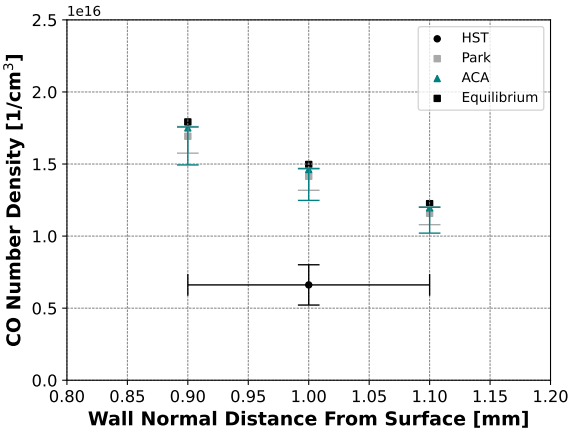

(d) Sampled comparisons.

Figure 4.30: Case 2 ensemble predictions of CO number density for Park and ACA models due to uncertainty in rate coefficient pre-exponential factors and compared to nominal equilibrium ($B^{'}$) solution. Data probed along profile normal to the surface along a 65-degree measurement plane for 4 km/s freestream conditions. Surface temperature is set to 1626 K. Experimental measurement from HST LAS system includes 95% confidence intervals and approximate $\pm$ 0.1 mm measurement location error.

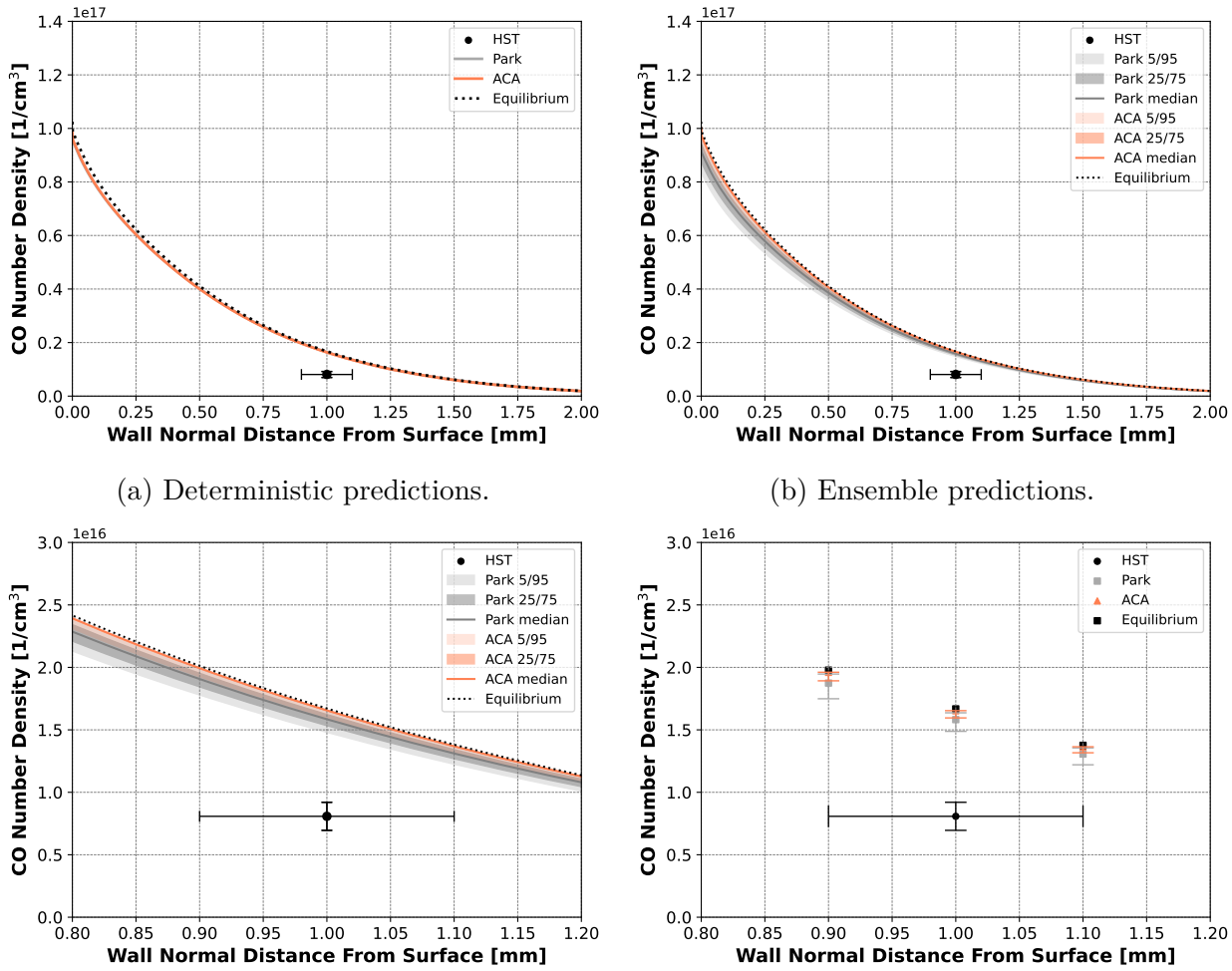

(a) Deterministic predictions.

(b) Ensemble predictions.

(c) Close up from Figure 4.31b.

(d) Sampled comparisons.

Figure 4.31: Case 3 ensemble predictions of CO number density for Park and ACA models due to uncertainty in rate coefficient pre-exponential factors and compared to nominal equilibrium (B') solution. Data probed along profile normal to the surface along a 65-degree measurement plane for 4 km/s freestream conditions. Surface temperature is set to 2146 K. Experimental measurement from HST LAS system includes 95% confidence intervals and approximate $\pm$ 0.1 mm measurement location error.

4.4 Conclusions

A framework for validation with quantified uncertainty has been demonstrated to assess Park and ACA model predictions under high enthalpy conditions in Sandia's HST facility. Park and ACA models were also compared with an equilibrium model and showed good

agreement, which may indicate that the surface ablation regime is diffusion-limited. The large concentration of atomic oxygen at the surface (approximately 8× that of O_2) and surface temperature are primary drivers of the sensitivity results, which identified reactions where atomic oxygen is a primary reactant to produce CO, CO_2, and adsorbed oxygen as most influential on the predicted CO number density at the measurement location. Lower enthalpy conditions with a larger concentration of molecular oxygen interacting with the surface are expected to activate corresponding portions of the model (e.g., reactions A16-20 of the ACA model). More gas-phase kinetics data is needed to understand the chemical pathways across all species in the coupled model.

Initial comparisons of deterministic and ensemble predictions are within an order of magnitude of the measured CO number density; however, all models overpredict this quantity including the equilibrium approach. Future work will begin to assess the impact of experimental uncertainty of surface temperature and inflow conditions on CO predictions in the boundary layer. Additionally, more research is needed to understand and quantify model uncertainties of the ACA model rate constant parameters and extended versions formed from molecular beam data and theory.

Chapter 5

Ablation Regime Characterization for a Shock Tunnel Environment

5.1 Introduction

Simulations are performed to characterize selected air/carbon finite-rate models under reaction- and diffusion-limited surface ablation regimes. A flight enthalpy condition in Sandia's hypersonic shock tunnel is simulated to compare species concentration model predictions and supplement predictions from higher enthalpy flow conditions discussed in Chapter 4. An approach to identify reaction- and diffusion-limited ablation regimes (oxygen-consumption Damköhler analysis) is introduced and demonstrated to compare ablation model predictions between HST cases. Finally, sensitivity analysis results for the flight enthalpy condition are presented to assess reaction parameter influence on species mass fraction quantities.

5.2 Modeling Approach

The presented flight enthalpy case is defined by a freestream velocity of 3 km/s. This case is compared to model predictions conducted for a higher enthalpy case with a freestream velocity of 4 km/s that was previously presented in Chapter 4. The nozzle and test sample geometry configuration in this chapter mirrors those in the previous assessment, where the test assembly is shown in Figure 4.1. Inflow conditions are extracted from a nonequilibrium

flow simulation of the HST nozzle and described in Table 5.1. These conditions represent a separate experimental test campaign; however, a low measurement signal-to-noise ratio prevented the acquisition of CO number density quantities to support a model validation assessment. Additional details about measured shock tunnel conditions and nozzle simulations for 3 km/s and 4 km/s freestream conditions are discussed by Jans et al. [96].

To match the boundary conditions applied in Chapter 4, a constant surface temperature, T_s, is prescribed along the test sample strip to match the experiment. Three runs are performed for temperature cases defined in Table 4.2. The boundary condition for the upper wedge surface that represents the clamp is set to an isothermal wall at 333 K. Additional modeling choices including assumptions and grid features are described in Section 4.2.2. Global sensitivity analysis parameter and sampling design choices are discussed in Section 4.2.4.

Table 5.1: Computed 3 km/s freestream conditions for the HST test chamber.

Inflow Parameter	Quantity
U_∞	2967 m/s
T	278 K
T_v	719 K
ρ_∞	4.05×10^{-3} kg/m^3
y_{N_2}	0.738
y_{O_2}	0.198
y_{NO}	0.061
y_O	0.003

5.3 Identification of Reaction-Limited and Diffusion-Limited Ablation Regimes

A Damköhler analysis approach is demonstrated to identify the surface ablation regime and recommended model for a given flight or experimental flow condition. We define the Damköhler number at the surface, Da_s, as the ratio between gas-surface chemistry reaction

rate and the mass transfer rate.

$$Da_s = \frac{\text{Reaction Rate}}{\text{Mass Transfer Rate}} \tag{5.1}$$

The surface is in a diffusion-limited regime if the boundary layer mass transport rate is much smaller than the rate of gas-surface chemical kinetics. If the boundary layer mass transport rate is much larger than the rate of gas-surface chemical kinetics, ablation is limited by the kinetic barrier and the surface is in a reaction-limited regime [4, 9]. The reaction rate leverages an oxidation Damköhler analysis approach recently developed at Sandia National Laboratories [9, 97] with modifications to compute mass flux per unit area (kg/m^2-s). The Damköhler number is then defined as a ratio between the concentration-normalized oxygen-consumption reaction and boundary layer mass transfer rates as

$$Da_s = \left(\frac{y_{O,w}}{y_{O,w} + y_{O_2,w}}\right) \frac{k_O y_{O,w} \rho_w}{\rho_e u_e C_H} + \left(\frac{y_{O_2,w}}{y_{O,w} + y_{O_2,w}}\right) \frac{k_{O_2} y_{O_2,w} \rho_w}{\rho_e u_e C_H}. \tag{5.2}$$

Atomic and molecular oxygen-consumption reaction rates approximate the total oxygen consumption at the wall. For the current demonstration, k_O and k_{O_2} are defined from Park's mechanisms for oxidation of graphites and are shown in Table 5.2. Rate coefficients may be leveraged from dominant oxidation mechanisms of other air/carbon ablation models (e.g., ACA, ZA). Rate coefficients are multiplied by a mass concentration, $y_{O,w}\rho_w$ and $y_{O_2,w}\rho_w$, for atomic and molecular oxygen at the wall. The mass transfer rate, $\rho_e u_e C_H$, is defined by transfer coefficient methodology approximations that extend to boundary layer governing equations and thin film theory that relates fluid heat and mass transfer. Details about the formulation are discussed in Chapter 2.

Table 5.2: Selected surface oxidation rates for graphite [5].

Reaction	Rate Coefficient (m/s)	Reaction Rate (kg/m^2-s)
O + C(b) $\rightarrow$ CO	$k_O = \frac{1}{4}\sqrt{\frac{8k_BT}{\pi m_O}}0.63\exp\left(\frac{-1160.0}{T_s}\right)$	$k_O y_O \rho_w$
O_2 + C(b) $\rightarrow$ CO + O	$k_{O_2} = \frac{1}{4}\sqrt{\frac{8k_BT}{\pi m_{O_2}}}\frac{1.43\times10^{-3}+0.01\exp(\frac{-1450.0}{T_s})}{1+2\times10^{-4}\exp(\frac{13000.0}{T_s})}$	$k_{O_2} y_{O_2} \rho_w$

A Damköhler analysis is performed by extracting wall and boundary layer edge conditions along the longitudinal axis of the test sample geometry for each HST freestream case and surface temperature case. The analysis location is shown in Figure 5.1 for a sample test case. All cases are run with an isothermal wall. Damköhler quantities much greater than one are expected to indicate the surface is in a diffusion-limited ablation regime, where quantities much less than one are expected to show that the surface is in a reaction-limited regime.

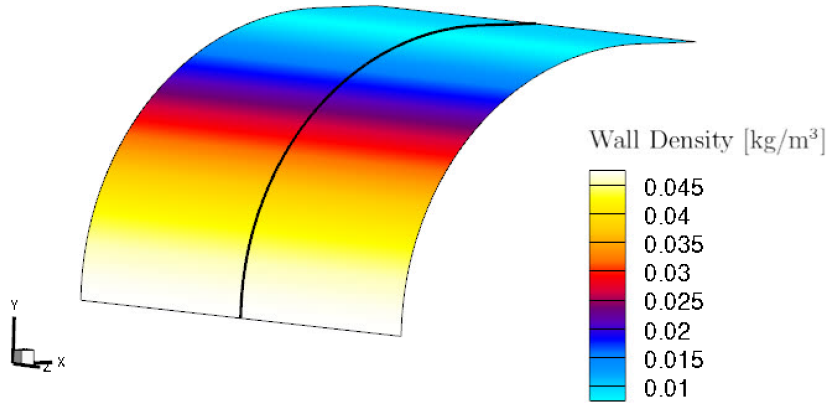

Figure 5.1: Wall density predictions along the test sample surface. The location of extracted input quantities for the Damköhler analysis along the wall is indicated by a black line. The surface temperature boundary condition is set to an isothermal wall at 2146 K. HST freestream conditions are shown in Table 5.1.

5.4 Results and Discussion

5.4.1 Deterministic Model Comparisons

Nominal ACA, Park, and equilibrium model predictions are compared in Figure 5.2. Carbon monoxide concentrations for HST 3 and 4 km/s freestream conditions are shown in Figures 5.2a-5.2b and 5.2c-5.2d respectively. The 4 km/s freestream condition results include experimental data (HST) with a 95% confidence interval on the measured quantity and $\pm$ 0.1 mm error on the measurement location, where a comprehensive validation assessment is presented in Chapter 4. Model predictions are extracted normal to the surface and along a 65-degree measurement plane from the stagnation streamline for each condition.

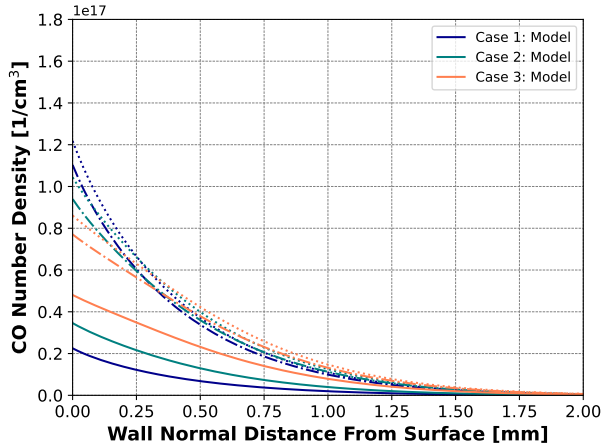

(a) 3 km/s freestream conditions.

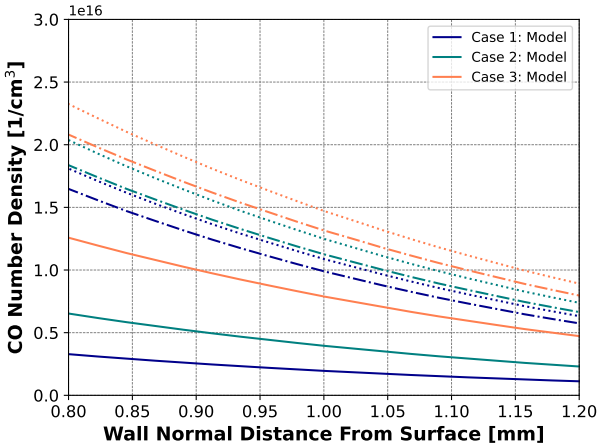

(b) Close up from Figure 5.2a.

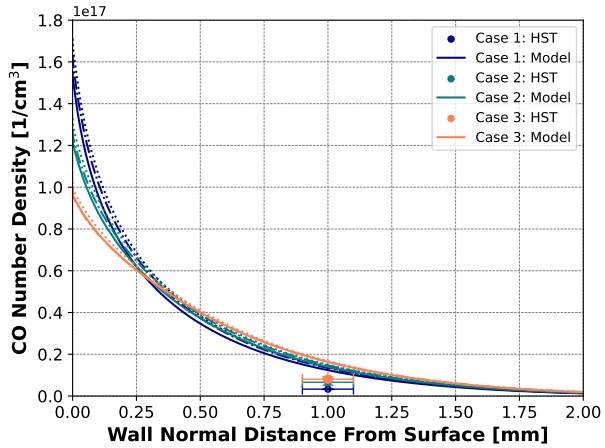

(c) 4 km/s freestream conditions.

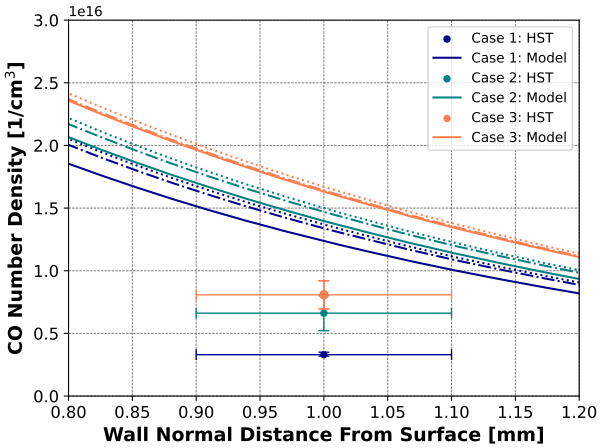

(d) Close up from Figure 5.2c.

Figure 5.2: Carbon monoxide number density comparisons between Park (dash-dot), ACA (solid), and equilibrium (dotted) models and experiment (HST) along a 65-degree measurement plane from the stagnation streamline. Surface temperatures for Cases 1-3 are shown in Table 4.2. HST freestream conditions are in Table 4.1 and Table 5.1 for the 4 km/s and 3 km/s conditions respectively.

At the 3 km/s freestream conditions presented in Figure 5.2a, finite-rate and equilibrium CO predictions diverge at the wall and begin to converge toward the limit of the CO layer away from the wall. Equilibrium model predictions are the most conservative and are followed by Park and then ACA predictions. Additionally, decreasing surface temperature increases the spread in predicted CO concentration between ACA and equilibrium models. At the 4 km/s freestream conditions shown in Figure 5.2c, finite-rate and equilibrium CO

predictions agree more closely. However, prediction trends mirror the lower enthalpy case. The ACA model predictions are the least conservative and are followed by Park and then equilibrium models with increasing CO predictions. Surface temperature also impacts the spread in predicted CO between the ACA and equilibrium models, which increases as surface temperature decreases.

Damköhler numbers for the HST cases presented in this study are shown in Figure 5.3. Computed values mildly decrease along the surface in the streamwise direction. However, the Damköhler number begins to increase approximately 18.0 mm axially from the stagnation point, which corresponds to the beginning of a flow recirculation region before the copper clamp and a sudden decrease in the computed mass transfer coefficient. A reverse trend is shown near the stagnation point, with a small decrease in the Damköhler number and a sudden increase in the mass transfer coefficient. The computed mass transfer coefficient along the wall is shown in Figure 5.4.

The computed Damköhler numbers for each freestream condition and corresponding surface temperature case corresponds to the observed model predictions shown in Figure 5.2. If $Da_s = 1$ indicates a transition point between diffusion- and reaction-limited regimes, the 4 km/s condition produces a surface ablation regime that is transitioning toward diffusion-limited. Equilibrium and finite-rate models should predict equal ablation rates in a diffusion-limited regime, which are insensitive to individual reaction rate coefficient values. The computed CO concentrations in Figure 5.2c indicate a transition toward diffusion-limited model behavior at and near the wall. Additionally, the 3 km/s condition produces a reaction-limited ablation regime. In this case, there are enough diffused reactant species (e.g., oxygen) at the surface and ablation rates are limited by the kinetic barrier. A finite-rate modeling approach is required and expected to produce a less conservative prediction, which is seen in Figure 5.2a. As surface temperature is decreased for each set of results, the Damköhler number also decreases toward a more reaction-limited regime.

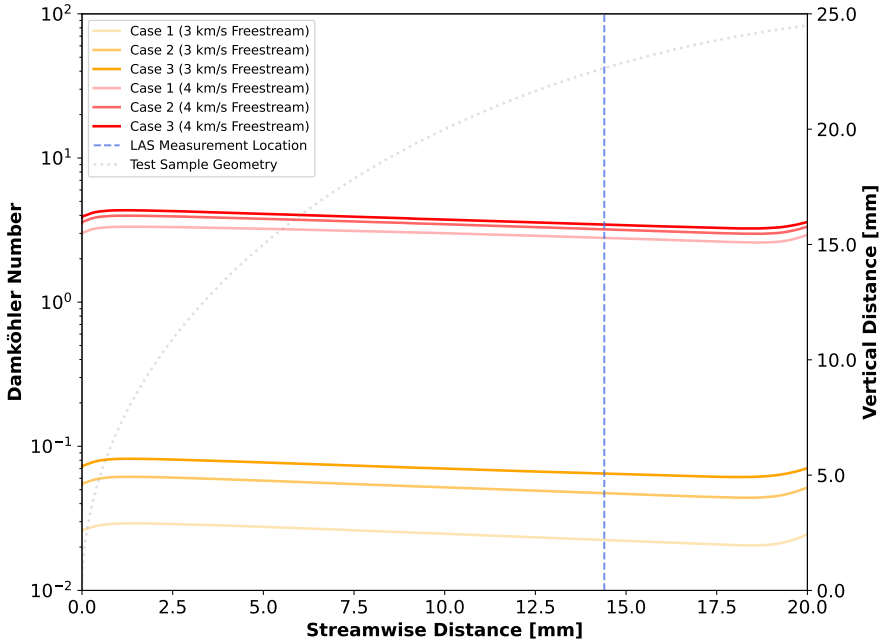

Figure 5.3: Comparisons of Damköhler number along the wall. Surface temperatures for Cases 1-3 are shown in Table 4.2. HST freestream conditions are in Table 4.1 and Table 5.1 for the 4 km/s and 3 km/s cases respectively. The geometric profile of the test sample is also shown for reference.

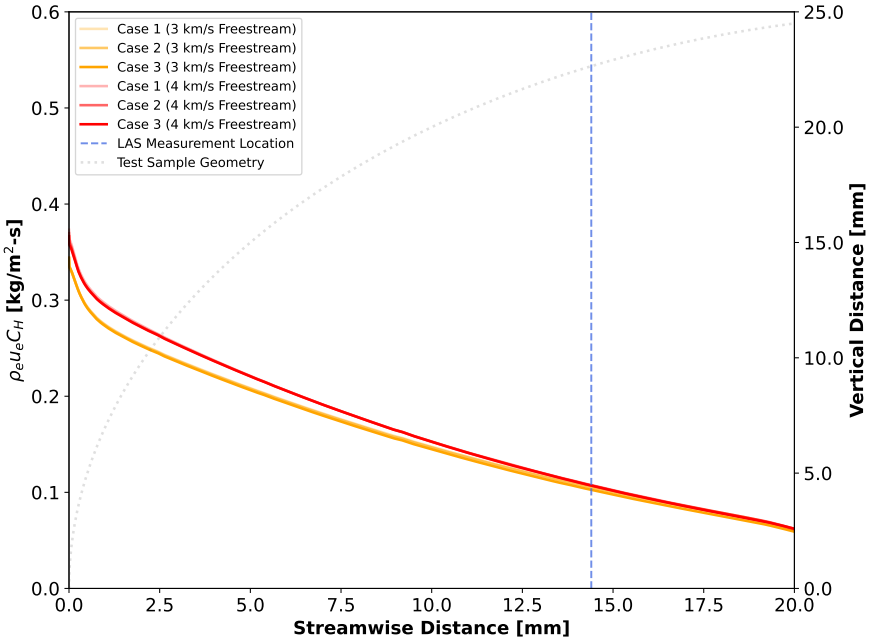

Figure 5.4: Comparisons of mass transfer coefficient along the wall. Surface temperatures for Cases 1-3 are shown in Table 4.2. HST freestream conditions are in Table 4.1 and Table 5.1 for the 4 km/s and 3 km/s cases respectively. The geometric profile of the test sample is also shown for reference.

Number density profiles for air and carbon ablation product species are shown in Figures 5.5-5.7 and are plotted on a logarithmic scale. Molecular oxygen is present in larger quantities than atomic oxygen across all surface temperature cases. In the previous assessment conducted for freestream conditions of 4 km/s, atomic oxygen is observed as the dominant oxidation species in Figures 4.8 through 4.10. Additionally, atomic nitrogen quantities are smaller than in the previous assessment by approximately 10^{-2}-10^{-3} at the surface. Gas temperature profiles are shown in Figure 5.8, which converge at approximately 1.0 mm from the surface. While the converged gas temperatures for the 4 km/s freestream condition (Figure 4.7) approach 4000 K moving from the wall in the boundary layer, gas temperatures for the 3 km/s condition increase to approximately 3000 K.

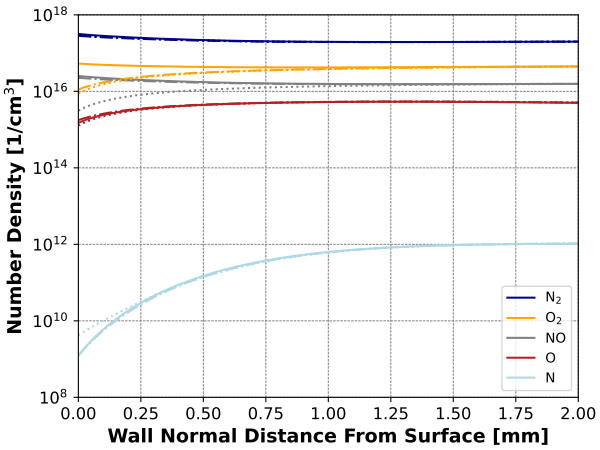

(a) Air species.

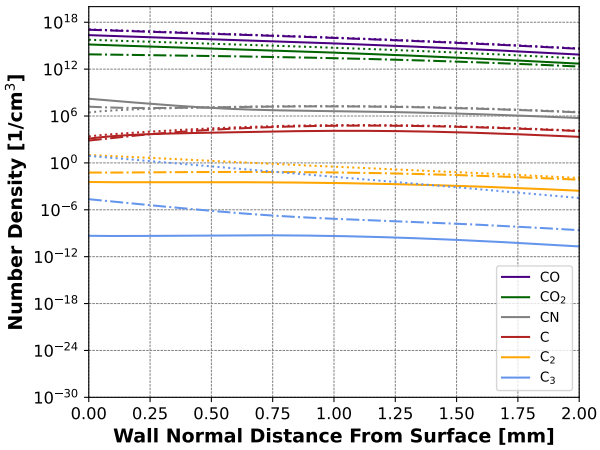

(b) Carbonaceous species.

Figure 5.5: Number density profile comparisons between Park (dash-dot), ACA (solid), and equilibrium (dotted) models along a 65-degree measurement plane for 3 km/s freestream conditions. Case 1 surface temperature is set to 1246 K.

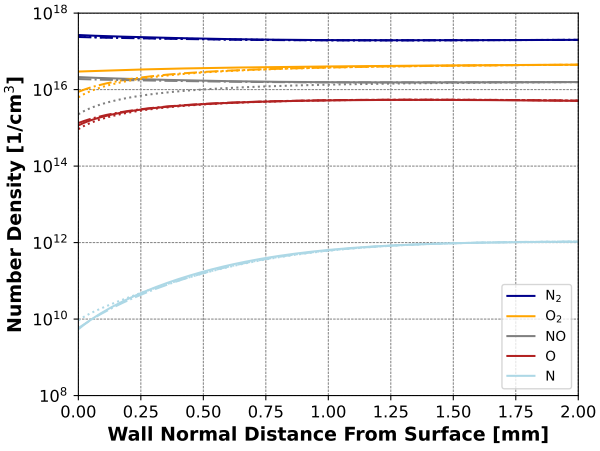

(a) Air species.

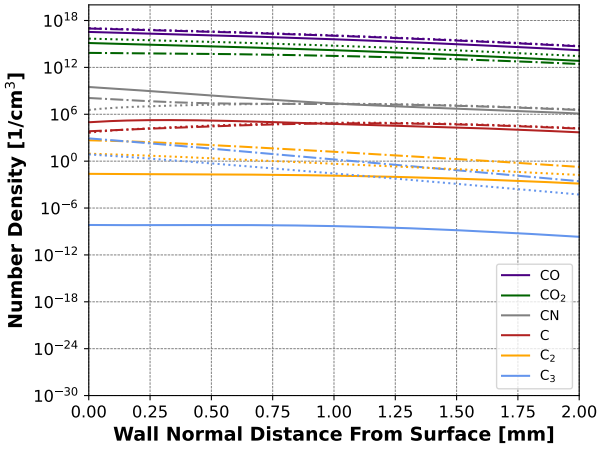

(b) Carbonaceous species.

Figure 5.6: Number density profile comparisons between Park (dash-dot), ACA (solid), and equilibrium (dotted) models along a 65-degree measurement plane for 3 km/s freestream conditions. Case 2 surface temperature is set to 1626 K.

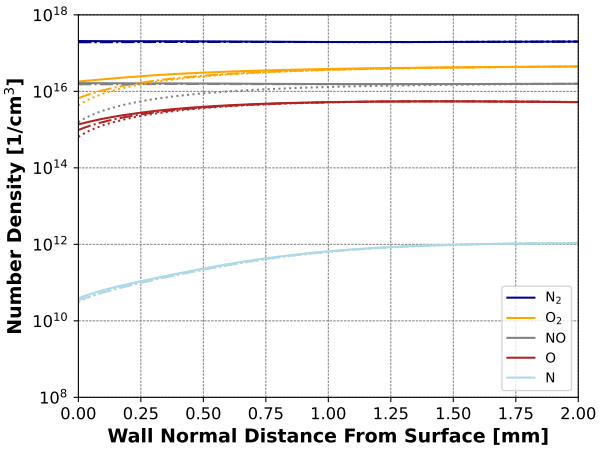

(a) Air species.

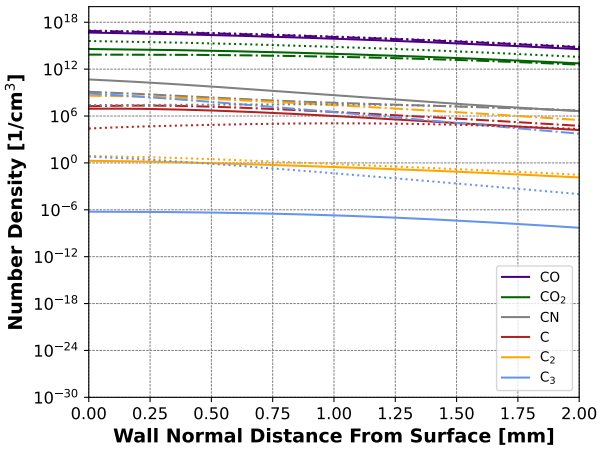

(b) Carbonaceous species.

Figure 5.7: Number density profile comparisons between Park (dash-dot), ACA (solid), and equilibrium (dotted) models along a 65-degree measurement plane for 3 km/s freestream conditions. Case 3 surface temperature is set to 2146 K.

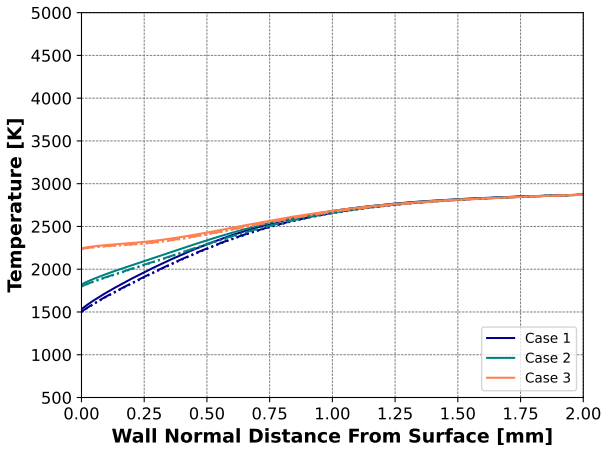

(a) Translational-rotational temperature.

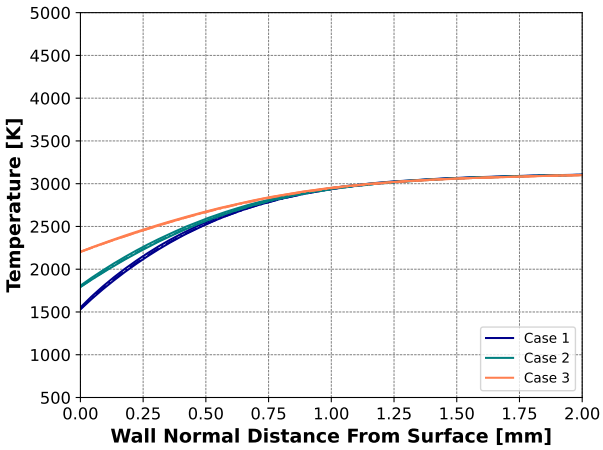

(b) Vibrational-electronic temperature.

Figure 5.8: Gas temperature comparisons between Park (dash-dot), ACA (solid), and equilibrium (dotted) models along a 65-degree measurement plane for 3 km/s freestream conditions.

5.4.2 Global Sensitivity Analysis

Sobol' indices for Park and ACA model mass fraction predictions are shown in Figures 5.9-5.26. To mirror the analysis performed in Chapter 4, ensembles of 256 and 512 simulations were performed for each model respectively and incremental LHS simulation responses were

monitored for Sobol' index convergence. Sobol' quantities and companion scatter data are plotted directly following the heat maps for each surface temperature case. A limit is also imposed on the raw scatter data to remove species with mass fraction quantities below 10^{-12}.

At the probed locations shown in Figures 5.9-5.17, the reaction efficiency, γ_2, for the Park O_2 oxidation reaction (P2) rate coefficient is strongly influential for the predicted mass fraction of CO across all surface temperature cases. The P2 reaction rate efficiency coefficient is also influential on predicted CO_2 at the surface, where the sensitivity increases as surface temperature increases. It remains strongly influential on predicted CO_2 at 1.0 mm from the surface for all temperature cases. While the quantities of CO and CO_2 increase with increasing reaction efficiency coefficient, γ_2, the magnitude of CO is 10^2-10^3 times greater than CO_2 when probed at 1.0 mm away from the wall and at the surface respectively. An increase in the O-atom oxidation reaction (P1) efficiency coefficient, γ_1, is also correlated to a decrease in CO_2 with moderate and low sensitivity for surface temperature Case 1 and 2 respectively.

A strong correlation is also observed between oxidation reactions (P1 and P2) with atomic and molecular oxygen consumption at the surface. As γ_1 and γ_2 increase, O and O_2 decrease. At the probed location 1.0 mm from the surface, an increase in γ_2 is highly influential on increased O and decreased O_2 quantities. As previously discussed, there is no CO_2 production reaction in the Park gas-surface chemistry model. The interaction between O, O_2, CO, and CO_2 consumption and production in Park's gas-phase kinetics model (Reactions 1 and 17 in Table 2.1) help to illustrate these observed trends.

Additionally, an increase in the nitridation reaction (P3) efficiency coefficient, γ_3, is strongly influential on an increase in trace mass fraction quantities of CN at the surface that are on the order of 10^{-11}-10^{-9} with increasing surface temperature. The reaction efficiency coefficients for C_3 sublimation and condensation reactions (P4 and P5), γ_4 and γ_5, have a low to moderate influence on C, C_2, and C_3 products at the highest surface temperature case (Case 3) at the wall. As γ_4 increases, the mass fractions of C, C_2, and C_3 increase on the

order of 10^{-9} for molecular carbon and 10^{-11} for atomic carbon. With increasing γ_5, there is a low decreasing trend in C, C_2, and C_3 quantities.

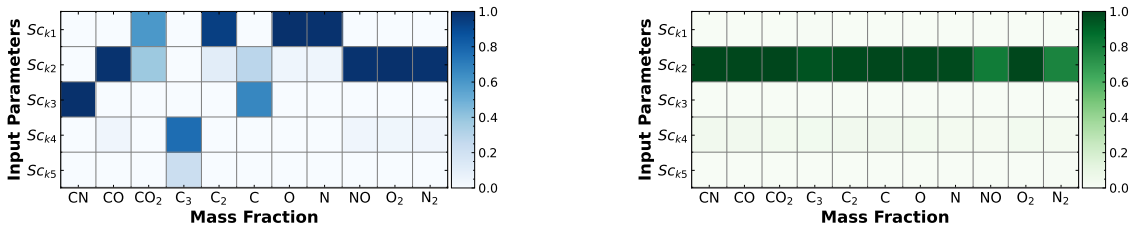

(a) 0.0 mm.

(b) 1.0 mm.

Figure 5.9: Case 1 Sobol' indices for the Park model that show influence of rate coefficient pre-exponential factors on predicted species mass fractions at locations normal to the surface along a 65-degree measurement plane for 3 km/s freestream conditions. Surface temperature is set to 1246 K.

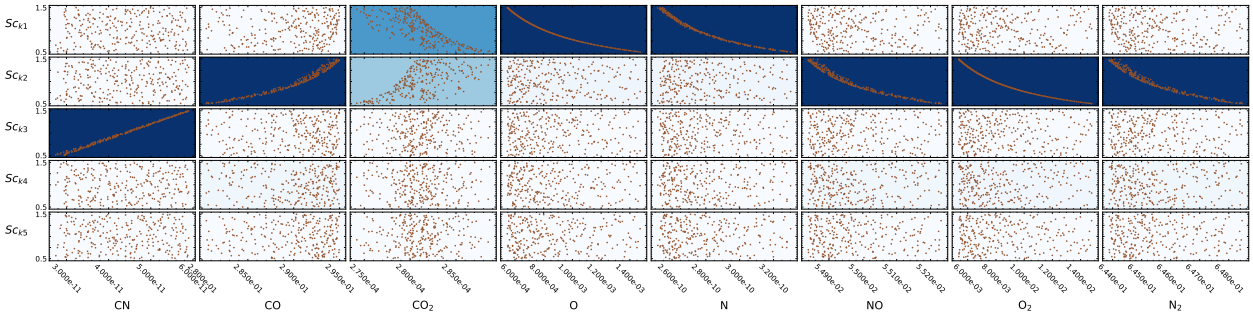

Figure 5.10: Case 1 scatter and Sobol' data for the Park model at surface on a 65-degree measurement plane for 3 km/s freestream conditions. Sensitivity scaling parameters are described along the y-axis with corresponding lower and upper bounds used for sampling. Predicted mass fractions are shown along the x-axis. Sobol' index contours are mapped onto plots from Fig. 5.9a.

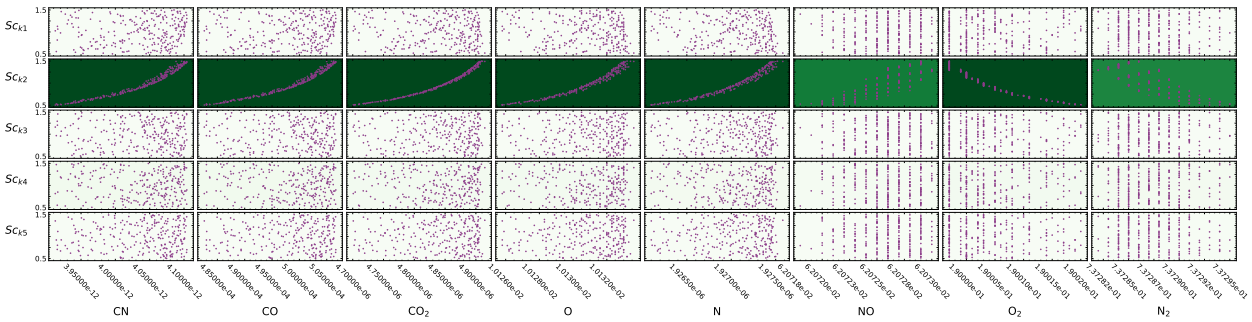

Figure 5.11: Case 1 scatter and Sobol' data for the Park model at surface on a 65-degree measurement plane for 3 km/s freestream conditions. Sensitivity scaling parameters are described along the y-axis with corresponding lower and upper bounds used for sampling. Predicted mass fractions are shown along the x-axis. Sobol' index contours are mapped onto plots from Fig. 5.9b.

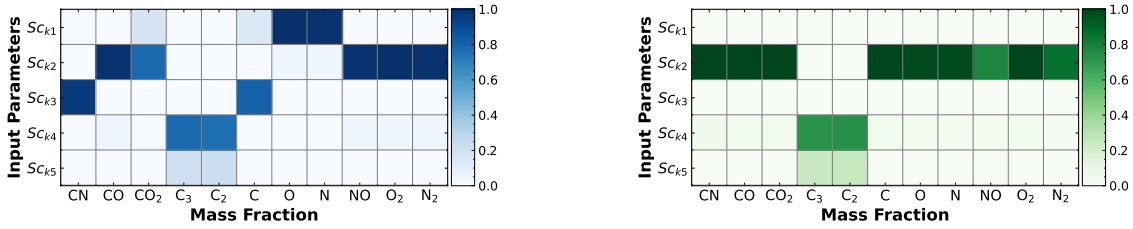

(a) 0.0 mm.

(b) 1.0 mm.

Figure 5.12: Case 2 Sobol' indices for the Park model that show influence of rate coefficient pre-exponential factors on predicted species mass fractions at locations normal to the surface along a 65-degree measurement plane for 3 km/s freestream conditions. Surface temperature is set to 1626 K.

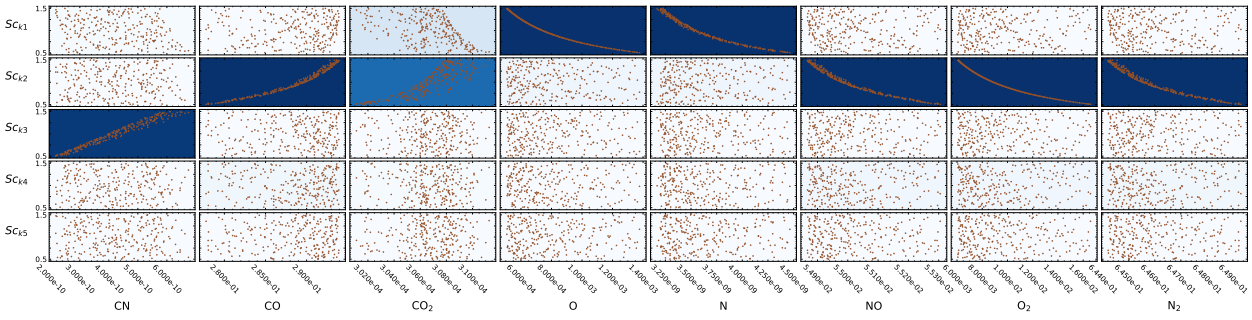

Figure 5.13: Case 2 scatter and Sobol' data for the Park model at surface on a 65-degree measurement plane for 3 km/s freestream conditions. Sensitivity scaling parameters are described along the y-axis with corresponding lower and upper bounds used for sampling. Predicted mass fractions are shown along the x-axis. Sobol' index contours are mapped onto plots from Fig. 5.12a.

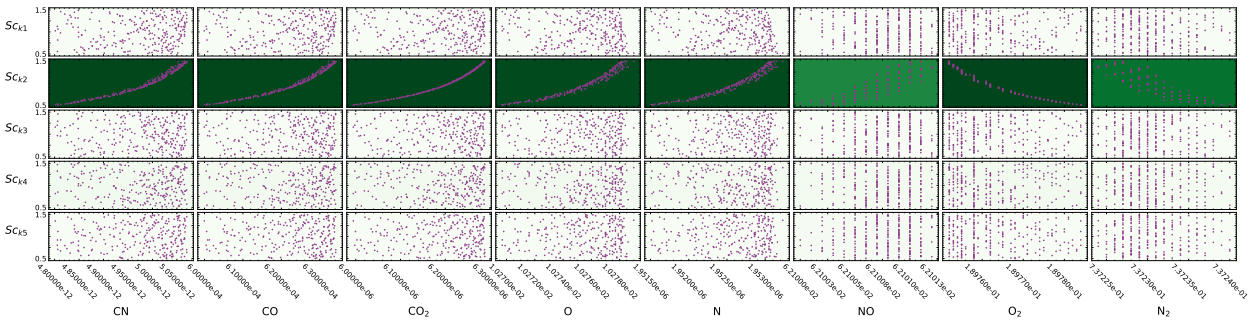

Figure 5.14: Case 2 scatter and Sobol' data for the Park model at surface on a 65-degree measurement plane for 3 km/s freestream conditions. Sensitivity scaling parameters are described along the y-axis with corresponding lower and upper bounds used for sampling. Predicted mass fractions are shown along the x-axis. Sobol' index contours are mapped onto plots from Fig. 5.12b.

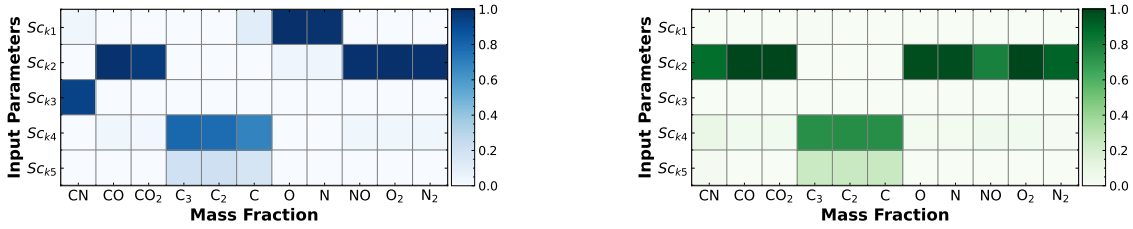

(a) 0.0 mm.

(b) 1.0 mm.

Figure 5.15: Case 3 Sobol' indices for the Park model that show influence of rate coefficient pre-exponential factors on predicted species mass fractions at locations normal to the surface along a 65-degree measurement plane for 3 km/s freestream conditions. Surface temperature is set to 2146 K.

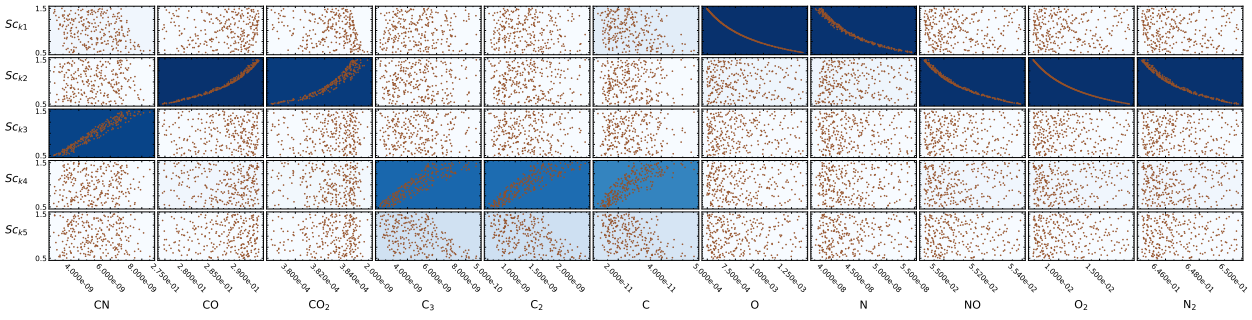

Figure 5.16: Case 3 scatter and Sobol' data for the Park model at surface on a 65-degree measurement plane for 3 km/s freestream conditions. Sensitivity scaling parameters are described along the y-axis with corresponding lower and upper bounds used for sampling. Predicted mass fractions are shown along the x-axis. Sobol' index contours are mapped onto plots from Fig. 5.15a.

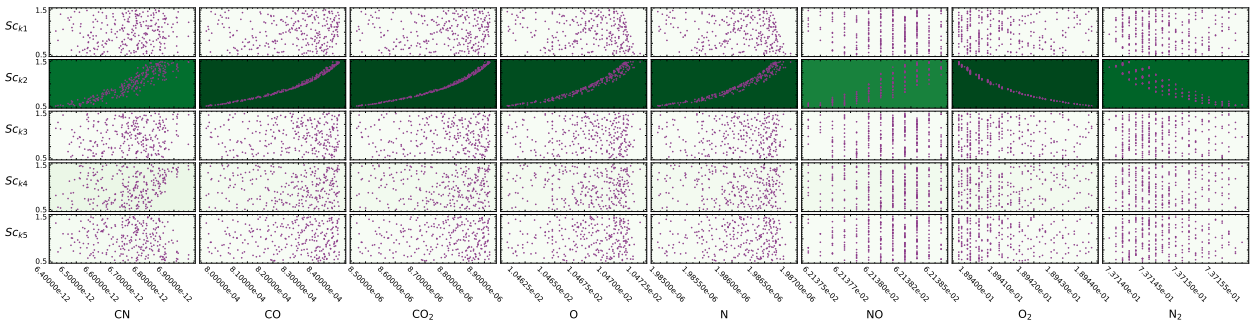

Figure 5.17: Case 3 scatter and Sobol' data for the Park model at surface on a 65-degree measurement plane for 3 km/s freestream conditions. Sensitivity scaling parameters are described along the y-axis with corresponding lower and upper bounds used for sampling. Predicted mass fractions are shown along the x-axis. Sobol' index contours are mapped onto plots from Fig. 5.15b.

The dominance of O_2 reactions for CO predictions is also present in the ACA model, where Sobol' indices and raw scatter data are shown in Figures 5.18-5.26. Sticking coefficients for O_2 adsorption reactions A16 and A19 to form O(s) and O*(s), S_{16} and S_{19}, have moderate to high influence on predicted CO at both probed locations. As these sticking coefficients increase, the predicted quantities of CO also increase. The influence of S_{19} on predicted CO production increases with higher surface temperature with peak sensitivity for Case 2. Strongly (double) bonded oxygen, O*(s), is more strongly bonded than O(s) and has longer residence time at high temperatures. Eley-Rideal reactions A7 or A20 are what likely form CO and are rate-limited by formation of O*(s) from reaction A19. As discussed in Chapter 4, strongly-bonded oxygen was included in the ACA model to enable CO production at high temperatures above 1300 K [31]. If the CO reaction mechanism is solely dependent on adsorbed species and the rate is limited due to high surface coverage, the reaction probability of CO formation will decrease at high surface pressure. Peak CO production will shift to higher surface temperature with increasing pressure, where a fall in production will occur above the temperature threshold [4]. Reaction efficiency coefficients for Eley-Rideal reactions A17 and A18, γ_{17} and γ_{18}, are moderately influential on predicted CO_2 at both probed locations. As the reaction efficiency coefficient increases for reaction A17 to form CO and O_2, predicted CO_2 decreases. Additionally, as the reaction efficiency coefficient for reaction

A18 to form CO_2 and O increases, predicted CO_2 increases.

Sticking coefficients S_{16} and S_{19} are moderately to highly influential on O_2 consumption for both probed locations across the surface temperature cases. At the highest surface temperature (Case 3), S_{19} has a higher sensitivity than S_{16}; whereas, the reverse relationship is true at the lowest surface temperature (Case 1). Atomic oxygen trends are described through two pathways at the probed locations. At the surface, the sticking coefficient for reaction A5 to form O*(s) is highly influential on predicted O quantities. However, S_{16} and S_{19} are the most influential on predicted O at 1.0 mm from the surface.

At the surface, sticking and reaction efficiency coefficients for reactions A10 and A15 are moderately influential on predicted trace quantities of CN. The sticking coefficient for reaction A10 to form N(s) from atomic nitrogen, S_{10}, has a positive correlation with increasing CN. Additionally, as the reaction efficiency coefficient for reaction A15 to form CN from N(s) and bulk carbon, γ_{15} is increased, predicted CN quantities also increase. Nitridation reactions are confined within reactions A10-A15. However, N(s), O(s), O*(s), and (s) compete for a conserved quantity of surface sites. An example of this competition may be seen in Figure 5.25, where there is a reverse relationship between sticking coefficients for reactions A5 to produce O*(s) from atomic oxygen and A10 in relation to predicted CN. If more O*(s) is produced via A5, then the quantity of N(s) decreases and reduces the amount of CN produced. At 1.0 mm from the surface, the sticking coefficient, S_{10}, is highly influential on trace CN predictions. Interactions between C, N, N_2, CO, and CN in the gas-phase kinetics model may greatly impact these CN prediction quantities, where a number of potential pathways exist to increase quantities of CN. No sensitivity was observed for the active site density parameter, B, on predicted gas species quantities in the present analysis.

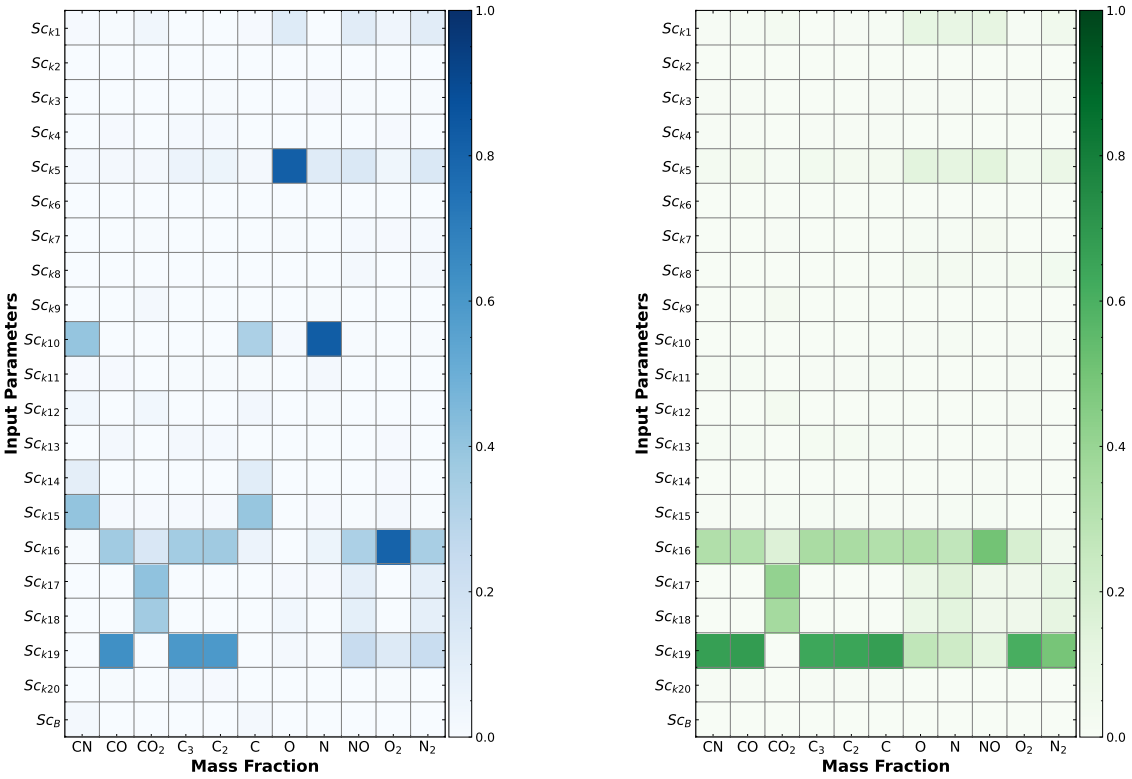

(a) 0.0 mm.

(b) 1.0 mm.

Figure 5.18: Case 1 Sobol' indices for the ACA model that show influence of rate coefficient pre-exponential factors on predicted species mass fractions at locations normal to the surface along a 65-degree measurement plane for 3 km/s freestream conditions. Surface temperature is set to 1246 K.

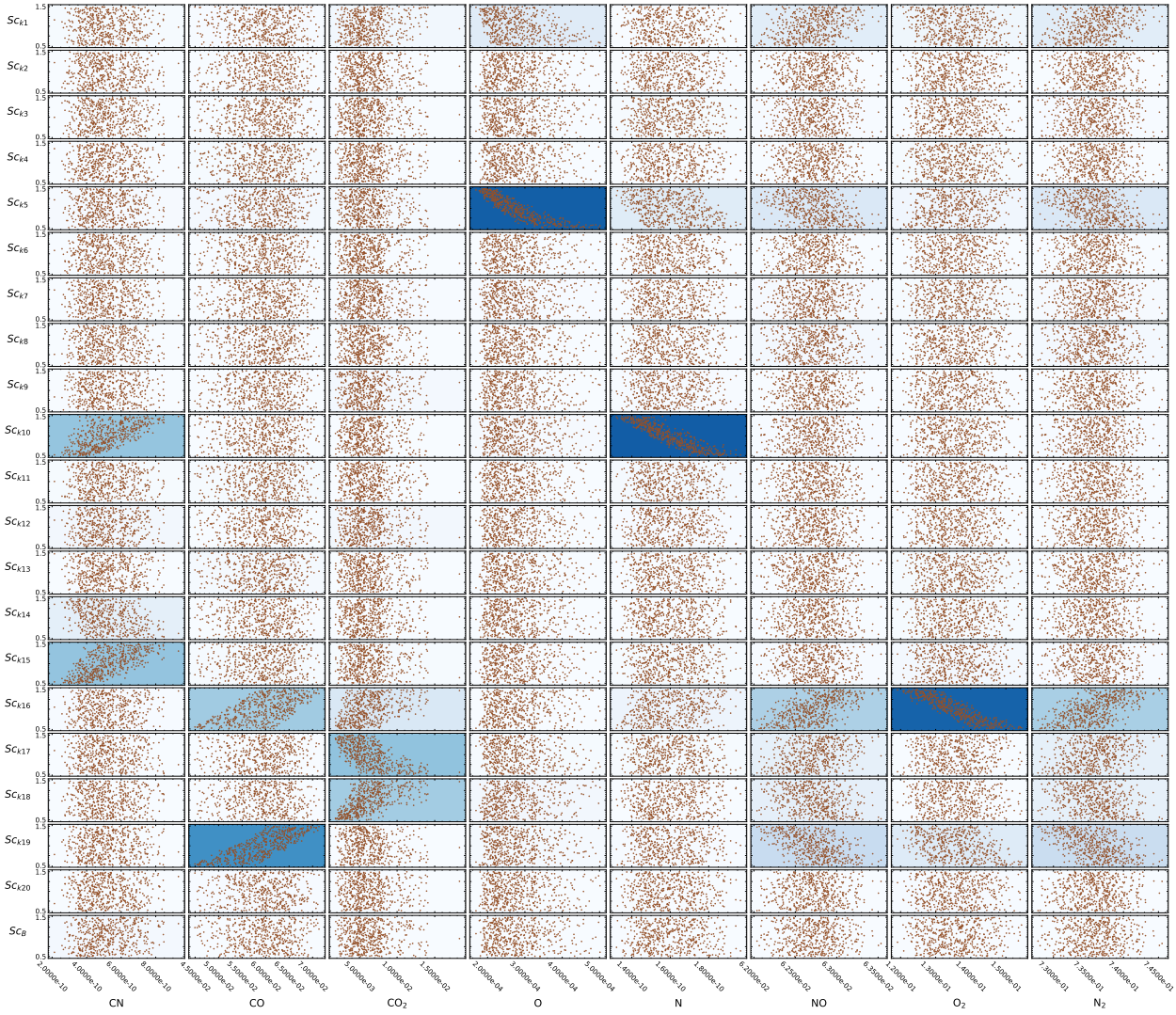

Figure 5.19: Case 1 scatter and Sobol' data for the ACA model at surface on a 65-degree measurement plane for 3 km/s freestream conditions. Sensitivity scaling parameters are described along the y-axis with corresponding lower and upper bounds used for sampling. Predicted mass fractions are shown along the x-axis. Sobol' index contours are mapped onto plots from Fig. 5.18a.

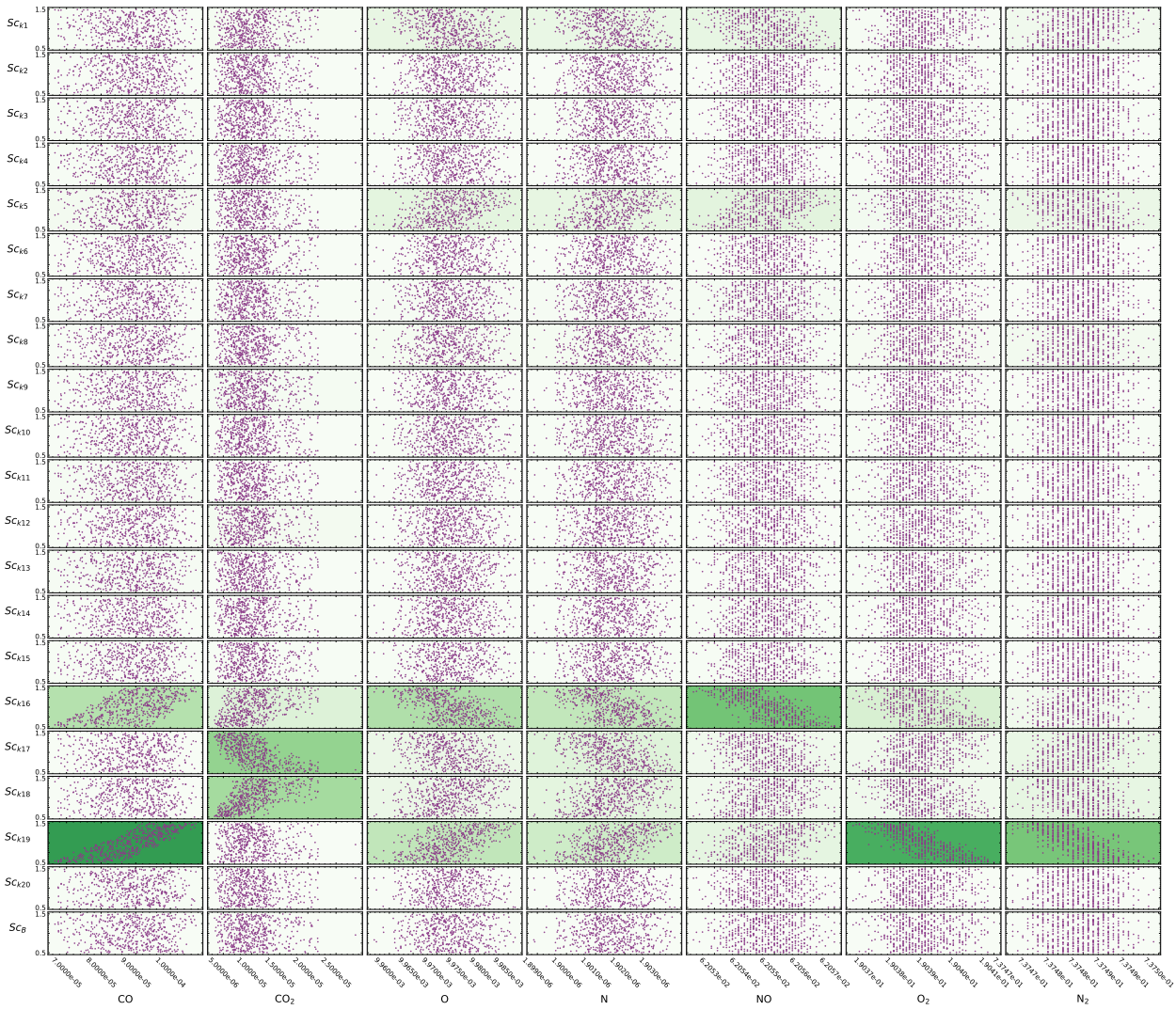

Figure 5.20: Case 1 scatter and Sobol' data for the ACA model at surface on a 65-degree measurement plane for 3 km/s freestream conditions. Sensitivity scaling parameters are described along the y-axis with corresponding lower and upper bounds used for sampling. Predicted mass fractions are shown along the x-axis. Sobol' index contours are mapped onto plots from Fig. 5.18b.

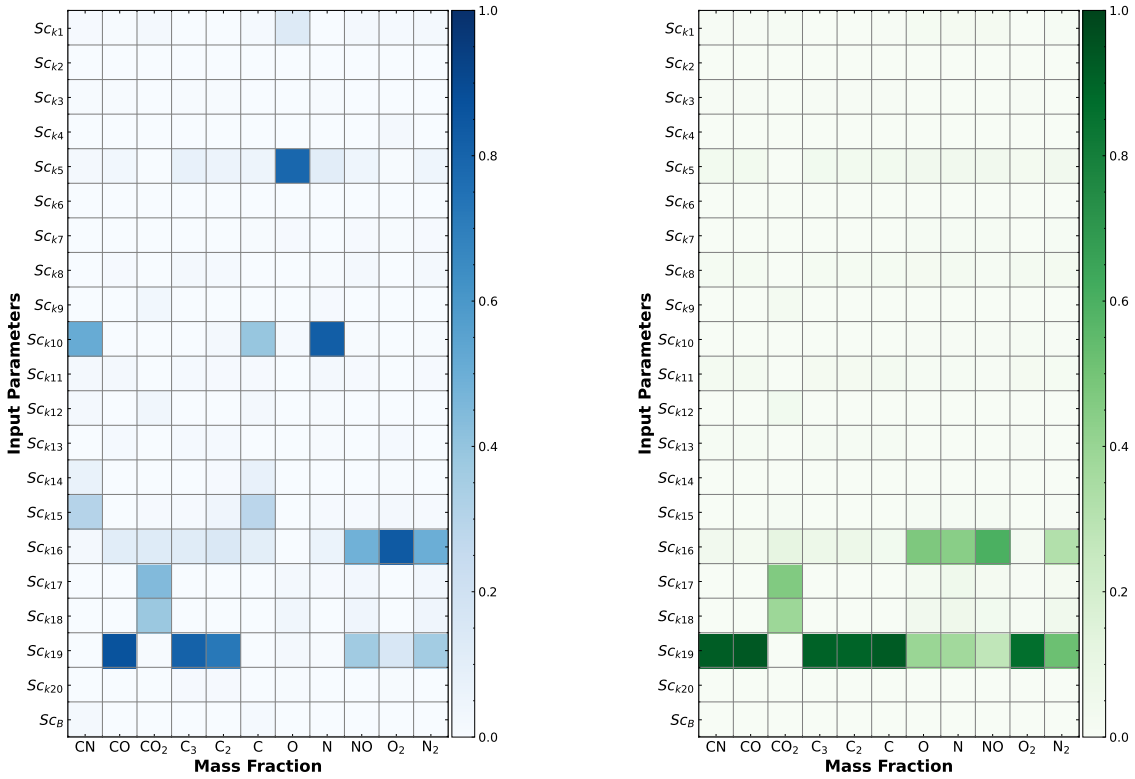

(a) 0.0 mm.

(b) 1.0 mm.

Figure 5.21: Case 2 Sobol' indices for the ACA model that show influence of rate coefficient pre-exponential factors on predicted species mass fractions at locations normal to the surface along a 65-degree measurement plane for 3 km/s freestream conditions. Surface temperature is set to 1626 K.

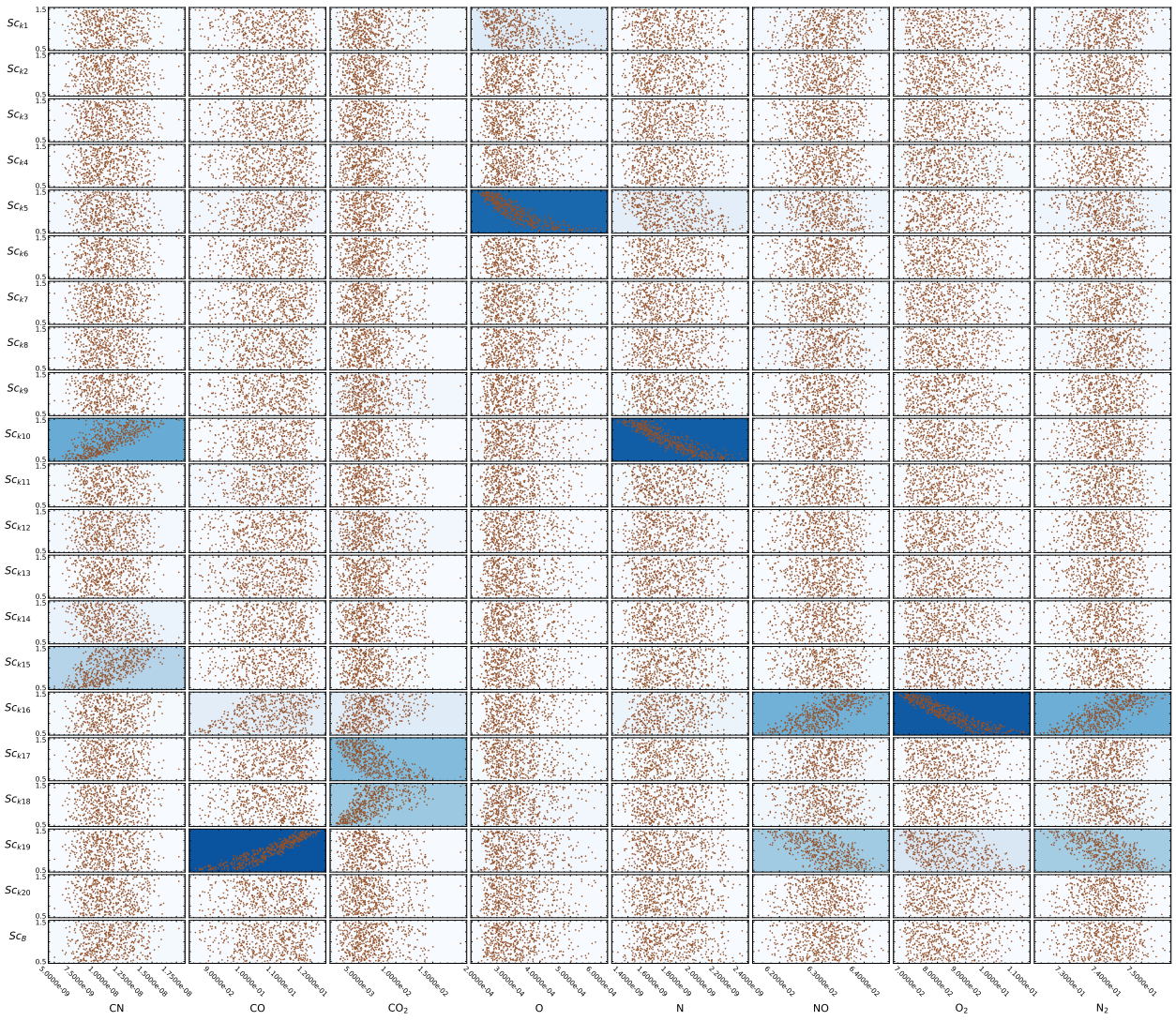

Figure 5.22: Case 2 scatter and Sobol' data for the ACA model at surface on a 65-degree measurement plane for 3 km/s freestream conditions. Sensitivity scaling parameters are described along the y-axis with corresponding lower and upper bounds used for sampling. Predicted mass fractions are shown along the x-axis. Sobol' index contours are mapped onto plots from Fig. 5.21a.

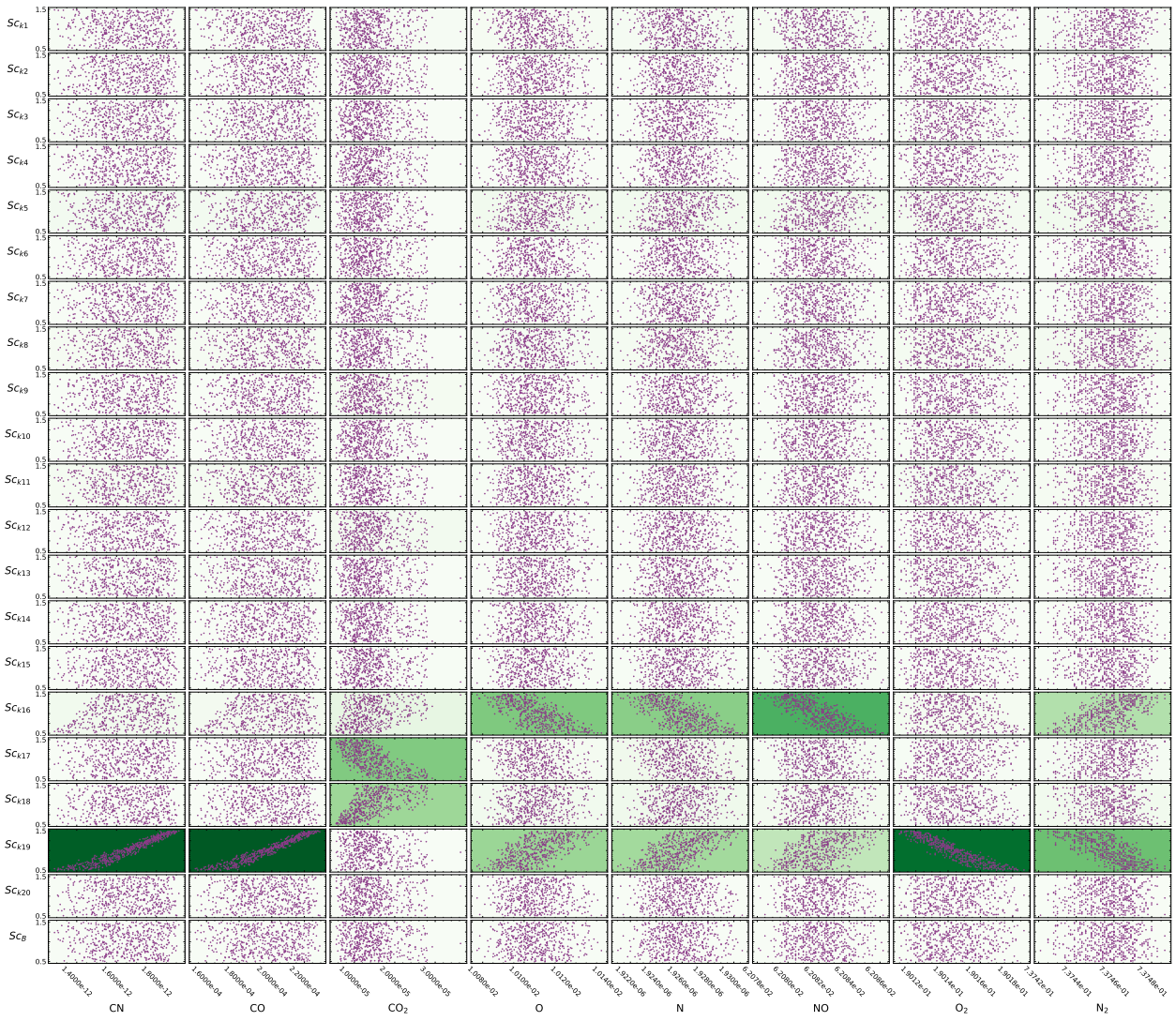

Figure 5.23: Case 2 scatter and Sobol' data for the ACA model at surface on a 65-degree measurement plane for 3 km/s freestream conditions. Sensitivity scaling parameters are described along the y-axis with corresponding lower and upper bounds used for sampling. Predicted mass fractions are shown along the x-axis. Sobol' index contours are mapped onto plots from Fig. 5.21b.

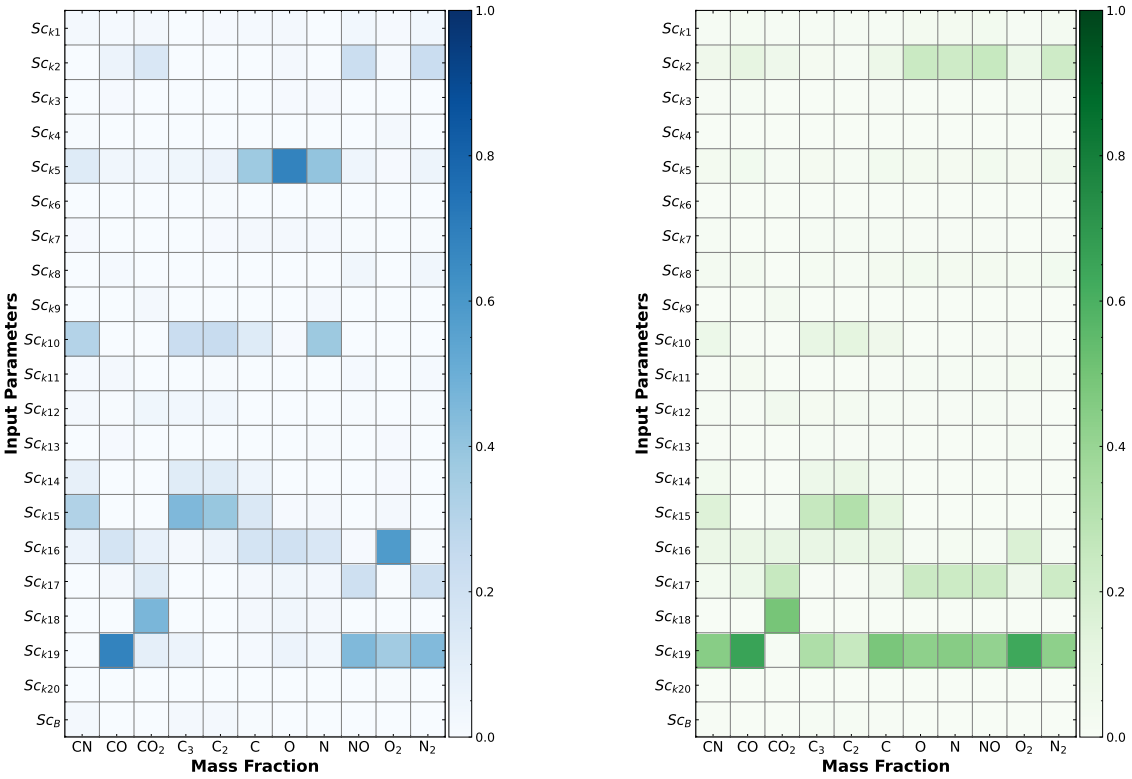

(a) 0.0 mm.

(b) 1.0 mm.

Figure 5.24: Case 3 Sobol' indices for the ACA model that show influence of rate coefficient pre-exponential factors on predicted species mass fractions at locations normal to the surface along a 65-degree measurement plane for 3 km/s freestream conditions. Surface temperature is set to 2146 K.

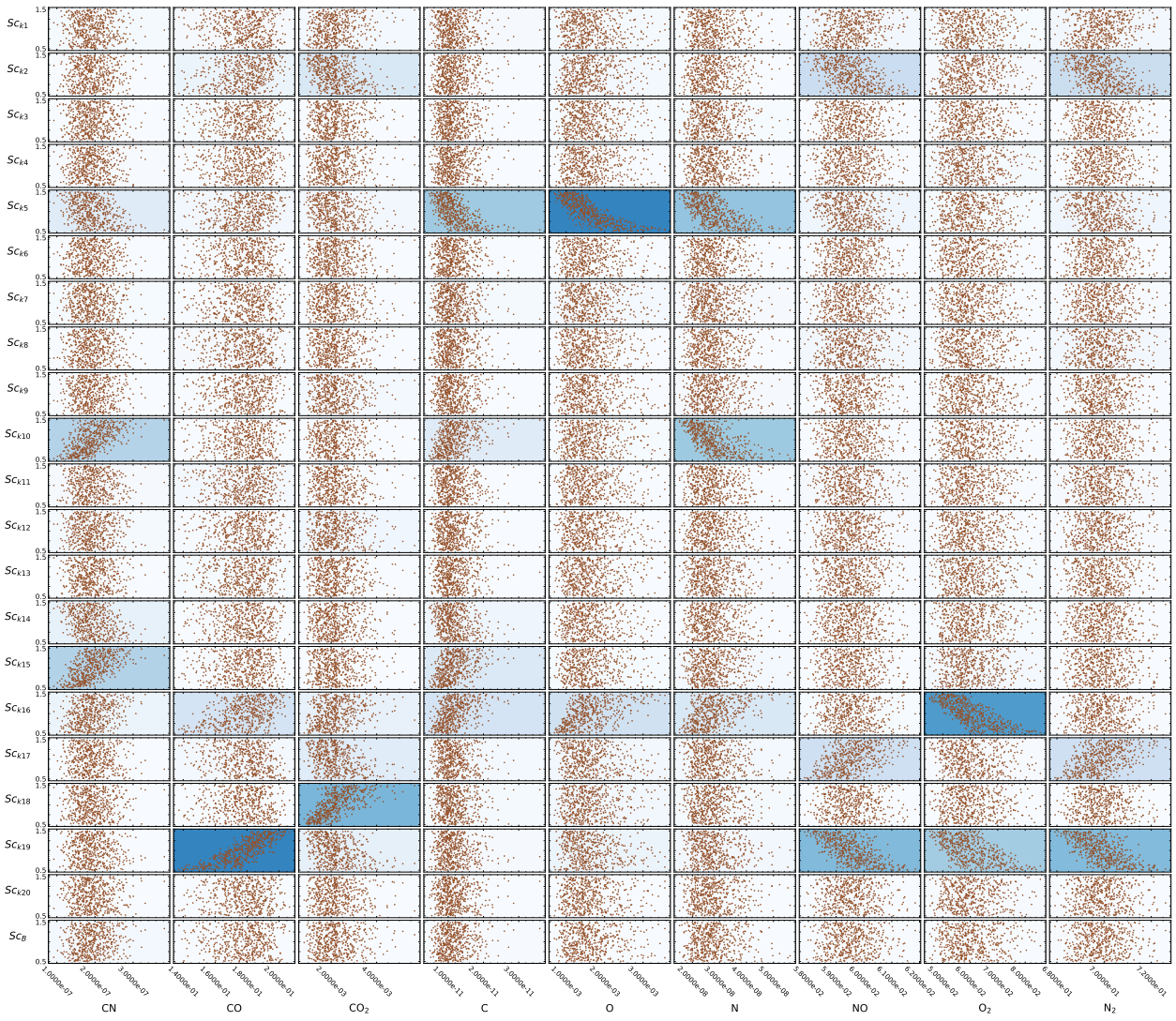

Figure 5.25: Case 3 scatter and Sobol' data for the ACA model at surface on a 65-degree measurement plane for 3 km/s freestream conditions. Sensitivity scaling parameters are described along the y-axis with corresponding lower and upper bounds used for sampling. Predicted mass fractions are shown along the x-axis. Sobol' index contours are mapped onto plots from Fig. 5.24a.

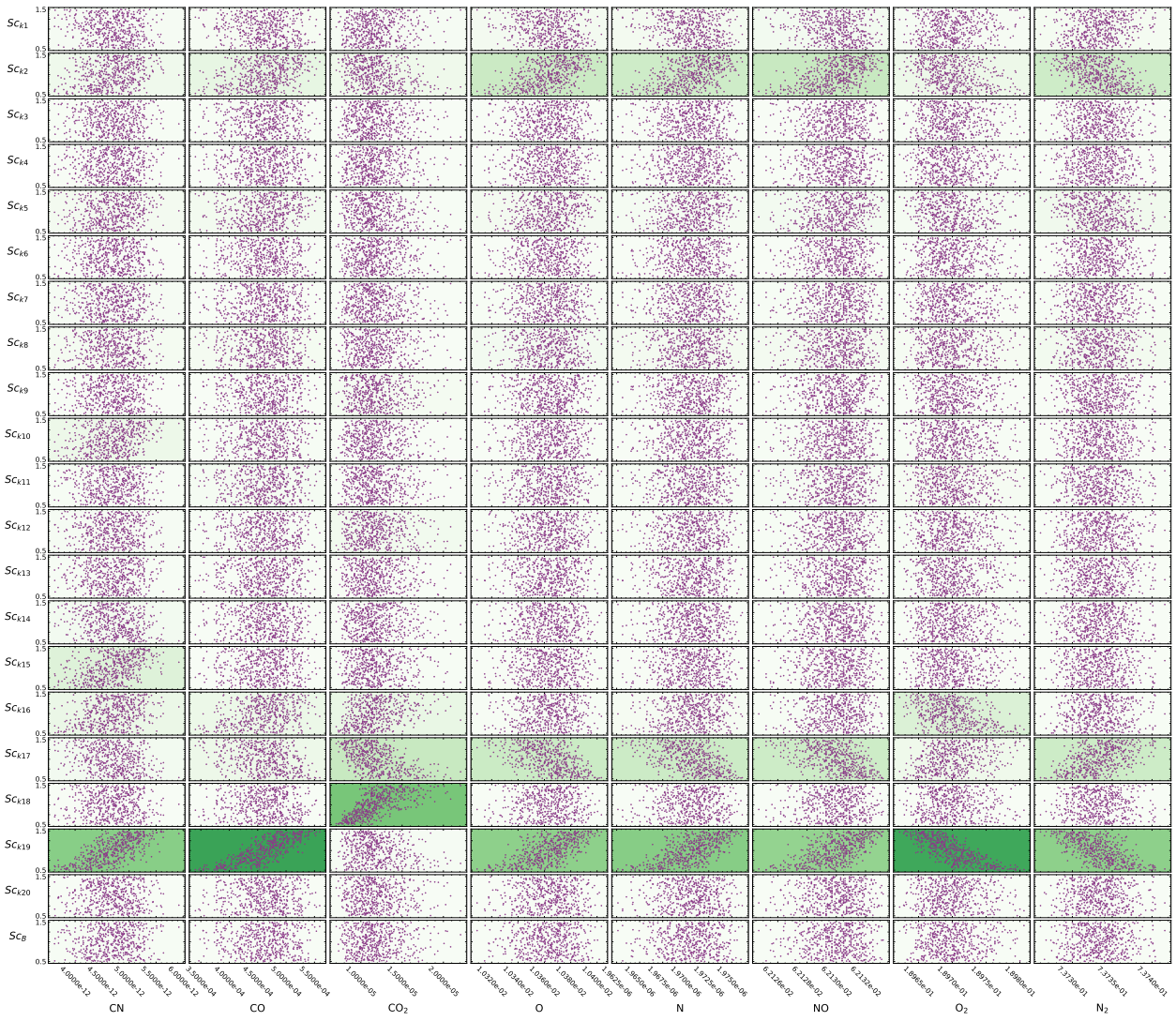

Figure 5.26: Case 3 scatter and Sobol' data for the ACA model at surface on a 65-degree measurement plane for 3 km/s freestream conditions. Sensitivity scaling parameters are described along the y-axis with corresponding lower and upper bounds used for sampling. Predicted mass fractions are shown along the x-axis. Sobol' index contours are mapped onto plots from Fig. 5.24b.

5.5 Conclusions

A Damköhler analysis has been demonstrated to identify reaction- and diffusion-limited surface ablation regimes and compare selected finite-rate model predictions for a test sample geometry under different flow enthalpy conditions. A global sensitivity analysis framework

introduced in Chapter 4 was demonstrated to characterize Park and ACA models for a 3 km/s freestream condition in the Sandia hypersonic shock tunnel and compare prediction behavior with results previously discussed 4 km/s freestream condition case. Rate coefficient pre-exponential factors for reactions with molecular oxygen as a reactant were dominant when assessing predicted CO mass fractions in both Park and ACA models at the present enthalpy conditions, due to the dominant O_2 flux to the surface. The dominant O flux presented for the higher enthalpy case in Chapter 4 resulted in highly influential pre-exponential factors for reactions with atomic oxygen as reactants for each model, where different complex pathways contributed to predicted CO. Supplementary sensitivity analysis is located in Appendix B that assesses the influence of potential experimental uncertainties in the nozzle outlet flow conditions on predicted mass fractions of gas species, which are used as inflow conditions of the present CFD and surface ablation simulations.

Future work will begin to assess sensitivity interaction effects between rate coefficient parameters with gas species concentration predictions. Damköhler, sensitivity, and validation assessments will also continue as experimental data becomes available. The presented Damköhler analysis approach will continue to be matured and validated to further characterize the surface and inform the required model for a given flight or experimental condition.

Chapter 6

Conclusions and Future Work

6.1 Conclusions

A validation and uncertainty quantification methodology was implemented to assess the predictive behavior of air/carbon ablation models in describing the surface state within a chemically ablating boundary layer for nonequilibrium high-enthalpy flows. This work leveraged recent advances in finite-rate model development to characterize the performance of selected legacy and state-of-the-art surface ablation models. Simulations were run using US3D [56], where surface kinetics models were implemented as a boundary condition that was coupled with the flow solver through a mass balance at the wall.

Models were characterized through global sensitivity analysis for selected experimental and flight conditions. The influence of one-way interactions between individual model parameters and mechanisms on predicted surface and boundary layer species quantities was quantified and compared across models and conditions. Validation assessments compared model predictions of a primary carbon oxidation product, CO, with measured data at Sandia's hypersonic shock tunnel. Finally, an approach to identify reaction- and diffusion-limited ablation regimes through an oxygen-consumption Damköhler analysis was employed to compare ablation model predictions between shock tunnel test cases. The contributions of this dissertation provide credibility evidence for analyzed finite-rate models and demonstrate a rigorous framework for continued assessments as more experimental data become available and models continue to be developed and matured.

A global sensitivity analysis was initially performed to survey existing legacy and state-of-the-art finite-rate surface ablation models for a set of freestream flight conditions for a sphere-cone geometry and select ideal models for further analysis. Sobol' indices were computed to assess the influence of pre-exponential factors for the corresponding gas-surface reaction rate coefficients on predicted mass flux quantities of air and carbon ablation product species. Legacy Park [13] and new molecular beam-surface scattering experiment-driven ACA [31] finite-rate models were selected for further characterization and validation in this work for oxidation-dominant high-enthalpy environments.

Sensitivity and validation assessments in this work targeted air/graphite gas-surface interactions for hypersonic shock tunnel experiments. Finite-rate and equilibrium surface ablation modeling approaches were compared in their ability to predict CO products near the surface. A Damköhler analysis was also demonstrated to identify reaction- and diffusion-limited surface ablation regimes for 3 and 4 km/s flight- and high-enthalpy conditions respectively. At the higher enthalpy condition, the surface is in a diffusion-limited ablation regime for wall temperatures of 1246, 1626, and 2146 K. At these conditions, Park, ACA, and equilibrium models showed good agreement with one another, which is further evidence that the surface ablation regime is near diffusion-limited.

Predictions are within an order of magnitude for measured CO number density; however, all models overpredict this quantity. Additional sources of error may include experimental uncertainties that impact the nozzle exit conditions and resulting inflow conditions used in the model and measurement errors (e.g., surface temperature, CO concentration). Sources of uncertainty on the modeling side may be due to model form error as well epistemic uncertainties related to empirical rate coefficients (e.g., activation energies). A combined deterministic prediction and sensitivity analysis methodology identified key chemical process drivers in the models. Due to the high surface temperatures and large atomic oxygen flux to the surface, key O-atom reactions were identified across Park and ACA models that drive predicted CO quantities. In the ACA model, adsorption and Eley-Rideal recombination

reactions were identified where atomic oxygen is a primary reactant to produce CO, CO_2, and adsorbed oxygen as most influential on the predicted CO number density at the measurement location. O-atom oxidation of the bulk carbon was the primary influential reaction for predicted CO in the Park model.

At the flight enthalpy condition, the surface was determined to be likely in a reaction-limited ablation regime. In this case, there are enough diffused reactant species (e.g., oxygen) at the surface and ablation rates are limited by the kinetic barrier. Park and ACA models predicted a less conservative estimate of CO near the surface when compared to the equilibrium model. As surface temperature decreased for each set of results, the Damköhler number also decreased toward a more reaction-limited regime. Additionally, it was shown that the higher molecular oxygen flux interacting with the surface activated related sections of both Park and ACA model gas-surface reaction sets. Pre-exponential factors of the rate coefficients for reactions with molecular oxygen as a reactant were dominant when assessing predicted CO mass fractions for this flight enthalpy condition. In the ACA model, adsorption of molecular oxygen to create weakly and strongly bonded oxygen were highly influential on predicted CO quantities. For the Park model, oxidation of carbon with molecular oxygen was the primary driver in predicted CO quantities.

The demonstrated framework enables researchers to interrogate complex models to understand potential chemical pathways as part of the ablation process. While the sensitivity and uncertainty propagation methodology was demonstrated for gas-surface chemistry mechanisms, the analysis identified dependencies from the coupled gas-phase kinetics model for predicted species concentrations in the boundary layer flow. Additionally, identifying the most influential parameters will benefit follow-on uncertainty quantification estimates through mechanism reduction of expensive multi-species models and by defining parameters of interest with uncertainty (e.g., reaction efficiencies) that are propagated through the models for further evaluation. The presented cases are only a small subset of relevant environments; however, this work provides a comprehensive analysis that may be leveraged for

other experimental or flight environments.

6.2 Future Work

As discussed in this work, a number of uncertainty sources still remain when validating existing air/carbon finite-rate models using hypersonic shock tunnel facilities. Next steps will begin with assessing the impact of experimental uncertainties in nozzle exit conditions and surface temperature measurements when predicting ablation products in the boundary layer. Additionally, future work should assess the impacts of gas-phase kinetics models and their uncertainties on ablation model predictions.

Damköhler, sensitivity, and validation assessments will also continue as experimental data becomes available. The presented Damköhler analysis approach should be matured and validated to further characterize the surface state and inform the required ablation model for a given flight or experimental condition. There is also a need to assess sensitivity interaction effects between rate coefficient parameters with gas species concentration predictions.

Finally, more research is needed to understand and quantify parameter uncertainties of the ACA model and extended versions formed from molecular beam data and theory. Additional optimization of the ACA reaction rate parameters may be required to produce more realistic pre-exponential factors such as sticking coefficients. Inclusion of a set of gas-surface reactions to support sublimation are needed to enhance the model across realistic flight environments.

Appendix A

Model Validation with Corrected Nozzle Conditions

A.1 Overview

A correction to the nozzle conditions for the 4 km/s freestream case discussed in Chapter 4 was recently suggested by the Sandia HST team. The updated conditions are shown in Table A.1 and are compared with the original quantities used for the previous analysis. Notable differences are a reduction in total density by 30% and an increase in mass fraction of atomic oxygen by 66%. A validation assessment is performed to identify differences in model predictions due to updates in inflow conditions. This study leverages the model set up discussed in Chapter 4.

Table A.1: Computed 4 km/s freestream conditions for the HST test chamber with revised quantities.

Inflow Parameter	Original Quantity	Updated Quantity
U_∞	4070 m/s	4236 m/s
T	614 K	634 K
T_v	1021 K	1099 K
ρ_∞	2.24×10^{-3} kg/m^3	1.56×10^{-3} kg/m^3
y_{N_2}	0.738	0.740
y_{O_2}	0.162	0.137
y_{NO}	0.059	0.055
y_O	0.041	0.068

A.2 Results

Model predictions are presented below for the three surface temperature cases described in Table 4.2. Deterministic predictions shown in Figures A.1-A.5 correspond to results shown in Figures 4.6-4.10, where inflow conditions were revised for the results shown here. Carbon monoxide number density quantities decrease by approximately 20-25% at the wall for the revised simulations; however, they remain nearly consistent with the previous analysis results at the measurement location taken 1.0 mm from the wall. This phenomenon may be due to other dominant influences in the boundary layer such as gas-phase kinetics model.

The computed Damköhler numbers for each surface temperature case is shown in Figure A.6, where the revised 4 km/s freestream conditions are compared with the original 4 km/s and 3 km/s conditions. The revised freestream conditions result in a small increase in the predicted Damköhler numbers when compared to the original conditions and are further into the diffusion-limited regime. This observation may help explain why the finite-rate and equilibrium predictions are so close with these updated conditions. As discussed in Chapter 5, equilibrium and finite-rate models should predict equal ablation rates in a diffusion-limited regime, which are insensitive to individual reaction rate coefficient values. Deterministic and ensemble predictions shown in Figures A.7-A.9 highlight the similar CO number density predictions from finite-rate and equilibrium model models. Predicted uncertainty bounds are unable to capture the experimentally measured values, which was also observed for the previous assessment.

A.2.1 Deterministic Model Comparisons

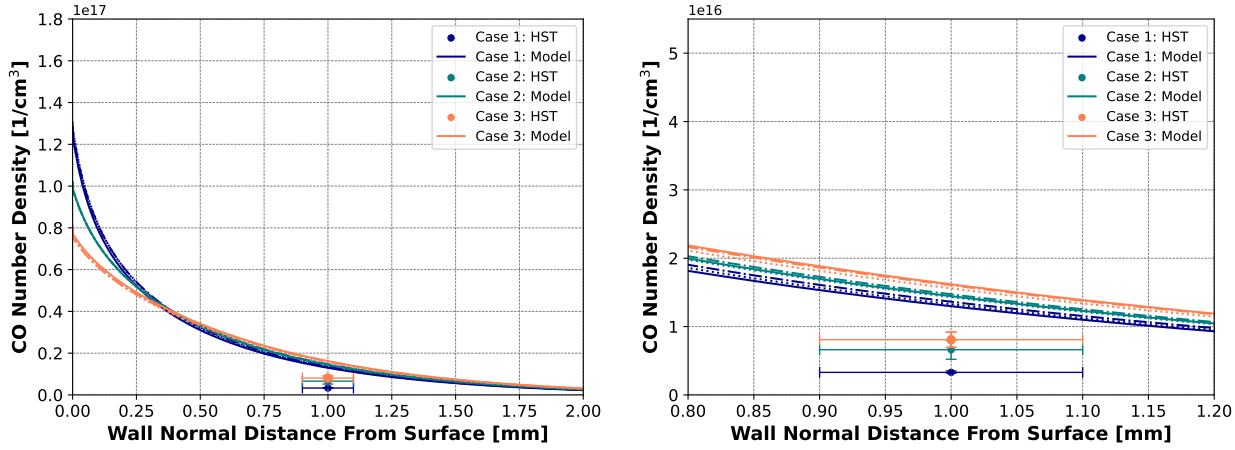

(a) Profile view across CO layer thickness.

(b) Zoomed in view.

Figure A.1: Carbon monoxide number density comparisons between Park (dash-dot), ACA (solid), and equilibrium (dotted) models and experiment (HST) along a 65-degree measurement plane for 4 km/s freestream conditions with revised inflow quantities.

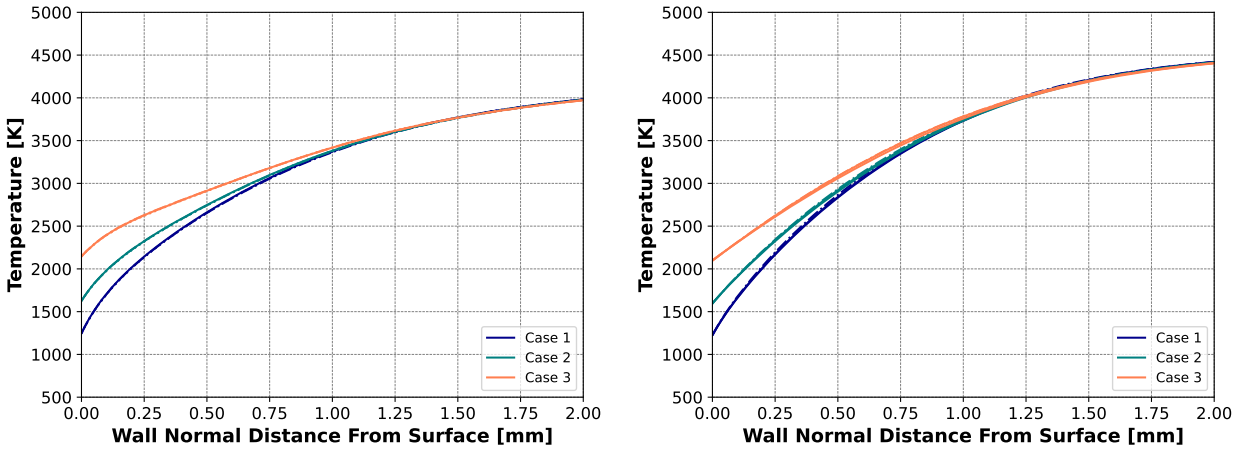

(a) Translational-rotational temperature.

(b) Vibrational-electronic temperature.

Figure A.2: Gas temperature comparisons between Park (dash-dot), ACA (solid), and equilibrium (dotted) models along a 65-degree measurement plane for 4 km/s freestream conditions with revised inflow quantities.

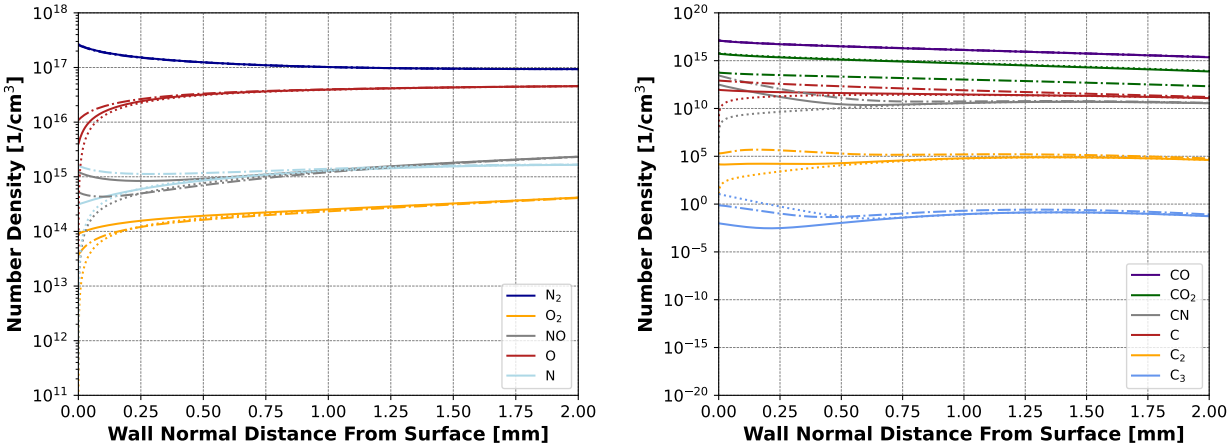

(a) Air species.

(b) Carbonaceous species.

Figure A.3: Number density profile comparisons between Park (dash-dot), ACA (solid), and equilibrium (dotted) models along a 65-degree measurement plane for 4 km/s freestream conditions with revised inflow quantities. Case 1 surface temperature is set to 1246 K.

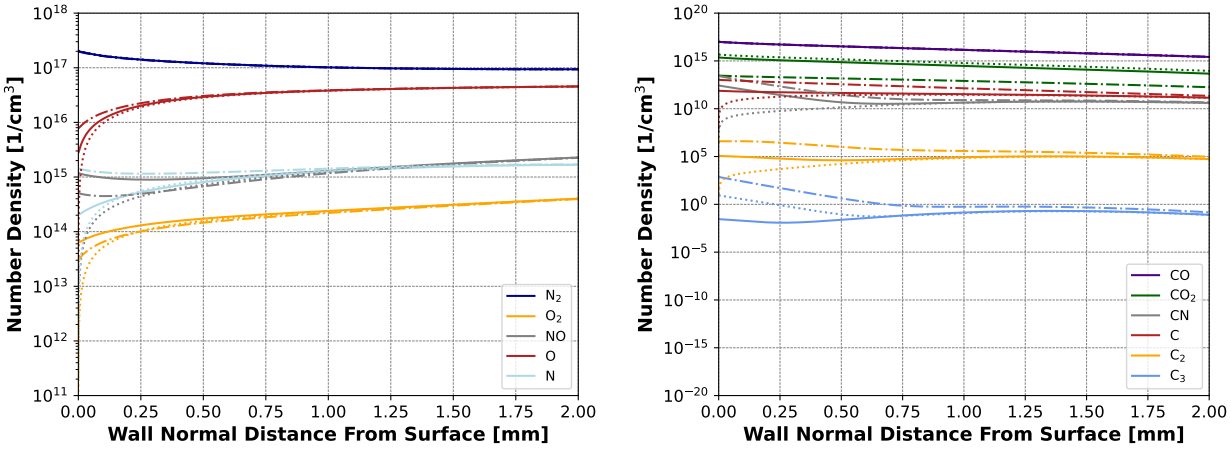

(a) Air species.

(b) Carbonaceous species.

Figure A.4: Number density profile comparisons between Park (dash-dot), ACA (solid), and equilibrium (dotted) models along a 65-degree measurement plane for 4 km/s freestream conditions with revised inflow quantities. Case 2 surface temperature is set to 1626 K.

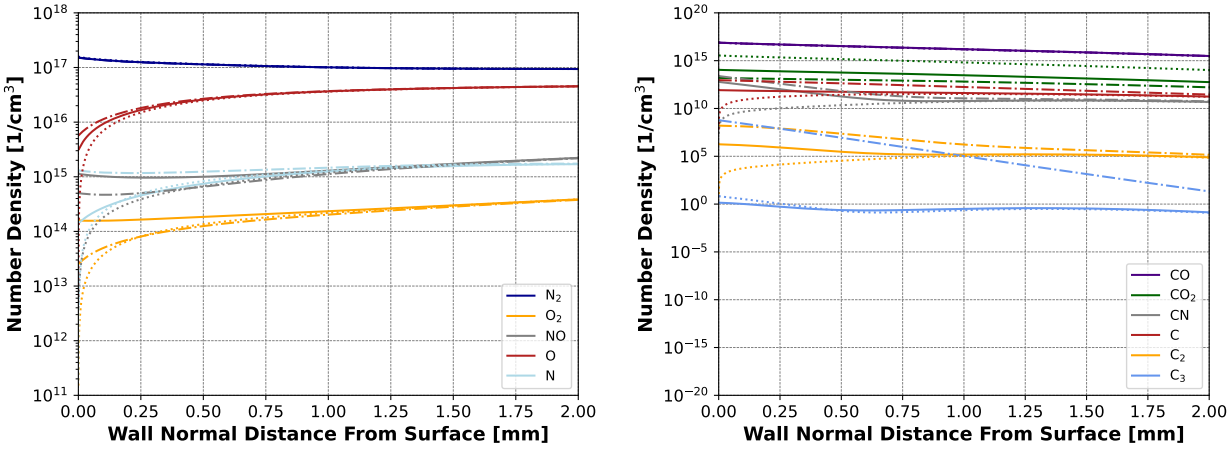

(a) Air species.

(b) Carbonaceous species.

Figure A.5: Number density profile comparisons between Park (dash-dot), ACA (solid), and equilibrium (dotted) models along a 65-degree measurement plane for 4 km/s freestream conditions with revised inflow quantities. Case 3 surface temperature is set to 2146 K.

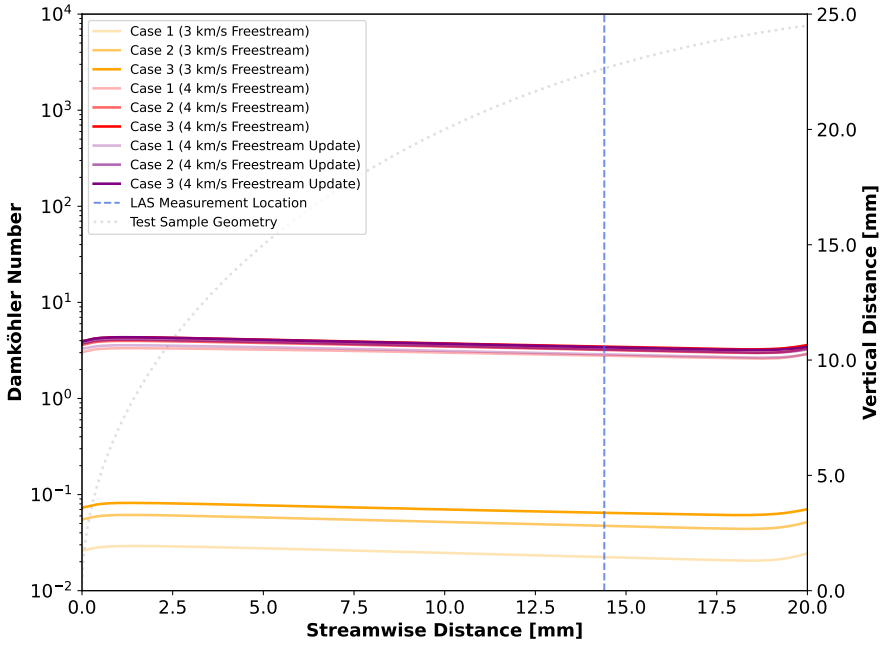

Figure A.6: Comparisons of Damköhler number along the wall. Surface temperatures for Case 1-3 are shown in Table 4.2. HST freestream conditions are in Table A.1 and Table 5.1 for the 4 km/s and 3 km/s cases respectively. The geometric profile of the test sample is also shown for reference.

A.2.2 Validation with Propagated Model Uncertainty

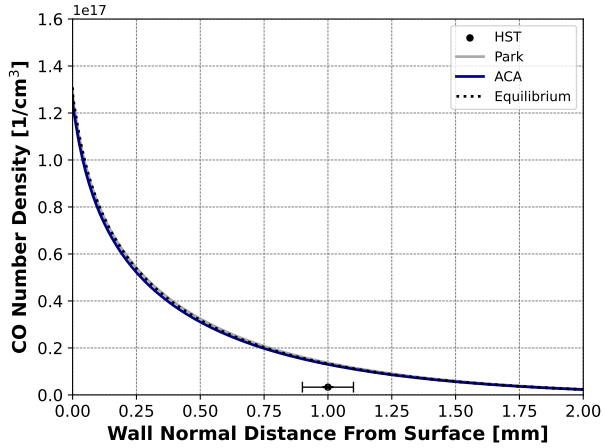

(a) Deterministic predictions.

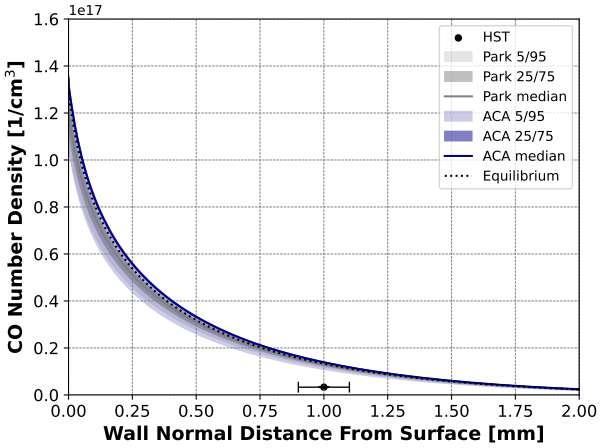

(b) Ensemble predictions.

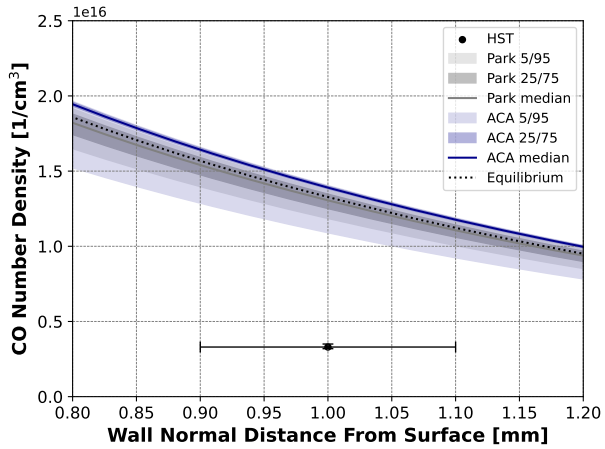

(c) Close up from Figure A.7b.

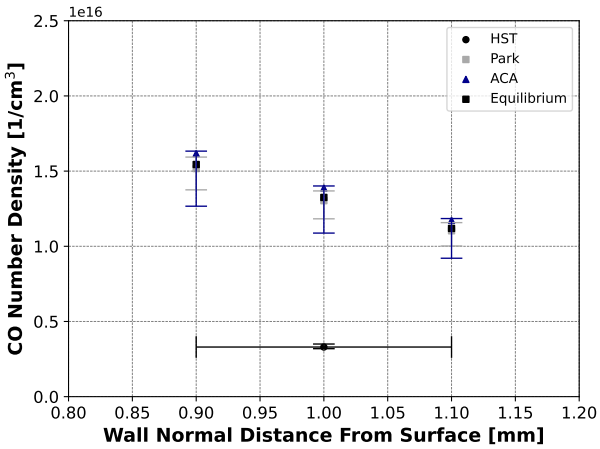

(d) Sampled comparisons.

Figure A.7: Case 1 ensemble predictions of CO number density for Park and ACA models due to uncertainty in rate coefficient pre-exponential factors and compared to a nominal equilibrium (B') solution. Data is probed along the profile normal to the surface along a 65-degree measurement plane for 4 km/s freestream conditions with revised inflow quantities. Surface temperature is set to 1246 K. Experimental measurement from HST LAS system includes 95% confidence intervals and approximate $\pm$ 0.1 mm measurement location error.

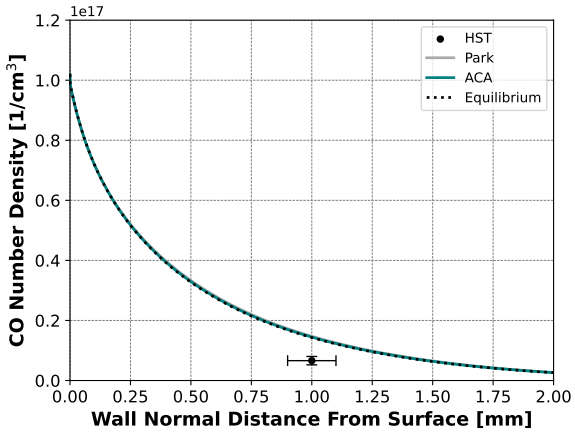

(a) Deterministic predictions.

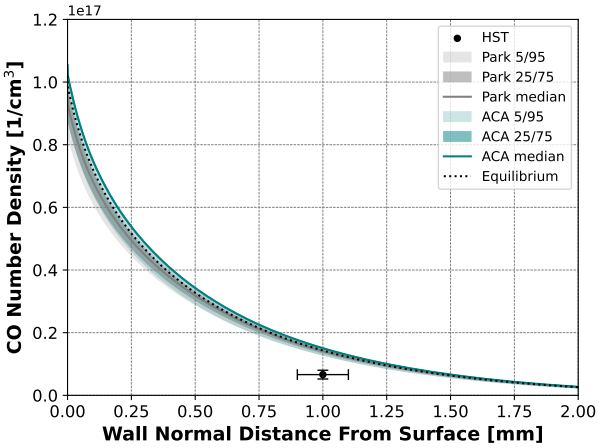

(b) Ensemble predictions.

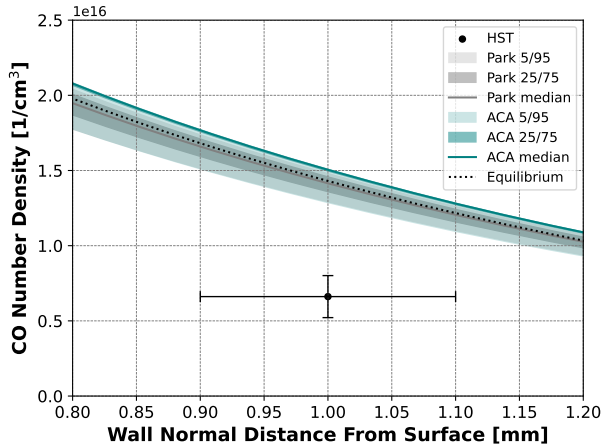

(c) Close up from Figure A.8b.

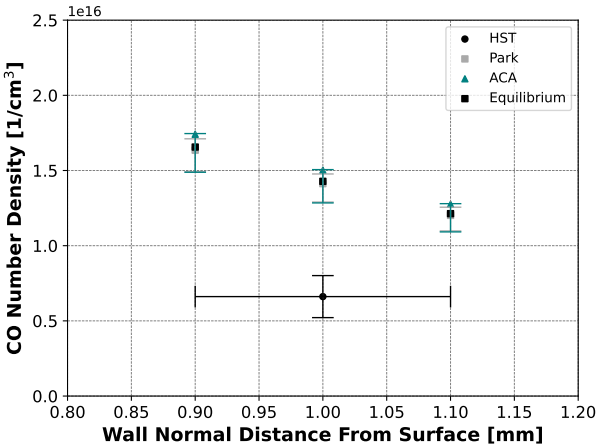

(d) Sampled comparisons.

Figure A.8: Case 2 ensemble predictions of CO number density for Park and ACA models due to uncertainty in rate coefficient pre-exponential factors and compared to a nominal equilibrium (B') solution. Data is probed along the profile normal to the surface along a 65-degree measurement plane for 4 km/s freestream conditions with revised inflow quantities. Surface temperature is set to 1626 K. Experimental measurement from HST LAS system includes 95% confidence intervals and approximate ± 0.1 mm measurement location error.

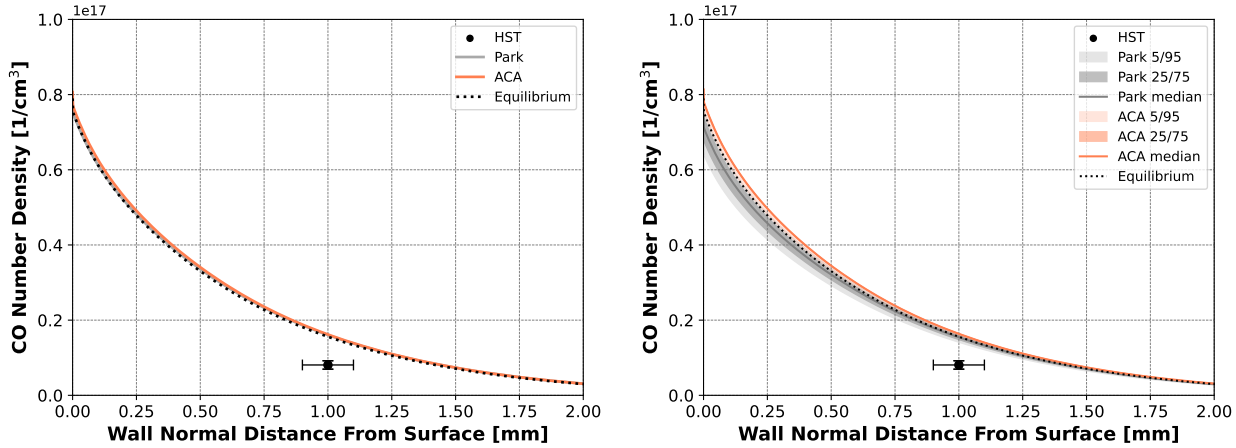

(a) Deterministic predictions.

(b) Ensemble predictions.

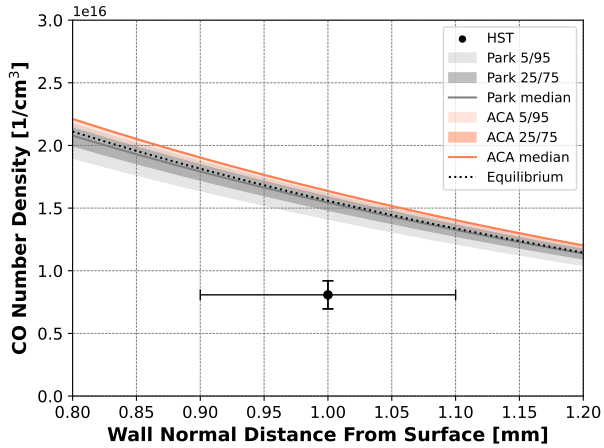

(c) Close up from Figure A.9b.

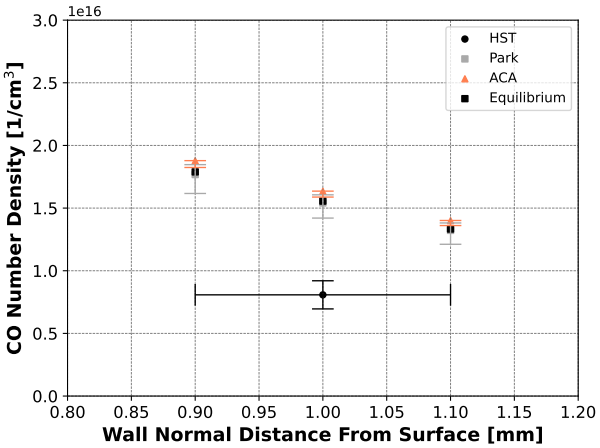

(d) Sampled comparisons.

Figure A.9: Case 3 ensemble predictions of CO number density for Park and ACA models due to uncertainty in rate coefficient pre-exponential factors and compared to a nominal equilibrium (B') solution. Data is probed along the profile normal to the surface along a 65-degree measurement plane for 4 km/s freestream conditions with revised inflow quantities. Surface temperature is set to 2146 K. Experimental measurement from HST LAS system includes 95% confidence intervals and approximate $\pm$ 0.1 mm measurement location error.

Appendix B

Influence of Experimental Uncertainty on Model Predictions

B.1 Overview

A series of sensitivity analyses were performed to assess the influence of inflow freestream quantities and surface temperature on predicted species quantities at and near the surface. The presented results are supplementary to the study shown in Chapter 5, which explores the 3 km/s freestream condition for three surface temperature cases in the Sandia hypersonic shock tunnel experiments. Surface temperatures are defined in Table 4.2 and freestream conditions are shown in Table 5.1.

Sensitivity bounds are prescribed by applying a set scaling factor of $\pm 50\%$ to inflow quantities, surface temperature, and pre-exponential factors for each model's reaction rate coefficients. The scaling factor is also prescribed to the active site density term in the ACA model. A uniform distribution is used for each input parameter. Quantities of interest are predicted mass fractions of gas species at 0.0 and 1.0 mm from the surface along a 65-degree measurement plane from the stagnation plane.

B.2 Global Sensitivity Analysis Results

Initial results show that freestream velocity and surface temperature are influential on predicted quantities at the probed surface location. Inflow density is influential on carbon ablation products and air species when measured 1.0 mm normal from the surface. Velocity remains highly influential on predicted air species quantities, where its influence on oxidation and nitridation carbon ablation products quantities (e.g., CO, CN) is higher for the Park than the ACA model. A more detailed analysis is required; however, this preliminary study demonstrates the impact of experimental facility uncertainties in the present work. Overall, the sensitivities of selected inflow properties and surface temperature are approximately equivalent or much larger than the sensitivities of the pre-exponential factors in the explored cases.

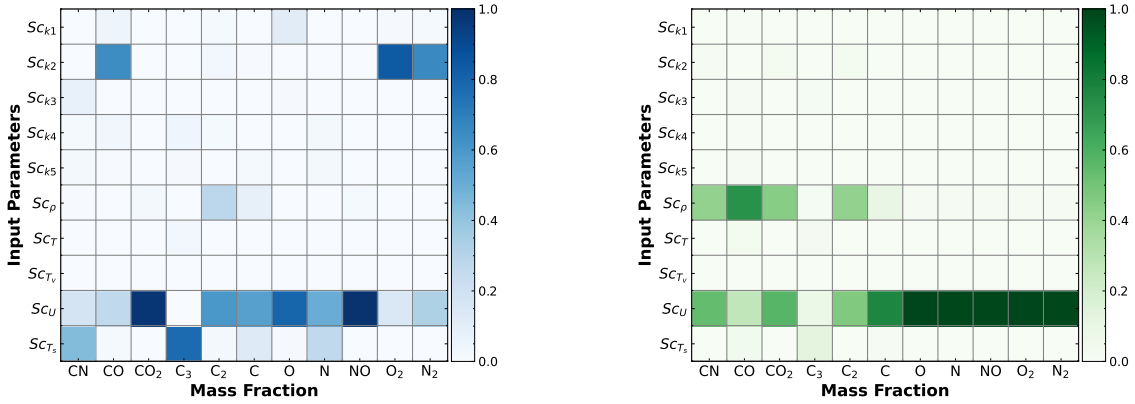

(a) 0.0 mm.

(b) 1.0 mm.

Figure B.1: Sobol' indices for the Park model that show influence of rate coefficient pre-exponential factors, inflow properties, and surface temperature on predicted species mass fractions at locations normal to the surface along a 65-degree measurement plane for surface temperature of 1246 K.

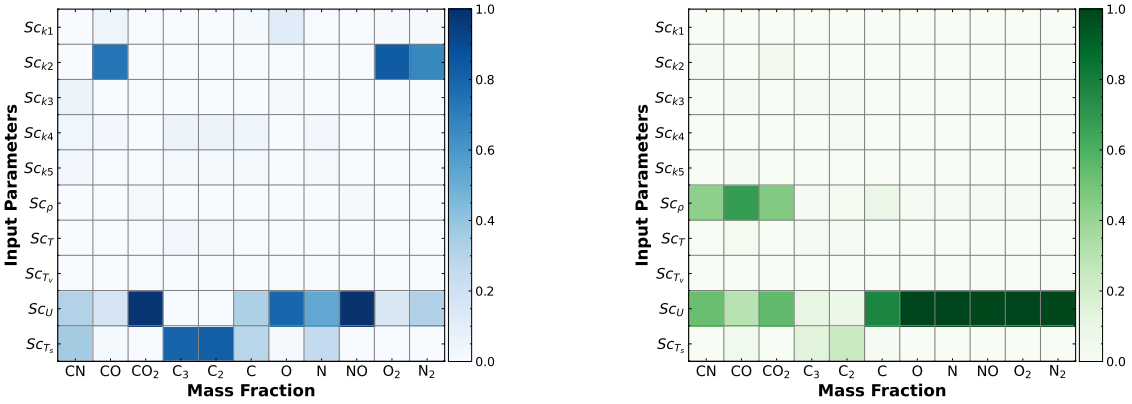

(a) 0.0 mm.

(b) 1.0 mm.

Figure B.2: Sobol' indices for the Park model that show influence of rate coefficient pre-exponential factors, inflow properties, and surface temperature on predicted species mass fractions at locations normal to the surface along a 65-degree measurement plane for surface temperature of 1626 K.

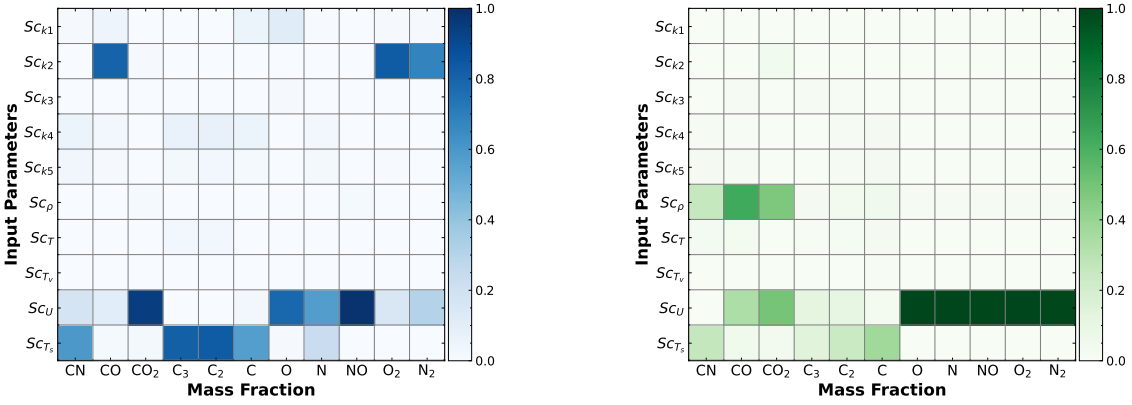

(a) 0.0 mm.

(b) 1.0 mm.

Figure B.3: Sobol' indices for the Park model that show influence of rate coefficient pre-exponential factors, inflow properties, and surface temperature on predicted species mass fractions at locations normal to the surface along a 65-degree measurement plane for surface temperature of 2146 K.

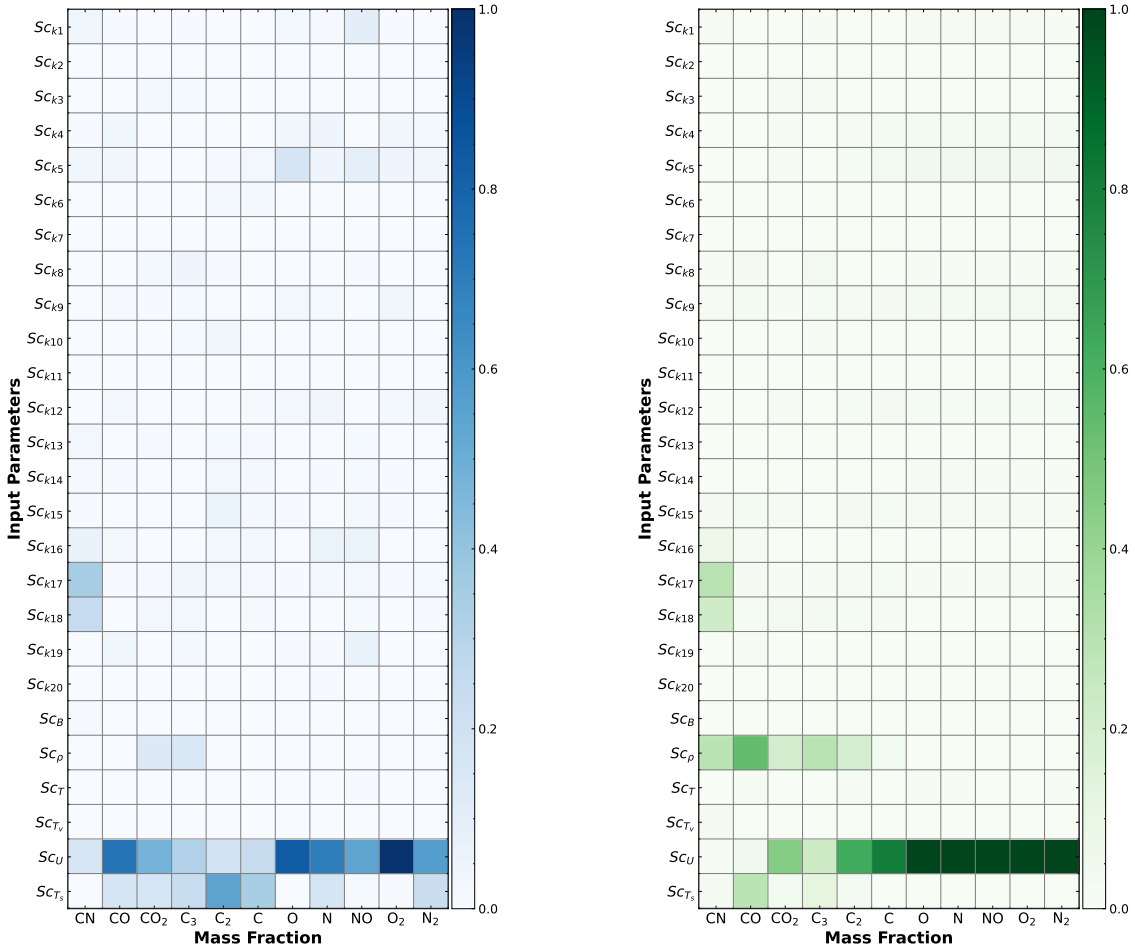

(a) 0.0 mm.

(b) 1.0 mm.

Figure B.4: Sobol' indices for the ACA model that show influence of rate coefficient pre-exponential factors, inflow properties, and surface temperature on predicted species mass fractions at locations normal to the surface along a 65-degree measurement plane for surface temperature of 1246 K.

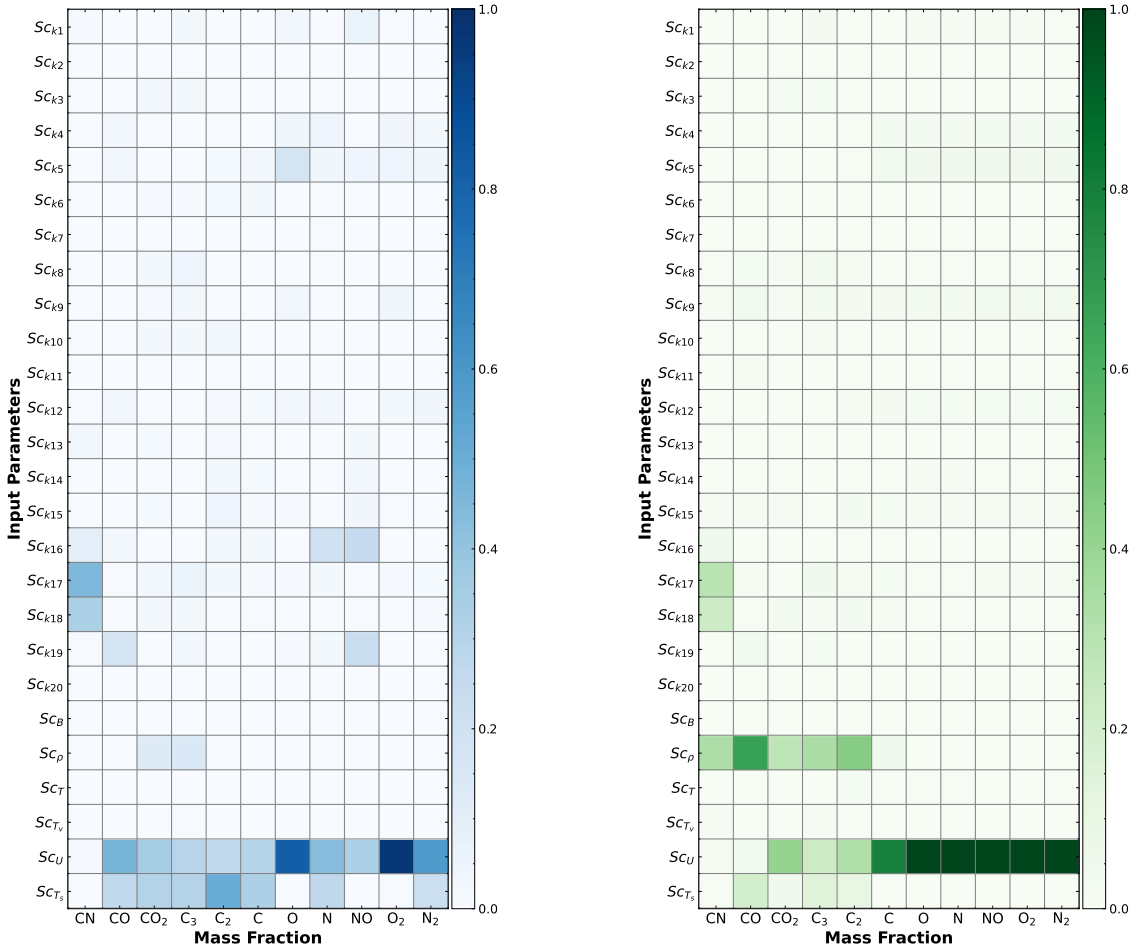

(a) 0.0 mm.

(b) 1.0 mm.

Figure B.5: Sobol' indices for the ACA model that show influence of rate coefficient pre-exponential factors, inflow properties, and surface temperature on predicted species mass fractions at locations normal to the surface along a 65-degree measurement plane for surface temperature of 1626 K.

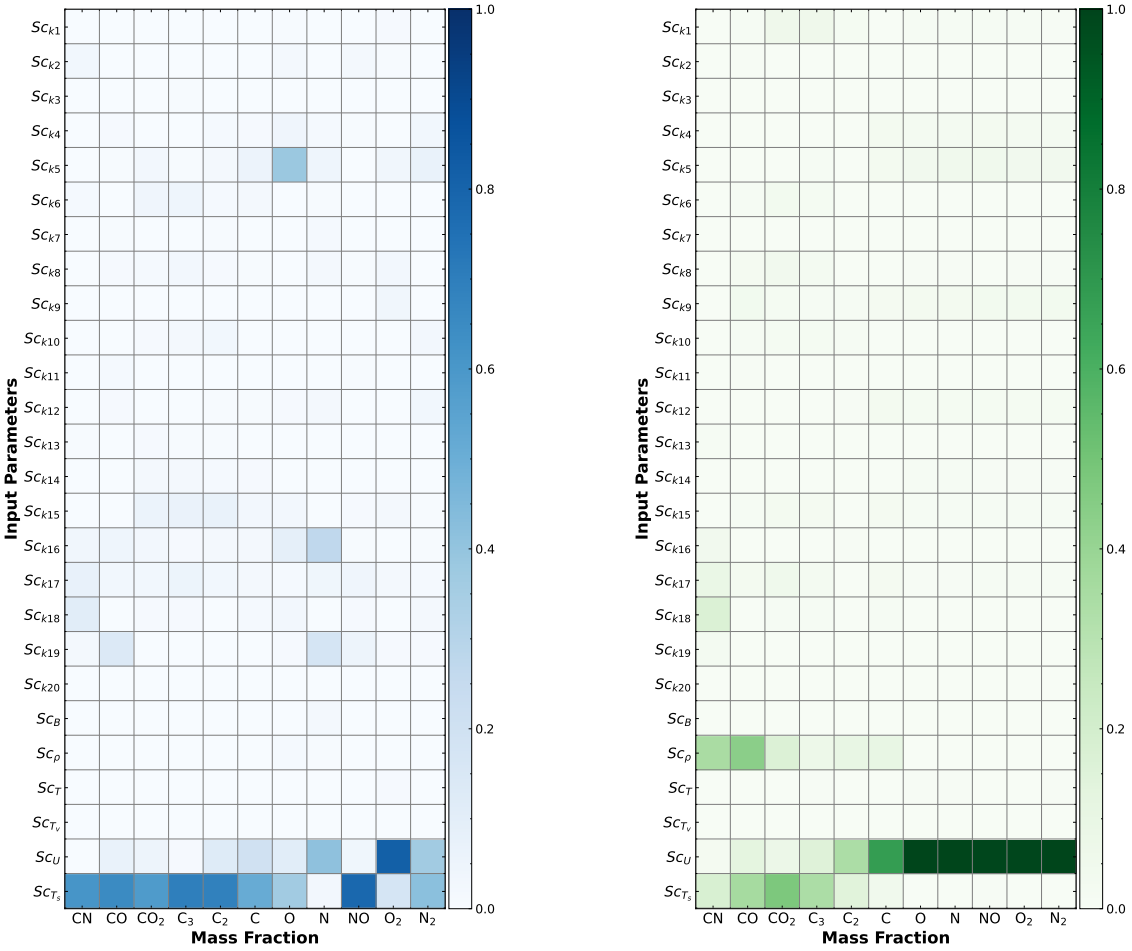

(a) 0.0 mm.

(b) 1.0 mm.

Figure B.6: Sobol' indices for the ACA model that show influence of rate coefficient pre-exponential factors, inflow properties, and surface temperature on predicted species mass fractions at locations normal to the surface along a 65-degree measurement plane for surface temperature of 2146 K.

Appendix C

Model Characterization in an Expansion Tube Environment

C.1 Overview

Sensitivity and Damköhler analyses are performed to characterize finite-rate models for high-enthalpy conditions that correspond to experiments performed by Lewis et al. [40] at the X-2 expansion tunnel facility at the University of Queensland. In the experimental campaign, half-cylinder graphite samples were electrically preheated to surface temperatures of 1920 K and 2410 K (Table C.2) and tested in 8.5 km/s flow conditions representative of hypersonic flight [51]. The half-cylinder test sample had a 50 mm diameter, a height of 10 mm, and a wall thickness of 2 mm. Freestream conditions are shown in Table C.1, where the flow is assumed to be laminar.

A quarter-volume grid is constructed due to symmetry of the test article. A three-dimensional grid of the flowfield is shown in Fig. C.1 and contains 400,000 hexagonal elements. The gas is assumed to be in thermochemical nonequilibrium and Park's 11-species gas-phase model is selected to simulate the kinetics of the reacting flowfield [65], which is described in Table 2.1. Simulations use Park's two-temperature model that defines corresponding temperatures for translational and rotational (T) and vibrational and electronic (T_v) energy modes in equilibrium.

Table C.1: Computed 8.5 km/s freestream conditions for the X-2 test chamber [6].

Inflow Parameter	Quantity
U_∞	8500 m/s
T	2040 K
T_v	2040 K
ρ_∞	1.45×10^{-3} kg/m^3
y_{N_2}	0.751
y_{O_2}	0.225
y_{NO}	8.53×10^{-3}
y_O	2.37×10^{-3}
y_{CO}	1.26×10^{-5}
y_{CO_2}	4.65×10^{-4}
y_{Ar}	1.3×10^{-2}

Table C.2: Prescribed X-2 graphite surface temperature cases.

	Case 1	Case 2
T_s (K)	1920	2410

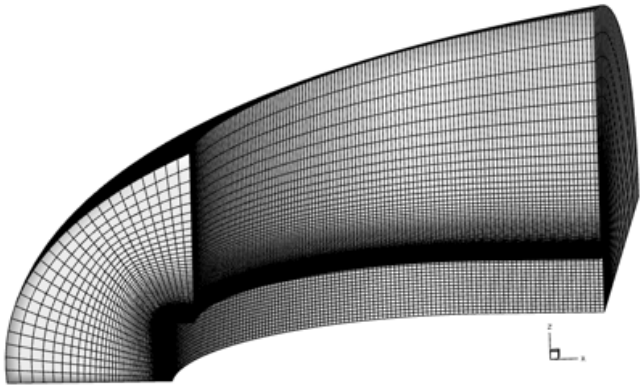

Figure C.1: X-2 flowfield grid for the half-cylinder geometry.

Sensitivity bounds are prescribed by applying a set scaling factor of ±50% to pre-exponential factors for each model's reaction rate coefficients. The scaling factor is also prescribed to the active site density term in the ACA model. A uniform distribution is used for each input parameter. Quantities of interest are predicted mass fractions of gas species at 0.0, 0.25, 0.5, and 1.0 mm from the surface along the stagnation streamline. These locations are selected due to their proximity to the CN layer near the surface.

C.2 Global Sensitivity Analysis Results

Simulations were performed for Park and ACA finite-rate models at the prescribed freestream conditions for each surface temperature case. Mass fractions of CN predicted by the Park model are shown in Figure C.2 for a surface temperature of 2410 K. Sobol' indices for the Park and ACA models are shown in Figures C.3-C.14, and ensembles of 256 and 512 simulations were performed for each model respectively. Differences in sample size are due to the number of input parameters for the Park and ACA models and reflected the methodology used in previous chapters. Incremental LHS simulation responses were monitored to ensure convergence of Sobol' indices. Index values close to unity indicate that the quantity of interest is highly sensitive to the input parameter and shown by a darker color. Companion scatter data of raw prediction models are plotted directly after the heat maps for each surface temperature case. Sensitivity coloring is mapped over and plotted on top of the scatter data. A limit was imposed in the scatter plots for mass fraction quantities below 10^{-12}. Quantities of interest include mass fractions for all 11-species included in our gas-phase kinetics model.

Sensitivity results for the Park model presented in Figures C.3-C.8 show that O-atom oxidation (P1) and N-atom nitridation (P3) reaction rate coefficient pre-exponential factors are highly influential on CO and CN quantities at the surface respectively. Results for the ACA model are shown in Figures C.9-C.14. The pre-exponential factors for reactions A5 (creation of O^*(s) via (s) and O) and A12 (creation of CN and N via recombination of C(b), N(s), and N) are the most influential on CO and CN quantities at the surface respectively. A more detailed analysis is needed; however, this dataset may be used to further understand pathways and aid in UQ analysis through identification of dominant parameters and mechanism reduction.

Finally, the computed Damköhler numbers along the wall for each surface temperature case are shown in Figure C.15. The Damköhler is at its maximum value near the stagnation point and decreases while moving away from the wall. This result may be due to similar

behavior seen in the predicted solution mass transfer coefficient (Equation 5.2), which is plotted in Figure C.16. The surface ablation regime near the stagnation point is further in the diffusion-limited regime than further downstream on the test sample. However, all surface values are close to the transition region that might be expected from this Damköhler definition. Future work will compare model predictions to radiance measurements in the shock layer, where ultraviolet spectrometry was used to measure radiation emitted from the CN violet bands [6, 40]. This analysis supplements deterministic validation work by Alba et al. [6], which focused on Park and ZA finite-rate model predictions.

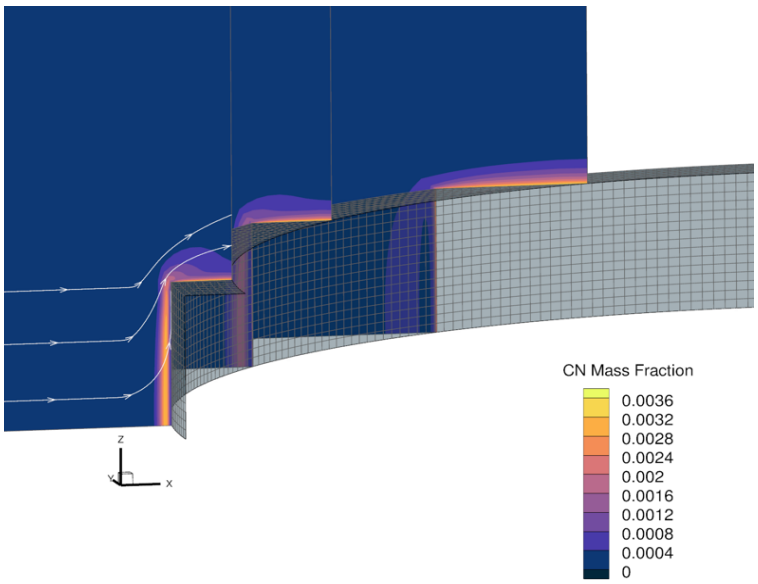

Figure C.2: Park CN mass fraction model predictions in the flowfield. Surface temperature is set at 2410 K.

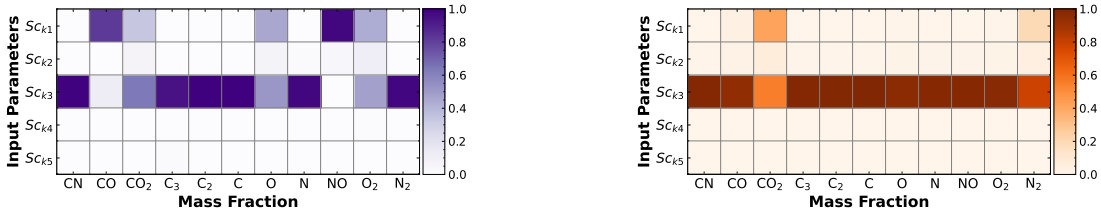

(a) 0.0 mm.

(b) 0.25 mm.

(c) 0.5 mm.

(d) 1.0 mm.

Figure C.3: Sobol' indices for the ACA model that show influence of rate coefficient pre-exponential factors on predicted species mass fractions at wall normal locations along the stagnation streamline. Surface temperature is set to 1920 K.

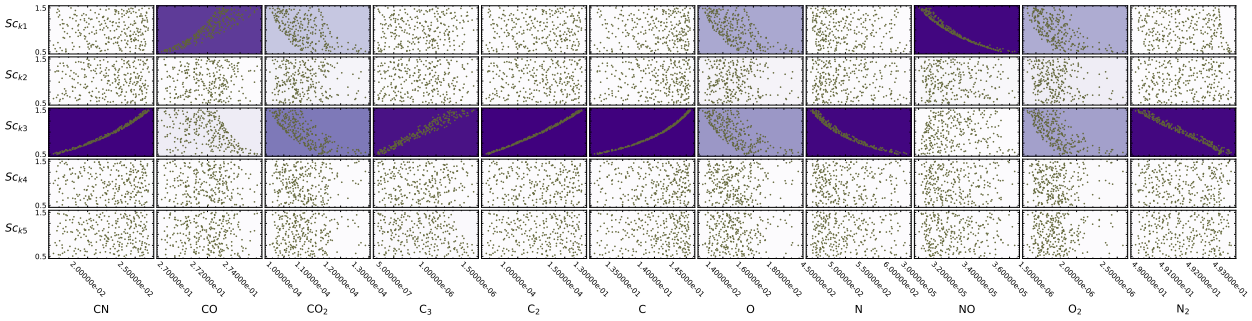

Figure C.4: Scatter and Sobol' data for the ACA model at wall normal locations along the stagnation streamline. Sensitivity scaling parameters are described along the y-axis with corresponding lower and upper bounds used for sampling. Predicted mass fractions are shown along the x-axis. Sobol' index contours are mapped onto plots from Fig. C.3a.

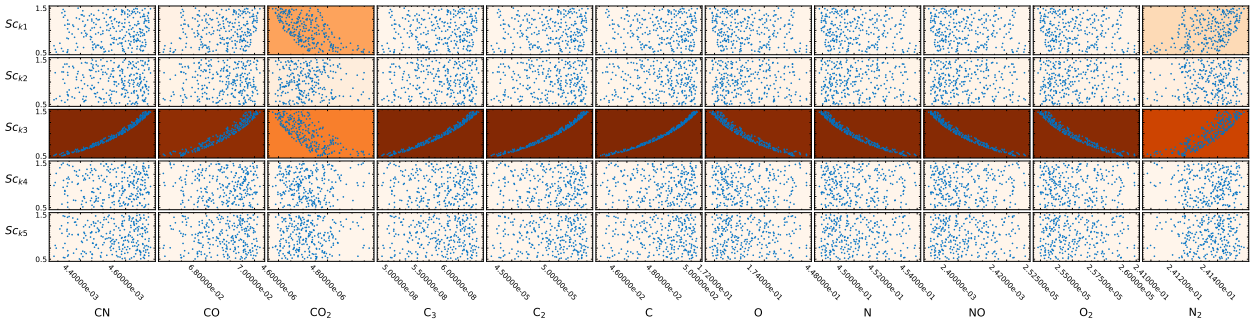

Figure C.5: Scatter and Sobol' data for the ACA model at wall normal locations along the stagnation streamline. Sensitivity scaling parameters are described along the y-axis with corresponding lower and upper bounds used for sampling. Predicted mass fractions are shown along the x-axis. Sobol' index contours are mapped onto plots from Fig. C.3b.

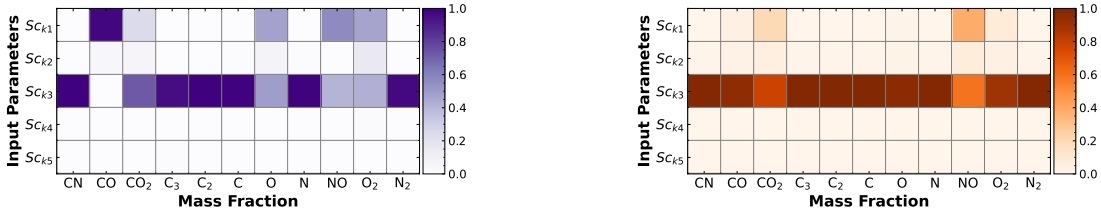

(a) 0.0 mm.

(b) 0.25 mm.

(c) 0.5 mm.

(d) 1.0 mm.

Figure C.6: Sobol' indices for the ACA model that show influence of rate coefficient pre-exponential factors on predicted species mass fractions at wall normal locations along the stagnation streamline. Surface temperature is set to 2410 K.

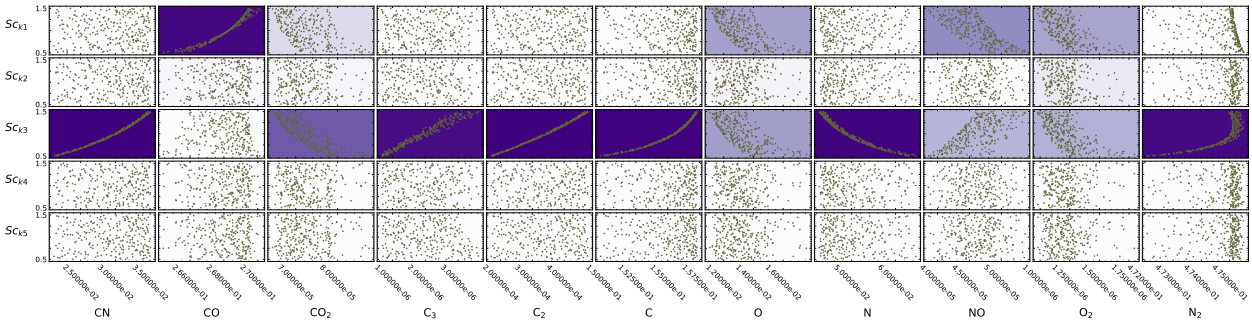

Figure C.7: Scatter and Sobol' data for the ACA model at wall normal locations along the stagnation streamline. Sensitivity scaling parameters are described along the y-axis with corresponding lower and upper bounds used for sampling. Predicted mass fractions are shown along the x-axis. Sobol' index contours are mapped onto plots from Fig. C.6a.

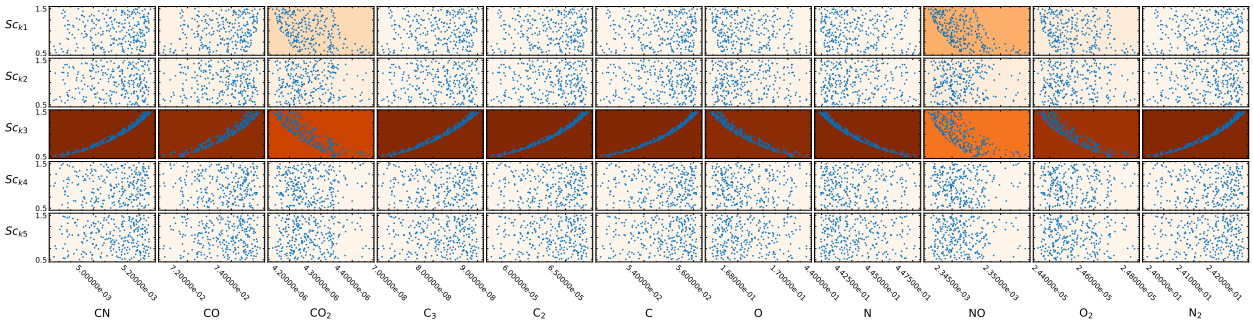

Figure C.8: Scatter and Sobol' data for the ACA model at wall normal locations along the stagnation streamline. Sensitivity scaling parameters are described along the y-axis with corresponding lower and upper bounds used for sampling. Predicted mass fractions are shown along the x-axis. Sobol' index contours are mapped onto plots from Fig. C.6b.

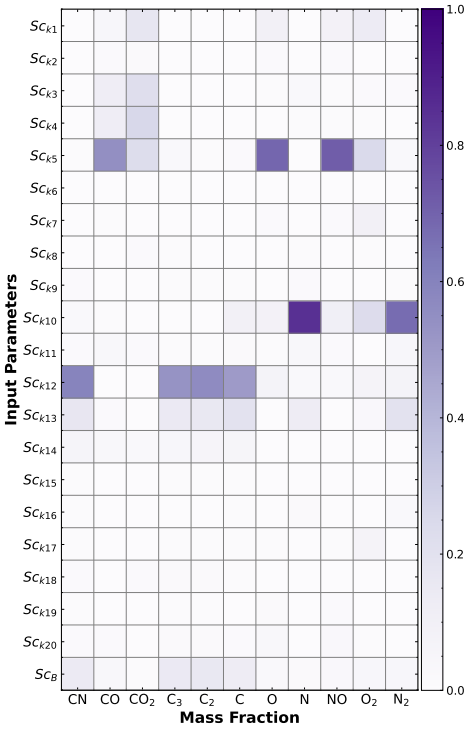

(a) 0.0 mm.

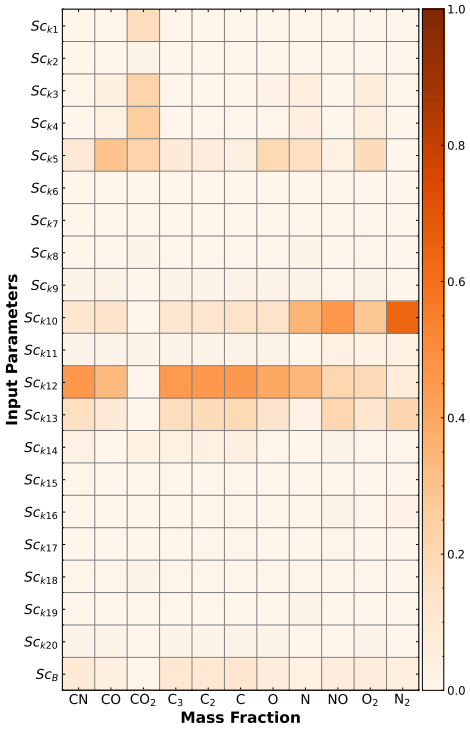

(b) 0.25 mm.

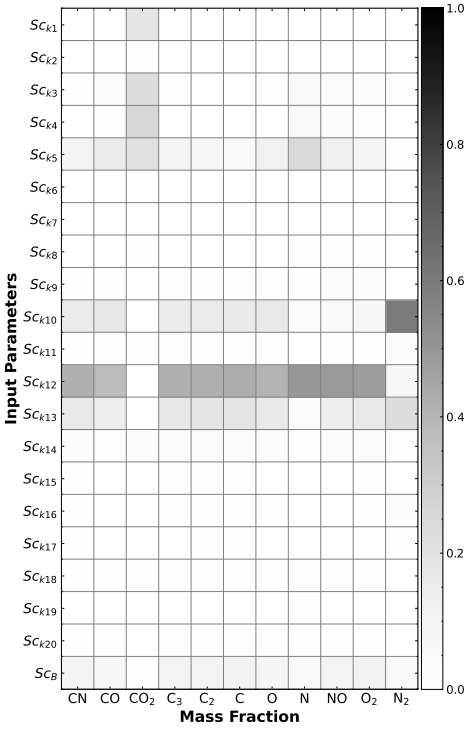

(c) 0.5 mm.

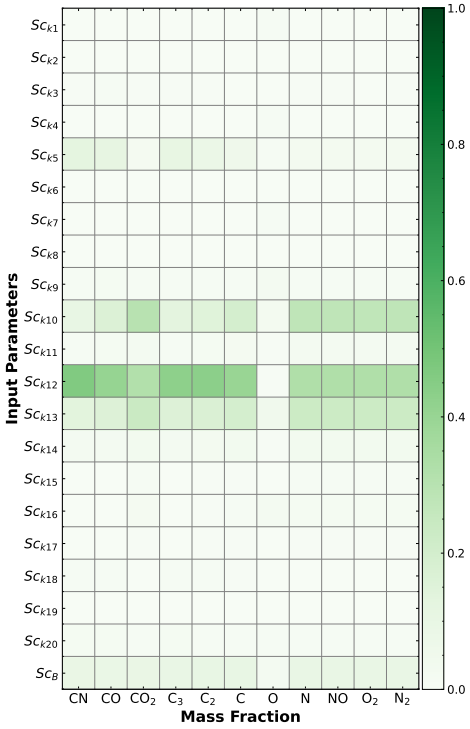

(d) 1.0 mm.

Figure C.9: Sobol' indices for the ACA model that show influence of rate coefficient pre-exponential factors on predicted species mass fractions at wall normal locations along the stagnation streamline. Surface temperature is set to 1920 K.

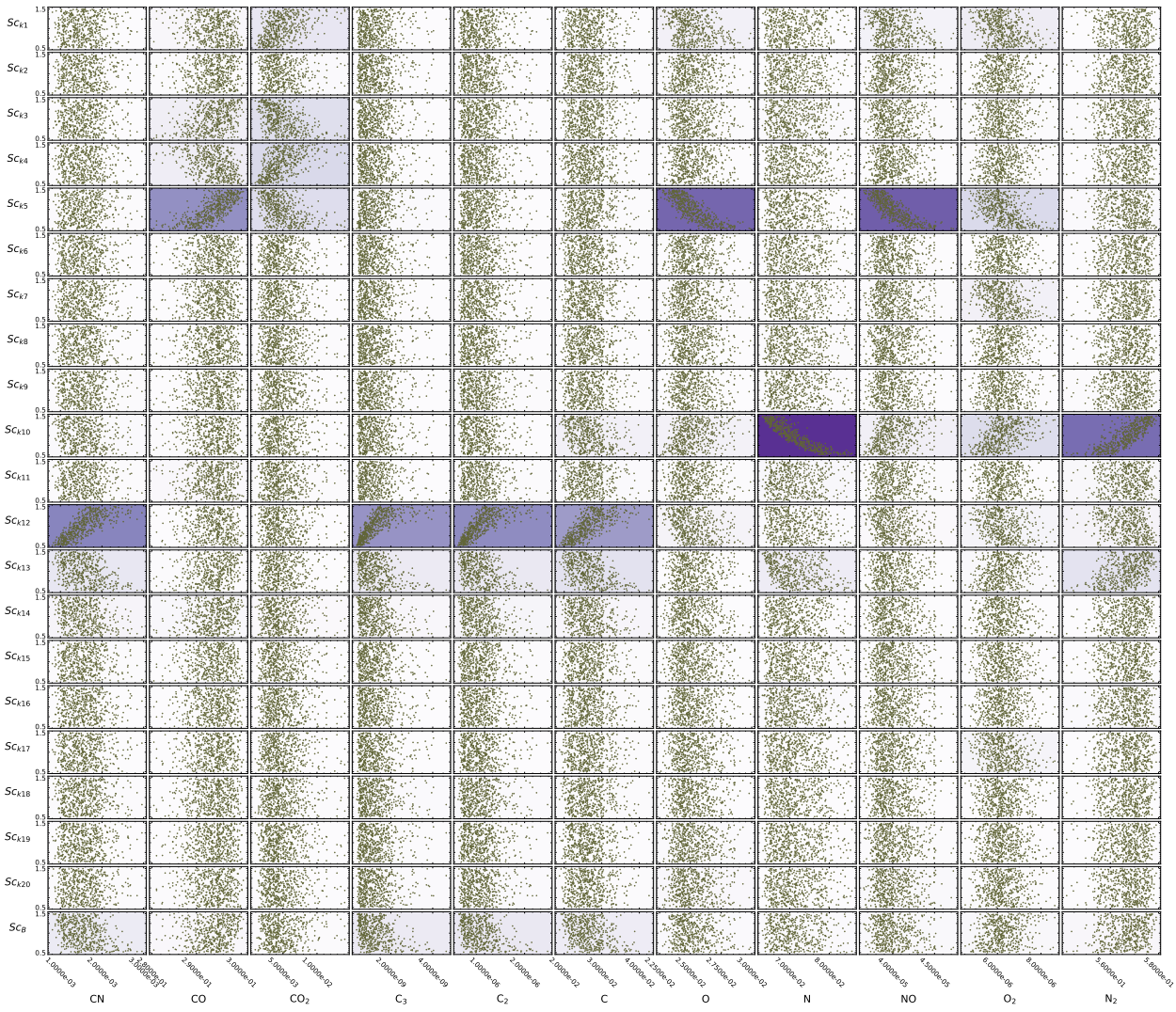

Figure C.10: Scatter and Sobol' data for the ACA model at wall normal locations along the stagnation streamline. Sensitivity scaling parameters are described along the y-axis with corresponding lower and upper bounds used for sampling. Predicted mass fractions are shown along the x-axis. Sobol' index contours are mapped onto plots from Fig. C.9a.

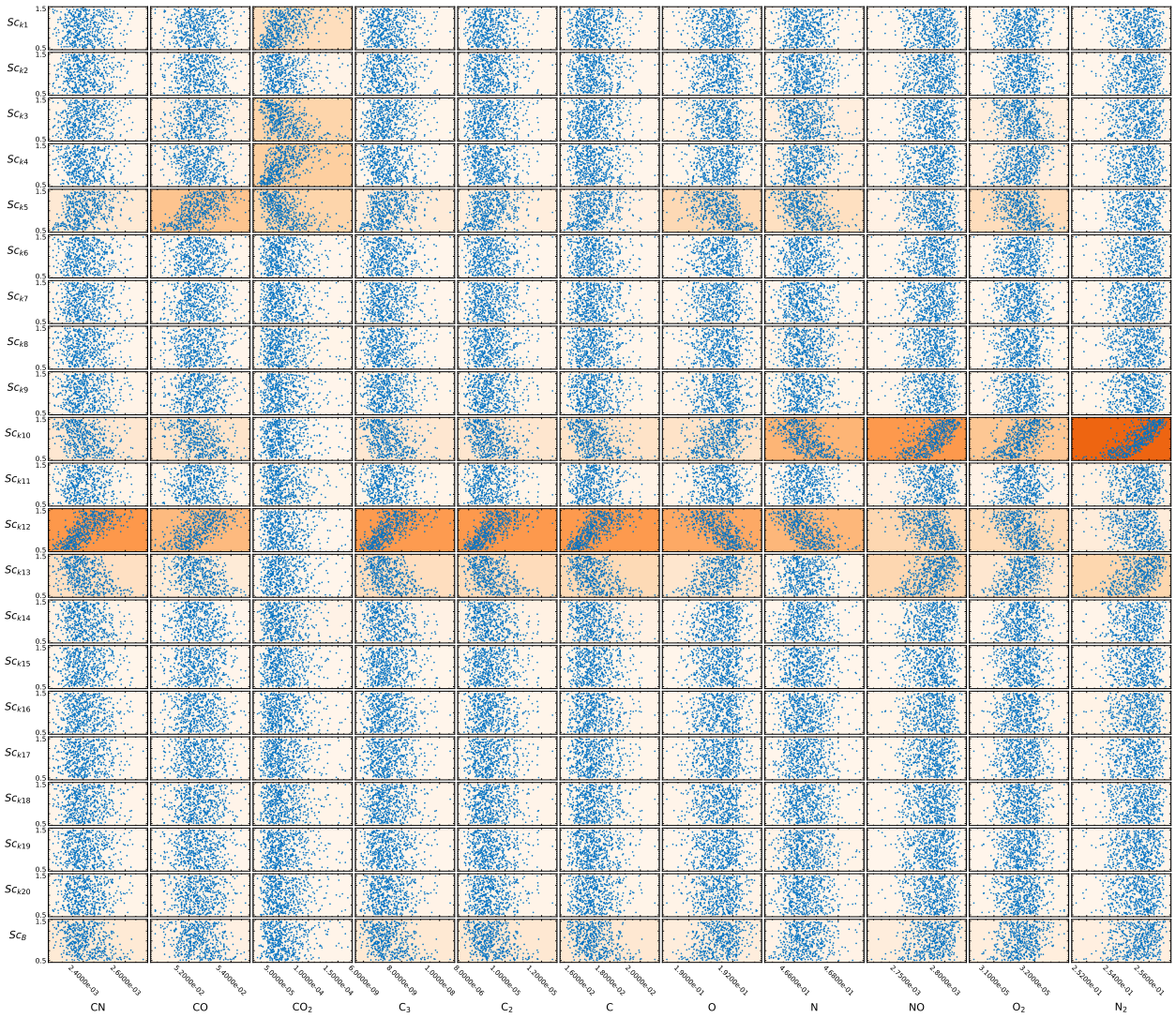

Figure C.11: Scatter and Sobol' data for the ACA model at wall normal locations along the stagnation streamline. Sensitivity scaling parameters are described along the y-axis with corresponding lower and upper bounds used for sampling. Predicted mass fractions are shown along the x-axis. Sobol' index contours are mapped onto plots from Fig. C.9b.

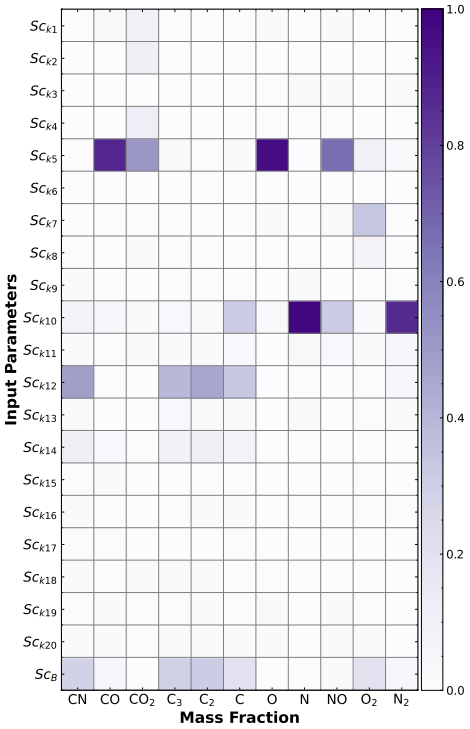

(a) 0.0 mm.

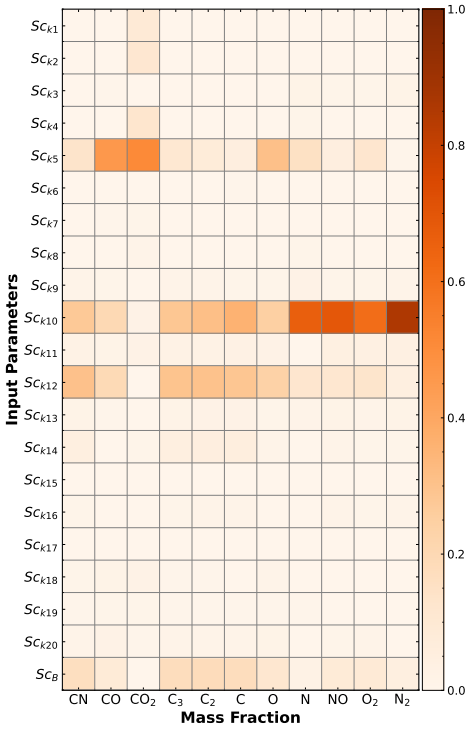

(b) 0.25 mm.

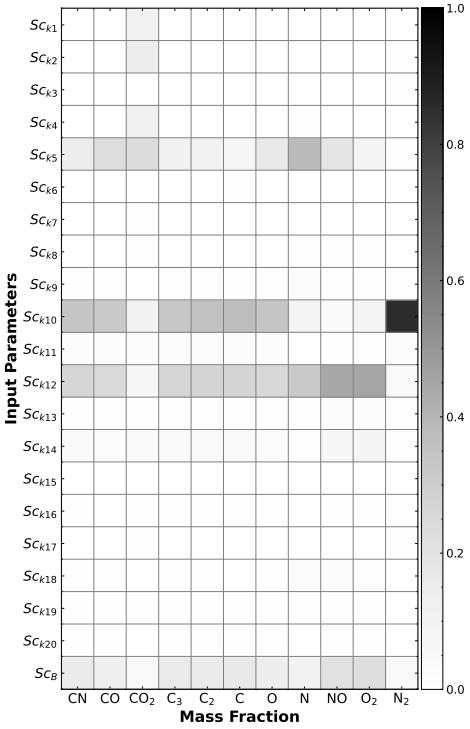

(c) 0.5 mm.

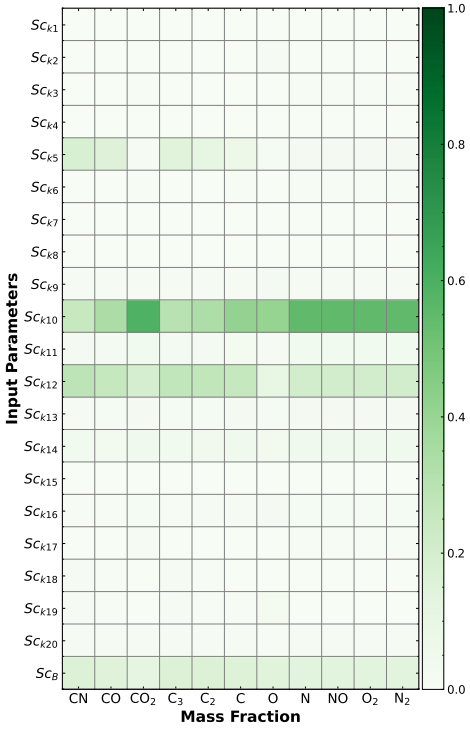

(d) 1.0 mm.

Figure C.12: Sobol' indices for the ACA model that show influence of rate coefficient pre-exponential factors on predicted species mass fractions at wall normal locations along the stagnation streamline. Surface temperature is set to 2410 K.

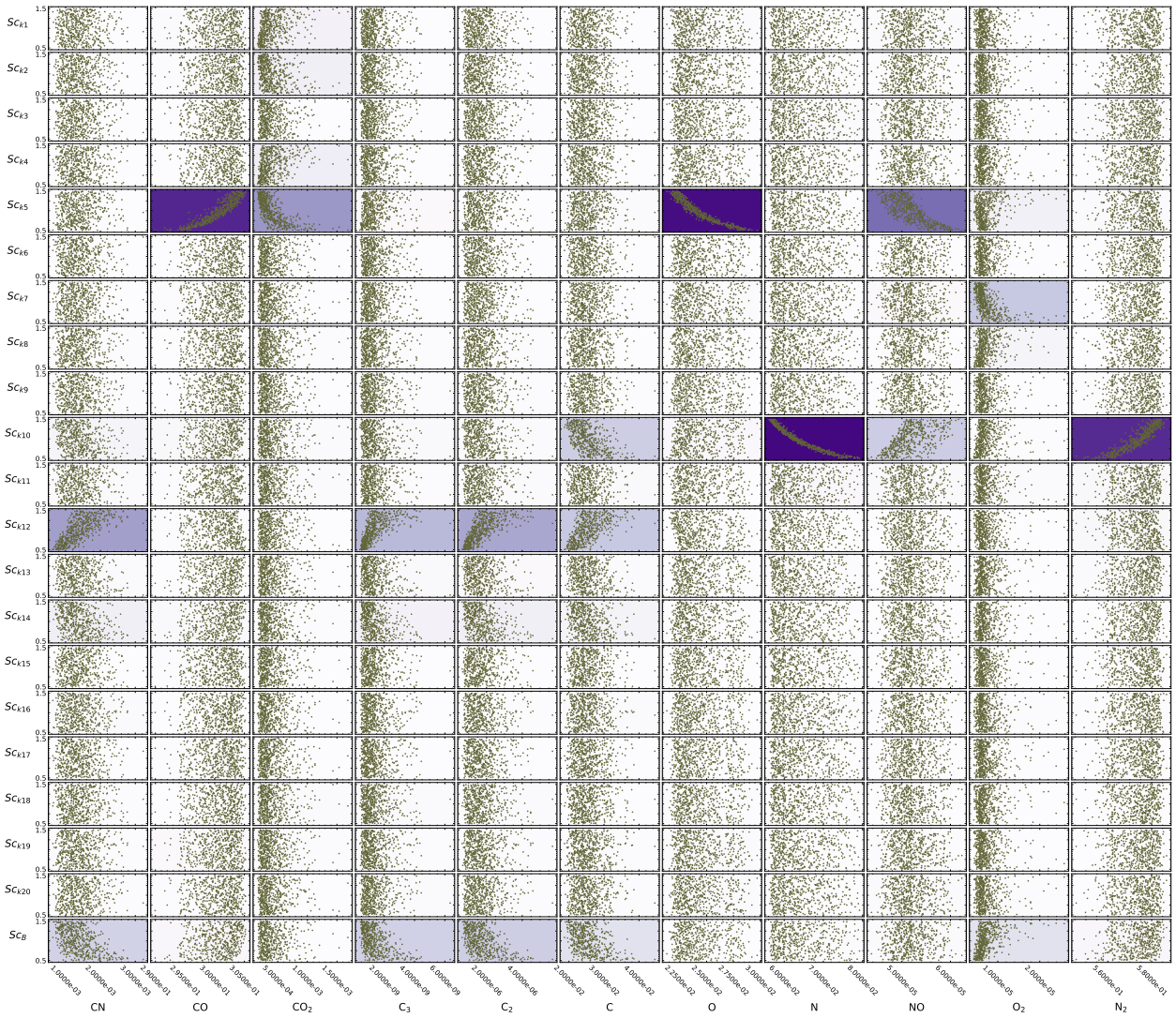

Figure C.13: Scatter and Sobol' data for the ACA model at wall normal locations along the stagnation streamline. Sensitivity scaling parameters are described along the y-axis with corresponding lower and upper bounds used for sampling. Predicted mass fractions are shown along the x-axis. Sobol' index contours are mapped onto plots from Fig. C.12a.

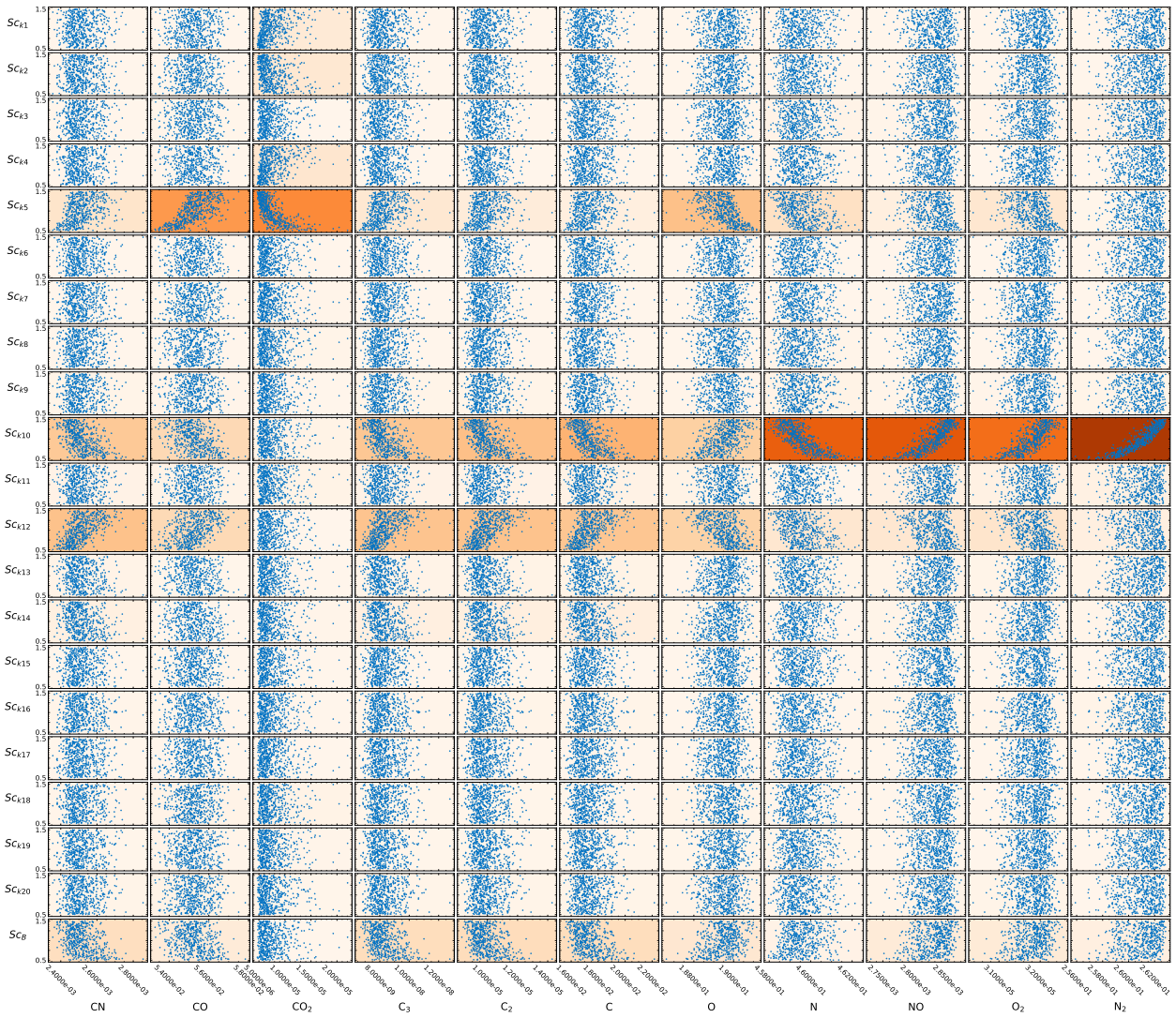

Figure C.14: Scatter and Sobol' data for the ACA model at wall normal locations along the stagnation streamline. Sensitivity scaling parameters are described along the y-axis with corresponding lower and upper bounds used for sampling. Predicted mass fractions are shown along the x-axis. Sobol' index contours are mapped onto plots from Fig. C.12b.

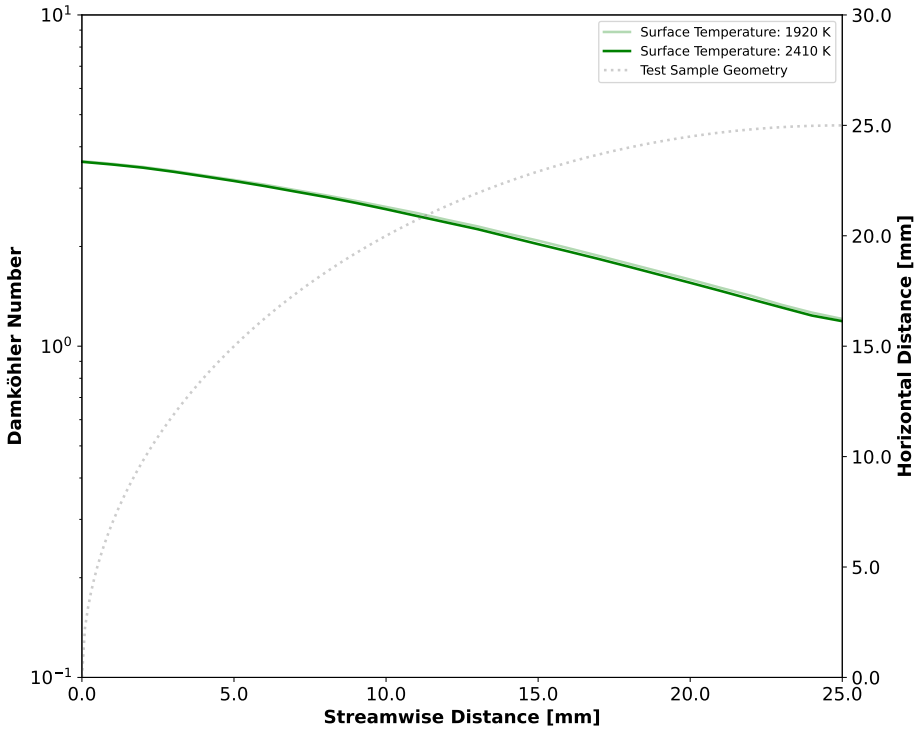

Figure C.15: Comparisons of Damköhler number along the wall for surface temperatures of 1920 and 2410 K. X-2 freestream conditions are in Table C.1. The geometric profile of the test sample is also shown for reference.

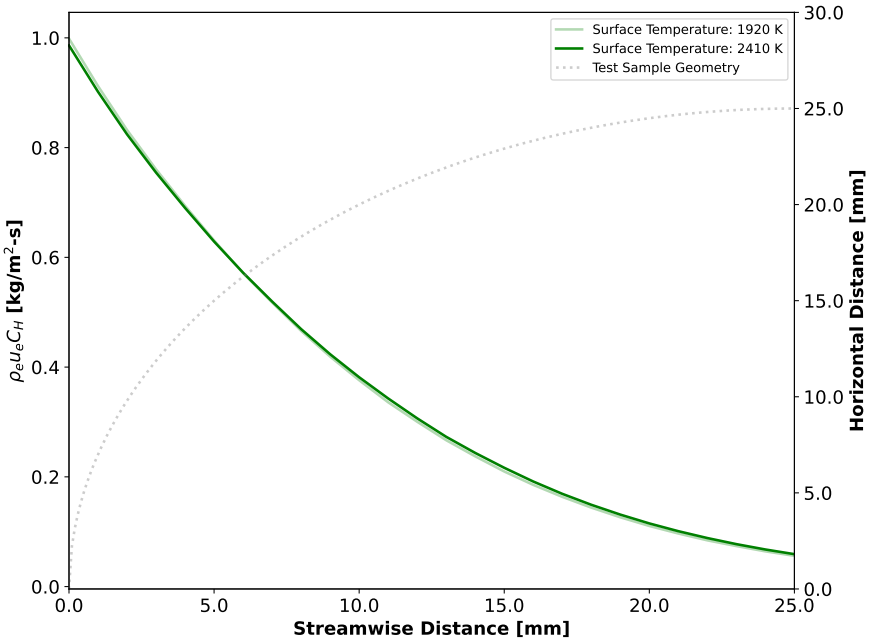

Figure C.16: Comparisons of mass transfer coefficient along the wall for surface temperatures of 1920 and 2410 K. X-2 freestream conditions are in Table C.1. The geometric profile of the test sample is also shown for reference.

References

[1] C.R. Alba. *A Nonequilibrium Finite-Rate Carbon Ablation Model for Radiating Earth Re-entry Flows*. PhD thesis, Air Force Institute of Technology, 2015.

[2] J. Mullins. Credibility process and the predictive capability maturity model (PCMM). Technical Report SAND2017-11636PE, Sandia National Laboratories, Albuquerque, NM, October 2017.

[3] J. Marschall and M. MacLean. Finite-rate surface chemistry model, I: Formulation and reaction system examples. *AIAA Paper 2011–3783*, 2011.

[4] K.S. Prata. *Air-Carbon Ablation for Hypersonic Flow Environments*. PhD thesis, University of Minnesota, 2022.

[5] C. Park. Effects of atomic oxygen on graphite ablation. *AIAA Journal*, 14(11):1640–1642, 1976.

[6] C.R. Alba, R.B. Greendyke, S.W. Lewis, R.G. Morgan, and T.J. McIntyre. Numerical modeling of Earth reentry flow with surface ablation. *Journal of Spacecraft and Rockets*, 53(1):84–97, 2016.

[7] G.V. Candler. Rate effects in hypersonic flows. *Annual Review of Fluid Mechanics*, 51 (1):379–402, 2019.

[8] J.D. Anderson. *Hypersonic and High-Temperature Gas Dynamics*. AIAA Education Series. AIAA, Virginia, 2006.

[9] E. Mussoni, J. Engerer, L. Collins, R. Wagnild, E. Smoll, M. Hansen, B. Hernandez-Sanchez, and S. Babiniec. Advanced finite-rate surface ablation for hypersonic flight.

Technical Report SAND2023-15005R, Sandia National Laboratories, Albuquerque, NM, December 2023.

[10] G. Duffa. *Ablative Thermal Protection Systems Modeling.* AIAA Education Series. AIAA, Virginia, 2013.

[11] D.E. Glass. Ceramic matrix composite (CMC) thermal protection systems (TPS) and hot structures for hypersonic vehicles. *AIAA Paper 2008–2682*, 2008.

[12] S. Poovathingal, T.E. Schwartzentruber, V.J. Murray, T.K. Minton, and G.V. Candler. Finite-rate oxidation model for carbon surfaces from molecular beam experiments. *AIAA Journal*, 55(5):1644–1658, 2015.

[13] F.S. Milos and Y.K. Chen. Ablation and thermal response property model validation for phenolic impregnated carbon ablator. *Journal of Spacecraft and Rockets*, 47(5):786–805, 2010.

[14] R.A. Brewer and D.N. Brand. Thermal protection system for the Galileo mission atmospheric entry probe. *18th Aerospace Sciences Meeting*, 1980.

[15] R.A. Brewer, J.A. Wolfe, and J.W. Metzger. Utilization of a ground test facility to obtain verification of the full scale Pioneer Venus nosecap heat shield. *12th Thermophysics Conference*, 1977.

[16] D. Ellerby. Overview of heatshield for extreme entry environment technology (HEEET). Technical Report ARC-E-DAA-TN73549, National Aeronautics and Space Administration, 2019.

[17] M. Stakepoole. TPS architectures and the influence of material and architecture on failure mode evolution. In *10th Ablation Workshop*, 2018.

[18] S.M. Johnson. Thermal protection materials and systems: Past and future. In *40th International Conference and Exposition on Advanced Ceramics and Composites*, 2015.

[19] D. Kontinos, K. Gee, and D. Prabhu. Temperature constraints at the sharp leading edge of a crew transfer vehicle. *AIAA Paper 2001–2886*, 2001.

[20] T. Ogasawara, T. Aoki, M.S. Aly-Hassan, Y. Mizokami, and N. Watanabe. Ablation behavior of SiC fiber/carbon matrix composites under simulated atmospheric reentry conditions. *Composites: Part A*, 42(3):221–228, 2011.

[21] F.S. Milos and D.J. Rasky. Review of numerical procedures for computational surface thermochemistry. *Journal of Thermophysics and Heat Transfer*, 8(1):379–402, 1994.

[22] M.E. Ewing, T.S. Laker, and D.T. Walker. Numerical modeling of ablation heat transfer. *Journal of Thermophysics and Heat Transfer*, 27(4):615–632, 2013.

[23] D. Bose, M. Olson, B. Laub, T. White, J. Feldman, J. Santos, M. Mahzari, M. MacLean, A. Dufrene, and M. Holden. Initial assessment of Mars Science Laboratory heatshield instrumentation and flight data. *Journal of Thermophysics and Heat Transfer*, 23(3): 425–432, 2009.

[24] A.F. Beerman, M.J. Lewis, R.P. Starkey, and B.Z. Cybyk. Significance of nonequilibrium surface interactions in Stardust Return Capsule ablation modeling. *Journal of Thermophysics and Heat Transfer*, 23(3):425–432, 2009.

[25] D.W. Kuntz. Finite rate carbon ablation. Memo, Sandia National Laboratories, 2008.

[26] S.M. Scala and L.M. Gilbert. Sublimation of graphite at high speeds. *AIAA Journal*, 3(9):1635–1644, 1965.

[27] S.M. Scala. The ablation of graphite in dissociated air, Part I: Theory. Technical Report 62SD72, General Electric Co., September 1962.

[28] D.E. Rosner and H.D. Allendorf. High-temperature kinetics of graphite oxidation by dissociated oxygen. *AIAA Journal*, 3(8):1522–1523, 1965.

[29] V.J. Murray, B.C. Marshall, P.J. Woodburn, and T.K. Minton. Inelastic and reactive scattering dynamics of hyperthermal O and O_2 on hot vitreous carbon surfaces. *The Journal of Physical Chemistry*, 119(26):14780–14796, 2015.

[30] V.J. Murray, P. Recio, A. Caracciolo, C. Miossec, N. Balucani, P. Casavecchia, and T.K. Minton. Oxidation and nitridation of vitreous carbon at high temperature. *Carbon*, 167: 388–402, 2015.

[31] K.S. Prata, T.E. Schwartzentruber, and T.K. Minton. Air-carbon ablation model for hypersonic flight from molecular beam data. *AIAA Journal*, October 2021.

[32] S. Poovathingal, T.E. Schwartzentruber, V.J. Murray, and T.K. Minton. Molecular simulation of carbon ablation using beam experiments and resolved microstructure. *AIAA Journal*, 54(3):995–1006, 2016.

[33] K. Swaminathan-Gopalan, A. Borner, V.J. Murray, S. Poovathingal, T.K. Minton, N.N. Mansour, and K.A. Stephani. Development and validation of a finite-rate model for carbon oxidation by atomic oxygen. *Carbon*, 137:313–332, 2018.

[34] K. Swaminathan-Gopalan, A. Borner, J.C. Ferguson, F. Panerai, N.N. Mansour, and K.A. Stephani. Gas–surface interactions in lightweight fibrous carbon materials. *Computational Materials Science*, 205, 2022.

[35] A. Borner, K. Swaminathan-Gopalan, K.A. Stephani, V. Murray, S. Poovathingal, T. Minton, F. Panerai, and N.N. Mansour. Detailed DSMC surface chemistry modeling of the oxidation of light-weight carbon preform ablators. *AIAA Paper 2017–3687*, 2017.

[36] S.V. Zhluktov, , and T. Abe. Viscous shock-layer simulation of airflow past ablating blunt body with carbon surface. *Journal of Thermophysics and Heat Transfer*, 13(1): 50–59, 1999.

[37] Y. Chen and F.S. Milos. Navier-Stokes solutions with finite rate ablation for planetary mission Earth reentries. *Journal of Spacecraft and Rockets*, 42(6):961–970, 2005.

[38] M. MacLean and J. Marschall. Finite-rate surface chemistry model, II: Coupling to viscous Navier-Stokes code. *AIAA Paper 2011–3784*, 2011.

[39] O.M. Schroeder, J. Brock, E. Stern, and G.V. Candler. A coupled ablation approach using Icarus and US3D. *AIAA Paper 2021–0924*, 2021.

[40] S.W. Lewis, R.G. Morgan, T.J. McIntyre, C.R. Alba, and R.B. Greendyke. Expansion tunnel experiments of Earth reentry flow with surface ablation. *Journal of Thermophysics and Heat Transfer*, 53(5):887–899, 2016.

[41] S.W. Lewis, C.M. James, R.G. Morgan, T.J. McIntyre, C.R. Alba, and R.B. Greendyke. Carbon ablative shock-layer radiation with high surface temperatures. *Journal of Thermophysics and Heat Transfer*, 31(1):476–484, 2017.

[42] C. Park, G.A. Raiche, D.M. Driver, J. Olejniczak, I. Terrazas-Salinas, T.M. Hightower, and T. Sakai. Comparison of enthalpy determination methods for arc-jet facility. *Journal of Thermophysics and Heat Transfer*, 20(4):672–679, 2006.

[43] A. del Val, T.E. Magin, and O. Chazot. Uncertainty assessment on the characterization of testing conditions in arc-jet facilities. *AIAA Paper*, 2017.

[44] A.J. Brune and C.C. Morrow. Uncertainty analysis of slug calorimeters in the NASA HyMETS arc-jet facility. *Journal of Thermophysics and Heat Transfer*, 38(2):232–249, 2024.

[45] P.M. Danehy, B.F. Bathel, C.T. Johansen, M. Winter, S. O'Byrne, and A.D. Cutler. *Hypersonic Nonequilibrium Flows: Fundamentals and Recent Advances*, chapter Molecular-Based Optical Diagnostics for Hypersonic Nonequilibrium Flows. Progress in Astronautics and Aeronautics. AIAA, 2015.

[46] C.O. Johnston, A. Brandis, and D. Bose. Radiative heating uncertainty for hyperbolic Earth entry, Part 3: Comparisons with electric arc shock-tube measurements. *Journal of Spacecraft and Rockets*, 50(1):48–55, 2013.

[47] J. Ray, S. Kieweg, B. Carnes, G. Weirs, B. Freno, M. Howard, T. Smith, I. Nompelis, and G.V. Candler. Estimation of inflow uncertainties in laminar hypersonic double-cone experiments. *AIAA Journal*, 58(10):4461–4474, 2020.

[48] S. Gu and H. Olivier. Capabilities and limitations of existing hypersonic facilities. *Progress in Aerospace Sciences*, 113:1–27, 2020.

[49] T. Hermann, S. Löhle, U. Bauder, R. Morgan, H. Wei, and S. Fasoulas. Quantitative emission spectroscopy for superorbital reentry in expansion tube X2. *Journal of Thermophysics and Heat Transfer*, 31(2):257–268, 2016.

[50] U.A. Sheikh, R.G. Morgan, and T.J. McIntyre. Vacuum ultraviolet spectral measurements for superorbital Earth entry in X2 expansion tube. *AIAA Journal*, 53(12):3589–3602, 2015.

[51] F. Zander, R.G. Morgan, U. Sheikh, D.R. Buttsworth, and P.R. Teakle. Hot-wall reentry testing in hypersonic impulse facilities. *AIAA Journal*, 51(2):476–484, 2013.

[52] C.R. Alba, R.B. Greendyke, and J. Marschall. Development of a nonequilibrium finite-rate ablation model for radiating Earth reentry flows. *Journal of Spacecraft and Rockets*, 53(1):98–120, 2016.

[53] N. Banerji, P. Leyland, E. Fahy, and R. Morgan. Earth reentry flow over a phenolic aeroshell in the X2 expansion tube. *Journal of Thermophysics and Heat Transfer*, 32 (52):414–428, 2017.

[54] O. Chazot and F. Panerai. *Hypersonic Nonequilibrium Flows: Fundamentals and Recent*

Advances, chapter High-Enthalpy Facilities and Plasma Wind Tunnels for Aerothermodynamics Ground Testing. Progress in Astronautics and Aeronautics. AIAA, 2015.

[55] A.L. Zibitsker, J.A. McQuaid, E. Stern, G. Palmer, B. Libben, C. Brehm, and A. Martin. Finite-rate and equilibrium study of graphite ablation under arc-jet conditions. *Computers & Fluids*, 267:1–20, 2023.

[56] G.V. Candler, H.B. Johnson, I. Nompelis, V.M. Gidzak, P.K. Subbareddy, and M. Barnhardt. Development of the US3D code for advanced compressible and reacting flow simulations. *AIAA Paper 2015–1893*, 2015.

[57] I. Nompelis and G.V. Drayna, T.W. Candler. Development of a hybrid unstructured implicit solver for the simulation of reacting flows over complex geometries. *AIAA Paper 2004–2227*, 2004.

[58] I. Nompelis and G.V. Drayna, T.W. Candler. A parallel unstructured implicit solver for hypersonic reacting flow simulation. *Parallel Computational Fluid Dynamics 2005*, 2005.

[59] G.V. Candler, C.R. Alba, and R.B. Greendyke. Charactertization of carbon ablation models including effects of gas-phase chemical kinetics. *Journal of Thermophysics and Heat Transfer*, 31(3):512–526, 2017.

[60] C. Park. Assessment of two-temperature kinetic model for ionizing air. *Journal of Thermophysics and Heat Transfer*, 3(3):233–243, 1989.

[61] W.G. Vincenti and C.H. Kruger. *Introduction to Physical Gas Dynamics*. Krieger Publishing Company, London, 1965.

[62] R.C. Millikan and D.R. White. Systematics of vibrational relaxation. *Journal of Chemical Physics*, 39(12):3209–3213, 1963.

[63] C.R. Wilke. A viscosity equation for gas mixtures. *Journal of Chemical Physics*, 18(4): 517–519, 1950.

[64] A. Eucken. On the thermal conductivity, the specific heat and the viscosity of gases. *Physikalische Zeitschrift*, 14(4):324–333, 1913.

[65] C. Park. Review of chemical-kinetic problems of future NASA missions. I-Earth entries. *Journal of Thermophysics and Heat Transfer*, 7(3):385–398, 1993.

[66] C. Park. *Nonequilibrium Hypersonic Aerodynamics*. Wiley, 1990.

[67] G.V. Candler. Nonequilibrium processes in hypervelocity flows: An analysis of carbon ablation models. *AIAA Paper 2012–0724*, 2012.

[68] M.J. Wright, T. White, and N. Mangini. Data parallel line relaxation (DPLR) code user manual: Acadia-version 4.01.1. Technical Report TM-2009-215388, NASA, 2009.

[69] I.G. Pitt and R.G. Gilbert. Application of transition-state theory to gas-surface reactions: Barrierless adsorption on clean surfaces. *Journal of Physical Chemistry*, 98(49): 13001–13010, 1994.

[70] C. Park. Stagnation-point ablation of cabonaceous flat disks - Part I: Theory. *AIAA Journal*, 21(11):1588–1594, 1983.

[71] C. Park and D.W. Bogdanoff. Shock-tube measurement of nitridation coefficient of solid carbon. *Journal of Thermophysics and Heat Transfer*, 20(3):487–492, 1983.

[72] D.M. Driver and M. Maclean. Improved predictions of PICA recession in arc jet shear tests. *AIAA Paper 2011–0141*, 2011.

[73] C. Xu and T.K. Minton. Effect of N atoms on O-atom reactivity with carbon. *Journal of Spacecraft and Rockets*, 58(3):906–909, 2021.

[74] D.Z. Chen. *The Effects of Atomic Oxygen on Silicon-Carbon Systems in Extreme Environments*. PhD thesis, Montana State University, 2021.

[75] S. Poovathingal. *Predictive Finite Rate Model for Oxygen-Carbon Interactions at High Temperature*. PhD thesis, University of Minnesota, 2016.

[76] R. Edel, B.W. Grabnic, and S.J. Sibener. Atomically-resolved oxidative erosion and ablation of basal plane HOPG graphite using supersonic beams of O_2 with scanning tunneling microscopy visualization. *Journal of Chemical Physics*, 122(26):14706–14713, 2018.

[77] D.R. Olander, W. Siekhaus, and J.A. Schwarz. Reactions of modulated molecular beams with pyrolytic graphite. I. Oxidation of the basal plane. *Journal of Physical Chemistry C*, 57(1):408–420, 2018.

[78] J. Cooper, G. Salazar, and A. Martin. Numerical investigation of film coefficient engineering methodology for dissociated, chemically reacting boundary layers. *AIAA Paper 2022–1907*, 2022.

[79] D.B. Spalding. The art of partial modeling. *Symposium (International) on Combustion*, 9(1):833–843, 1963.

[80] D. Kuntz, B. Hassan, and D. Potter. An iterative approach for coupling fluid/thermal predictions of ablating hypersonic vehicles. *AIAA Paper 1998–3460*, 1998.

[81] C.B. Moyer and R.A. Rindal. An analysis of the coupled chemically reacting boundary layer and charring ablator. Part 2 - Finite difference solution for the in-depth response of charring materials considering surface chemical and energy balance. Technical Report NASA-CR-1061, NASA, 1968.

[82] W.L. Oberkampf, M. Pilch, and T.G. Trucano. Predictive capability maturity model

for computational modeling and simulation. Technical Report SAND2007-5948, Sandia National Laboratories, Albuquerque, NM, 2007.

[83] L.P. Swiler and G.D. Wyss. A user's guide to Sandia's latin hypercube sampling software: LHS UNIX library/standalone version. Technical Report SAND2004-2439, Sandia National Laboratories, Albuquerque, NM, 2004.

[84] B.M. Adams. The Dakota toolkit for parallel optimization and uncertainty analysis. Technical Report SAND2008-3204C, Sandia National Laboratories, Albuquerque, NM, 2008. An optional note.

[85] I.M. Sobol. Sensitivity Estimates for Nonlinear Mathematical Models. *Math. Model. Comput. Exp.*, 1:407–414, 1993.

[86] T. Homma and A. Saltelli. Importance measures in global sensitivity analysis of nonlinear models. *Reliability Engineering & System Safety*, 52(1):1–17, 1996.

[87] G. Blyholder and H. Eyring. Kinetics of graphite oxidation. *Journal of Physical Chemistry*, 61(5):682–688, 1957.

[88] J.W. Hargis, C. Murzyn, E. Mussoni, W. Swain, and J.L. Lynch, K.P. Wagner. Carbon monoxide laser absorption spectroscopy measurements over ablating graphite in a shock tunnel. *AIAA Journal*, submitted for review.

[89] K.P. Lynch, T. Grasser, P. Farias, K. Daniel, R. Spillers, C.R. Downing, and J.L. Wagner. Design and characterization of the Sandia free-piston reflected shock tunnel. *AIAA Paper 2022–0968*, 2022.

[90] E. Mussoni, R. Wagnild, J. Winokur, and J.P. Delplanque. Sensitivity analysis of air/carbon finite-rate surface ablation models. *AIAA Paper 2022–3944*, 2022.

[91] A. Turchi, P.M. Congedo, and T.E. Magin. Thermochemical ablation modeling forward uncertainty analysis - Part I: Numerical methods and effect of model parameters. *International Journal of Thermal Sciences*, 118:497–509, 2017.

[92] C. Park, R.L. Jaffe, and H. Partridge. Chemical-kinetic parameters of hyperbolic Earth entry. *Journal of Thermophysics and Heat Transfer*, 15(1):76–89, 2001.

[93] C. Park and D. Bogdanoff. Shock-tube measurement of nitridation coefficient of solid carbon. *Journal of Thermophysics and Heat Transfer*, 20(3):487–492, 2006.

[94] G. Palmer, D. Prabhu, and B.A. Cruden. Uncertainty determination for aeroheating in Uranus and Saturn probe entries by the Monte Carlo method. *AIAA Paper 2013–2776*, 2013.

[95] C. Sorensen, P. Valentini, and T.E. Schwartzentruber. Uncertainty analysis of reaction rates in a finite-rate surface-catalysis model. *Journal of Thermophysics and Heat Transfer*, 26(3):407–416, 2012.

[96] E. Jans, K.P. Lynch, R. Wagnild, W.E. Swain, C. Downing, S.P. Kearney, J.L. Wagner, J.J. Gilvey, and C.S. Goldenstein. Laser-based characterization of reflected shock tunnel freestream velocity and multi-species thermal nonequilibrium with comparison to modeling. *AIAA Paper 2024–1753*, 2024.

[97] J.D. Engerer and L.N. Collins. Pre-tabulated thermochemistry for finite-rate ablation via the oxygen-consumption Damköhler number. In *13th Ablation Workshop*, Mountain View, CA, November 2023.